The Initial Mass Function and star-formation history in the 30 Doradus super-association

Thesis by

Fernando J. Selman

In Partial Fulfillment of the Requirements
for the Degree of
Doctor of Philosophy

California Institute of Technology
Pasadena, California

2004
(Defended October 28, 2003)

I dedicate this thesis
to my mother,
and to the memory of my father,
my rocks;
to Timothy and Mireya,
my stars;
with love.

"... the will is infinite, and the execution confined; ... the desire is boundless, and the act a slave to limit."

Willian Shakespeare
Troilus and Cressida, Act III, Scene II

"..., miro este querido mundo que se deforma y que se apaga en una pálida ceniza vaga que se parece al sueño y al olvido."

Jorge Luis Borges
Poem of Gifts

Acknowledgements

I would like to thank Jorge Melnick for the help he gave me at a crucial moment of my life. Without his guidance and support this thesis and the completion of my PhD would not have been possible. Many thanks also to the other members of the Tarantula gang, Roberto and Elena Terlevich, and Guille Bosch.

I thank Nick Scoville for accepting being my advisor, and for all the guidance he gave me. This work was much improved thanks to his rigorous approach to observational astronomy, and his many comments and suggestions. The astronomy faculty at Caltech was unanimous in their welcoming and opening of doors giving me all their support. Special thanks go to Sri Kulkarni, Wall Sargent, Judy Cohen, George Djorgovsky, Peter Goldreich, and Tony Redhead. Thanks also to the staff at Robinson: Ferne, Gita, Loly, Gina, and Judith; your help, encouragement and support are much appreciated.

Going back to Caltech after so many years was a very beautiful experience. The walls of Robinson brought to me many memories. Particularly vivid were those of the late Alain Porter, Helen Knudsen, and of my classmates and friends Jim McCarthy, Pawan Kumar, Marcus Chown, Mike Rich, Abi Saha, Joshua Roth, Rick Edelson, Dany Neuhauser, and Mary Barsony. Those were special times in my life, much enriched by the inspired teachings of the late Richard Feynman. To all of them many thanks.

I would like to thank the Observatories of the Carnegie Institution which supported me during my graduate studies with a Carnegie-Chile fellowship. The staff members of the observatories were always available, my thanks specially to Alan Dressler, Steve Schectman, and Paul Schechter.

Closer in space and time are the people at ESO and La Silla. Without their continuous support this work would have been much more difficult if not impossible. Dietrich Baade gave me his support at the right moment. My direct supervisors, Olivier Hainaut and Rene Mendez, cleared large spans of time in my schedule so that

I could spend several months at Caltech. The operators at the 2.2 m MPG/ESO telescope, Jorge Araya, Roberto Castillo, Jose Cortes, Cristian Esparza, Pancho Labraña, and Mauricio Martinez, all of them at one time or another offered their help so that I could finish this project. To all the people at La Silla, thank you. The people at ESO Santiago have always being of much help; special thanks to Mar'ıa Eugenia y Andrea for the many times they have gone out of their way to help.

My special thanks to the new Chilean gang in Pasadena: to Marco, Pamela, Catalina, and Bianca Bonatti, a family that opened their doors and their hearts and gave me a home away from home; to Dany and Claudia, although you made me take the Supershuttle, my thanks anyhow; and to Solange and her beautiful family, I will never forget "Felipe tiene hambre."

The years at Universidad de Chile seem so distant yet so vital. It was there where everything really got started thanks to the efforts of Igor Saavedra and the other teachers: Romualdo Tabensky, Francisco Brieva, Patricio Cordero, Fernando Lund, Danilo Villarroel, and Lincoyan Gonzalez. These were special, magical times, that I specially enjoyed thanks to the company of my classmates Hugo Arellano, Christian Elphick, and Victor Fuenzalida.

No man is an island, and my family and friends are my continent. My mother and father, Juan y Adriana, always believed in me, and taught me the meaning of the words *faith* and *loyalty,* and showed by example that life can be made beautiful. Lili, Juan Carlos, Ana María, Jose Miguel, and Juan Cristian, my brothers and sisters, were always there despite time and distance. Juan Carlos placed the seed that started me in the direction of science, in effect rescuing me from the routines of school. My godparents, Antonio and Rebeca Chanes, also gave me a home away from home. These are the kind of debts that can never be payed back. My friends Francisco, Juan Ignacio, y Fernando Gago are also part of the continent. Many thanks also to Pancho, Pablo, Mireya, Cristian, and Pitu, the latest members of our extended family, for their friendship and support (and for more than a few character building episodes).

The completion of a project like this while working full time with a turno schedule at an observatory places extreme demands on one's time. I thank my wife, Mireya, for all her love, kindness, and patience during these hard times. My largest debt of time is for my son, Tim, whom I love so much. I hope to have enough life to honor it. It will be a pleasure to start paying them back.

Abstract

We present a study of the star-formation history (SFH), and the initial mass function (IMF) in the 30 Doradus super-association. The study is divided in six natural stages: (1) profile fitting photometry; (2) characterization of the instrument; (3) calibration using stars with spectroscopy; (4) visualization of the stellar properties using the color-magnitude stereogram; (5) Bayesian analysis to obtain physical quantities; and (6) the construction of the SFH and IMF. The reduction and characterization of systematic errors are the most important steps of any IMF study: we note the following sources of systematic errors: (a) the upper magnitude cut-off, used to filter out saturated and non-linear stars, results in a false steepening of the high-mass end of the IMF, particularly affecting older systems; (b) Be stars and blue B-type supergiants mimic luminosity class V stars of higher effective temperatures, thus flattening the IMF; (c) the magnitude limit effect introduced by variable reddening, that flattens the low mass end of the derived IMF. For IMF determination we have identified the mass window $10M_{\odot} \leq M \leq 40M_{\odot}$, that is free of effects (a) and (c) in our photometry. We have found that the SFH of the region is characterized by a 7-15 My old burst, *across the whole area studied,* followed by a period of reduced, nearly constant, star-formation activity. This activity has been punctuated by clustered, burst-like, star-formation episodes of varying intensity in several places. For NGC2070, the OB association LH104, and the field, the derived IMFs are consistent with a power law with Salpeter slope *only if they have different SFH:* a young and almost instantaneous burst for NGC2070, and nearly constant star formation, after the 7-15 My burst for the field and LH104. Other studies reveal star-formation episodes across the LMC, starting 15-30 My ago. We propose that the origin of such an apparently synchronized, large-scale, activity, is the recent entry of the LMC into a thick disk of ionized gas, analogous to that proposed by Moore and Davis (1994) to explain the origin of the Magellanic Stream.

Contents

List of Figures

List of Tables

.

Chapter 1

Introduction

In this thesis we present a study of the star-formation history of the 30 Doradus super-association going from its important central cluster, NGC2070, to the larger area of the super-association. The motivation for this project is twofold. In the first place is the study of the universality of the high-mass end ($M > 10M_{\odot}$) of the Initial Mass Function (IMF). 30 Doradus allows us to probe a wide range of densities and hence study the effect of environment on the IMF. The assumed IMF has been an uncertainty for studies as diverse as the origin of elliptical galaxies and the energetics of starbursts. It is a prerequisite to understand what is behind the light we observe from faint galaxies at high redshift. The chemical enrichment of the universe also depends strongly on the IMF.

Any theory of star formation should account for the origin of the IMF and its environmental dependencies. If these are not firmly established by observations there is no hope for a meaningful comparison between observations and theory. In a recent review article, Kroupa (2002) concludes that the massive star IMF is nearly universal, while the opposite view has been advocated by others (i.e., Scalo 2000), *based on the same data set!* The study of a region with sub-components of varying density using the same methodology, therefore, would be an important contribution.

The second motivation for this study is to understand the sequence of events that resulted in the extreme star-formation activity observed in 30 Doradus. What is the star-formation history (SFH) of the super-association? Are there age gradients? Does it show the fingerprints of a trigger, and if so, what triggered it?

30 Doradus allows us to study the dynamics of star formation because we can study its stellar population in detail, determining stellar positions, masses, and ages on an individual basis for a large number of stars. In this regard 30 Doradus can be

called a mini-universe, and, although it does not allow us to do controlled experiments, it is the closest thing to a star-formation laboratory that we will find. We can find supernovae, blackholes, young massive clusters of different ages, supergiant shells, giant HII regions, OB associations, protostars, Wolf-Rayet stars, and some of the most massive stars known. This research presents the first steps by the author into this mini-universe.

In the rest of this chapter we will give a short description of the 30 Doradus super-association (an overview of the Magellanic Clouds, focused on those aspects that are relevant to what will follow can be found in Appendix A). Our previous work on NGC2070, the ionizing cluster of 30 Doradus, is summarized directing the reader to the published papers reprinted in Appendix C. Finally, we enumerate the questions that we address in this thesis. In Chapter 2 we describe the procedures and programs used to perform profile fitting photometry and to calibrate the Wide Field Imager at the MPG/ESO 2.2-m telescope. We also present a method to determine the spatial variations of the photometric zero points, a problem that plagues most wide-field imagers with focal reducers. In Chapter 3 we describe the Bayesian technique used to determine stellar physical parameters from UBV photometry. In Chapter 4 we use a 3-D visualization tool, developed by myself, to present the final catalog of physical quantities. Some particular issues related to the calibration are also discussed. In Chapter 5, after first comparing the HR diagrams of a few selected regions with those published by other authors, we present the SFH and IMF of selected regions, and those of the field. Finally, Chapter 6 discusses the impact of these results to our understanding of star formation in the LMC, and of the universality of the IMF.

1.1 The 30 Doradus super-association

The concept of super-association was introduced by Ambartsumian (1963) to describe the brightest star-forming regions in late-type galaxies. They are the largest structures in a hierarchy that goes from OB associations, "the closest thing to nothing that is still something" (Garmany 1992), to these large complexes of giant HII regions, OB associations, star clusters, etc, extending over areas with characteristic sizes $\sim$1 kpc (Melnick 1986). 30 Doradus is the prototype super-association and the only one that can be studied in detail from the ground. Figure 1.1 shows the whole super-association with some of its most conspicuous features. Spread over an area

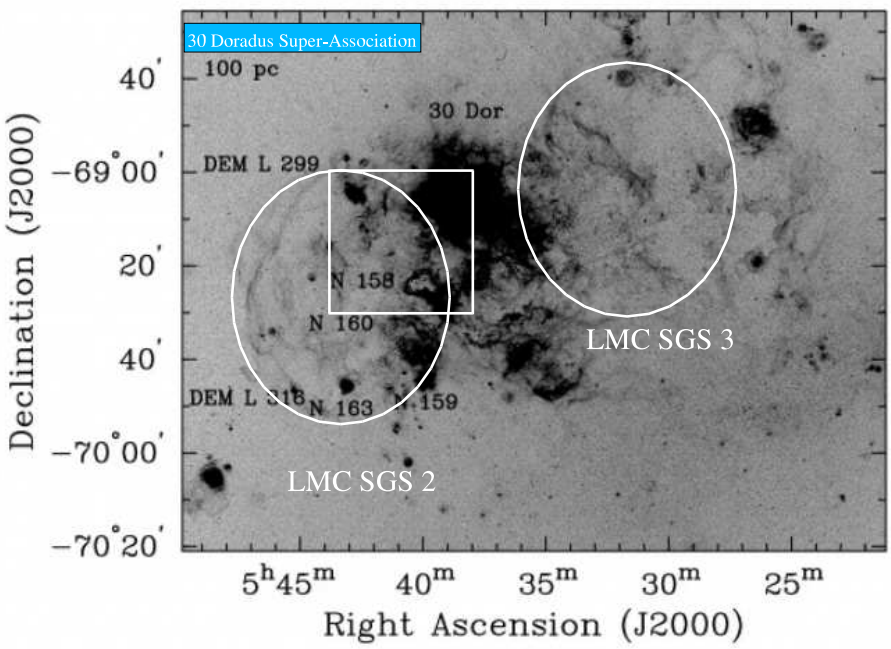

Figure 1.1: H_α image of the 30 Doradus super-association. The image was taken from Dunne et al. (2001) showing the main components of the super-association. We have superimposed the outlines of the two super-giant shells, and the WFI field studied in this thesis.

approximately 2 kpc × 1 kpc running diagonally from LMC SGS 2 to the SE, the Tarantula nebula near the center, and LMC SGS 3 to the NW (for the nomencalture see Appendix A and Figure A.2), corresponding to Shapley Constellation II, and to N135 (Henize 1956). Here we find the two super-giant shells mentioned (Meaburn 1980), the Tarantula nebula, N157A (N157 ≡ DEM263), a giant HII region (Chu and Kennicutt 1994; Melnick et al. 1999) ionized by the cluster NGC2070; many other lesser HII regions (Henize 1956; Davies et al. 1976; Kennicutt and Hodge 1986); numerous young OB associations (Lucke and Hodge 1970) with ages ranging between 3 My to 10 My (Lucke 1974); large numbers of Wolf-Rayet (WR) and other emission-line stars (Melnick 1985); large numbers of supergiants (Lortet and Testor 1984); and several supernova remnants (Mathewson et al. 1983) including SN1987A.

Kennicutt et al. (1995) measured the total H_α luminosity of the LMC to be 2.7×10^{40}erg/s corresponding to a total star-formation rate (SFR) of $0.26 M_\odot$/y; 30% of this comes from within 1^o of 30 Doradus. Of the two supergiant shells, only LMC SGS 2 has been extensively studied (Points et al. 1999; 2000). The major conclusions are that this SGS does not show a global coherent expansion, but only localized expansion structures. The total H_α luminosity of this shell is 2×10^{39}erg/s

(Kennicutt et al. 1995), corresponding to a SFR $\sim 0.02 M_{\odot}/y$. Points et al. (2000) present a model in which the SGS is attributed to gas expanding between two sheets of HI gas seen face on and bordered to the west by a high density ridge of molecular gas.

1.2 Published work and objectives

We have extensively studied the properties of the central cluster (NGC2070) in a series of published papers (Selman et al. 1999a, Paper I; Bosch et al. 1999, Paper II; Selman et al. 1999b, Paper III; and Bosch et al. 2001, Paper IV). The photometry, the extinction properties of the region, and the introduction of a novel visualization tool, the color-magnitude stereogram, were the subject of Paper I; the spectral classification of a large number of stars was the subject of Paper II; Paper III combines the photometry of Paper I with the spectral classification from Paper II to determine the IMF and star-formation history of the central cluster; finally, Paper IV uses the spectral data from Paper II to study the dynamics of the cluster. These papers are reprinted in Appendix C. Here we present a summary of the results relevant for the rest of this thesis:

- The reddening law of the region was found to be nearly the same as in the Milky Way. The ratio of total-to-selective extinction is constant, close to the normal value, $R_V = 3.05$. The slope of the projection of the reddening vector in the color-color plane was found to be

$$S = \frac{E(U-B)}{E(B-V)} = 0.82 \pm 0.03,$$

  where the error quoted is the standard error of the mean of 81 stars with spectral types (the standard deviation is 0.27 (Paper I)).

  In Paper III we found that, for $M > 10 M_{\odot}$ the reddening is independent of stellar mass, and increases toward the center confirming the findings of Paper I.

  The extinction was found to vary widely within the cluster. There is a smooth, moderate, component of the reddening most likely associated with NGC2070 that decreases from the center outward (Paper I, Paper III).

- The *magnitude-limit* effect was described in Paper III and found to be the most

important systematic effect near the limit of the photometry. The meaning of "near" is dictated by the range in reddening values: if the range in reddening values is 1.5 mag, then we can only analyze stars 1.5 mag brighter than the limit of the photometry. This effect, if not corrected for, leads to a false flattening of the IMF for small masses which could be mistakenly interpreted as turn-offs or flattening.

- The star-formation history was found to be dominated by three burst-like episodes at $\leq$ 1.5 My, $\sim$ 2.5 My, and $\sim$ 5 My ago. These three *bursts* appear to be spatially disjoint with the youngest stars concentrated toward the center while the 2.5 My stars appear to delineate a spherically symmetric structure of 6 pc radius, slightly off-center. The observations are consistent with a picture where star formation propagated inward (Paper III).

- For r $>$ 15″ the IMF is found to be well represented by a power law with $\Gamma = -1.37 \pm 0.08$ for 3 $M_\odot$ $<$ M $<$ 120$M_\odot$, consistent with the Salpeter slope. For 4.6″ $<$ r $<$ 19″ and 10 $M_\odot$ $<$ M $<$ 120$M_\odot$ we find $\Gamma = -1.37 \pm 0.10$. Combining our data with HST observations there is marginal evidence for a flattening of the IMF toward the center of the cluster.

- The spatial density profile of stars between 0.4 pc and 6 pc is well represented by a single power law with slope -2.85, steeper than isothermal. This means that the total mass increases very slowly with radius as $r^{0.15}$.

  The density profile clearly shows the excess of stars at 6 pc. Moreover, this shell appears to have a larger than normal proportion of high-mass stars, providing evidence that Elemegreen's (1997) stochastic model of star formation is not dominant here. The steeper profile of the cluster, together with the features in the density profile in the outer radial bins, indicates that the cluster is not relaxed, but might still have memory of its collapse (Paper III).

  The total mass in stars more massive than $3M_\odot$ is found to be $\sim 7 \times 10^4 M_\odot$. If we extrapolate the IMF down to $0.1 M_\odot$ this number increases to $3 \times 10^5 M_\odot$.

- The study of the stellar kinematics carried out in Paper IV concluded that the velocity dispersion was much too large to be due to the self-gravity of the cluster. Instead, the observed dispersion seems to be dominated by binary star orbital

motions. There is no evidence for energy equipartition: the data are consistent with the same velocity distribution function independent of mass. The dynamical mass of the cluster obtained assuming that all the stars are binaries was found to be consistent with the photometric mass derived in Paper III from the IMF.

The work on NGC2070 had a rather limited scope, as we were mainly interested in the determination of the slope of the IMF in this extreme environment. Nevertheless, in the course of this research several questions arose that led us to extend the work to a larger area in the super-association:

- Can we recognize the same bursts of star-formation in other areas of the super-association? If so, can we see age gradients?
- What is the space distribution of stars in the region and how does it vary with age? In the previous work there appears to be a relation between age and spatial correlation function, which we did not quantify. The relation is in the sense that stars belonging to the younger burst appear to cluster more tightly than the older ones. Can we find, and quantify, a similar trend in the larger area?
- The IMF of the central cluster was found to be nearly Salpeter down to the core of the cluster. Nevertheless, it appears that there are some variations in some specific regions (e.g., the 6-pc "ring"). Can we identify similar features in other areas of the super-association? Is the IMF a Salpeter function throughout? Can we confirm the steep IMF found for the massive field population (Massey 1995)?
- What triggered the large burst of star-formation activity that we are seeing today? When did it start?

In the remaining of this thesis we address these issues by extending the previous work on NGC2070 to the larger 30 Doradus super-association. At 50 kpc, the assumed distance to the LMC, the scale at 30 Doradus is $0.24 pc/''$. At 30 km/s, a reasonable upper limit to the speed of propagation in a $10,000$K plasma, any disturbance would travel ~ 300 pc in 10 My. Then, by studying an area $\sim 30' \times\ 30'$, or ~ 500 pc $\times\ 500$ pc, we have, in this thesis, the possibility of detecting propagation effects.

Chapter 2

Data reduction

In this chapter we give a short summary of the data upon which this thesis is based, and the instrumentation used to obtain it. We then present the method used to perform profile fitting photometry in this large data set. The process of calibrating the data is presented, concluding that, as a result of the large range in reddening values and luminosity classes of the program stars, it is impossible to bring the WFI ubv magnitudes to standard Johnson UBV, concluding that it is necessary to work in the WFI instrumental system itself. We then present a problem that affects the photometry of wide-field imagers with focal reducers, that of light concentration. We solve this problem by designing, and implementing, a method to determine the systematic variation of zero points across the mosaic.

2.1 The instrument and the raw data

The data was obtained with the Wide Field Imager (WFI) attached to the MPG/ESO 2.2-m telescope. The telescope is a $f/8$ Ritchey-Chretien, with a telescope-instrument scale of $15.9''$/mm, or $0.238''/15$ μm pixel. The sampling is an excellent match to the intrinsic optical quality of the system with 80% of the energy enclosed in a circle of $0.4''$ diameter. Figure 2.1(a) shows the main component of the WFI (Baade 2000): the dewar with the detector system at bottom; the two focal reducer triplets (hatched); and the filter magazine, with space for 50 filters.

Figure 2.1(b) shows the heart of the system, the mosaic consisting of 8 main CCDs plus one CCD for guiding (tracker CCD), all of them 2046k $\times$ 4098k EEV 44-82 CCDs. The pixel size is 15 μ m, the readout noise is 4.5 e^-, the inverse gain is $2e^-$/ADU, and the saturation limit is > 200000 e^-. The dynamic range is 16 bits, limiting

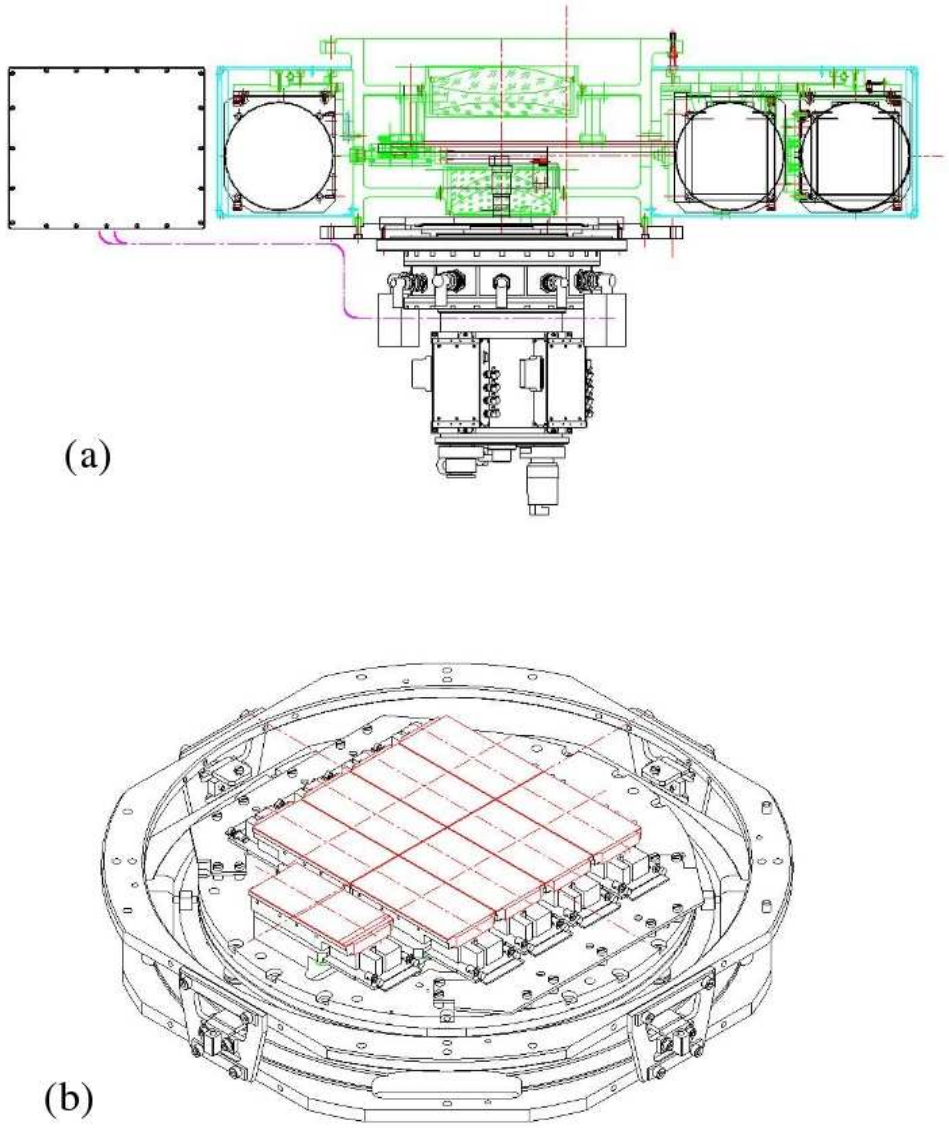

Figure 2.1: (a) The WFI with its dewar, filter magazine, and double triplet system. (b) The mosaic of 8 CCDs, together with the "tracker" chip, used for guiding (Baade 2000.)

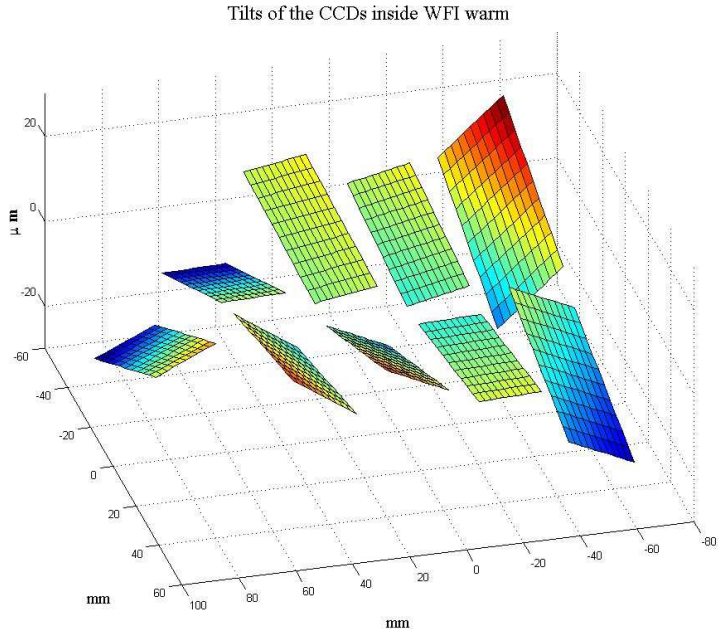

Figure 2.2: 3-D view of the orientation and vertical position of the WFI chips. Notice that the scale of the vertical axis has been expanded by a factor of 1000 to show the effect.

the maximum signal to ∼65000 ADU. For the whole system (telescope, triplets, and detector), a V = 12.5 B1 V star in 10 seconds integration in the B-band (the most sensitive of the UBV bands in the WFI system) is a factor of two below the limit of saturation, with a peak pixel value of approximately ∼ 100000 e^- (data simulated for the airmass and seeing of observations). For any star fainter than V=12.5 the non-linearities are less than 1.5% peak-to-valley. The whole mosaic and tracker chip lies behind a single disk shutter, with a spatial uniformity better than 0.2%, and overall accuracy better than 1% for integration times longer than 10 s.

The 8 CCDs are read in parallel in 27 s and the images from each chip are appended in a single 142 MB multi-extension FITS file. In this format there is a main header followed by an extension header and image for each of the chips. In Figure 2.1(b) the tracker chip is due East of the main mosaic. North is up (and to the left). There are several numbering schemes that might cause confusion. First, there is the ESO numbering: north row, from East to West goes from 50 to 53, bottom row from West to East goes from 54 to 57. There is the multi-extension FITS file storage order in which extension [1] corresponds to chip 50, and extension [8] corresponds to chip 57. We will adhere to the FITS numbering scheme.

Table 2.1: Log of data used in this thesis.

ESO Archive Frame Name	RA (2000)	Dec (2000)	Filter	Exposure [s]
WFI2001-02-02T01:27:38.563.fits	5:40:56.3	-69:15:15.1	BB#V/89_ESO843	9.918
WFI2001-02-02T01:29:25.872.fits	5:41:01.9	-69:16:14.8	BB#V/89_ESO843	9.918
WFI2001-02-02T01:31:16.982.fits	5:41:01.9	-69:14:44.2	BB#V/89_ESO843	9.918
WFI2001-02-02T01:35:00.240.fits	5:40:56.4	-69:15:15.3	BB#B/99_ESO842	9.918
WFI2001-02-02T01:36:47.030.fits	5:41:01.9	-69:15:14.6	BB#B/99_ESO842	9.918
WFI2001-02-02T01:38:44.966.fits	5:41:01.9	-69:14:44.1	BB#B/99_ESO842	9.918
WFI2001-02-02T01:43:09.350.fits	5:40:56.4	-69:15:15.5	BB#U/38_ESO841	59.918
WFI2001-02-02T01:45:46.512.fits	5:41:01.9	-69:15:15.3	BB#U/38_ESO841	59.918
WFI2001-02-02T01:48:32.573.fits	5:41:01.9	-69:14:44.5	BB#U/38_ESO841	59.918

The plate scale is constant to better than 0.1% across the field, but, as we will see, the Point Spread Function (PSF) shows spatial variations. Figure 2.2 shows a flatness map of the WFI (ESO-ODT 2002). All chips lie in a volume bounded by two parallel planes separated by 40 μ m, having tilts as high as 20 μ m from one corner to the opposite one. Experience at the telescope shows that the focus has to change by at least 40 μ m to be noticeable in excellent seeing conditions. Nevertheless, we can expect variations in the PSF which can not be modeled for the whole mosaic by simple smooth functions. These variations will be modeled with a linear function in a chip-by-chip basis.

Table 2.1 shows the log of the data used in this thesis. The data, which is currently freely available in the ESO archive, was obtained in a clear night with a 0.75″ seeing in the V band.

Figure 2.3 is a "true" color rendition of the nine frames in Table 2.1. The gaps are eliminated due to the dither between the frames. Together with this data there are associated calibrating data in the form of bias frames and twilight sky flats. No darks are necessary for the short exposure times used. Illumination correction frames were obtained in a different night, and the process to analyze them will be presented in a latter section.

2.2 Profile fitting photometry

We are interested in the study of stellar populations in regions of varying density. One of the characteristics of the 30 Doradus super-association, and perhaps of all star-forming regions, is the hierarchical distribution of stars. Even the low density

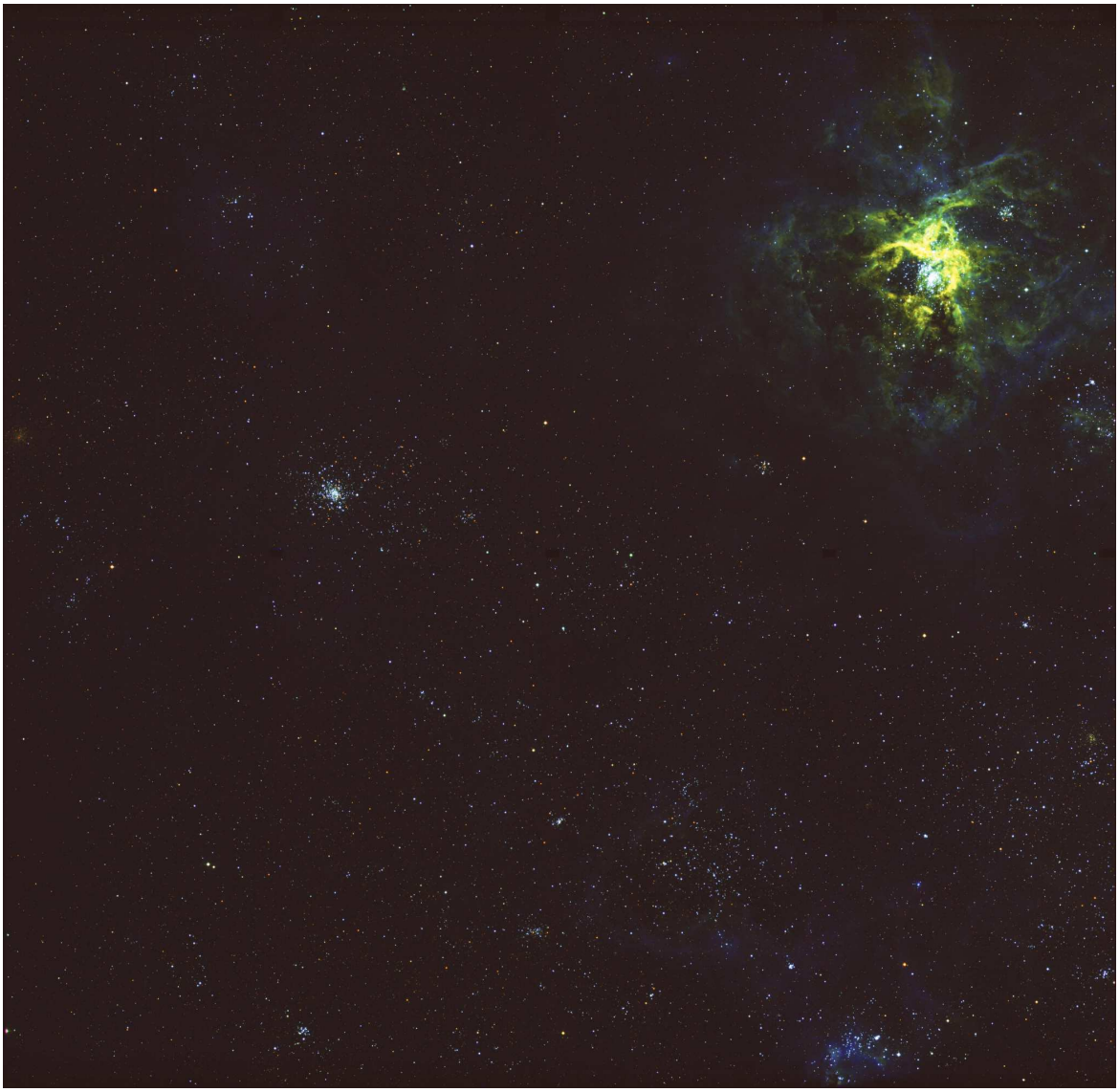

Figure 2.3: True color combination of the nine WFI images analyzed in this thesis.

field contains, scattered here and there, small higher-density stellar associations, some of them very compact. Profile fitting photometry, or PSF fitting photometry, being the only technique for accurate photometry of stars in crowded regions, becomes necessary even for the study of the field population.

The sheer volume of the data set makes this project a rather challenging enterprise. The data consist of 4 pointings in three filters, with three dithers per pointing and filter. Each WFI image is a mosaic of 8 sub-images, so we need to analyze 36x8 different frames, *each with a variable PSF.* One of the challenges of such an undertaking is the management of the large amount of data that is generated in the process. In this thesis we will present the results and the challenges that we had to overcome for the reduction and analysis of the data from the NE field. A *gluescript* written in Tcl–`psfCommander--`guided and organized the data reduction every step of the way. We used IRAF's implementation of DAOPHOT (Davis 1994; Stetson 1987, 1991, 1997). There are five routines that we have used repeatedly in each of the mosaic chips: (1) `daofind` is used to detect stars; (2) `phot` is used to do a preliminary *aperture* photometry on the stars detected with `daofind`; (3) `pstselect` is used to create a list of suitably bright isolated stars for PSF determination; (4) `psf` is used to determine the stellar profile using the previous list of stars; and (5) `allstar` is used to carry out the actual fit of the profile to each of the stars detected by `daofind` and to create a frame with all the stars subtracted.

The PSF is obtained interactively for the individual chips for each of the exposures. In DAOPHOT the PSF is characterized by several parameters: (1) the PSF radius, the distance out to which we will determine the stellar profile beyond which it is assumed that the profile of the brightest star to be fit falls below the sky noise level; (2) the fixed analytical component, i.e., Gaussian, Moffat, Lorentz, etc; (3) the order of the variable part implemented using 2-D lookup tables; (4) the fit radius determining which pixels will be used when the PSF is fitted to an actual stellar profile; and (5) the number of stars to be used in the PSF determination.

In DAOPHOT part of the PSF is implemented by interpolating lookup tables using a 2-D polynomial either of 0-th order for a constant PSF (1 lookup table), first-order for a linearly varying PSF (3 lookup tables), or 2nd order for a quadratically varying PSF (6 lookup tables). After some experimentation it was decided to use a first-order PSF as it reduced the χ^2 of the fit by more than 20%. It is recomended to use at least 3 stars per degree of freedom. The second-order PSF would require

too many stars not necessarily available in the complex area we are studying. With 3 lookup tables and two Gaussian width parameters (one each for x and y) we would need 15 stars per chip for the first-order PSF, something within the realm of the possible (although, as found out by the author, for some chips rather difficult).

The procedure used to determined the PSF follows closely that described by Massey and Davis (1992). A preliminary PSF is determined using the PSF stars, chosen with the help of `pstselect`. This routine produces a list of suitable candidates leaving out any stars too close to the borders, or that are affected by saturation or by the presence of bright companions. We then go through this list selecting a subgroup of stars as free of nebulosity as possible and covering the chip uniformly. Using this subgroup of stars we determine a preliminary PSF using the routine `psf` which averages the profiles of the selected stars with appropriate weights. If all the stars thus selected are free of nebulosity and neighboring stars we are done and we could determine a *clean* PSF. Nevertheless, the first PSF thus determined usually contains features produced by either nebulosity or overlooked neighbors near some of the PSF stars. In the case of nebulosity we just delete the affected PSF star from the list. To determine which of the PSF stars are affected by undetected neighbors is simple, but tedious: psfCommander displays the neighborhood of all the PSF stars automatically permitting their easy identification. If we have enough clean stars we just delete the ones with near neighbors. Otherwise we need to subtract the neighbors from the frames. But we can only do this if we have the PSF. So if we do not have bright stars free of neighbors, we are in a dilemma.

There is a standard way out of this dilemma: during a first pass of PSF determination, we reduce the PSF radius to less than half the smallest distance between any PSF star and its closest neighbor. This *truncated* PSF is then fit to the neighbors and subtracted from the frame that will now be used to determine a new PSF with the full radius. Finally the neighbors of the PSF stars are fit with this improved PSF and the resulting cleansed PSF stars are used to determine a new, better approximation of the PSF. This procedure can be applied iteratively.

The above process requires the examination of approximately 50 stars per chip to yield a total of approximately 25 PSF stars per chip. Each of the necessary tasks is carried out by pressing a button in `psfCommander.` The script manages all the permanent and temporary files created in the process. It takes typically 5 hours to process the 8 images of a single WFI frame. The process is slower in regions of high

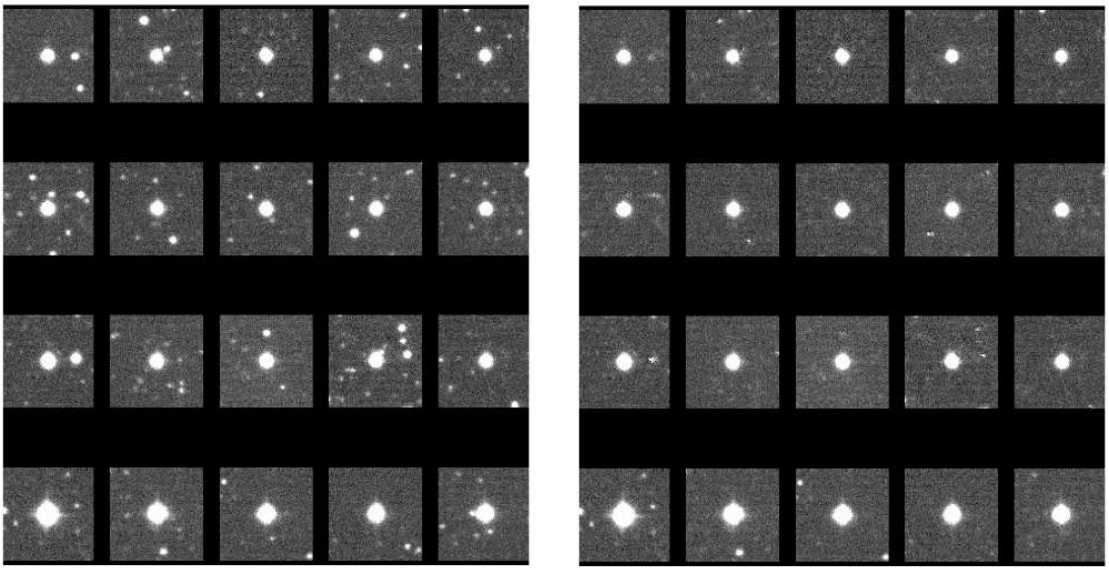

Figure 2.4: Left, a set of PSF stars as they appear in the original image. Right, the same stars with the neighbors subtracted.

stellar density and/or bright nebulosity where many of the bright stars are not useful as PSF stars and must be replaced by a larger number of fainter stars. Figure 2.4 shows an example of a list of PSF stars as presented by `psfCommander` at the start of the process (left), and after their neighbors have been subtracted (right).

Once the PSF has been determined, we are ready for the last step of the process which consists of (1) doing profile fitting photometry using `allstar` on the current list of finds; (2) subtract all stars found so far using the PSF; (3) finding missed stars in the PSF subtracted frames; and (4) doing profile fitting photometry on these stars. This four step process, `allstar-daofind-phot` loop, is repeated three times. This is not the final profile fitting loop. For that we will need to cross-correlate all the finds, in all pointings and all filters to produce a single master list of detections. This will be done with the program `daomaster` as explained below.

The steps carried out by the script are thus the following:

1. use `daofind` to create a first list of stars;

2. run `phot` on the list of stars found in the previous step;

3. create a suitable PSF:

    3a. determine a list of suitable PSF candidate stars from the previous list;

3b. run `psf` with a reduced PSF radius to create a PSF to be used for neighbor subtraction;

3c. subtract, using the previous PSF, all the neighbors of the PSF stars;

3d. examine neighborhood of each PSF star for un-subtracted neighbors, if there are any, go into interactive neighbor identification loop– goto 3c;

3e. create a PSF with a full radius;

3f. If the PSF created shows un-subtracted neighbors artifacts, go to 3a, otherwise we are done with the PSF determination loop;

4. run the preliminary `allstar-daofind-phot` loop three times;

As a result of the previous process one ends up with one list of PSF-fitting photometry per WFI CCD chip, per frame, per filter. The next step consists in cross-correlating the lists to discard false detections and generate the *master* list which contains only those stars which will be considered *real* detections. The program `daomaster` (Stetson 1993) gives three parameters to manage this. The first parameter—*minimum number of frames*—gives the absolute minimum number of frames in which a star has to appear before we consider it real; the second parameter—*minimum fraction*—deals with the fact that because we are dithering some stars will not be in the field of view of some of the frames; this parameter sets the *minimum fraction* of the frames that can contain a star that actually contain it. The third and last parameter—*enough frames*—enforces that if the star is found in a certain minimum number of frames the star will be considered a real detection. The actual choice of parameters does not matter much in our case because we are interested in the brightest stars. We have a total of nine frames divided in three small amplitude dithers in each filter. The amplitude of the dither was just large enough to cover the gaps. We have chosen 50% as the minimum fraction of frames, that is 5 out of nine. The amplitude and direction of the dithers will imply that there are three levels of coverage: (1) further than 24″ from the edges a star can appear in all three frames of a given filter; (2) within 24″ from the edge, but further than 24”″ from a corner, a star can only appear in 1 out of 3 frames; and (3) within 24″ from the corners, a star can appear in none of the frames, as these are blind spots. More than 90% of the area has full coverage, case (1) above; approximately 5% of the area belongs to case (2) above; and only 0.2% of the area corresponds to case (3). We have set the *enough frames* parameter to 2, this insures that it is enough for a star to be observed

in only two filters to be considered real irrespective of whether it is in an area of full or reduced coverage. This choice, together with a relatively high 5σ detection threshold for `daofind`, was shown to keep spurious detections to a minimum. The other parameters were set so that this was the dominating parameter. Specifically, *minimum number* was set to 2 and *minimum fraction* was set to 50%. With this choice of parameters we recover a few more fainter stars in the U filter close to the limit of the photometry, but that if fitted, could give a reasonable estimate of their magnitude. *The final completeness of the catalog thus produced will be gauged by comparing with our previous work in the crowded NGC2070 region for which we did a full set of Monte Carlo simulation to estimate the completeness as function of magnitude, color, and stellar crowding.*

We underline again the importance of working from a single master list of detections in all filters. Otherwise we will have many stars recognized in some filters, but not in others, or stars will be recognized as multiple in one filter and single in another. This would lead to inconsistent magnitudes and colors. Once we determine the master list of detections we run `allstar` one final time, in each exposure with the same master list to produce the tables with the final profile fitting magnitudes.

After this we need to determine the best magnitude for each filter for all stars. In a given filter some of the stars will have three measurements, some two, some one, and some none. To combine the multiple measurements we need to tie the photometric system of one frame to the photometric system of the other. Also, the profile fitting magnitudes of different chips of the same WFI frame have different zero points. This happens because the program `psf` normalizes the PSF to the magnitude of the first star in the list of PSF stars which has a different value in every chip. Thus, for each of the eight chips in a frame we determine the conversion factor to the aperture magnitudes in that frame. Then we determine the conversion factors of each of the three frames per filter to the aperture magnitudes of the first frame. Thus,

- first tie the zero points of the PSF-fitting photometry for each chip to the aperture magnitudes of the frame to which the chip belongs to;
- then tie the zero points of the aperture photometry of each of the three frames per filter, to the aperture photometry of the first frame.

Thus, if k indexes each of the three frames per filter, the process is: *tie profile fitting magnitudes of each of the 8 chips in frame k to the aperture magnitudes in*

frame k; then tie the aperture magnitudes of frame k to that of frame 1. The process is carried out with the python gluescript `extractphot.py` found in Appendix B.

This is all we would need to do if there were no zero point variations across the WFI mosaic. But we know that they vary by $\sim 10\%$ peak-to-valley (see section 2.4). Thus, we need to incorporate this information in the process by normalizing the magnitudes to a fiducial reference point in the mosaic. Because we will tie the photometric system to that of Paper I which in turn is tied to that of Parker (1993), the position of NGC2070 is the natural fiducial point. The process is carried out with the python gluescript `getPhotometricZeroPoints.py` found in Appendix B.

2.3 Absolute calibration of the WFI system

Once we have the instrumental ubv magnitudes in the WFI band-pass the generally agreed upon best procedure would be to transform these magnitudes to standard UBV system. This procedure is preferred because in this way we can compare our magnitudes with those published in other studies. We will show below that this is not entirely possible and that probably much of the published UBV CCD photometry of highly reddened stars suffers from systematic errors as high as 15%. We will go below through the steps of the calibration to the standard system and will point out where the problems lie.

In the Johnson standard system, as calibrated by Landolt (1992), the basic reduction equations are

$$\begin{pmatrix} u-u_0 \\ b-b_0 \\ v-v_0 \end{pmatrix} = \begin{pmatrix} 1+k_u & -k_u & 0 \\ 0 & 1+k_b & -k_b \\ 0 & k_v & 1-k_v \end{pmatrix} \times \begin{pmatrix} U \\ B \\ V \end{pmatrix},$$

where ubv represent the instrumental system, UBV represent the standard system, u_0, b_0, and v_0 are the zero points to be determined, and k_u, k_b, and k_v are the color terms.

For calibration we used observations of the Landolt fields RU149 and TPhe taken in a different night. We observed both these fields in Chip2 and all filters at air-masses of 1.1, 1.3 and 2.0; and Ru149 in all chips and all filters, at air-masses between 1.1 and 1.3. The atmospheric extinction in UBV was 0.414, 0.179, and 0.119, respectively.

Table 2.2: Zero points and color term for WFI.

		u_0	k_u	b_0	k_b	v_0	k_v
Chip 1	This thesis	-21.66	-0.10	-24.56	-0.29	-24.16	+0.05
	EIS	-	-	-24.77	-0.33	-24.31	+0.06
Chip 2	This thesis	-21.65	-0.12	-24.53	-0.31	-24.12	+0.07
	EIS	-	-	-24.74	-0.31	-24.26	+0.09
Chip 3	This thesis	-21.62	-0.09	-24.53	-0.29	-24.11	+0.06
	EIS	-	-	-24.75	-0.29	-24.26	+0.07
Chip 4	This thesis	-21.72	-0.09	-24.60	-0.29	-24.21	+0.08
	EIS	-	-	-24.78	-0.30	-24.33	+0.07
Chip 5	This thesis	-21.71	-0.10	-24.59	-0.29	-24.21	+0.07
	EIS	-	-	-24.77	-0.31	-24.32	+0.08
Chip 6	This thesis	-21.64	-0.08	-24.54	-0.30	-24.15	+0.07
	EIS	-	-	-24.75	-0.30	-24.27	+0.07
Chip 7	This thesis	-21.62	-0.08	-24.52	-0.30	-24.13	+0.07
	EIS	-	-	-24.73	-0.30	-24.27	+0.07
Chip 8	This thesis	-21.68	-0.09	-24.57	-0.29	-24.18	+0.07
	EIS	-	-	-24.78	-0.29	-24.34	+0.09

Table 2.2 summarizes the zero points and color terms in all chips. It also compares with the published values by the ESO Imaging Survey group (ESO-EIS 2000).

We can see from Table 2.2 that, although there are variations in the zero points measured by the two groups (due to different apertures, and definitions), the color terms are extremely consistent. We can compare with the average over all chips published by the Capodimonte group (Cappacioli et al. 2002): $k_b = -0.340$ and $k_v = 0.130$. Considering that this group used a standard atmospheric extinction coefficient the agreement is still good.

Although from the above discussion everything seems fine, there are some problems, already discussed in Paper I, but whose importance was not completely realized then: (1) the ubv system for the WFI is quite different to the standard Johnson UBV system, a fact already seen in the large color term for the b filter; (2) due to the Balmer jump at 3767Å the conversion from standard U to WFI U is not only non-linear, but it is many-valued having a strong dependence on the luminosity class of the star; and (3) the Landolt standard stars are much less reddened than our program stars, and thus have very different spectral energy distributions. We will see that these problems and their interplay make it extremely difficult to have an accurate conversion from instrumental to standard magnitudes.

To investigate the nature of the color equation for U we have used the Kurucz (2002) model atmospheres to calculate synthetic color equations for the WFI system. First we determined the colors of stars in the Johnson system using the Buser (1978)

reconstruction. This reconstruction uses the UBV passbands given by Azusienis and Straizys (1969) together with a new representation, B·p, which includes atmospheric extinction p at airmass 1.3, to calculate the U-B colors. After reproducing the previous work, thus showing that our procedures work correctly, the WFI UBV synthetic colors were calculated. The ingredients for the WFI UBV response function calculation are: (1) 2 aluminum reflections (Paquin 1995); (2) the throughput of the WFI double triplet corrector (Baade 2002); (3) the measured transmission curves for the WFI filter set (ESO-LIN 2002); and (4) the individual CCD quantum efficiencies as measured by ESO's Optical Detector Team (ESO-ODT 2002). The top panel of Figure 2.5 shows the curves for the UBV responses for the 8 CCDs.

The bottom panel of Figure 2.5 shows the (normalized) WFI and Johnson bandpasses together with the model spectra for a 40000 K star ($\log g = 4.5$), for a 10000K dwarf ($\log g = 4.5$), and for a 10000K giant ($\log g = 2$). These spectra show the number of photons as a function of wavelength, N_λ, as this is the one relevant for *photon counting* devices. The method follows closely the work of Buser and Kurucz (1978) using the latest ATLAS9 models from the web (Kurucz 2002) and the latest Vega calibration (Castelli and Kurucz 1994; Kurucz 2002).

Figure 2.6 shows the resulting simulated color equations. The upper left panel shows the color-color diagram for the following three sets of data: (1) the Schmidt-Kaler (1982) locus for dwarfs; (2) the Kurucz model atmosphere colors for dwarfs, giants, and supergiants, somewhat arbitrarily defined as having $\log g$ of 4.0, 2.0, and 0.5, respectively; and (3) the observed colours for the Landolt (1992) stars in the fields Ru149, and TPhe used to determine the observed color equations. The upper right panel shows the observed color equation for U together with the simulated color equations for dwarfs, giants, and supergiants. The lower two panels show the same for B (left) and V (right). Figure 2.6 shows that to within $\sim 1\%$ the simulations of the B and V bands agree with the observations for all stellar types of interest (we ignore the extreme red objects in this work).

We first notice from Figure 2.6 that the simulated color equation for the U band shows a strong dependence on the luminosity class. Had we not simulated the WFI system we might have been tempted to apply a non-linear functional dependence on the color term. However, we know from the simulations that *no functional relationship represents the transformation from WFI U to standard Johnson U.* Were we to use such a non-linear correction term we would be introducing a luminosity class de-

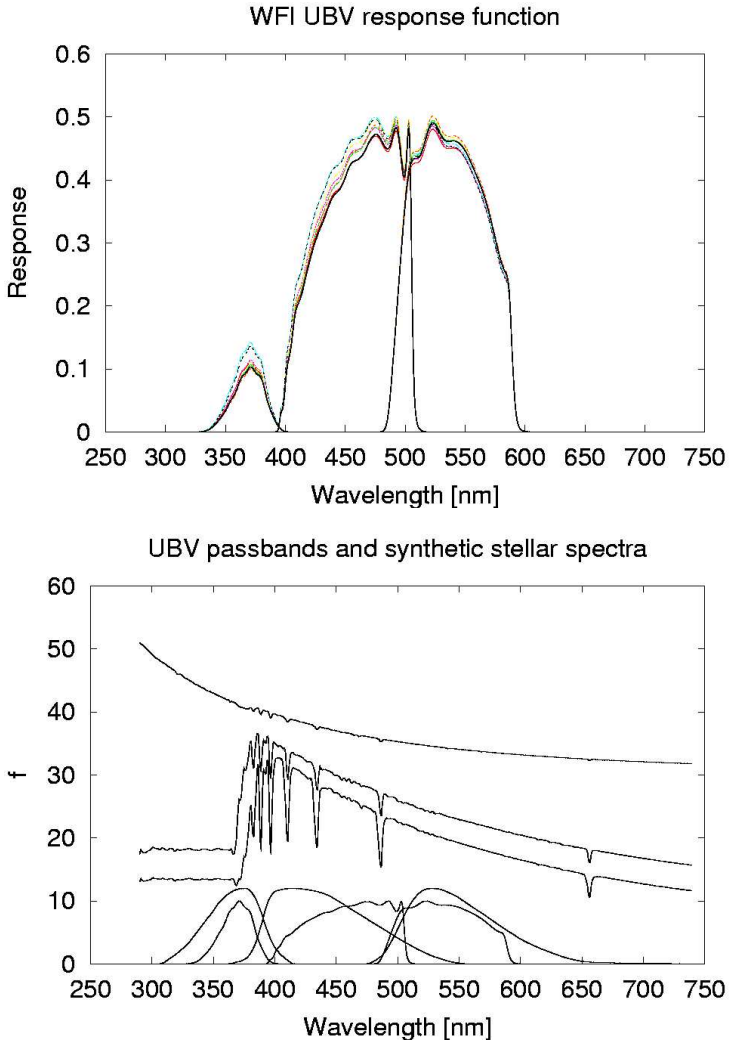

Figure 2.5: The top panel shows the response of the WFI UBV system for the 8 CCD chips. The bottom panel shows the Kurucz (2002) model atmospheres spectra (number of photons as a function of wavelength), together with Johnson and WFI overall response functions (the WFI curves the lower ones). The upper curve corresponds to a $\log g = 4.0$, 40000 K star; the middle curves corresponds to 10000K dwarf ($\log g = 4.0$), and, slightly above, a 10000K giant ($\log g = 2.0$). All these curves have been scaled to fit in the viewport; in particular, the continua shortward of the Balmer jump is almost identical for the the 10000K stars. Notice the large deviations of the WFI system from the standard Johnson system, specially for U and B.

pendent error of almost 10%. The only way to deal with such an effect is to work in the WFI ubv system itself and to transform the theoretical colors to this system.

Figure 2.6 also shows that to within $\sim 1\%$ the simulations of the B and V bands agree with the observations for all stellar types of interest (we ignore the extreme intrinsically red objects in this thesis). Nevertheless, most of the Landolt standards have low to moderate reddening values, while most program stars are strongly reddened. Figure 2.7 shows the effect of reddening on the instrumental equations for the U band, upper panel, and for the B band, lower panel (the effect on V is almost negligible). The solid line is the simulated transformation equation for zero reddening while the dashed line corresponds to $E(B-V) = 1.0$. We can see that a reddened extreme O star has a zero point which differs from that of an unreddened star of the same color by approximately 8% in B and 5% in U, but in the opposite direction. The change in (U-B) is thus a full 13%! Not knowing a priori the reddening of the program stars, it is impossible to transform the magnitudes to the standard system with an acceptable uncertainty.

Thus, we will work in the instrumental WFI ubv system. We will use the transformation equations, which work reasonably well for unreddened stars, to transform the theoretical UBV colors of stars of different effective temperature and surface gravities to WFI ubv colors. For the U filter we will need in addition to apply a luminosity class correction based on the simulated transformation equation. We will then need to use our simulations to determine the reddening law in the WFI ubv system. Finally, we will fulfill the need of an external comparison by directly comparing the physical parameters of the stars we determine with our photometric method with those obtained independently using spectroscopy.

Canonical form for the transformation equations. Although working in an unfamiliar photometric system can be confusing, we can regain most of our familiarity with the Johnson UBV system by writing the transformation equations appropriately. It is particularly useful to preserve the blue limits for the (U-B) and the (B-V) colors. This can be accomplished by simple zero point offsets.

Following the discussion in Section 2.2 we will refer our photometry to the zero points in Parker (1993). Using the first frame of each filter observation in the northeast quadrant as defining our instrumental magnitudes we can then write the equations

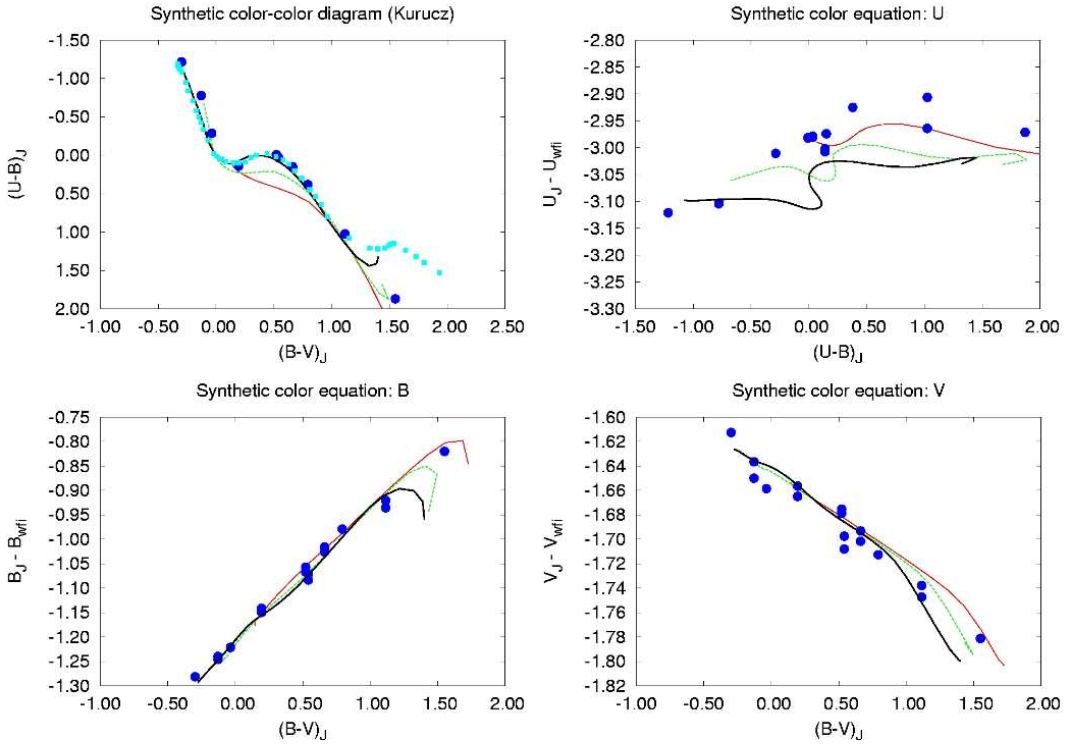

Figure 2.6: The top left panel shows the positions in the color-color diagram of the Landolt standard stars (large blue dots) used in the determination of the color equations. This panel also shows the locus of the dwarfs (small filled green squares) according to Schmidt-Kaler (1982), and the locus of the simulated stars (black line for dwarfs, green line for giants, and red line for super-giants). The upper right panel shows the observed and simulated color equation for U; lower left and right panels show the observed and simulated color equations for B and V, respectively. We can see that the B and V filters can be calibrated, but not the U filter (see text for details).

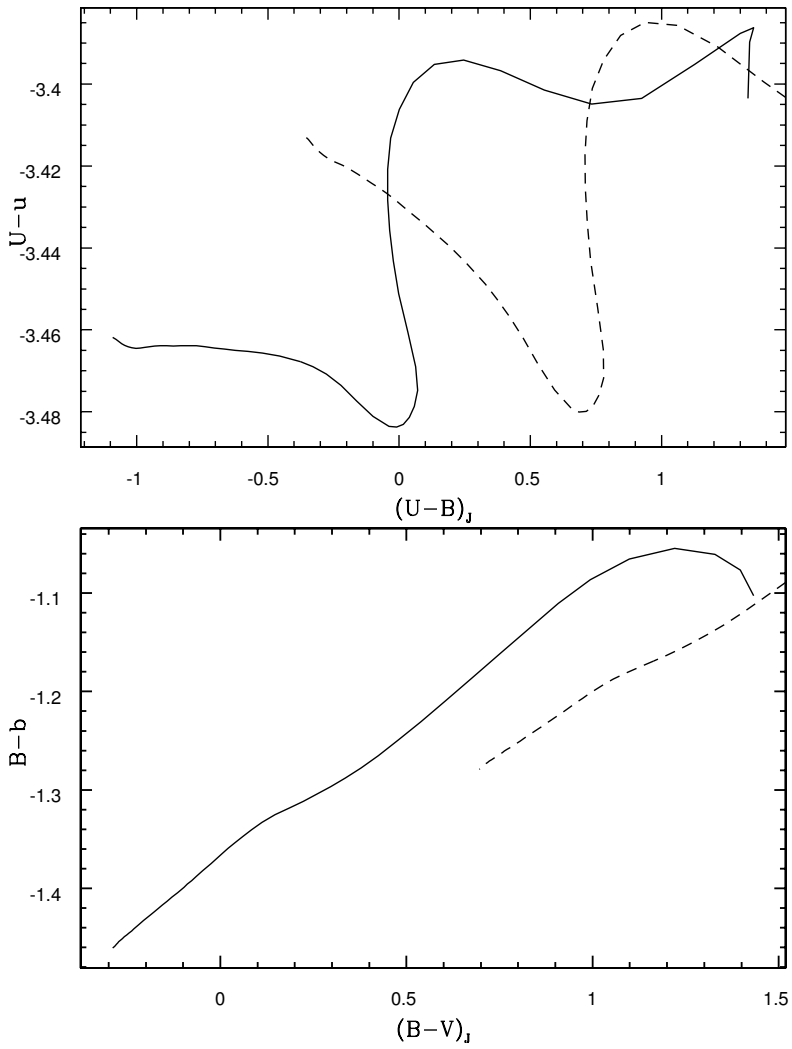

Figure 2.7: Simulated color equations for the WFI u and b band-passes for two different values of interstellar reddening: the solid line corresponds to E(B-V) = 0.0, while the dotted line corresponds to E(B-V) = 1.0. We can see that a reddened extreme O star has a zero point which differs from that of an unreddened star of the same color by approximately 8% in B and 5% in U. The change in (U-B) is thus a full 13%!

$$
\begin{aligned}
v &= V + 0.08 \times \{0.33 + (B - V)\} \\
b &= B - 0.30 \times \{0.33 + (B - V)\} \\
u &= U + 0.00 \times \{1.229 + (U - B)\} \\
b - v &= (B - V) - 0.38 \times \{0.33 + (B - V)\} + 0.0 \times \{1.229 + (U - B)\} \\
u - b &= (U - B) + 0.30 \times \{0.33 + (U - B)\},
\end{aligned}
\tag{2.1}
$$

where $v = v' + v0$, $b = b' + b0$, and $u = u' + u0$, and prime quantities refer to the raw WFI instrumental magnitudes, and subscripted quantities are the zero point shifts required to bring our photometry to the system of Parker (1993) for the hottest stars. In this system the colors of the hottest unreddened stars are the same as those in the Johnson system, that is: $(u - b)_0 = -1.229$ and $(b - v)_0 = -0.33$.

In this thesis we found a systematic shift in Parker's (1993) photometry. The method to uncover and to correct this error will be presented in Section 3.3.

2.4 Photometric flats: the challenge of wide-field photometry.

Even after applying a flat-field correction the photometric zero points vary with positions in the mosaic (Manfroid, Selman, and Jones 2001). We have designed a non-standard procedure to correct the data.

If the flat field screen illumination is uniform, then any observed variations in the flat field image are the result of variations in the transmission of the optics and the response of the pixels. Such a flat field image can then be used to remove the variations of sensitivity from all science frames.

However, it appears that for large area imagers with focal reducers, even if the illumination of the flat field screen (or twilight sky) is uniform there is redistribution of light by the optical system that corrupts the flat field images. In most cases the non-uniform illumination results in an increase of the amount of light reaching the central areas of the detector (*sky concentration*; Andersen et al. 1995). This *sky concentration* may fool us into believing that the relative response between the center and edge of the frame is larger than what it really is. Thus, when flat fielding with

such incorrect flat fields, the fluxes of the stars near the center will be artificially reduced.

A flat field image which measures the sensitivity variations, as opposed to the sky level intensities as a function of position, is called a *photometric flat*.

Figure 2.8 illustrates the effect of reducing data with a flat field which suffers from sky concentration. The figure shows the color equations determined using observations of the stars in the Landolt field Rubin 149. Eight exposures were obtained per filter while the telescope was offset between exposures so that the stars, which are very close together, were placed in each of the 8 chips. The images were flattened with flat field frames obtained during twilight. A full atmospheric extinction correction was obtained observing the same field at three different air-masses in the same chip. The magnitudes are then extra-atmospheric and should be independent of the position in the mosaic. The figure shows a large spread in zero-points independent of color. Thus, the sky concentration effect is manifest as a spatial variation in the zero points of the photometry. A correction frame which equals this spatial variation of the zero points will be called a *photometric flat field correction*, or *zero-point variation map.*

We have designed a convenient procedure to obtain a zero-point variation map. The main idea is that by imaging a reasonably dense stellar field three times, with two small perpendicular offsets between exposures, any errors in the flat field procedure will result in differences in the flux measured for stars in different parts of the image.

The zero point variations can be modeled with a set of two-dimensional basis functions (i.e., Cosine, or Chebyshev), and then use a least-squares procedure to determine the coefficients that best fits the data.

Denote the magnitude of the same set of n stars, in three frames taken in rapid succession, following a cross pattern,

$$\{m(x_i, y_i), m(x_i + h_x, y_i), m(x_i, y_i + h_y)\}_{i=1}^{n} .$$

The variations in zero points can be modeled as

$$zp = zp(x, y) = \sum_{j=1}^{l} b_j f_j(x, y),$$

where the set $\{f_j(x, y)\}$ is a set of l, two-dimensional, basis functions. Then, the

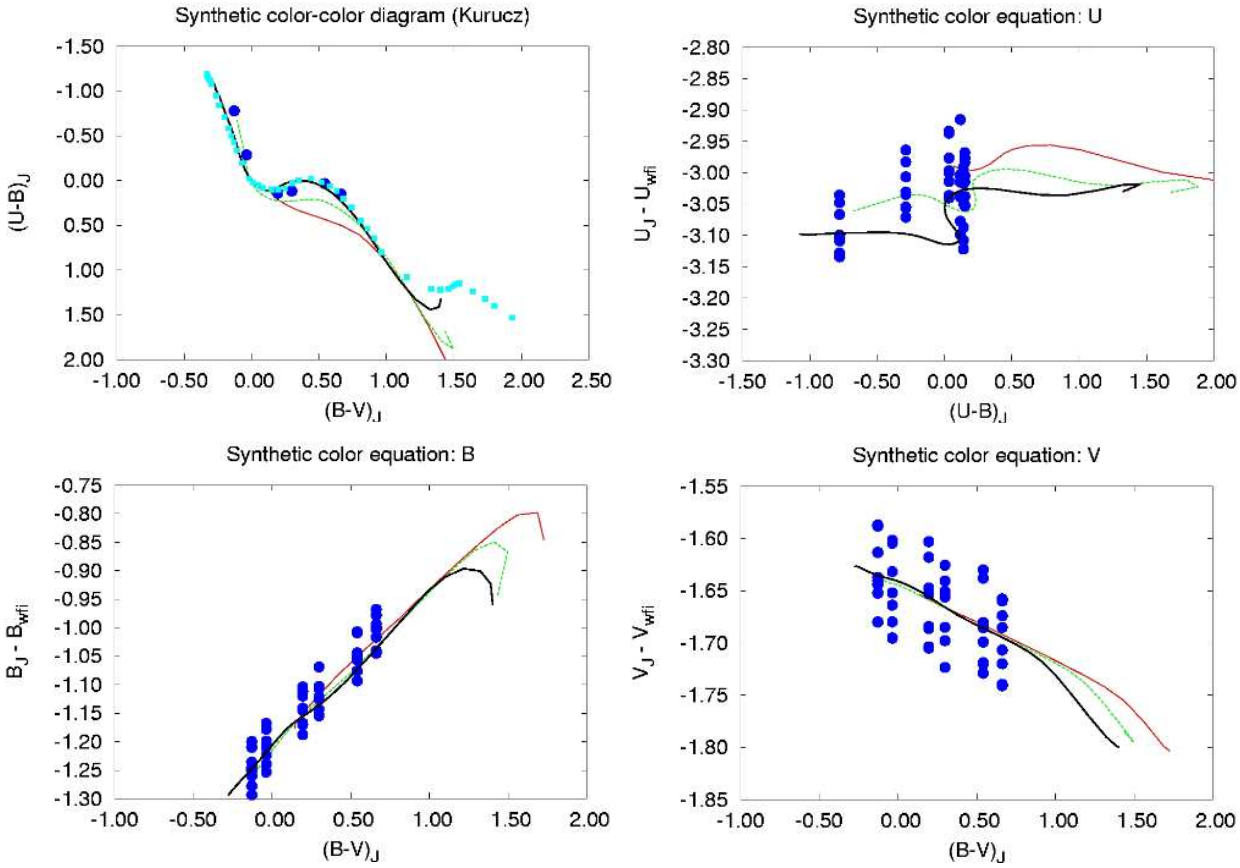

Figure 2.8: Same as Figure 2.6 but with the data of the observations of Ru149 in all chips. The rms residuals from linear color equations are 0.034, 0.029, and 0.040 for V, B, and U respectively.

following set of equations can be written as,

$$\begin{aligned}\delta m_i = m(\mathbf{x}_i + \delta\mathbf{x}_i) - m(\mathbf{x}_i) &= \sum_{j=1}^{n} b_j((f_j(\mathbf{x}_i + \delta\mathbf{x}_i) - f_j(\mathbf{x}_i)) \\ &= \sum_{j=1}^{n} \delta f_{ij} b_j,\end{aligned}$$

where $m(\mathbf{x}_i)$ is the magnitude of star i, measured at position $\mathbf{x}_i$; and $m(\mathbf{x}_i + \delta\mathbf{x}_i)$ is the magnitude of the same star measured at $\mathbf{x}_i + \delta\mathbf{x}_i$ ($\delta\mathbf{x}_i = (h_x, h_y)^T$). The previous system of equations in matrix form is,

$$\begin{pmatrix} \delta m_1 \\ \vdots \\ \delta m_n \end{pmatrix} = \begin{pmatrix} \delta f_{11} & \dots & \delta f_{1l} \\ \vdots & \ddots & \vdots \\ \delta f_{n1} & \dots & \delta f_{nl} \end{pmatrix} \times \begin{pmatrix} b_1 \\ \vdots \\ b_l \end{pmatrix} \quad \Leftrightarrow \quad \mathbf{\Delta M} = \mathcal{A} \times \mathbf{b}, \qquad (2.2)$$

where δm_i is the i-th magnitude difference; δf_{ik} represents the k-th basis function evaluated at the positions for the i-th magnitude difference. $\mathcal{A}$ is called the design matrix. If we use 25 basis functions, and 1000 magnitude differences, then the design matrix has 25 columns and 1000 rows. Typically, the number of basis functions used is less than 100, and the number of magnitude differences is several thousands. Thus, the simultaneous equations represented by the design matrix must be solved using *least-squares*.

Denote a set of estimates of the parameters by $\tilde{b} = (\tilde{b}_1, \dots, \tilde{b}_l)^T$. These parameters lead to the fitted values $\mathbf{\Delta\tilde{M}} = (\tilde{\delta m}_1, \dots, \tilde{\delta m}_n)^T = \mathcal{A} \times \tilde{\mathbf{b}}$. The residual errors are given by $\tilde{e} = (e_1, \dots, e_n)^T = \mathbf{\Delta M} - \mathcal{A} \times \tilde{\mathbf{b}}$. The *residual sum-of-squares* $E = \sum_{i=1}^{n} e_i^2$ is the sum of the square differences between the actual and fitted values, measuring the fit of the model with these parameter estimates. The *least-squares* estimates are the parameter estimates which minimize the residual sum-of-squares,

$$E = \sum_{i=1}^{n} (\delta m_i - \delta f_{i1}\tilde{b}_1 - \dots - \delta f_{il}\tilde{b}_l)^2.$$

E is minimized when

$$\frac{\partial E}{\partial \tilde{b}_k} = 2\sum_{i=1}^{n} (-\delta f_{ik})(\delta m_i - \delta f_{i1}\tilde{b}_1 - \dots - \delta f_{il}\tilde{b}_l) = 0,$$

or in matrix form,

$$\mathcal{A}^T \mathbf{\Delta M} = (\mathcal{A}^T \mathcal{A})\tilde{\mathbf{b}}.$$

These equations are called the *normal equations.* If $(\mathcal{A}^T\mathcal{A})$ is invertible, then the least squares estimates are

$$\tilde{\mathbf{b}} = (\mathcal{A}^T \mathcal{A})^{-1} \mathcal{A}^T \mathbf{\Delta M}.$$

Of all the possible unbiased estimates of the parameters $\tilde{\mathbf{b}}$, if the errors are Gaussian, the least-squares estimates have the smallest variance (Gauss-Markov theorem; Brandt 1998).

It is very common for the design matrix to have linearly dependent columns, that is, the problem is *over-parameterized,* and the matrix $(\mathcal{A}^T\mathcal{A})$ is singular and has no inverse. In this case one can use the Moore-Penrose pseudo inverse (Brandt 1998) which chooses a particular set of parameters from the infinitely many possibilities. I have used the method of singular value decomposition to solve the problem. For the details see Brandt (1998).

Because of a well-known theorem from information theory the effective resolution of a flat determined with this procedures does not depend on the size of the spatial offset between exposures, but instead depends only on the effective density of stars.[1]

[1] Consider a one-dimensional function $f(x)$, which we want to reconstruct if we are only given the difference function $dif(x,h) = f(x+h) - f(x)$. The Fourier transform of the latter is

$$\begin{aligned}
\mathcal{F}(dif) &= \int_{-\infty}^{\infty} e^{ikx}(f(x+h) - f(x))dx \\
&= \int_{-\infty}^{\infty} e^{ikx} f(x+h)dx - \int_{-\infty}^{\infty} e^{ikx} f(x)dx \\
&= (e^{-ikh} - 1)\mathcal{F}(f) \\
&= \tilde{\mathcal{F}}(f).
\end{aligned}$$

From the above equation we can see that the Fourier transforms are related by the multiplication of an oscillatory term, which does not suppress any information. If $\mathcal{F}(f)$ is band-limited, then $\tilde{\mathcal{F}}(f)$ also is band-limited. The sampling theorem still holds, thus the assertion of the previous section, that the effective resolution is only determined by the density of stars, and not by the size of the dither amplitude is justified.

With this we can determine that the optimal conditions for the dither are such that the magnitude differences must be maximized. That is, h should be on the order of half the field size, and the field should be as crowded as possible, but still adequately sparse for aperture photometry.

2.4.1 The method in practice

The main complications arise from variations in atmospheric extinction between exposures. To understand the problem better it is useful to consider a case in which there are no zero point variations in the mosaic. After taking two dithered exposures the difference in magnitudes of the same stars measured in both frames will only be a reflection of the change in atmospheric extinction between the two exposures. If we do not recognize this, we will wrongly conclude that there is a linear gradient in the zero points variations across the mosaic. The solution is to subtract the median change in magnitude from all stellar magnitudes. But, when we allow for zero point variation this procedure is no longer valid because the group of stars used to determine the median magnitude difference will be located in a different part of the mosaic in the second exposure and will thus have a different median zero point. The problem is particularly troublesome when we maximize the signal by using a large dither amplitude (δx). In principle it is possible to disentangle changes in atmospheric transparency from spatial zero point variations if the images are obtained quickly on a photometric night and with small offsets. In practice, however, this is not possible because some filters, e.g., U, require long integrations; and if the offsets are small the signal (δm_i) is also small. To solve this we need an independent way to determine the change in extinction between the two frames, or to use small enough offsets so that the changes in average zero point is small but large enough for the individual signals to be detectable. We have implemented the second solution, with mixed results.

The three frames of each field are processed in two stages. The first is a preparation stage in which we find stars in one frame and do aperture photometry in all three. This procedure is encapsulated in the python gluescript `zpPreparedData.py`, whose output is a file with the difference in magnitudes versus position.

The second stage is the analysis of the data using the python gluescript `zpAnalyze.py`. Here we assume, following the previous section, that there is a function of the form $zp = zp(x, y)$ which represents the change in zero point across the mosaic. We parametrize that function as an expansion in 2D Cartesian Chebyshev polynomials. Then we find the coefficients through the least-squares procedures outlined above.

To make the method robust we have decided to make it interactive in order to do sigma-clipping of deviant points. The output of this procedure is a file with the coefficients of the 2D Chebyshev polynomial that best fits the data. Both gluescripts

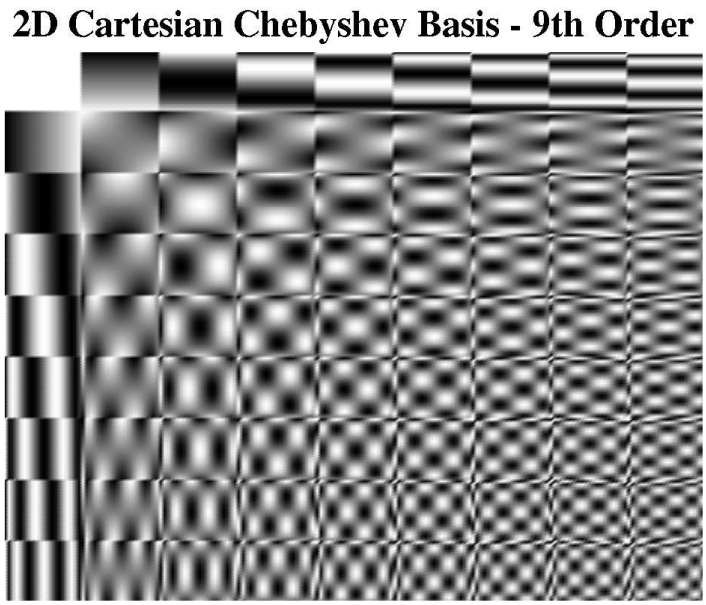

Figure 2.9: The figure displays the 81 basis functions used in the least-squares procedure outlined in the text.

use the library `zplib.py` found in Appendix B. Figure 2.9 shows the ninth-order Chebyshev basis typically used to analyze the data.

The zero-point polynomial thus determined for the V filter is shown in Figure 2.10 which is a ninth-order 2-D polynomial (91 coefficients) that best represented the variations in zero points for the V filter. This zero point map was obtained, after some experimentation, with spatial offsets of 100″.

Figure 2.11 shows the color equations determined after applying the zero-point correction map to the V filter. The V filter correction works well even for the U and B filters (probably due to problems associated with atmospheric transparency variations, the corrections determined for U and V did not work as well). Using the V zero-point correction map for all filters the 1σ residuals from the standard stars transformations were reduced from 0.034 to 0.009 in V, from 0.029 to 0.010 in B, and from 0.040 to 0.014 in U; i.e., typically a factor of 3 reduction in the residuals. This yield photometry of sufficient accuracy for the IMF studies presented in the following chapters.

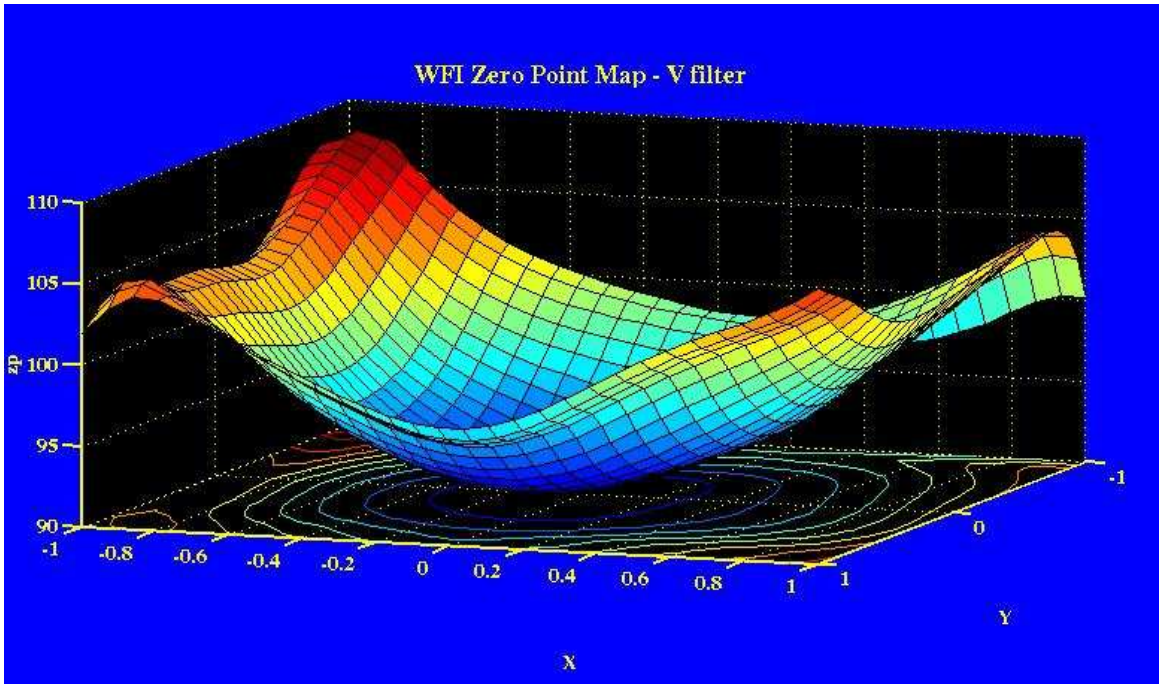

Figure 2.10: Zero point variation of the WFI mosaic for the V filter. The surface represents the percentual variation of the zero point as a function of position. Lower values means that the magnitudes of stars which were measured at those positions (near the center of the mosaic) needs to be made more negative (brightened).

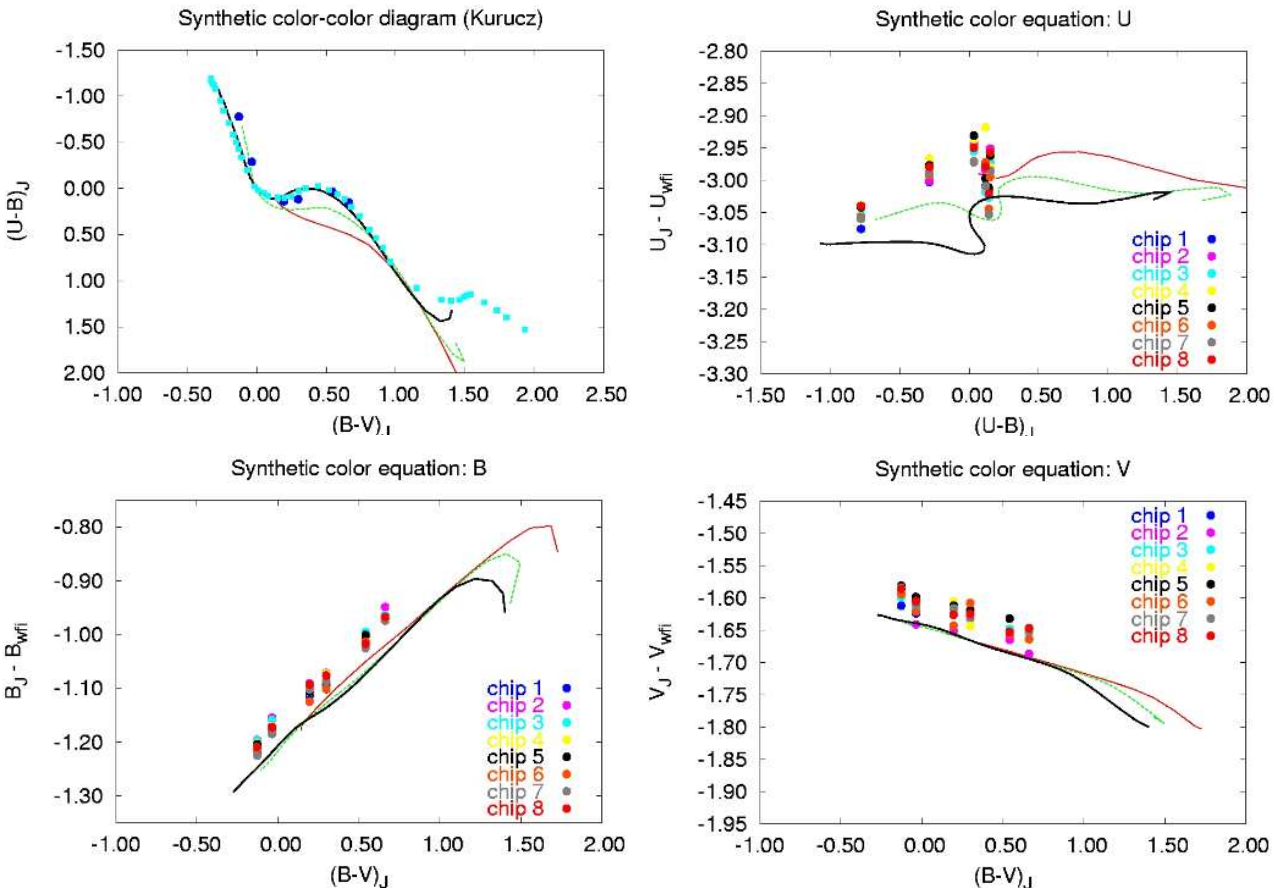

Figure 2.11: All chips data corrected for zero point variations using the method described in the text. The residuals are now 0.009, 0.010, and 0.014 in V, B, and U respectively.

Chapter 3

Data analysis

In this chapter we describe the method used to derive masses and ages for our program stars. There are three different stages in the conversion of magnitudes and colors to physical quantities. The first is the use of theoretical evolutionary models to predict effective temperatures and surface gravities as a function of age for a grid of masses and chemical compositions. The second is the conversion from effective temperature (T_{eff}), surface gravity ($\log g$), and reddening values ($E(B-V)$), to observable colors and magnitudes. And the third is the use of Bayes theorem to go back from the colors and magnitudes of the program stars to the most likely values for their masses, ages, and surface gravities. These stages are described below.

3.1 Empirical calibrations

Several semi-empirical calibrating relationships, as indicated in Figure 3.1, are used to convert physical parameters into UBV magnitudes.

For each point along an evolutionary track we need to determine the intrinsic colors ($(U-B)_0$ and $(B-V)_0$) and the unreddened magnitudes (V_0) as a function of the model parameters, T_{eff}, and g.

3.1.0.1 V_0 as a function of T_{eff}

For this we need the *bolometric correction*, $B.C.$, as a function of T_{eff}. The visual magnitude, V_0, is given by

$$V_0 = M_{bol} - B.C. + (m-M)_0,$$

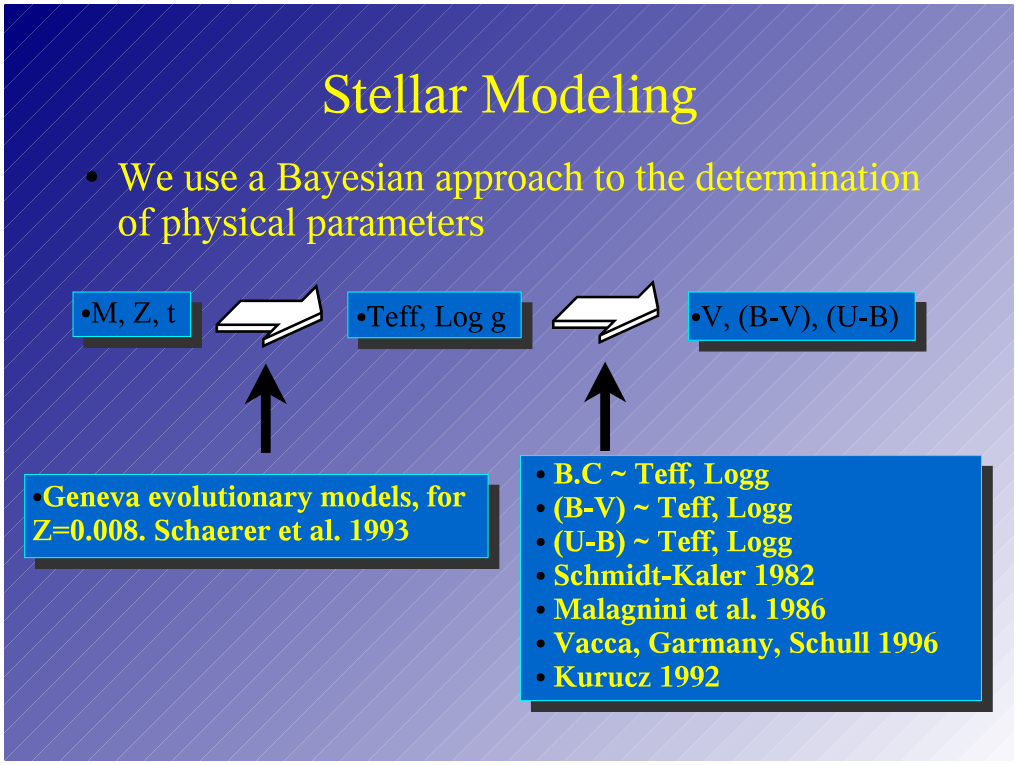

Figure 3.1: Schematics of the process of translating physical parameters to observable ones (and back).

where M_{bol} is the bolometric magnitude given by the evolutionary models and $(m - M)_0$ is the distance modulus.

There are several published recompilations of stellar data that can be used to determine $B.C.$ as a function of T_{eff}. One of the first ones was that of Code et al. (1976) in which they used data for 32 stars with known apparent diameters from interferometric measurements. This calibration was latter revised by Malagnini et al. (1986) to deal with a discrepancy with Kurucz (1979). Malagnini et al. used (1) spectrophotometric scan data from Breger (1976a,b), and the extension to the O stars by Ardeberg and Virdefors (1980); (2) UV data from IUE (Wu et al. 1983; Heck et al. 1984); (3) UBV photometry from Nicolet (1978); (4) spectral types from Jaschek (1978); (5) color excesses derived from the $(B - V)_0$ by FitzGerald (1970). They then used Kurucz (1979) *LTE* model atmospheres to determine $B.C.$

For the hotter stars the most frequently used calibrations are those of Chlebowski and Garmany (1991) and Vacca, Garmany, and Shull (1996). The former calibration, usually referred to as the colder scale, uses bolometric corrections and effective temperatures for a total of 12 stars obtained from plane-parallel, hydrostatic, *non-LTE*

models atmosphere analysis of hot stars by different authors (Kudritzki 1980; Kudritzki, Simon, and Hamman 1983; Simon et al. 1983; Bohannan et al. 1986; Voels 1988; Voels et al. 1989). The latter, or hotter scale, is based on similar data for 58 stars from non-line-blanketed non-LTE plane-parallel hydrostatic, model atmospheres (Kudritzki and Hummer 1990; Lennon et al. 1991a, 1991b; Kolb 1991; Herrero et al. 1992; and Herrero 1994). For spectral classification they used mostly Walborn (1972, 1973).

For the cooler stars, $T_{eff} < 28000K$, we will use the calibration by Malagnini et al. (1986). For $T_{eff} > 28000K$ we will use Vacca et al. (1996).

3.1.0.2 Colors as a function of T_{eff} and g

We will use the calibration by Schmidt-Kaler (1992) to convert spectral types and luminosity classes to UBV colors. Schmidt-Kaler presents the data as tables of $(U-B)_0$, and $(B-V)_0$ versus spectral type for each of the luminosity classes. He derived these tables doing a compilation of a number of previous works, of which we mention here the most relevant for the OB area: Johnson and Iriarte (1958), Serkowski (1963), FitzGerald (1970), Deutschmann et al. (1976), Conti (1975), and Davis (1977). Some of these works are also critical reviews of the literature.

Figure 3.2 show these calibration relations (taken from Paper III).

Thus, for a a star of mass M, and age T, we use the evolutionary models to predict T_{eff}, and $\log g$, and from the above relations we find V_0, $(U-B)_0$, and $(B-V)_0$. We then use Equations 2.1, valid for small reddening values, to find v_0, $(u-b)_0$, and $(b-v)_0$. To find the predicted WFI magnitudes for different values of reddening we need to know the extinction law in the WFI system.

3.1.0.3 The extinction law

We found in Paper I that the extinction law, even in the extreme environment of the ionizing cluster of the Tarantula, was nearly normal in the UBV bands. Thus, we can model the effects of reddening with the observed normal galactic relationships

$$R_V = \frac{A_V}{E(B-V)} = 3.30 + 0.28(B-V)_0 + 0.04E(B-V),$$

$$S = \frac{E(U-B)}{E(B-V)} = \begin{cases} 0.65 - 0.05(U-B)_0 + 0.05E(B-V) & \text{for } (\mathrm{U-B})_0 < 0.0 \\ 0.64 + 0.26(B-V)_0 + 0.05E(B-V) & \text{for } (\mathrm{B-V})_0 > 0.0, \end{cases}$$

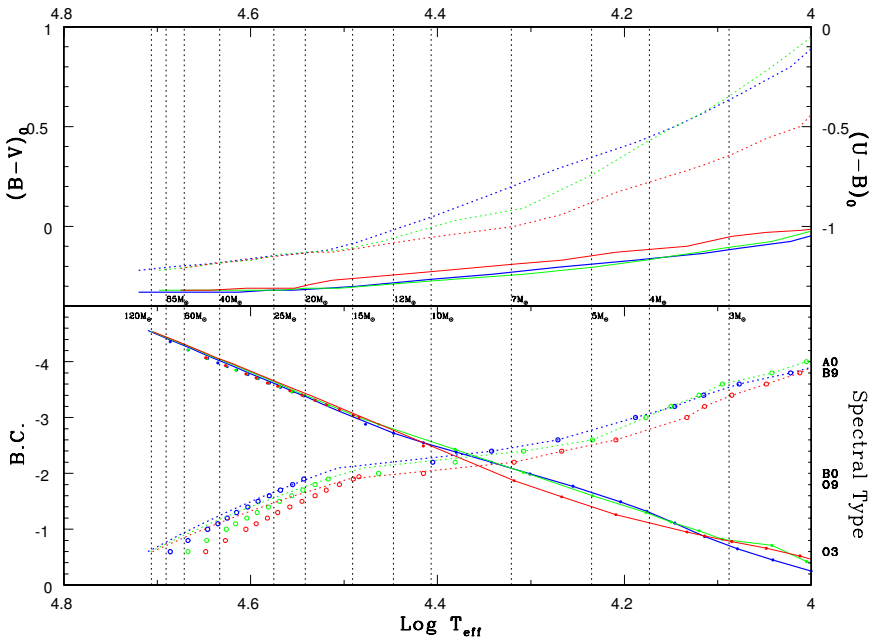

Figure 3.2: Calibration relations for the conversion of observable to physical quantities. The dotted lines use the right-hand axes and the solid lines use the left axes. Color transformations are from Schmidt-Kaler (1982); Bolometric Corrections (B.C.) and spectral type calibrations are and Malagnini et al. (1986) for the later spectral types merged smoothly with the calibrations for O-type stars of Vacca et al. (1996), lines, and Chlebowsky and Garmany (1991), dots. The effective temperatures of ZAMS stars of different masses have been drawn as vertical dotted lines.

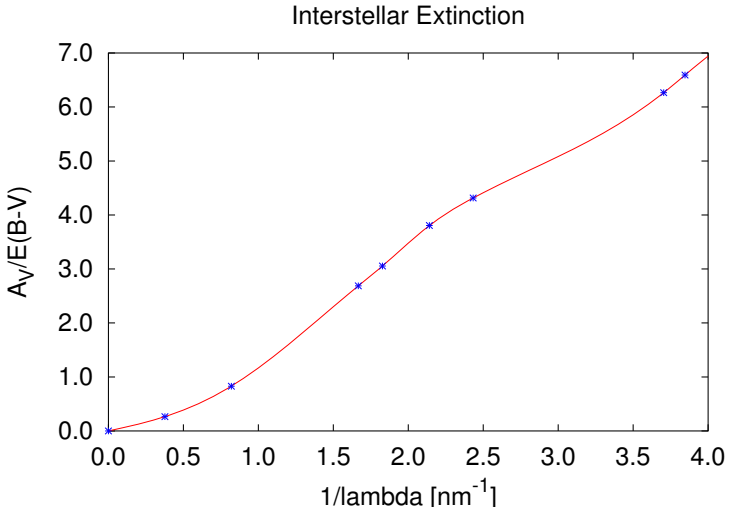

Figure 3.3: The extinction law parametrization of Fitzpatrick (1999).

where

$$\begin{aligned} E(U-B) &= (U-B)-(U-B)_0, \\ E(B-V) &= (B-V)-(B-V)_0, \\ A_V &= V-V_0. \end{aligned}$$

The properties of the WFI system, studied in section 2.3, show that we can not work in the standard UBV bands. Thus, we need to determine the equivalent of the above relations for the WFI ubv system. This was done with the Kurucz (2002) models atmospheres following Buser (1978). For the extinction law we used the better parametrization, based on splines, given by Fitzpatrick (1999) and plotted in Figure 3.3.

Figure 3.4 shows the plots of the *simulated* slope S, and total-to-selective extinction ratio R, as a function of unreddened Johnson (B-V). The solid lines represent the parametrizations of this section appropriate for $(B-V)_0 > 0$. Figure 3.5 shows the results of the simulations versus $(U-B)_0$. The upper data set in every panel corresponds to the simulation for the ubv WFI bandpasses, while the lower one corresponds to our simulation for the Johnson system. The figures also plot the previous formulas for the Johnson system *which represent the observed relations.* They give us an estimate of the accuracy of the simulation process. The equivalent relations for

the WFI system are also plotted as straight lines, and are given by

$$S_{wfi} = \frac{E(u-b)}{E(b-v)} = \begin{cases} 1.036 - 0.042(U-B)_0 & \text{for } (\mathrm{U-B})_0 < 0.0 \\ 1.020 + 0.288(B-V)_0 & \text{for } (\mathrm{B-V})_0 > 0.0, \end{cases}$$

$$R_{wfi} = \frac{A_v}{E(b-v)} = \begin{cases} 4.299 + 0.031(U-B)_0 & \text{for } (\mathrm{U-B})_0 < 0.0 \\ 4.282 + 0.281(B-V)_0 & \text{for } (\mathrm{B-V})_0 > 0.0, \end{cases}$$

where the standard, unreddened, Johnson colors have been used as independent variable.

We also simulated the ratio of total to selective extinction R_V. The values found for the Johnson system are around 3.1 (the same value which was input via the extinction law). For the WFI system the value found was around 4.3.

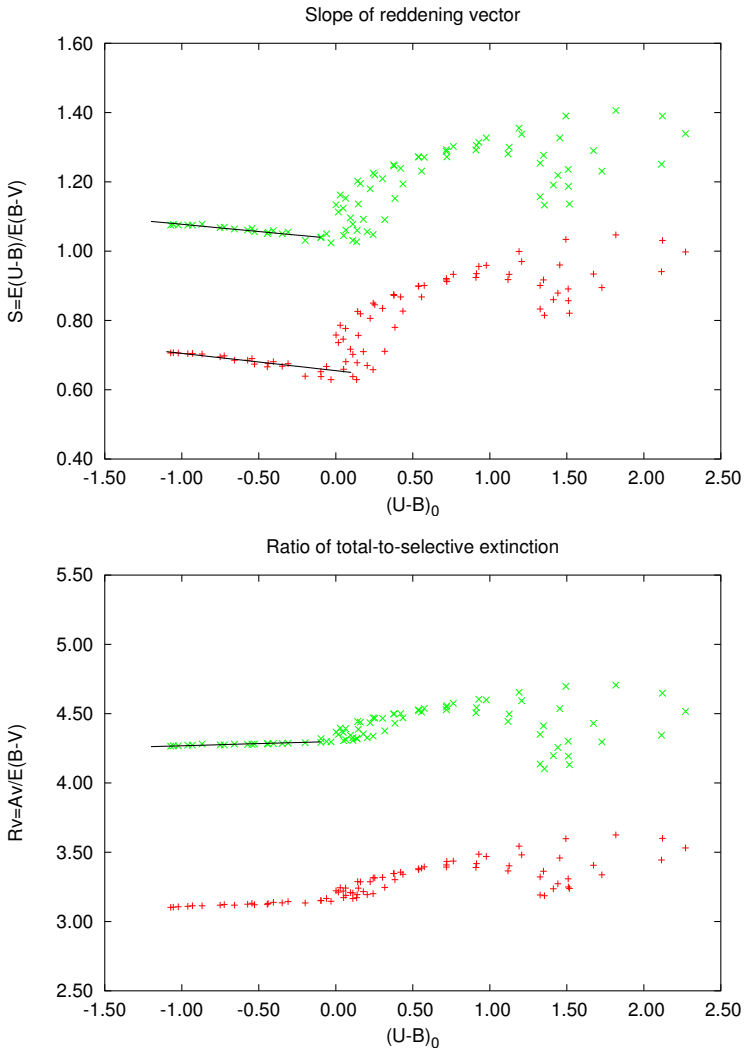

Figure 3.4: Simulated values of the slope of the projection of the reddening vector onto the color-color plane, and the total-to-selective extinction ratio as a function of unreddened color index $(U-B)_0$. The bottom set of data in both figures corresponds to the simulations for the standard Johnson UBV bands. The top set corresponds to the simulations for the ubv WFI system. Both are plotted versus unreddened, standard Johnson, color index. The straight lines drawn for the Johnson's simulations corresponds to the Schmidt-Kaler (1982) parametrization of the *observed* relations. The one for the WFI was determined in this thesis.

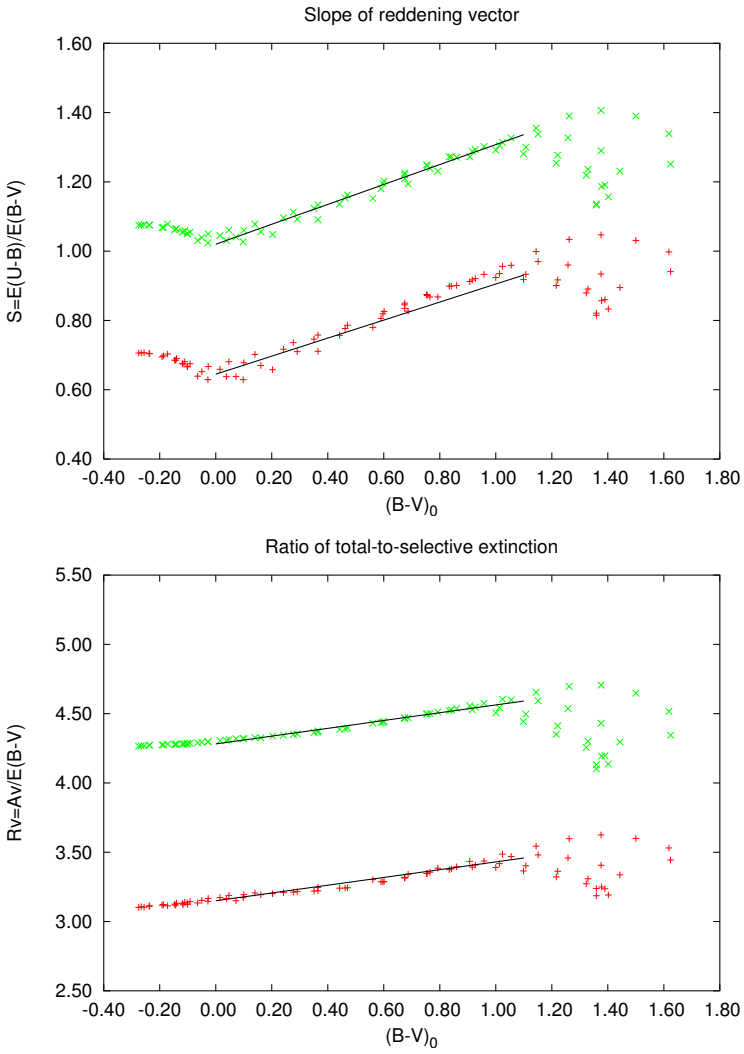

Figure 3.5: Simulated values of the slope of the projection of the reddening vector onto the color-color plane, and the total-to-selective extinction ratio as a function of unreddened color index $(B-V)_0$. The bottom set of data in both figures corresponds to the simulations for the standard Johnson UBV bands. The top set corresponds to the ubv WFI system. Both are plotted versus unreddened, standard Johnson, color index. The straight lines drawn for the Johnson's simulations corresponds to the Schmidt-Kaler (1982) parametrization of the *observed* relations. The one for the WFI was determined in this thesis.

Table 3.1: Simulated WFI extinction law.

Teff	*logg*	$(B-V)_0$	$(U-B)_0$	S_J	R_{V_J}	S_{wfi}	$R_{v_{wfi}}$
3500	1.0	1.624	2.115	0.941	3.444	1.251	4.345
3500	2.5	1.359	1.517	0.821	3.239	1.136	4.132
3500	3.5	1.359	1.355	0.815	3.186	1.133	4.102
3500	4.0	1.402	1.327	0.833	3.192	1.157	4.136
3750	1.0	1.618	2.271	0.998	3.531	1.339	4.517
3750	2.5	1.443	1.728	0.895	3.337	1.231	4.296
3750	3.5	1.378	1.510	0.857	3.249	1.187	4.193
3750	4.0	1.390	1.413	0.860	3.236	1.191	4.197
4000	1.0	1.500	2.121	1.031	3.600	1.390	4.648
4000	2.5	1.376	1.673	0.934	3.406	1.290	4.430
4000	3.5	1.329	1.509	0.891	3.308	1.236	4.301
4000	4.0	1.323	1.442	0.879	3.273	1.219	4.256
4250	1.0	1.376	1.818	1.047	3.625	1.406	4.706
4250	2.5	1.258	1.454	0.960	3.458	1.327	4.536
4250	3.5	1.221	1.349	0.917	3.363	1.277	4.412
4250	4.0	1.216	1.327	0.901	3.322	1.254	4.351
4500	1.0	1.262	1.494	1.034	3.598	1.390	4.697
4500	2.5	1.151	1.207	0.970	3.481	1.338	4.593
4500	3.5	1.107	1.126	0.933	3.402	1.300	4.497
4500	4.0	1.099	1.118	0.918	3.365	1.281	4.444
4750	1.0	1.144	1.190	0.999	3.544	1.355	4.654
4750	2.5	1.055	0.977	0.959	3.470	1.327	4.599
4750	3.5	1.013	0.914	0.935	3.418	1.305	4.543
4750	4.0	1.000	0.910	0.924	3.390	1.292	4.506
5000	1.0	1.024	0.929	0.956	3.486	1.314	4.604
5000	2.5	0.958	0.763	0.933	3.436	1.302	4.574
5000	3.5	0.927	0.718	0.921	3.408	1.293	4.548
5000	4.0	0.916	0.718	0.917	3.393	1.288	4.529
5250	1.0	0.907	0.721	0.912	3.434	1.272	4.557

continued on next page

Table 3.1: *continued*

Teff	*logg*	$(B-V)_0$	$(U-B)_0$	S_J	R_{V_J}	S_{wfi}	$R_{v_{wfi}}$
5250	2.5	0.860	0.574	0.901	3.395	1.271	4.538
5250	3.5	0.841	0.536	0.899	3.380	1.272	4.527
5250	4.0	0.834	0.538	0.899	3.374	1.272	4.521
5500	1.0	0.793	0.557	0.868	3.385	1.231	4.511
5500	2.5	0.765	0.421	0.868	3.356	1.239	4.501
5500	3.5	0.755	0.378	0.872	3.347	1.246	4.499
5500	4.0	0.753	0.376	0.875	3.346	1.249	4.497
5750	1.0	0.687	0.436	0.827	3.341	1.194	4.470
5750	2.5	0.675	0.304	0.835	3.319	1.209	4.466
5750	3.5	0.674	0.253	0.845	3.315	1.220	4.468
5750	4.0	0.675	0.243	0.850	3.316	1.225	4.470
6000	1.0	0.561	0.384	0.780	3.302	1.152	4.431
6000	2.5	0.590	0.223	0.806	3.287	1.180	4.434
6000	3.5	0.597	0.160	0.819	3.286	1.195	4.439
6000	4.0	0.601	0.142	0.826	3.288	1.202	4.443
6500	1.0	0.365	0.318	0.711	3.246	1.091	4.376
6500	2.5	0.442	0.146	0.757	3.241	1.136	4.387
6500	3.5	0.462	0.064	0.777	3.242	1.153	4.392
6500	4.0	0.470	0.029	0.786	3.244	1.162	4.396
7000	1.0	0.203	0.242	0.658	3.201	1.048	4.338
7000	2.5	0.291	0.179	0.710	3.216	1.092	4.354
7000	3.5	0.351	0.048	0.746	3.220	1.124	4.364
7000	4.0	0.365	0.002	0.758	3.222	1.134	4.367
7500	1.0	0.098	0.135	0.629	3.172	1.027	4.322
7500	2.5	0.161	0.204	0.670	3.194	1.056	4.326
7500	3.5	0.242	0.095	0.717	3.209	1.096	4.344
7500	4.0	0.277	0.017	0.736	3.212	1.113	4.350
8250	1.0	0.072	-0.096	0.638	3.150	1.041	4.320
8250	2.5	0.038	0.111	0.638	3.166	1.031	4.307
8250	3.5	0.100	0.139	0.678	3.194	1.060	4.318
8250	4.0	0.140	0.111	0.702	3.206	1.078	4.327

continued on next page

Table 3.1: *continued*

Teff	*logg*	$(B-V)_0$	$(U-B)_0$	S_J	R_{V_J}	S_{wfi}	$R_{v_{wfi}}$
9000	2.5	-0.028	-0.031	0.629	3.146	1.024	4.296
9000	3.5	0.015	0.051	0.659	3.173	1.045	4.305
9000	4.0	0.047	0.065	0.681	3.189	1.061	4.312
10000	2.5	-0.065	-0.199	0.639	3.134	1.031	4.290
10000	3.5	-0.050	-0.097	0.652	3.152	1.039	4.293
10000	4.0	-0.027	-0.060	0.667	3.167	1.050	4.299
12000	2.5	-0.101	-0.445	0.666	3.124	1.051	4.283
12000	3.5	-0.102	-0.348	0.668	3.135	1.050	4.284
12000	4.0	-0.092	-0.310	0.675	3.144	1.055	4.287
13000	2.5	-0.117	-0.528	0.674	3.121	1.056	4.281
13000	3.5	-0.119	-0.439	0.676	3.131	1.055	4.281
13000	4.0	-0.111	-0.405	0.681	3.139	1.059	4.284
15000	2.5	-0.143	-0.658	0.685	3.118	1.064	4.280
15000	3.5	-0.147	-0.572	0.685	3.125	1.061	4.278
15000	4.0	-0.140	-0.544	0.690	3.132	1.065	4.279
19000	2.5	-0.172	-0.868	0.703	3.114	1.078	4.281
19000	3.5	-0.192	-0.751	0.695	3.118	1.068	4.274
19000	4.0	-0.187	-0.724	0.698	3.123	1.069	4.274
26000	3.5	-0.238	-0.961	0.704	3.110	1.075	4.273
26000	4.0	-0.236	-0.931	0.705	3.114	1.075	4.273
31000	3.5	-0.256	-1.055	0.707	3.104	1.077	4.268
31000	4.0	-0.266	-1.023	0.706	3.107	1.075	4.268
35000	4.0	-0.275	-1.072	0.706	3.102	1.075	4.265

Ratio of selective absorptions in (U-B) and (B-V) simulated using the Kurucz model atmospheres. Columns 5 and 6 show the results for the Buser (1978) reconstruction of the Johnson response function. Columns 7 and 8 show the results for the WFI response functions defined in the text. These data are plotted in Figure 3.4, and Figure 3.5. Note that the values of S for the WFI system are nearly constant with color. See main text for details.

3.2 Stellar evolutionary models

In the previous sections we have shown how effective temperatures and surface gravities are converted to magnitudes and colors in the WFI ubv system. Although the results are applicable to Galactic metallicity stars, simulations using Kurucz model atmospheres show that for the metallicity of the LMC the differences are smaller than 1%.

The final ingredients necessary for the conversion of magnitudes to masses and ages are the evolutionary models for stars with the LMC metallicity. There are two sets of models now in common use, the Geneva grid (Schaller et al. 1992; Schaerer et al. 1993), and the Padova grid (Bertelli et al. 1994; Fagotto et al. 1994). These are not *ab initio* models. To describe the observations they introduce a series of semi-phenomenological ingredients: (1) they use the mixing length theory of convection adjusting l/H_p, the ratio of mixing length to pressure scale height, to predict the proper T_{eff} of red giant stars; (2) they adjust the convection overshooting parameter, d, to fit the width of the MS; they use a low enough mass to reduce the confusing effect of mass loss; (3) they use the observed rates of mass loss for massive stars determined by de Jaeger et al. (1988); and the mass loss rate for Wolf-Rayet stars from Langer (1989).

The main difference between the Geneva and Padova models is given by their input nuclear physics. The Padova group uses the Caughlan and Fowler (1988) rates, while the Geneva group uses the Caughlan et al. (1985), and Descouvemont (1989) rates. The Padova models use a lower rate for the reaction $^{12}C(\alpha,\gamma)^{16}O$, resulting in short or non-existent blue loops for massive stars, contrary to observations. They alleviate this by incorporating an extra free parameter: in addition to a core overshoot parameter they have an envelope overshoot parameter. Adjusting this parameter they increase the reach of the bottom of the convective envelope in the red supergiant phase so that it mixes parts of the envelope with material that has been processed at the core of the star; this produces a discontinuity in the molecular weight profile of the star. At later stages of evolution the hydrogen burning shell expands and reaches this discontinuity producing a blue loop with the mechanism described by Ziolkowski (1972).

The Geneva group supplied two sets of tracks, one with the observed mass loss from the references, and the second with twice that rate of mass loss. This was required to predict the proper ratios of BSG to RSG. Considering all the uncertainties in the models, and appealing to *Occam's razor*, we will base all our discussion on the simpler

Geneva models. But we should keep in mind that at the end the Padova models might turn out to be closer to reality.

Figure 4.10(b) shows the isochrones of the Geneva model with Z=0.008 and twice mass loss rate. The $2M_{\odot}$ and $12M_{\odot}$ tracks define the three recognized mass ranges: (1) low mass, $M < 2M_{\odot}$, develop a degenerate helium core and ignition occur with violent *flashes*; (2) intermediate mass stars, $2M_{\odot} \leq M < 12M_{\odot}$, avoid core He-flash but develop a highly electron-degenerate carbon-oxygen core; and (3) high-mass stars, $M \geq 12M_{\odot}$, avoid core degeneracy. Notice that the nature of the blue loops for the low and intermediate mass stars is related to thermal instabilities associated to the violent ignition of helium or carbon in a degenerate core, while for massive stars the blue excursions are produced by either the changing core to total mass ratio due to mass loss, or to the Ziolkowski mechanism mentioned above (Maeder 1986). The main sequence and the helium burning stages have been drawn with thicker lines to indicate the slower evolution. If we consider the speed of evolution, we find that most stars should be located preferentially in one of three regions: at the main sequence, ascending the red supergiant branch, or near the blue extremes of the blue loops. A better representation of the $12M_{\odot}$ track can be found in Figure 3.10 which represents it as a tube in the 3-D color-magnitude stereogram (see below) whose width is proportional to the time the star spends near a given point of the diagram.

3.2.1 Effects of rotation

It has been known for some time that early type stars are fast rotators, being in many cases close to the break-up velocity (Fukuda 1982): (1) the average rotation velocity of main sequence stars has been found to increase from early O stars to the early B stars, interpreted as an indication of higher losses of angular momentum and mass (Penny 1996); (2) the previous effect is more evident in stars of luminosity class IV, possibly due to the effects of mass loss being more noticeable at the end of the main sequence (Maeder and Meynet 2000); (3) for supergiants the opposite effect is observed, that is, the average rotation increases from early O stars to early B stars, the behavior one would expect from an ensemble of stars with similar initial masses (Langer 1988).

The role that the evolutionary models will play in this thesis is to give us the ability to determine masses and ages. They can only do this if they accurately represent the evolution of a star. Although there are no grids of rotating models that we could

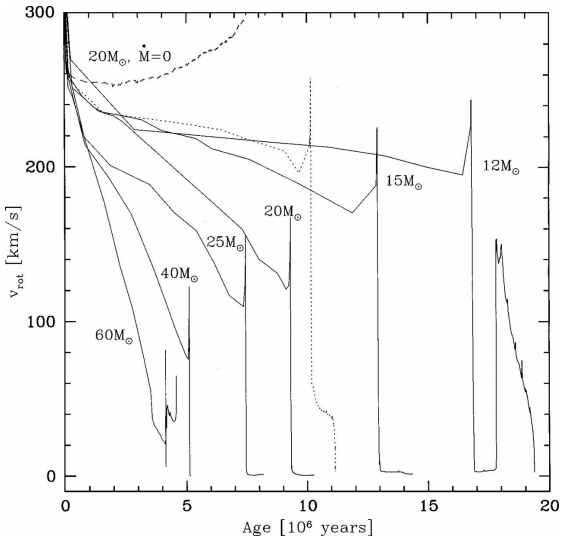

Figure 3.6: Evolution of the surface equatorial velocity as a function of time for stars of various initial stellar masses. All models have initial velocity of 300 km/s and solar metallicity, except the dotted line which corresponds to a Z=0.004 $20M_{\odot}$ star, and the dashed line which corresponds to a $20M_{\odot}$ without mass loss (reproduced from Maeder and Meynet, 2000).

use to model our data, we at least need to know how rotation affects our results. Figure 3.6, taken from Maeder and Meynet (2000), shows that, for massive stars, the time-scale for evolution of the rotation velocity is comparable to the the main sequence evolution time-scale. If rotation affects the photometric properties of a star, then we can expect it to affect the ages we derive using the no rotation assumption. Figure 3.7 shows the effect that rotation has on the HR diagram (Maeder and Meynet 2000). It compares the evolution of Z=0.020 stars of several masses, with and without rotation. The main sequence lifetime grows only 20% to 30% because although there is more nuclear fuel, the luminosity is larger.

Rotation not only affects the interior of the stars, but also their surfaces. We use the work by Collins et al. (1991) to model this effect. A rotating star will have its equatorial radius larger than the polar one, and through the von Zeipel theorem, which states that the local radiative flux is proportional to the local effective gravity, the polar temperature will therefore be larger than the equatorial temperature. Figure 3.8 shows the effect of rotation on the color and magnitude of B1 V, and B5 V stars. We can see in the color-magnitude diagram what Collins et al. calls the *rotational displacement fan* produced by most stars being viewed at intermediate angles between pole-on stars, which, as rotation speed increases, move almost vertically up in this diagram, and equatorial-on stars, which move horizontally to the red. For most

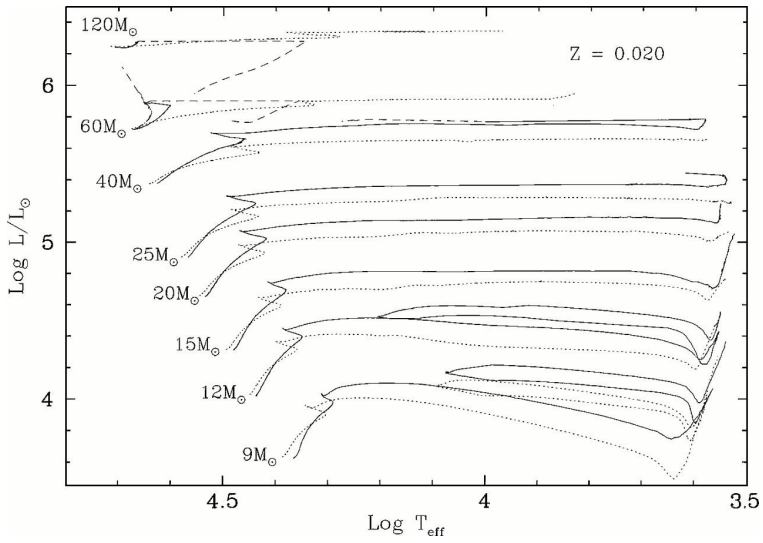

Figure 3.7: Comparison between non-rotating evolutionary tracks, dotted line, and rotating tracks ($v_{rot} = 300km/s$), solid lines, for stars with solar metallicity. The long dashed track corresponds to a very fast rotating star ($v_{rot} = 400km/s$) of 60M$_\odot$ (reproduced from Maeder and Meynet, 2000).

early B-type stars, which are sub-critical rotators (even the Be), we would expect $\Delta(B-V) \leq 0.02$, $\Delta(U-B) \leq 0.05$, and $\Delta M_v \leq 0.5$. Thus, we can expect rotation to induce some scatter in the diagrams, but *no major effect is expected.*

3.3 The Bayesian approach

We follow here the Bayesian method from Paper III, with slight modifications. The basis of the method is the use of Bayes theorem to invert the problem of prediction of observables given a physical model to that of finding the parameters that characterize the physical model given the observables.

We use the calibration relations from the previous section to determine, given an assumed mass, reddening, and age for a star, the theoretical values for $(UBV)_*$. These values will index the model. We construct a column vector with these magnitudes

$$\mathbf{m}_* = \begin{pmatrix} U_* \\ B_* \\ V_* \end{pmatrix}.$$

We next use a model of errors to assign to each physical model, now indexed with the vector of magnitudes, $\mathbf{m}_*$, the probability of observing a given set of UBV

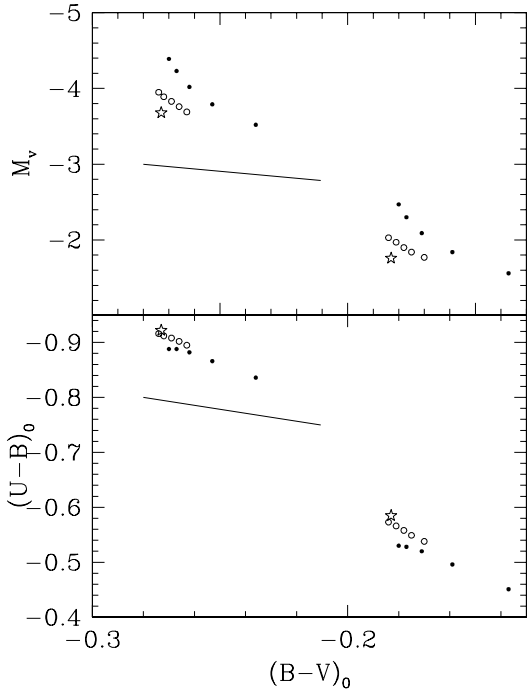

Figure 3.8: The large open stars represent non-rotating stars of type B1 V, and B5 V. The open circles represent stars rotating at 80% of the critical speed, for several viewing angles. The reddest point correspond to the equatorial view, while the bluest to the polar one. Filled circles represent stars rotating at the critical speed. The thick line represents E(U-B)=0.05 normal reddening (after Collins et al. 1991).

magnitudes. Assuming Gaussian errors we can write

$$p(\mathbf{m}|\mathbf{m}_*, Q_m^*) \propto e^{-\frac{1}{2}[\mathbf{m}-\mathbf{m}_*]^T Q_m [\mathbf{m}-\mathbf{m}_*]} \propto e^{-\frac{1}{2}\chi^2}$$

where $\mathbf{m}_*$ indexed the physical models, Q_m^* is the *curvature matrix*, and encapsulates our error model. It is given by $Q_m^* = Diag(\sigma_U^{-2}, \sigma_B^{-2}, \sigma_V^{-2})$, where we have assumed independent errors.

The use of Bayes theorem allows us to write

$$p(\mathbf{m}_*|\mathbf{m}Q_m) \propto p(\mathbf{m}|\mathbf{m}_* Q_m^*)$$

This relation is the one that allows us to assign, to each observation $\mathbf{m}$, the most probable model, $\mathbf{m}_*$.

Because we believe that visualization of the whole process is vital to keep in check the multitude of systematic effects that can affect the data, we have decided to work in the color-magnitude stereogram space, CMS. In this space a measurement will be characterized by a vector given by $\mathbf{x} = (B-V, U-B, V)^T$. Since $\mathbf{x}$ is related to $\mathbf{m}$ by a unitary transformation, the probability density of $\mathbf{x}$ is given by

$$p(\mathbf{x}) = e^{-\frac{1}{2}[\mathbf{x}-\mathbf{x}_*]^T Q_x [\mathbf{x}-\mathbf{x}_*]}$$

where $Q_x = O^T Q_m O$, $O\mathbf{x} = \mathbf{m}$. The price paid for working in color-magnitude space is that the covariance matrix, $C_x = Q_x^{-1}$ is no longer diagonal.

In the CMS space the process can be visualized with the help of the color-magnitude stereogram, shown in Figure 3.9. The figure shows the data, plotted together with three isochrones, and the *theoretical surface*, TS, for one of the isochrones. The TS was defined in Paper III as the locus of points in the stereogram where, for a fixed age, stars of all possible masses can be located: the 1-dimensional isochrones get *extruded* by the effect of reddening.

The Bayesian method finds for each star the *closest* point on the closest theoretical surface. Closest is understood here in the sense of most likely, taking into consideration the structure of the curvature matrix (see Paper I).

The method so far presented, although it makes use of Baye's theorem, is almost a Maximum Likelihood method. For it to be called Bayesian, in the sense currently given to that term (Loredo 1992), it should incorporate information on the prior

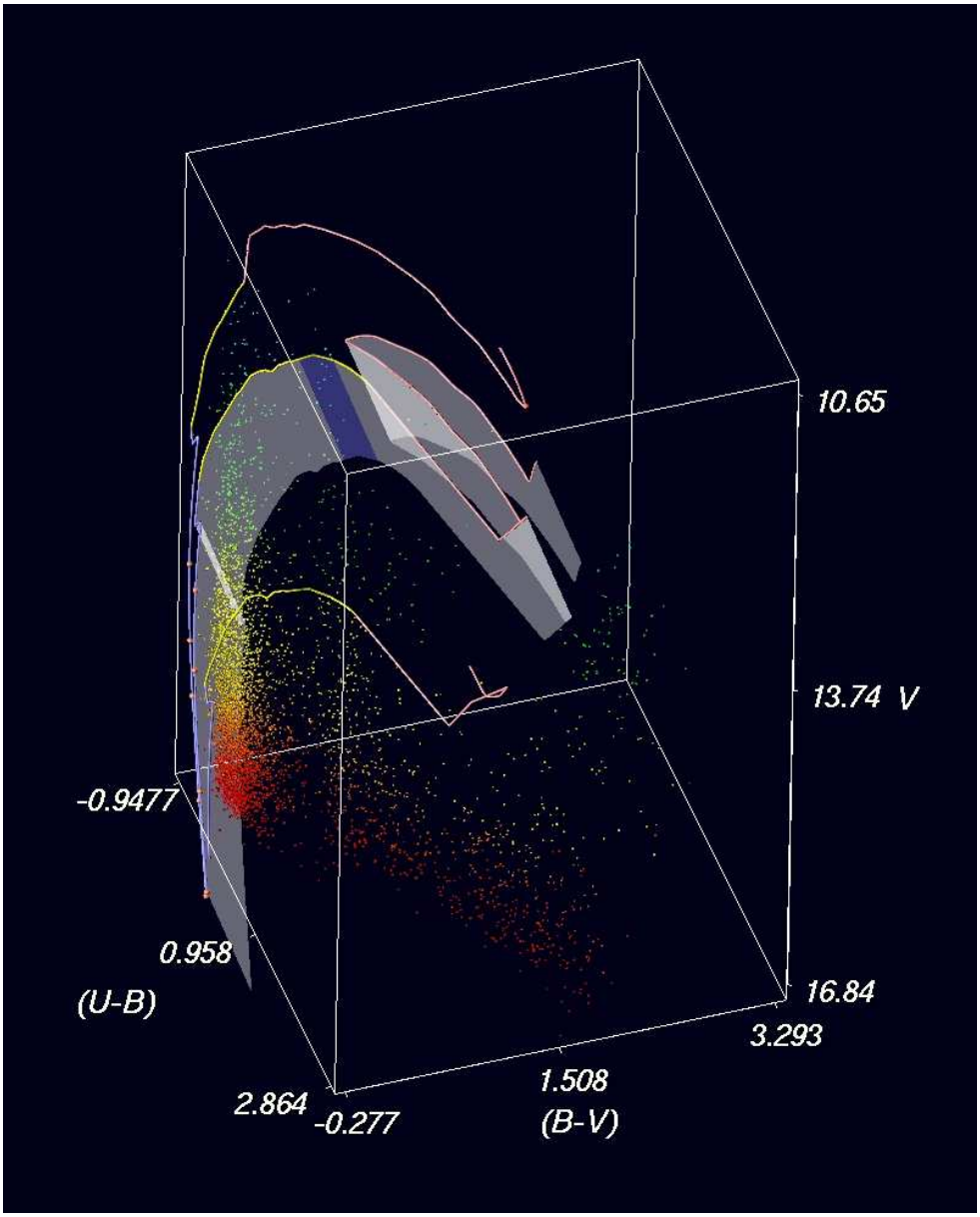

Figure 3.9: Observed stellar points, together with isochrones for 4.5 My, 12 My, and 50 My. The theoretical surface is drawn only for the 12 My isochrones. The tubes representing each isochrone have been painted blue, yellow, or red depending on whether the star is of luminosity class V, III, or I, respectively.

probabilities, or *priors.* That is, the *a priori* probability distribution of the different reddening values, masses, and ages. One could think in terms of an iterative scheme, in which once a solution is found for all stars in the sample, we can construct the priors, and use them in a second solution.

One further issue should be taken in consideration: during the course of its evolution, the star transits on its evolutionary track at different rates making the probability of observing a star in a given volume of the stereogram inversely proportional to the speed with which it moves. Figure 3.10 shows this effect for the $12M_{\odot}$ track. Again, the color of the tube represents the luminosity class of the star, but now its width represents the observing probability. We can see the well-known result that a star is most likely to be observed in the main sequence phase, in the ascent to the red giant branch (near the Hayashi edge), and at the bluest extremes of the blue loops.

In what follows we will only use the distribution of reddening values as a prior, and only to set limits to the maximum and minimum values allowed. This is done so that the method will not pick up stars with unreasonable reddening values, forcing them to populate the physically permitted regions of the HR diagram. For all the other variables we will *let the data speak for itself.*

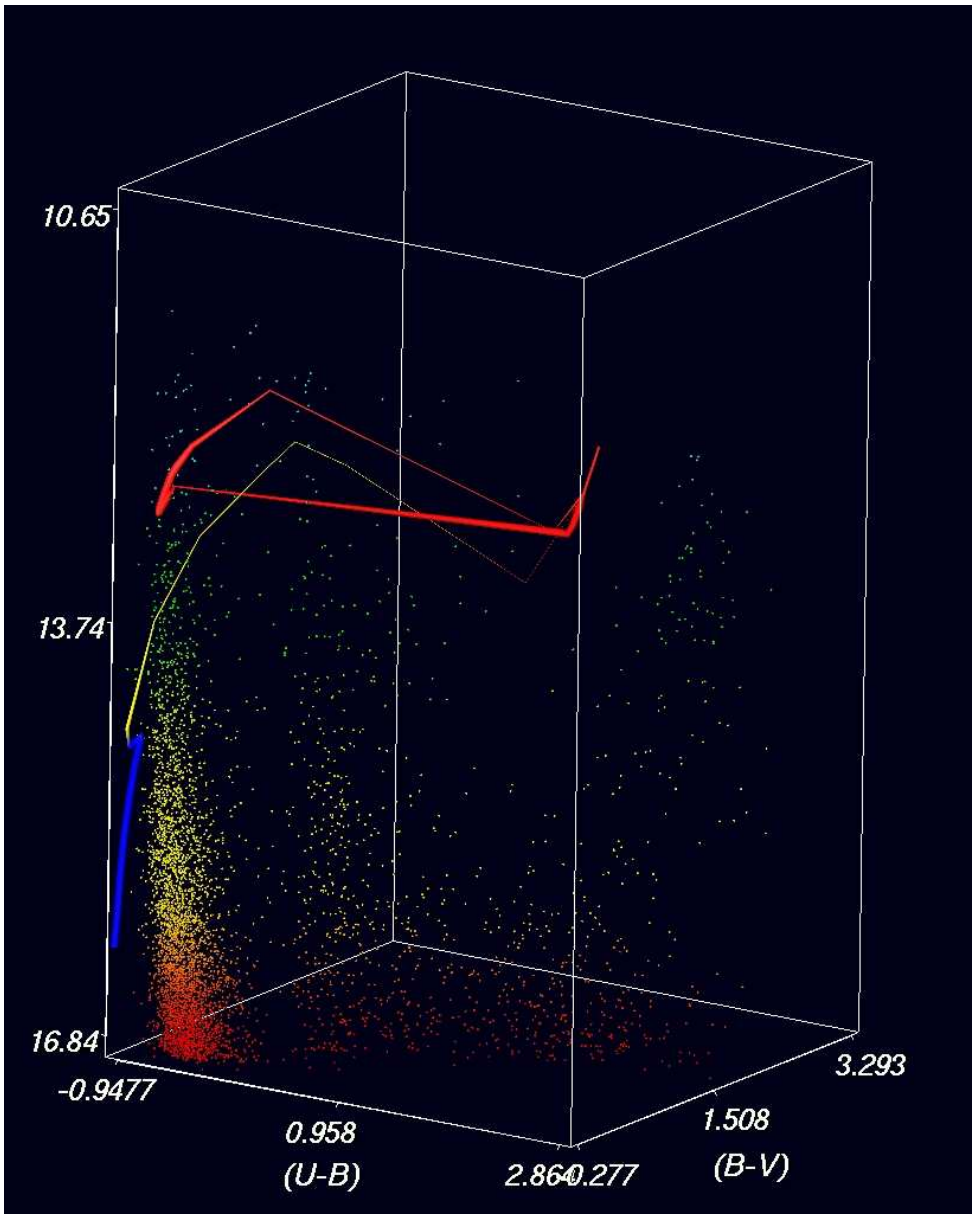

Figure 3.10: Evolutionary track for a $12M_{\odot}$ star. The color represents the luminosity class, and the width represents the observing probability.

Chapter 4

Data visualization and calibration issues

The color-magnitude stereogram, CMS, a tool to visualize the observed colors and magnitudes of program stars, together with the theoretical colors and magnitudes of stars of different masses and ages, is used for quick views of the data—for recognition of trends, correlations, and possible problems with the reduction. A systematic effect, inherited from a previous photometric work, is revealed, and a method to recalibrate the data, using the stars with spectroscopic observations is presented, and applied to produce the final catalog. Finally, the data from the re-calibrated catalog is described using classical views, identifying real features.

4.1 The catalog

Table 4.1 presents the first few entries of the catalog with the photometric properties of the stars in the region. The id assigned in this thesis is in the first column: the first number in the id refers to the pointing, 1 for the NE field analyzed in this thesis; the second number refers to the CCD chip in the mosaic, and the rest is a correlative identification number. For example, 1300007 refers to the seventh star, in chip 3, for the NE pointing. Columns (2) and (3) are the x,y values in the mosaic. Columns (4), and (5) give the v magnitude, and its estimated error; columns (6) and (7) give the (b-v) color and its error; column (8) and (9) give the (u-b) color and its error; columns (10), (11), and (12) give the derived T_{eff}, M_{bol}, and luminosity class; columns (13) and (14) give the derived age and initial mass; column (15) gives the derived E(b-v); and finally, column (16) gives an estimate of the goodness of the photometric fit, DAOPHOT's Chi value. The full catalog will be available through the web after

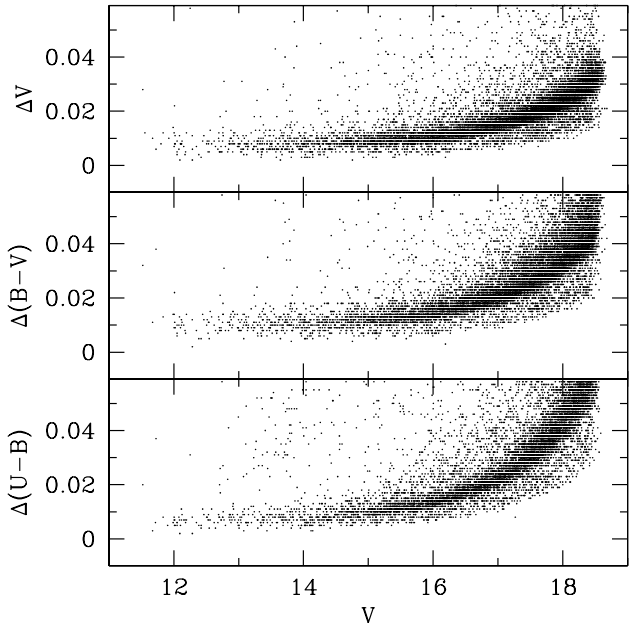

Figure 4.1: Errors reported by DAOPHOT for all the star. Errors of stars with multiple measurement were added in quadrature.

publication of the results.

Figure 4.1 shows the errors reported by DAOPHOT for the WFI magnitude and colors. We can see that the errors in magnitudes and colors are below 3% for all stars brighter than v = 17.5, the limiting magnitude for the stars of interest in this research.

Figure 4.2 shows the value of χ^2 reported by DAOPHOT for each star. This statistics is used to estimate how well does the PSF fit the profile of the star. If the errors are well estimated, the values should cluster symmetrically around one. We notice that the average of this statistic is slightly larger than one, a well known "feature" of DAOPHOT, that it somewhat underestimates the errors. We can also see that only the u filter shows the expected behavior for all magnitudes. Both b and v show departures for the brighter magnitudes. We believe that this figure shows the effect of the well known non-linearity, at the 2% level, of the WFI CCDs. The χ^2 statistics is very sensitive to such a non-linearity: 2% of 50,000 ADU is much larger than the 160 ADU of the Poisson noise. The bottom panel of Figure 4.2 shows the *sharpness* statistic for the catalog. This statistic is used to separate stars from objects that are either too sharp, e.g., cosmic rays, or too broad, e.g., galaxies, to be considered stars. It should be equally spread around zero, which is the observed

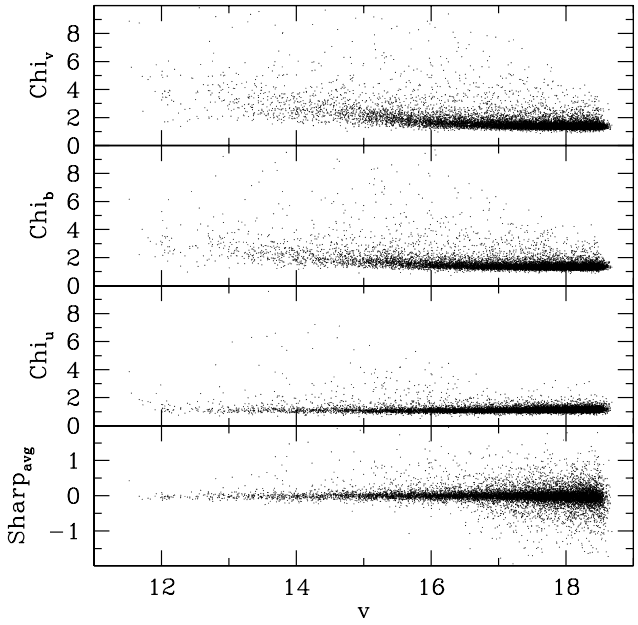

Figure 4.2: Upper three panels show the values reported by DAOPHOT for χ^2 in the different filters. The bottom panel shows the average for the sharpness parameter.

behavior. For details on the meaning of these parameters the reader is referred to our Paper I.

To have an independent measure of the non-linearity, we have compared our magnitudes with those from Parker (1993), whose data, taken with a smaller telescope and under much worse seeing should not be much affected by non-linearity effects. As previously discussed, we chose in this thesis not to work in the standard Johnson UBV system due to the difficulty of an appropriate conversion. Nevertheless, and just to study if the zero points vary with magnitude, we have applied the reddening-free transformation equations to our data, which after all is the same procedure followed by Parker. Figure 4.3 shows the difference between the Parker and the WFI magnitudes, $m_{parker} - m_{WFI}$, for the stars in common in the area of 30 Doradus. We can see that whatever trend with magnitude there is, it is in the opposite sense of what would be expected if the WFI magnitudes were much affected by non-linearity. We estimate from this figure that, between v = 12.5 and v = 17.5, such a variation is below 5%.

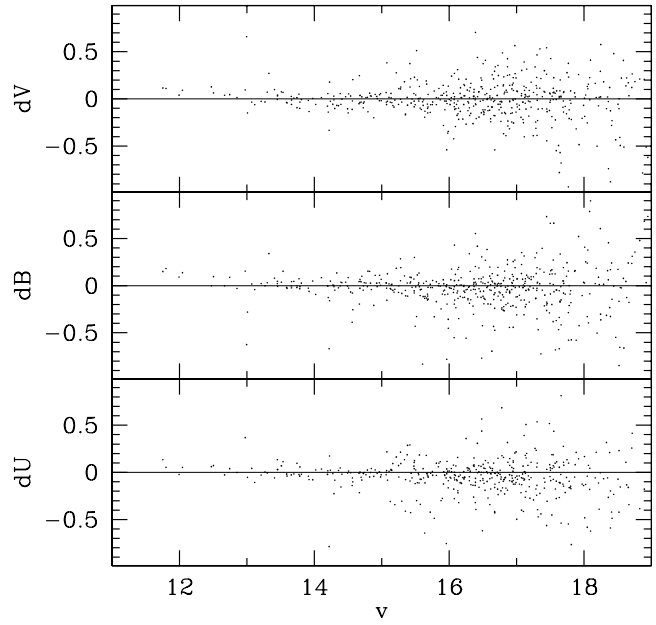

Figure 4.3: Comparison between the magnitudes of Parker (1993), and those of this thesis. The differences are in the sense $m_{parker} - m_{WFI}$.

4.2 Data visualization: the color-magnitude stereogram view of the data

It was claimed by Selman et al. (1999b) that it is possible to determine masses, ages, and reddening values for young massive stars using UBV photometry alone. Our method is based on the fact that, although the UBV colors of young massive stars are nearly degenerate, their luminosities are not. The Planck curves for different temperatures are non-intersecting and in the Rayleigh-Jeans regime the luminosities are proportional to temperature ($\times R^2$). Thus, an O3 star ($T_{eff} \approx 50000K$) has a luminosity at least twice as large as that of a star of type B0 ($T_{eff} \approx 27000K$). This large difference, together with the fact that in the 3-D color-magnitude stereogram differential reddening spreads the locus of stars of different masses over a surface, makes the conversion from UBV magnitudes to masses, ages and reddenings a practical undertaking.

Figure 4.4 shows four projections of the color-magnitude stereogram for the WFI data. Three of the projections correspond to the standard views: Figure 4.4(a) color-color; Figure 4.4(b) V-(U-B) CM diagram; Figure 4.4(c) V-(B-V) CM diagram; and

Figure 4.4(d) shows a reddening free view of the data. The 9 My, 15 My, and 50 My isochrones have been drawn together with the data. The 15 My isochrone has been *extruded* to show the *theoretical surface*, the locus on the stereogram for stars of that age and arbitrary reddening (see Section 3.1). Several features are worth noting:

- the Hertzsprung gap between the main sequence and the red super giants area is very clearly demarcated, close to where the models predict;
- the nearly flat geometry of the distribution of stars clearly stands out showing the quality of the data;
- the deviations of the data from exact flat geometry agree, with one exception, with the theoretical predictions;
- the exception is the set of stars extending to the blue from the *meander* in the MS locus, probably due to contamination from MW disk stars (Massey 2002);
- the main sequence is *clean* in terms of the separation of masses, ages, and reddening; while the red giants region is rather messy due to the multiple loops;

Thus, the color-magnitude stereogram shows that we can indeed determine ages, masses, and reddenings with photometric data. The problem is more complicated when the stellar population being analyzed is not coeval, but even in this case there is a separation if we restrict our population to main sequence stars.

The statistical technique developed in Paper III will be used for the quantitative analysis, and is the subject of the next section.

4.3 Zero-point calibration using stars with spectroscopy

We have seen that the large color terms of the U and B filters complicates the transformation to the standard system. Regrettably, this complication affects most CCD works on these passbands known to the author. Initially our intention was to use the photometry of Parker (1993) to establish the zero-points of our photometry. However, in doing this we noticed the presence of serious systematic errors in Parker's photometry. This is illustrated in Figure 4.5(a) that shows the color-color diagram for 47

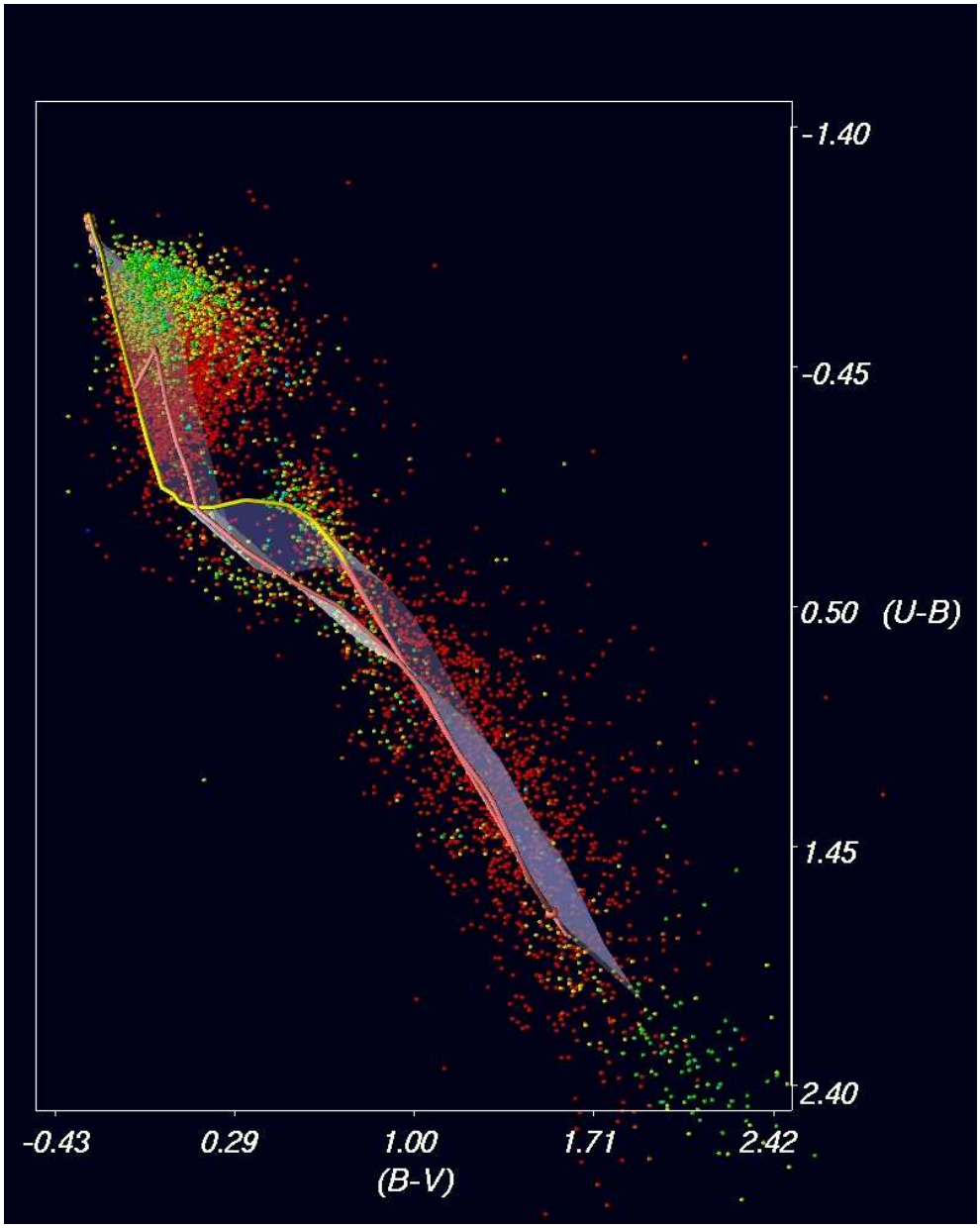

Figure 4.4: (a) Color-color stereogram projection showing main sequence, Hertzsprung gap, and red super-giant branches. Colors are used as an aid to follow stars on different projections; Plotted with the data are the isochrones for 9 My, 15 My, and 50 My. On the 15 My isochrone the theoretical surface has been drawn by extruding the isochrone by E(B-V)=1.

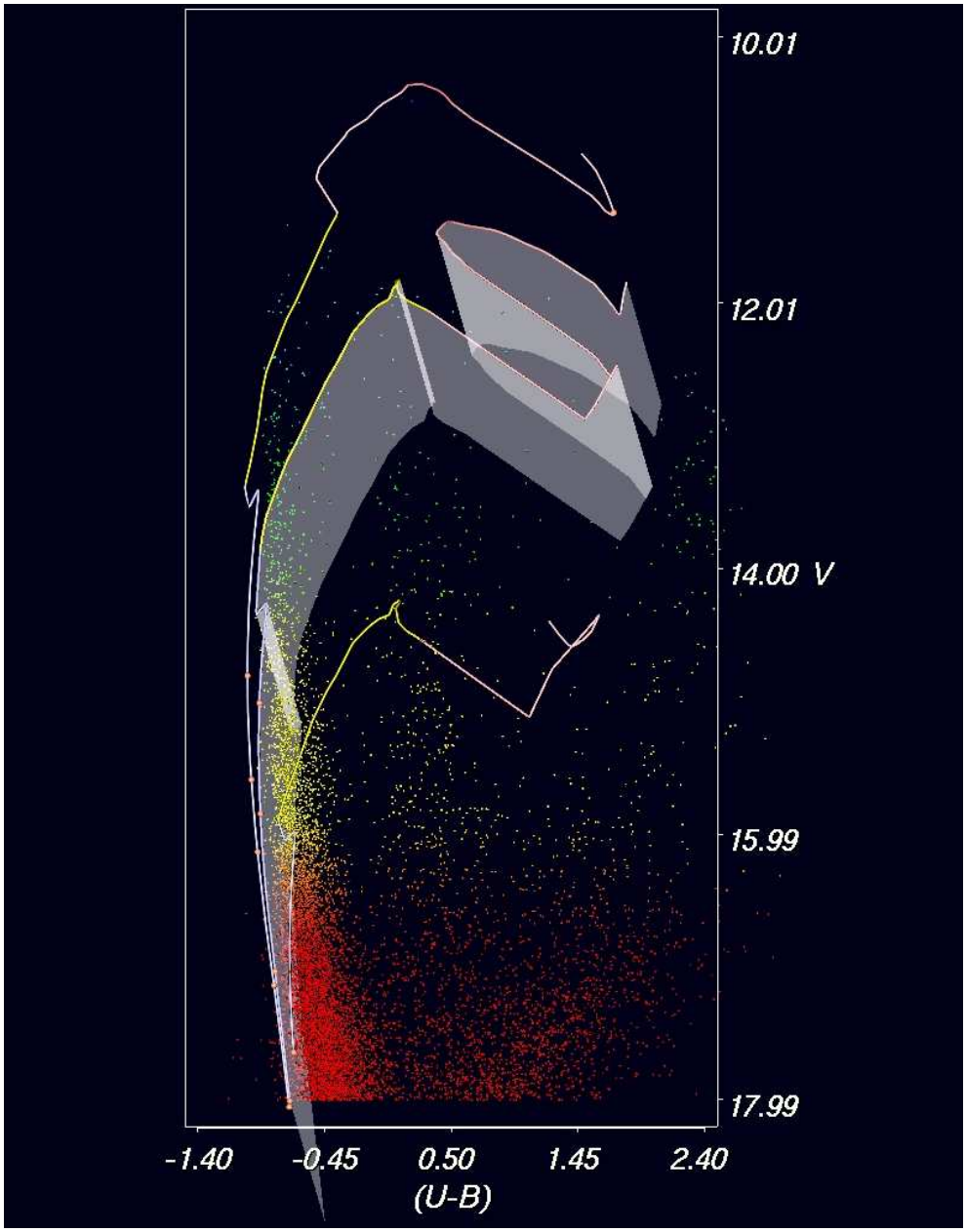

Figure 4.4: (b) V-(U-B) color-magnitude stereogram projection, corresponding to the classical V-(U-B) color-magnitude diagram. The parallel sequence seen between the main sequence and the red giant branch is made up to a large extent of Milky Way disk dwarfs and giants.

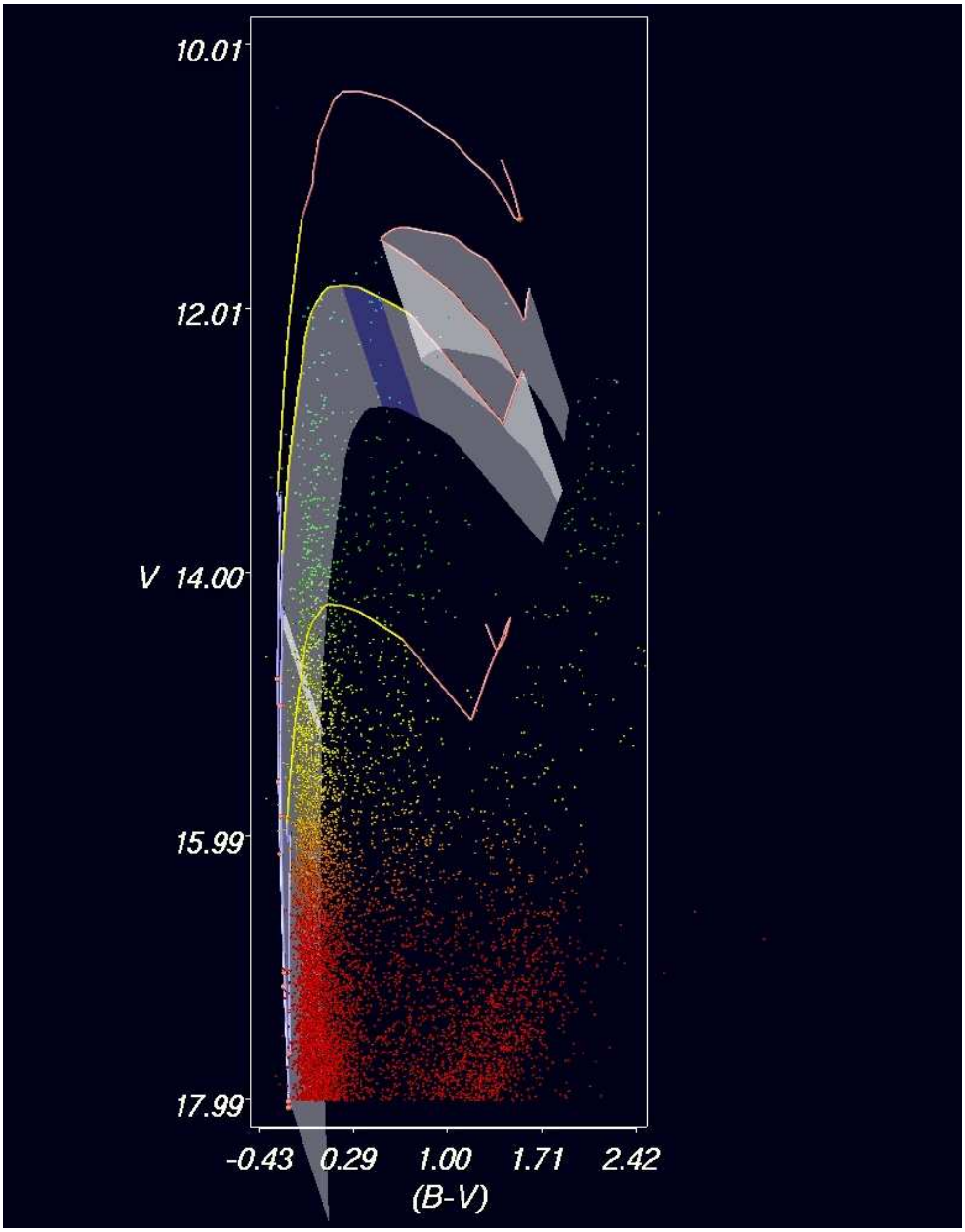

Figure 4.4: (c) V-(B-V) color-magnitude stereogram projection, corresponding to the classical V-(B-V) color-magnitude diagram.

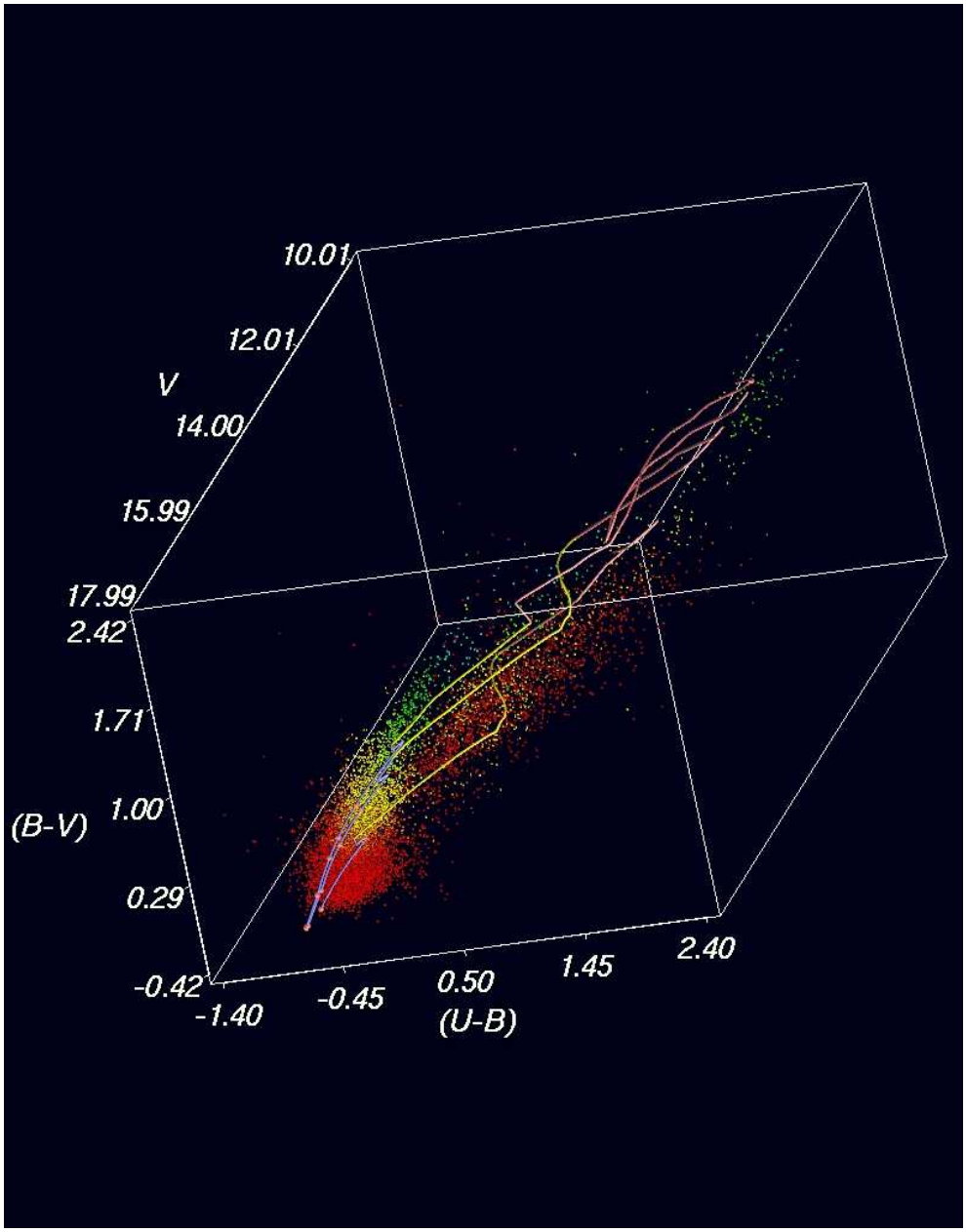

Figure 4.4: (d) reddening free stereogram projection in which the effects of reddening are absent. This projection corresponds to the view from a point infinitely distant, in the direction of the reddening vector.

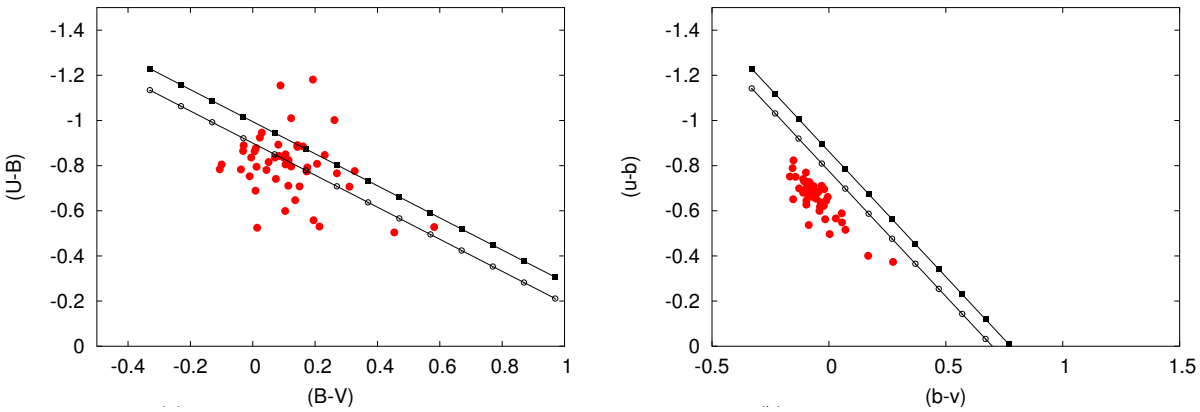

Figure 4.5: (left, a) The positions in the color-color diagram for stars of spectral types earlier than B9, according to Parker's (1993) photometry. (right, b) The WFI data, calibrated using Parker's photometry, for the same set of stars.

stars in the catalog of Parker in common with the present work, and for which we have photometry and spectral types from Papers II and III. The lines in the Figure represent the reddening vectors for an O3 and a B0 star, appropriate for the majority of the stars in the sample. The large dispersion in Parker's photometry is clearly illustrated in the diagram.

Figure 4.5(b) plots the WFI data for the same stars, this time in the WFI photometric system. The zero-points have been fixed using Parker's photometry. We see that now the stars do indeed define a narrow strip as expected, but we also clearly see that there is a systematic offset in the color-color diagram.

Clearly, therefore, the zero-points of our photometry cannot be set using Parker's work. However, we can use the spectral types of the same stars to determine the systematic shifts in the photometric zero points. This is done by applying zero point shifts to the data in (u-b) and (b-v), and comparing the spectral types obtained from our Bayesian method to the cataloged values. The resulting χ^2 contours are presented in Figure 4.6. We see that there is a well determined minimum given by the point at which we get the optimal correspondence between photometric and spectroscopic spectral types. We can now check the spectral types determined photometrically after applying the optimal zero-point offsets to the data.

Table 4.2 contains spectroscopic and photometric effective temperatures for a sample of stars with known spectral types from the literature. Figure 4.7 shows the comparison of the photometric effective temperatures with those determined in several sources: Paper II was used for stars around N2070, with several types from Walborn

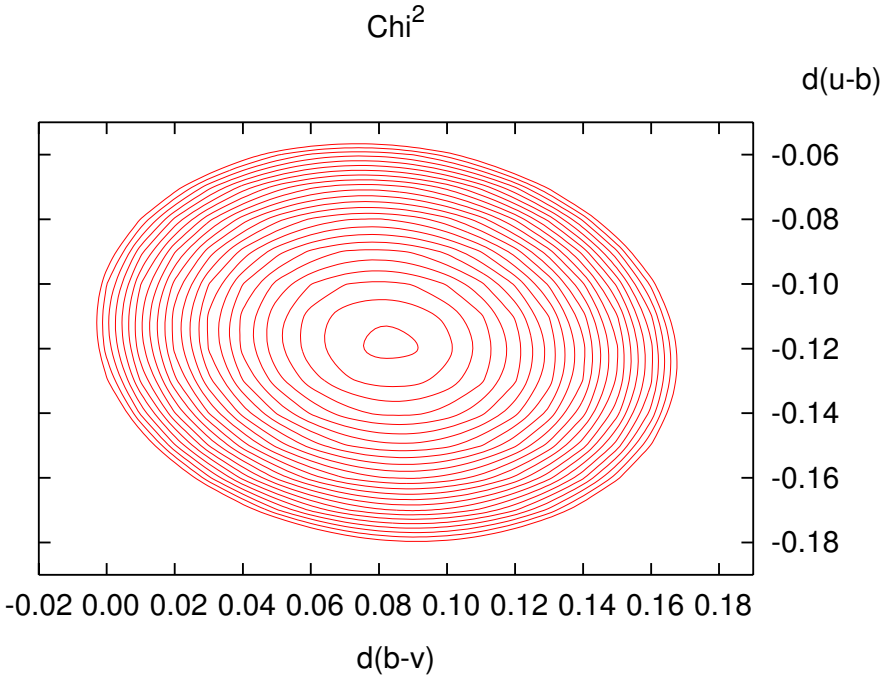

Figure 4.6: Values of χ^2 as a function of color offset for stars with spectroscopy.

and Blades (1997), and Melnick (1985); the compilation by Grebel and Chu (2000), was used for Hodge 301; Schild and Testor (1992), and Testor and Niemela (1998), were used for LH104. The diagonal line represents a perfect correlation, and the thick line below it represents the effect of a blue-ward shift of 0.05 magnitudes in (U-B). The three stars from LH104, which are located well below the line at $logT_{eff} \sim 3.75$, were marked as possessing unreliable classification by Schild and Testor (1992), they are stars 4-60, 4-58, and 4-67.

There are three interesting effects in Figure 4.7: (1) most early B-type supergiants have been assigned photometric temperatures which exceed the spectroscopic ones; (2) the stars represented by the open triangles from the Hodge 301 region, although not classified as supergiants, they are classified as Be; and (3) the stars from LH104 at $\log Teff \sim 4.30$ which are located below the line are all of type B2 III, while the stars on the correlation line are of mostly of types B1 V, and B2 V, with a few B0 V, B0.5 V, and two B1 III. We believe that these three effects are related to two well known properties of Be stars: (1) many Be stars have the continuum short-ward of the Balmer jump in emission giving rise to an excess in the U filter (Mendoza 1958); (2) red-ward of 500 nm, and extending into the near infrared, there is excess

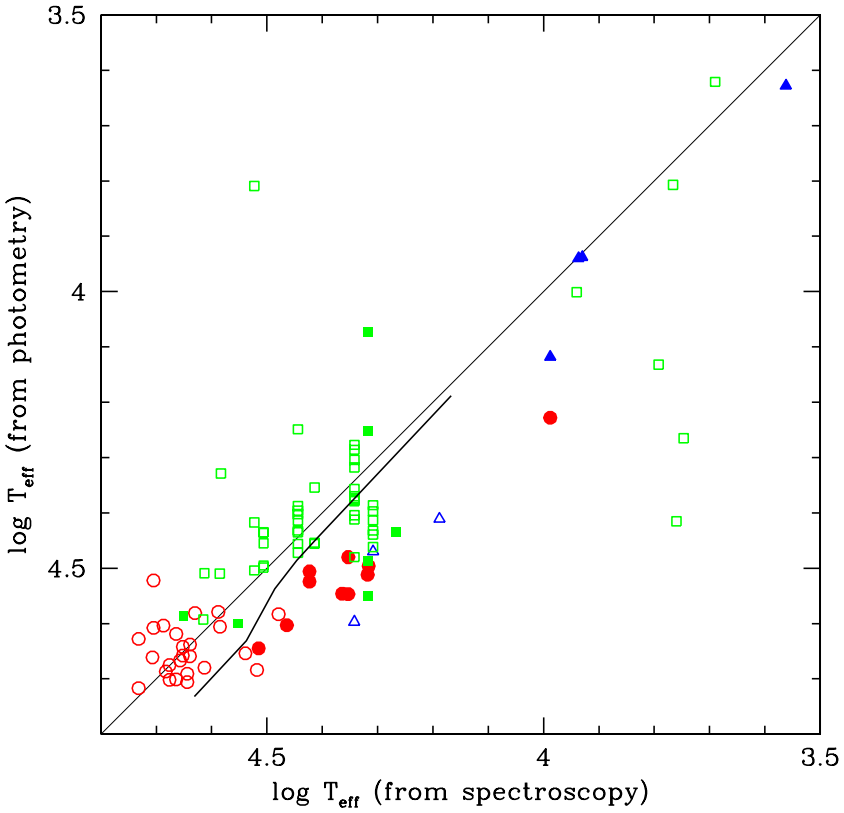

Figure 4.7: Comparison between photometrically determined effective temperatures and those measured with a spectroscope (data from Table 4.2). The circles correspond to N2070; squares to LH104; and triangles to Hodge 301. Filled symbols represent supergiants, while open symbols are used for all other luminosity classes. The thick line below the diagonal line illustrates the effect of a 0.05 blue-ward shift in (U-B).

emission affecting the V filter (Schild 1966). These excesses displace the position of the star in the color-color diagram to the upper right by as much as 0.3 magnitudes in some cases. We point out that a star is classified as Be if it has shown the Balmer lines in emission at some time, and it is not a supergiant. It is remarkable that all stars in the "parallel" sequence are either supergiants, giants, or Be stars, perhaps hinting at a deeper connection. Although this effect can be seen in the spectral energy distributions of B giants and supergiants, we will subsequently refer to it as the *Be effect*.

The number of Be stars can be a considerable fraction of the early B-types. In the area around Hodge 301, Grebel and Chu (2000) estimates the fractions at 60% for B0, 40% for B1, and 30% for B2. Keller et al. (1999) estimates that approximately 30% of the early B stars are Be. For field stars in the LMC that fraction is reduced to ∼15%. The Be stars and the B supergiants will consistently move to higher mass bins introducing biases on our determination of the IMF. Nevertheless, those biases can be estimated and proper correction factors applied (Grebel et al. 1996).

We also point out that non-linearity and saturation for very bright stars have a similar effect of moving these stars to higher effective temperatures. Star 14000009, at V=11.802, located at $logT_{eff} \sim 3.99$ might be affected by non-linearity of the detector at that magnitude range. Figure 4.10(b) shows the line demarcating the upper boundary above which strong non-linearity and saturation affects the photometry (v = 12.5). We see that the very young stars can be free of these effects up to 120 $M_{\odot}$, the highest mass covered by the models. Nevertheless, evolved stars of 40 $M_{\odot}$ or more can be affected by non-linearities. We believe that at least some of the B-type supergiants can be affected by this effect. To determine mass function slopes, for populations older than 5 My, we will only use stars in the mass range $10M_{\odot} < M < 40M_{\odot}$.

4.4 Taxonomy of the color-color and HR diagrams

Although we have obtained data for a square region $1^o \times 1^o$ covering almost the full super-association, in this thesis we restrict the analysis to the first quadrant of the region shown in Figure 4.8.

The data for this quadrant calibrated with the procedure outlined above can be seen in Figure 4.9. This figure, which plots the colors of nearly 13,000 stars, serves as

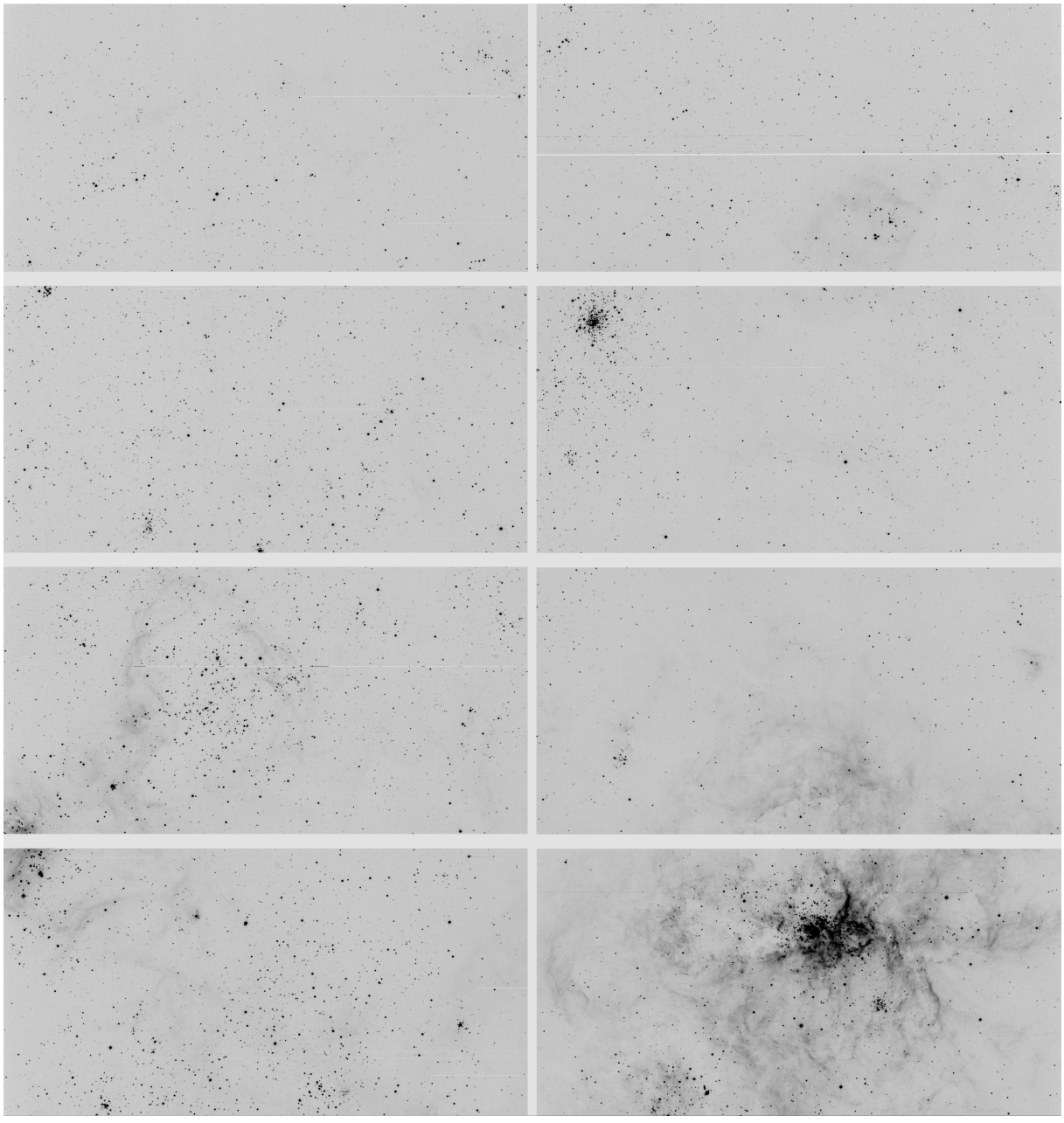

Figure 4.8: The NE field of the Tarantula nebula. North to the right, east to the top.

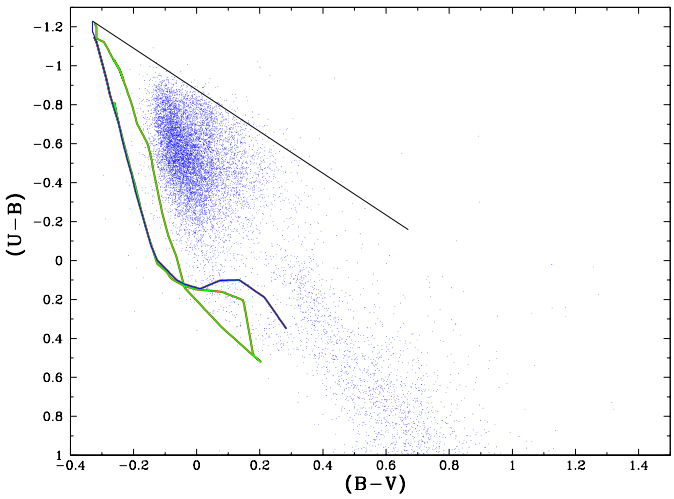

Figure 4.9: The WFI ubv color-color diagram. Also drawn are the ZAMS, and isochrones at 2.5 My and 4.5 My. The straight line marks the reddening vector for an O3 star.

an overall sanity check of the data showing that most stars lie on the allowed region of the diagram. In particular we point out that the stars span the strip defined by the reddening line of an O3 star and a parallel line tangent to the MS at $(b-v) = 0.0$, and $(u-b) = 0.1$. Such a strip define the area in the diagram where stars can be found if the transformation equation for unreddened stars (Equations 2.1) are valid.

Figure 4.10(a) shows the HR diagram for this quadrant. We have deliberately avoided to superpose tracks or isochrones to this plot in order to allow the reader to form an independent impression of the relevant features of the diagram. Our Bayesian analysis gives for each star its reddening, its effective temperature, its bolometric luminosity, its initial mass, and its age. Therefore, there is a wealth of information to be used in the study of the region. The analysis of some of the properties of the region are presented below.

Several real features of the HR diagram in Figure 4.10(a) can immediately be recognized: (1) the main sequence can be traced down to $7M_{\odot}$, corresponding to a zero age B2 V star; (2) a blue supergiant region above $M_{bol} = -7$; (3) a well-populated red supergiant and red giant region with $\log T_{eff} < 3.8$; (4) contamination from Milky Way disk giants at $4.0 > \log T_{eff} > 3.8$ and $-7 < M_{bol} < -2$; (5) contamination from Milky Way disk dwarfs in the region delimited by $4.3 > \log T_{eff} > 4.0$ and $-7 < M_{bol} < -2$. (6) a gap in the red supergiants branch at $M_{bol} = -6$, although this could be an artifact product of the non-unicity of solutions in this region of the

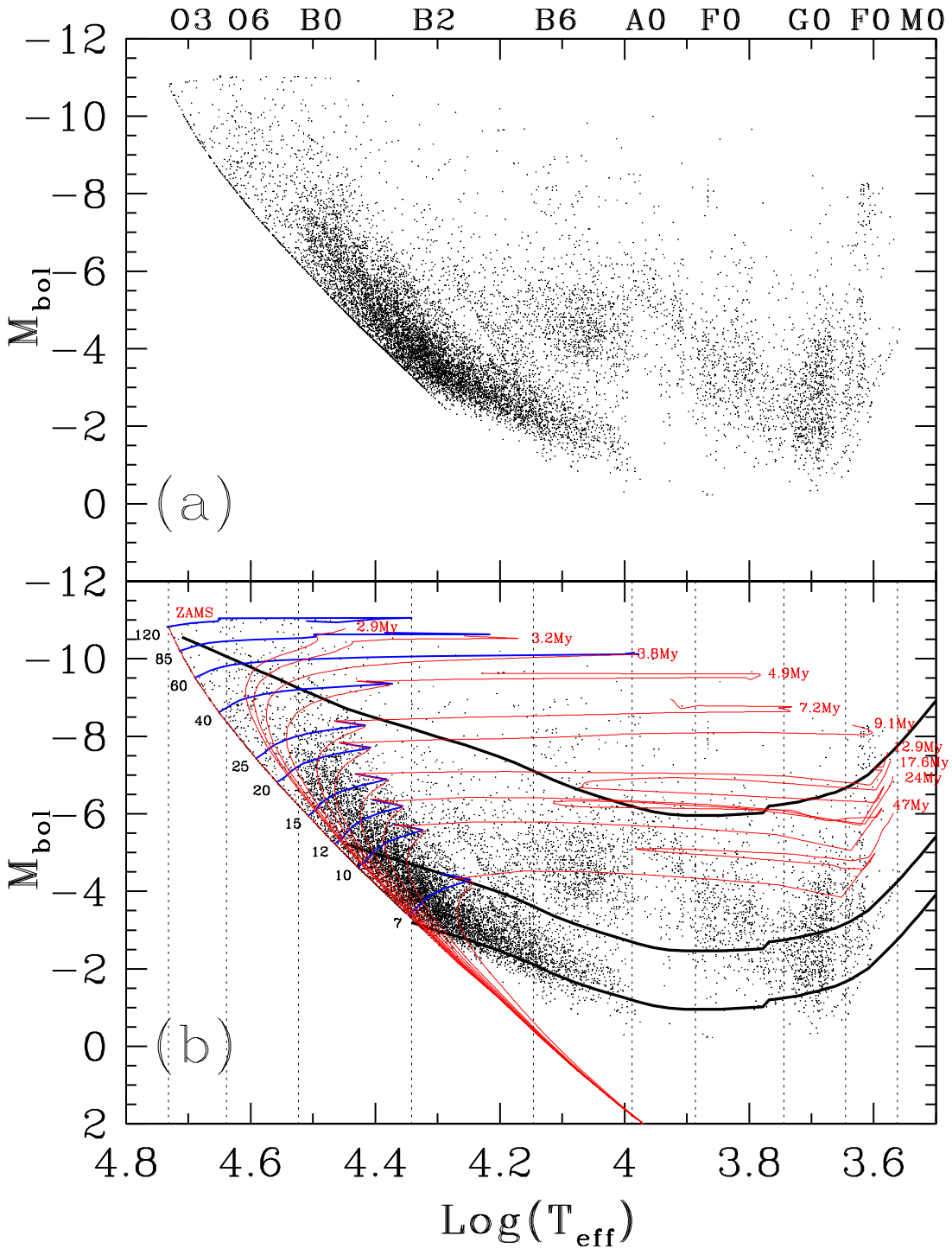

Figure 4.10: (a) The photometric HR diagram for the stars in the NE field. (b) same as (a) with main sequence evolutionary tracks, thick lines (labels in units of solar mass to the left of the ZAMS); isochrones, thin lines. The labels at the right end of the isochrones corresponds to the MS lifetimes. The very thick lines represents the v=17.5, 16.0, and 12.5. See main text for details.

diagram; (7) also a main-sequence turn-off (TO) between 7 and 15 My associated with a group of supergiants at the appropriate location.

A few spurious features can also be recognized: the ZAMS is populated by photometric outliers; the sharp blue border of the locus of the disk dwarfs; the "hole" between the MW disk and giant contamination, an artifact produced by the giants being assigned to the blue extremes of the blue loops while the disk stars are assigned to the unlikely region of the tracks between the end of the MS phase and the beginning of the red giant one; finally, there is a small group of stars at $M_{bol} = -8$ and $\log T_{eff} = 3.96$ which appears vertically aligned.

The thick line that envelopes the cloud of points from below in Figure 4.10(b) represents v = 17.5. It explains the lower boundary of the cloud of points showing the increasing bolometric correction at both temperature extremes. In Paper I we showed that variable extinction reduces the completeness of the sample by an extra 1.5 magnitudes. Thus, this effect is not important above v = 16.0 (next heavy line) corresponding to approximately 10 $M_{\odot}$. Strong non-linearities and saturation can be expected above v = 12.5 (upper heavy line). *The mass interval truly free of the above effects, therefore, is* $10M_{\odot} < M < 40M_{\odot}$. If the population is very young, with few or no evolved stars, the upper boundary extends to the full 120 $M_{\odot}$ covered by the models.

id (1)	xc (2)	yc (3)	V (4)	eV (5)	(B-V) (6)	e(B-V) (7)	(U-B) (8)	e(U-B) (9)	LogTeff (10)	Mbol (11)	Lc (12)	Age (13)	Mi (14)	E(B-V) (15)	Chi (16)
11000001	1352.0	7790.8	11.770	0.001	5.804	0.027	-6.965	0.027	4.589	-10.934	5	2.512	110.7	0.163	18.210
11000003	830.8	7740.3	12.112	0.001	0.418	0.002	0.097	0.002	4.156	-9.283	3	5.309	36.1	0.567	1.730
11000006	1812.6	5544.8	12.535	0.001	2.125	0.001	2.327	0.017	3.846	-10.428	1	3.758	60.7	1.476	1.620
11000004	1794.9	6707.8	12.680	0.003	0.071	0.003	-0.828	0.002	4.658	-10.942	5	1.585	118.5	0.320	3.200
11000005	1670.5	6819.9	12.883	0.002	-0.096	0.002	-0.899	0.002	4.712	-10.858	5	0.631	118.3	0.221	2.750
11000010	1210.2	6291.5	12.883	0.001	2.058	0.002	2.074	0.019	3.618	-8.212	1	8.913	21.4	0.629	2.000
11000014	1741.3	5279.7	13.063	0.000	2.061	0.000	2.347	0.024	3.596	-7.951	1	9.441	19.8	0.527	1.740
11000011	938.5	7311.9	13.214	0.001	0.605	0.001	0.110	0.001	4.223	-9.273	3	5.309	36.1	0.802	1.700
11000018	1557.4	7420.2	13.558	0.000	0.532	0.000	0.031	0.001	4.237	-8.835	3	6.310	29.4	0.746	2.110
11000007	1770.1	6703.5	13.676	0.004	-0.061	0.004	-0.876	0.001	4.711	-10.124	5	0.100	81.5	0.247	2.920
11000027	517.2	4964.1	13.825	0.000	0.652	0.002	0.267	0.002	4.172	-8.431	3	7.499	24.1	0.816	1.970
11201494	1148.6	8020.3	13.889	0.017	-0.104	0.020	-0.788	0.010	4.495	-8.247	5	5.957	26.5	0.196	5.040
11000009	1350.8	7701.2	13.942	0.001	-0.135	0.000	-0.845	0.000	4.549	-8.545	5	4.467	31.6	0.183	1.850
11000023	514.8	8152.7	13.960	0.007	0.767	0.008	-0.097	0.007	4.522	-11.023	5	2.512	117.7	1.068	2.920
11000035	1977.2	4564.4	13.990	0.015	0.494	0.015	0.055	0.001	4.212	-8.134	3	8.414	21.6	0.697	2.980
11003517	1095.4	7315.5	13.994	0.001	0.232	0.001	-0.710	0.001	4.730	-10.757	5	0.100	115.3	0.514	1.400
11200055	332.4	4305.1	14.082	0.001	-0.026	0.001	-0.791	0.001	4.636	-9.384	5	2.113	49.9	0.305	1.780
...	...	...	...	...	...	...	...	...	...	...	...	...	...	...	...

Table 4.1: Catalog of observed and physical parameters for the stars in the 30 Doradus super-association.

Table 4.2: Spectroscopic and photometric T_{eff} for stars in selected fields.

		Spectroscopic Information		Photometric Information	
Our Id	Reference Id	Spectral Type	$\log T_{eff}$	$\log T_{eff}$	χ
14000005	p987	B0.5-0.7 I	4.353	4.480	3.2
14000008	p548	B0.7-1.5 I	4.316	4.496	3.1
14000020	p1257	B0 Ia	4.423	4.524	2.6
14000016	p1253	BN0.5 Ia	4.364	4.546	2.6
14000040	p488	B0.5-0.7 Ia	4.353	4.547	2.7
14000033	p1500	B0 Ib	4.423	4.506	2.2
14000034	p871	O3 V:	4.732	4.628	2.8
14000045	p1018	O3 If*/WN6-A	4.705	4.608	2.5
14000056	p643	ON9: I	4.515	4.645	2.7
14002516	p493	BC1 Ia	4.318	4.512	3.2
14001015	p1150	O4 III(f)	4.683	4.687	2.5
14000072	p930	OC9.7 Ib	4.464	4.603	2.4
14000081	p666	O3If*/WN7-A	4.705	4.522	2.8
14000065	p1311	O3 III(f*)	4.707	4.661	2.2
14001743	p1163	O3 V((f*))	4.732	4.647	2.3
14000097	p1531	O5: V	4.664	4.619	2.0
14000123	p724	O6: V:	4.639	4.638	2.0
14001394	p805	O5-6 V	4.652	4.658	2.9
14000124	p713	O3-6	4.676	4.675	2.8
14000184	p974	O5-6 III	4.644	4.706	1.9
14000822	p661	O5: V	4.664	4.701	2.2
14000183	p761	O3-6 V	4.676	4.702	2.2
14000194	p169	O9-B0 III	4.518	4.684	2.1
14000235	p974	O5-6 III	4.644	4.691	1.8
14000335	p538	B0-1 III	4.479	4.583	1.8
14000739	p700	O7: V((f))	4.613	4.680	1.6

continued on next page

Table 4.2: *continued*

	Spectroscopic Information			Photometric Information	
Our Id	Reference Id	Spectral Type	$\log T_{eff}$	$\log T_{eff}$	χ
14000009	p499	A0 Ia	3.988	4.228	3.3
14000111	p1350	O6 III(f*)	4.630	4.581	1.8
14000106	p1563	O7.5 II-III(f)	4.585	4.606	1.9
14000119	p1607	O7: If	4.588	4.579	1.8
14000160	p1317	O4 V	4.687	4.604	2.4
14000202	p1614	O5-6 V((f))	4.652	4.642	1.5
14000240	p977	O6: V	4.639	4.659	1.8
14000338	p615	O4-6 III(f)	4.657	4.667	2.0
14000359	p1209	O9-B0 V	4.539	4.654	2.9
14000043	wb3	A Ib (B3-5 I)	3.937	3.940	2.7
14000225	wb6	B2 III (O7-B0 V)	4.308	4.470	6.5
14000149	wb7	M I	3.562	3.628	2.0
14000197	wb8	B5:p (O9-B0)	4.188	4.411	1.7
14000155	wb9	B2 V (O5-6 III)	4.342	4.597	2.0
14002499	wb10	A0 Ib	3.988	4.118	3.3
14000128	wb11	A5 Ib (B1-1.5 V)	3.930	3.938	2.3
16000013	st4-54	O8 I(f)	4.553	4.600	2.3
16000021	st4-61	B1 I	4.318	4.074	2.1
16000028	st4-18	O5 I f	4.650	4.586	2.1
16000042	st4-26	O6.5 III((f))	4.615	4.593	2.0
16000051	st4-16	B1 I	4.318	4.487	2.2
16000070	st4-13	B1 I	4.318	4.550	1.7
16000071	st4-56	G3	3.766-3.705	3.807	1.9
16000074	st4-33	O7 V	4.613	4.509	1.8
16000099	st4-35	O8 V	4.585	4.510	1.7
16000122	st4-20	B1 III	4.414	4.456	1.7
16000142	st4-46	A3 V	3.940	4.001	1.5
16000144	st4-45	B0.5 V	4.506	4.435	1.4
16000149	st4-27	B2 III	4.308	4.462	1.6
16000151	st4-30	B1 III	4.414	4.454	1.8

continued on next page

Table 4.2: *continued*

	Spectroscopic Information			Photometric Information	
Our Id	Reference Id	Spectral Type	$\log T_{eff}$	$\log T_{eff}$	χ
16000159	st4-55	B0 V	4.523	4.417	1.4
16000162	st4-63	B0.5 V	4.506	4.455	1.4
16000164	st4-50	B0.5 V	4.506	4.495	1.3
16000168	st4-39	B0 V	4.523	4.504	1.6
16000198	st4-1	B2 III	4.308	4.386	1.7
16000206	st4-4	B1 V	4.444	4.472	1.1
16000216	st4-28	B0.5 V	4.506	4.499	1.5
16000217	st4-11	B1 III	4.414	4.354	1.5
16000229	st4-43	B2 V	4.342	4.379	1.4
16000242	st4-21	B1 V	4.444	4.414	1.5
16000248	st4-29	B1 V	4.444	4.456	1.4
16000249	st4-44	B2 V	4.342	4.304	3.9
16000257	st4-23	B1 V	4.444	4.396	1.3
16000283	st4-24	B2 III	4.308	4.439	1.2
16000306	st4-67	B2 I	4.267	4.435	1.3
16000311	st4-2	B1 V	4.444	4.432	1.4
16000317	st4-3	B2 V	4.342	4.480	1.3
16000325	st4-15	B2 V	4.342	4.412	1.3
16000327	st4-48	G8 III	3.690	3.621	1.3
16000332	st4-69	G5:	3.760-3.686	4.415	1.4
16000345	st4-51	B2 III	4.308	4.413	1.3
16000352	st4-66	B2 III	4.308	4.397	1.4
16000353	st4-19	B1 V	4.444	4.402	9.8
16000408	st4-5	B2 V	4.342	4.374	1.3
16000443	st4-36	B2 III	4.308	4.432	1.6
16000458	st4-34	B0.5 V	4.506	4.436	1.3
16000492	st4-38	B1 V	4.444	4.435	1.2
16000518	st4-10	B2:	4.342-4.267	4.357	1.2
16000521	st4-7	B2 V	4.342	4.286	1.3
16000546	st4-60	F8 V	3.792	4.132	1.2

continued on next page

Table 4.2: *continued*

	Spectroscopic Information			Photometric Information	
Our Id	Reference Id	Spectral Type	$\log T_{eff}$	$\log T_{eff}$	χ
16000580	st4-37	B2 V	4.342	4.404	1.2
16000750	st4-31	B2 V	4.342	4.374	1.2
16000757	st4-14	B2 V	4.342	4.376	3.1
16000793	st4-8	B1:	4.444-4.318	4.388	1.1
16000796	st4-9	B1 V	4.444	4.249	1.3
16000959	st4-58	G8-K2	3.747-3.690	4.265	1.3
16001084	st4-53	B2:	4.342-4.267	4.370	1.3
16001127	st4-49	B2 V	4.342	4.277	1.1
16001150	st4-41	B0 V	4.523	3.809	1.6
16001198	st4-59	B2 V	4.342	4.318	1.1
16001211	st4-40	O8 V	4.585	4.329	1.2
16001268	st4-47	B1 I	4.318	4.253	1.3

Spectral types from several sources in the literature, the corresponding effective temperatures, the photometric effective temperature, and the goodnes of the psf profile fit. The reference identification are from: p, Parker 1993; wb, Walborn and Blade (1997); st, Schild and Testor (1992). The spectral types are taken from the compilation in Paper II, for the neighborhood of the Tarantula; from Walborn and Blades for Hodge 301; and from Schild and Testor for LH104.

Chapter 5

Results

We start by comparing the HR diagrams of some selected regions that have been previously studied. After acquiring familiarity with the potential and limitations of our method of deriving physical parameters we present the SFH and the IMF of two regions which have been previously studied with classical UBV photometry and spectroscopy: the core of the Tarantula nebula, representing a region of large average stellar density, and the OB association LH104, representing a low density environment. Finally, we close this chapter with the main problem studied in this thesis, that of the SFH and IMF of the field population.

5.1 Comparison with other work

To check the correctness of the rather complex procedure used to calibrate the photometry it is mandatory to compare our results with data taken independently for a different set of stars from those involved in the calibration. To that end we have searched the literature for reliable photometry and/or spectroscopy in our WFI field. Given the large region involved, and the highly heterogeneous nature of the published data, we concentrated in only a few fields that satisfied the following criteria: (a) reliable (i.e., modern) data; (b) wide range in colors and spectral types; (c) spread over the mosaic.

This led us to select 3 fields for comparison: (1) the small cluster Hodge 301 which is very close to the Tarantula Nebula and for which there is published spectroscopy and HST photometry; (2) NGC 2100 which is a rich, intermediate age, cluster for which there is a a recently published HR diagram based on UV observations with HST; and (3) the populous OB association LH104 for which there is published photometry

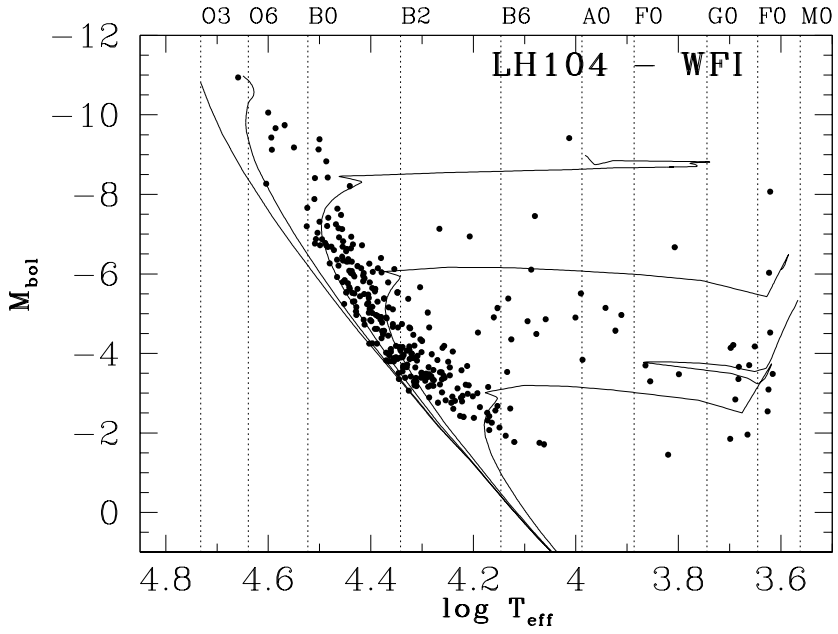

Figure 5.1: The photometrically derived HR diagram for LH104. The ZAMS, and the 2 My, 7 My, 20 My, and 100 My isochrones are also shown.

and spectroscopy for about 70 stars.

5.1.1 LH104

This OB association belongs, together with LH101, to the nebula N158 (Henize 1956), or DEM269 (Davies et al. 1976). LH104 is surrounded by a superbubble expanding at 40-45 km/s (White 1981). The dimensions of this expanding shell, 100 pc × 90 pc, results in a timescale of expansion ∼ 1 My. LH104 has been spectroscopically studied by Schild and Testor (1992) and Testor and Niemela (1998). Figure 5.1 shows the HR diagram we derive for the stars in the same region of LH104 studied by Schild and Testor. While our photometry contains a lot more stars than they publish, our HR diagram is morphologically similar to that shown in their Figure 6. In particular, the 2 My isochrone *hugs* the blue edge of the distribution of observed points.

Figure 4.7 (squares) shows the correlation between our photometrically determined spectral types with those determined by the above authors from low dispersion spectroscopy. We see that there is a remarkably good agreement between the two data sets. The three deviant points correspond to stars 4-58, 4-60, and 4-69 from Table 2

of Testor and Niemela (1998), for which they they do not give either effective temperature, or bolometric magnitude due to their spectroscopy being problematic. We can also see that of the seven supergiants, three are in the parallel sequence associated to the Be effect. These are classified as B1 I, or B2 I, and we have overestimated their temperatures. Note that these then migrate to the region around 2 My and 5 My. Note also the set of stars at $\log T_{eff} \sim 4.30$ below the line. All these stars are classified as B2 III and their presence in that part of the diagram is a hint that they could be Be stars. This is in analogy with the finding by Grebel et al. (1996) that rapid rotation and the properties of Be stars is what determined the position of the blue giants in the HR diagram of the SMC cluster NGC330.

It is interesting to note that in LH104 all other B-type stars of luminosity class V do not show anomalous effective temperatures. If we were to classify all B stars with anomalous effective temperatures as Be stars, then the fraction of Be stars in LH104 would be 13% of the total and 30% of the B2 stars. This complements the findings by Keller et al. (1999, 2000) of a considerably lower fraction of Be stars in the field than in the clusters of the LMC. LH104 being a low density OB association shows that this could be the property of being born in a low density environment.

In summary, our results for LH104 are affected by the Be effect discussed in Section 4.3. This effect causes B giants and supergiants to migrate to higher mass bins leading to systematically flatter IMFs and younger ages. As will be discussed below, the effect can be quantified (Grebel et al 1998). For all other stars our calibration, based mostly on O-B stars, does a reasonable job in the spectral range B-G.

5.1.2 Hodge 301

The small cluster Hodge 301 (Hodge 1988), also known as M87 (Melnick 1987), is located just a few arcmin to the north-west of NGC2070. In its immediate vicinity we can find the B0.5 I supergiant R132 (Feast, Thackeray, and Wesselink 1960), three A-type supergiants (Melnick 1985), three M-type supergiants (Hyland et al. 1992), and several B-type giants and dwarfs (Walborn and Blades 1997). Figure 5.3 shows the field of Hodge 301 with the identifications of some of the most conspicuous stars labeled. The spectral types are those reported in Grebel and Chu (2000) based on the work of Melnick (1985) and Walborn and Blades (1997). Figure 4.7 (triangles) shows the correlation between photometric and spectroscopic types.

It is not straightforward to compare with Grebel and Chu because they do not

present HR diagrams, but plot the isochrones on the color magnitude diagram instead. Figure 5.2 shows their color magnitude diagrams together with the 16 My, 20 My, and 25 My isochrones from the Geneva and Padua groups. They assume a constant reddening and displace the isochrones accordingly.

Figure 5.3 shows our HR diagram for the cluster together with three isochrones corresponding to the span of ages visible in the cluster (2–20 My). The youngest population (< 3 My) may correspond to stars from NGC2070, but also to Be stars that were assigned larger masses and younger ages as discussed above.

There is reasonable agreement between our photometry and the spectral types marked in the figure with deviations along the predictable direction due to the presence of Be stars which make us suspicious of features to the blue of the TO.

5.1.3 NGC2100

After the Tarantula cluster (NGC2070), NGC2100 is the richest cluster in the 30 Doradus super-association, and must have been the core of a luminous giant HII region 12 to 20 My ago. Figure 5.4 shows a comparison between our data and the HST investigation of the cluster by Keller et al. (2000) who use F160BW - F555W colors and F555W magnitudes to determine temperatures and luminosities using synthetic colors and bolometric corrections. They assume a single reddening for all the stars in the cluster. Notice that we are not comparing the same stars as the HST field is only 38″ wide. The filled circles in the WFI diagram comes from stars within that field of view; the open circles correspond to stars in a field twice as large. While the morphologies of the HR diagram are similar in the two studies (filled dots), there are some interesting differences which are mostly due to the different areas of the cluster sampled by the two studies. The red supergiants in the WFI field (all outside the HST field and far from the cluster core) have bolometric magnitudes 0.5 to 1.0 mag brighter than the HST stars, but similar effective temperatures.

Below the 15.8 My TO the WFI main sequence is completely within the locus of the allowed range (by construction), while the HST values spread equally around both sides of the ZAMS. Both WFI and HST show the presence of bluer and brighter stars, but these are more numerous in the WFI data. Their origin could be partly due to blending in WFI, or to saturation of HST photometry. We believe that the Be effect may also play a role in explaining these stars. A check against the finding charts of Be stars by Keller et al. (1999) shows that many, but not all, are Be stars.

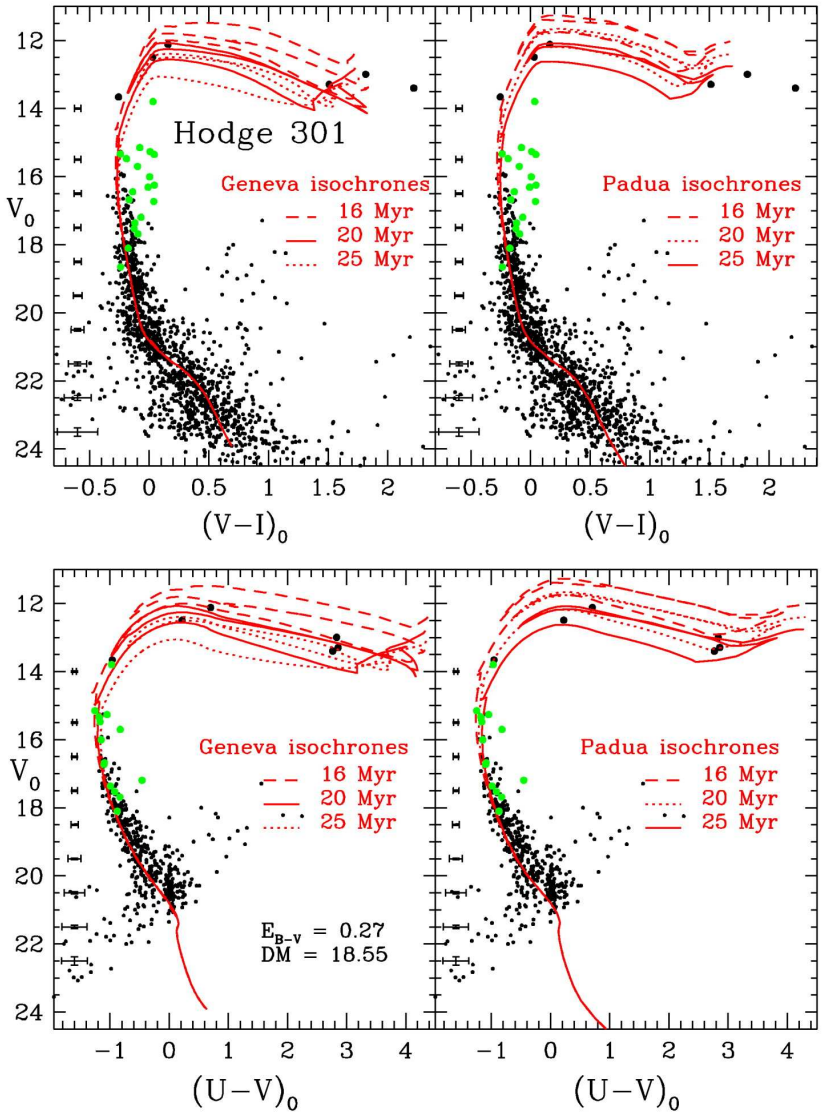

Figure 5.2: Color-magnitude diagrams obtained with HST data for Hodge 301 (from Grebel and Chu, 2000).

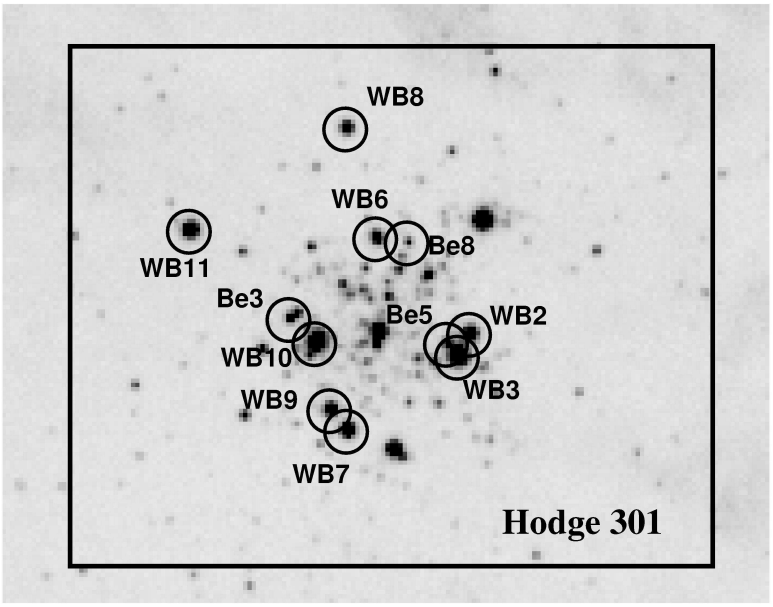

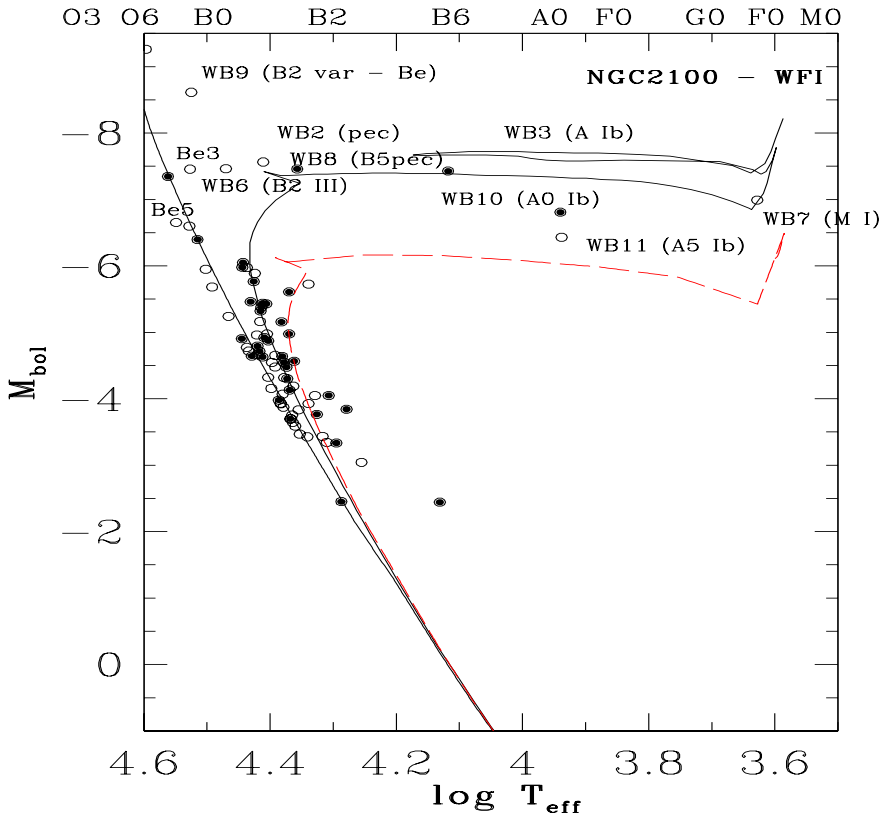

Figure 5.3: HR diagram of Hodge 301 and identifications. Solid dots correspond to stars in the HST field. Open circles are stars in an area twice as large. The solid curve plots the log(age)=7.1 (12 My) isochrone from Bertelli et al. (1994), which fits the WFI HR diagram of this cluster better. The dashed line shows the 20 My isochrone (Geneva) preferred by Grebel and Chu (2000).

We conclude that although there are differences between our work and the HST data of Keller et al. (2000), these can be understood as the result of the presence of Be stars in this cluster. According to Keller et al. (1999) they constitute approximately 40% of the early B stars. Since our data samples a different region of the cluster, both data sets are largely complementary and combined will yield a much more comprehensive study of the cluster, in particular regarding the red supergiant population and the fraction of Be stars.

5.2 Star-formation history and IMF

The determination of the IMF of a group of stars is intrinsically entangled with the determination of the ages of those stars, that is, the star-formation history of the group. We will use $b(t)$, *the birth rate*, to refer to the number of stars of any mass born per unit time, per unit area on the sky. We could explicitly write environmental dependences on $b(t)$ such as local gas density, temperature, chemical composition, etc., but this would clutter the notation excessively.

The number of stars born at time t in a mass interval $(m, m+dm)$, $f(m,t)dm$, is called the stellar *mass spectrum* at birth. Consider a region which started to produce stars at a time $t = 0$, but that we observe at a later time T. The number of stars per unit area, dN, observed in a mass interval $(m, m+dm)$, will be given by

$$dN = \int_{t=max(0,T-\tau(m))}^{T} b(t)f(m,t)dmdt, \tag{5.1}$$

where we have introduced the *lifetime* function, $\tau(m)$. $\tau(m)$ is the lifetime of a star of mass m given by the evolutionary models. It has a minimum value, τ_{min}, corresponding to the lifetime of the most massive stars.

We can see from Equation 5.1 that without knowing $b(t)$ it is impossible to determine $f(m,t)$ from observations at time T. Nevertheless it is customary to make the assumption that there is no time dependence in $f(m,t)$ in which case we can write

$$dN = \left[\int_{t=max(0,T-\tau(m))}^{T} b(t)dt\right] f(m)dm. \tag{5.2}$$

The term between brackets in Equation 5.2 depends on the mass m only through the

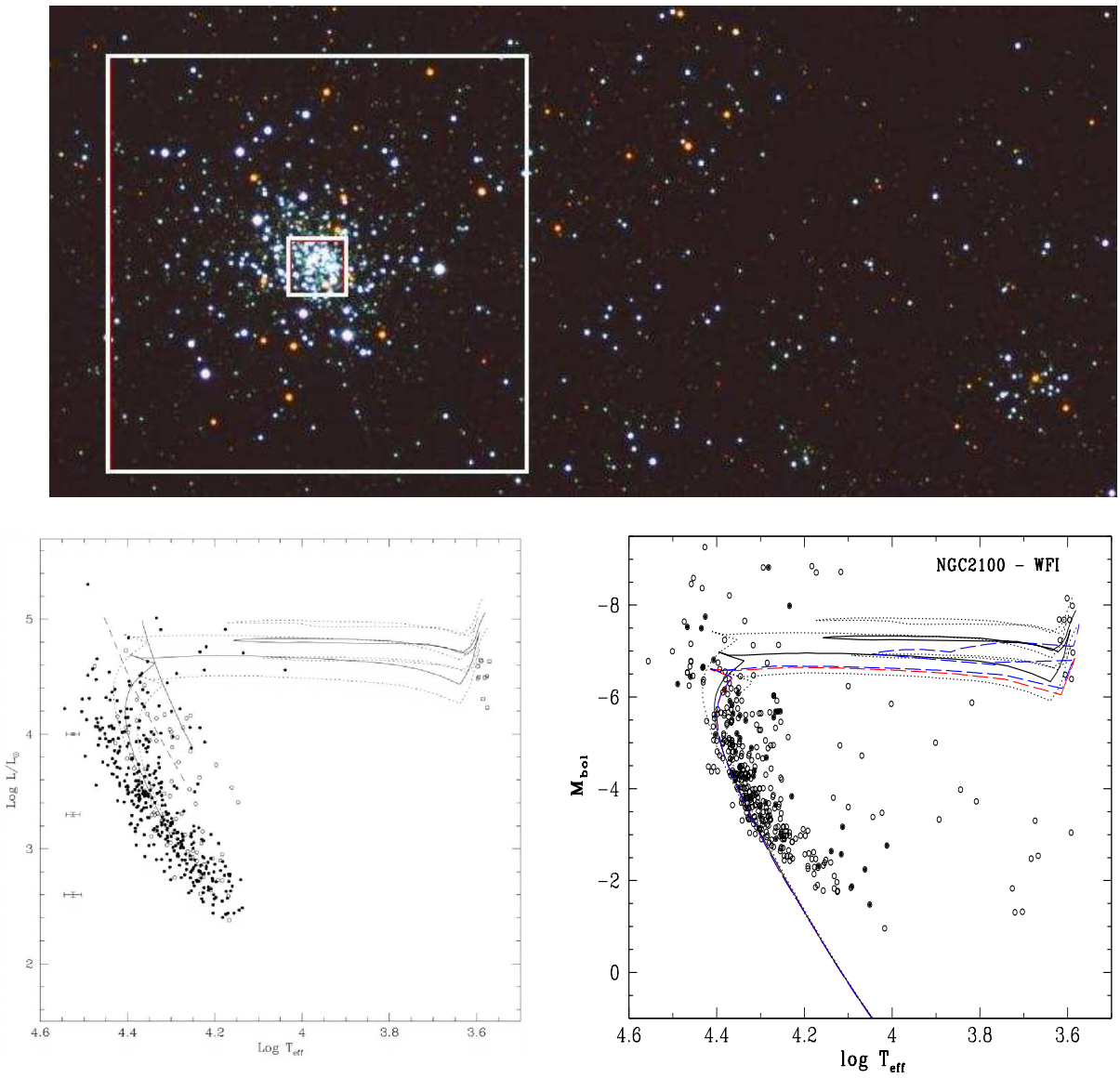

Figure 5.4: Comparison between the HR diagram of NGC2100 determined in this thesis, lower right, with the HST work of Keller et al. (2000), lower left. The upper panel compares the fields covered by the HST (small square) and this thesis (large square). The same isochrones from Bertelli et al. (1994) are drawn in both diagrams for log(age) = 7.2 (solid curve), 7.1, and 7.3 (dotted curves). The isochrones from Schaerer et al. (1993) for both mass loss prescriptions are also plotted (dashes). The filled dots in the WFI plot represent stars in HST field (35"); the open dot are the stars in the larger WFI area.

lifetime function. Therefore, if we know the star-formation history of the region we can find the mass spectrum at birth from the observed mass spectrum.

If we do not know the star-formation history, all we can do is to assume one and proceed. Two assumptions have been normally used: a coeval population, and a constant star-formation rate. The former is used when analyzing star clusters while the latter is used when analyzing a mixed population of stars (e.g., the solar neighborhood).

For a single burst of duration Δt a time T ago we can write

$$dN = b(0)\Delta t f(m)dm \quad \text{for} \quad m < m_{max}, \tag{5.3}$$

where m_{max} is the largest mass a star can have and survive for a time T. Equation 5.3 gives, up to a scale factor, the mass spectrum at birth. This equation, used to analyze star clusters, is valid if Δt is much smaller than the age of the most massive stars present in the cluster.

If star formation occurs at a constant rate we can write

$$dN = b_0 \min(T, \tau(m)) f(m)dm, \tag{5.4}$$

which for the mass range defined by $\tau(m) < T$ becomes

$$dN = b_0 \tau(m) f(m)dm, \tag{5.5}$$

and we can obtain the mass spectrum at birth from the observed mass spectrum simply by dividing it by the lifetime as a function of mass. In this latter case it is customary to count stars in logarithmic (base 10) mass intervals,

$$dN = b_0 \tau(m) m f(m)(\ln 10) d\log m = \tau(m)\xi(\log m) d\log m, \tag{5.6}$$

where now the function $\xi(\log m)$ receives the name *initial mass function* (see the encyclopedic review by Scalo (1986)).

Finally, it is customary to fit a power law function to the high mass end of the IMF. We can write,

$$f(m)dm \sim m^{\gamma} dm \sim m^{\Gamma=(\gamma+1)} d\log m. \tag{5.7}$$

For a Salpeter (1955) power law $\Gamma = -1.35$. Although in Paper III we used the opposite sign convention to that used by Scalo, reporting positive values for Γ, we will adhere here to the Scalo convention.

Sometimes people report the results of star counts in *initial mass* bins without any correction due to star-formation history or lifetimes. Such a function is called the *present day mass function,* and is usually denoted by PDMF. Notice that it does not count stars in bins of *present day* mass. Below we will present the PDMFs in the same diagram as the IMF, which can be understood as assuming a single 1 My duration burst.

In what follows we will fit a straight line to the portion of the mass spectrum more massive than the completeness limit. This lower bound will be determined by comparing with the counts in NGC2070 for which we did in Paper III a thorough completeness analysis. For the fit we will assume Poissonian errors in the counts and will assume that the error in the masses is half the width of the logarithmic mass interval. We will apply the routines for a straight line fit with errors in both axes from Press et al (1992). The output of that routine are the intersect and the slope with their respective errors. The routine also gives the χ^2 of the fit together with the value of the incomplete gamma function $Q(\frac{N-2}{2}, \frac{\chi^2}{2})$ for the probability of obtaining a value of χ^2 as poor as the one obtained if the model is good (N is the number of data points). According to Press et al. (1992), a Q value larger than ~ 0.1 is necessary to make the goodness of fit believable. We will present in the tables that follow the exact output of the routine while in the main text we will present the errors one would obtain were we to follow the procedure suggested in Press et al. (1992) to multiply the errors by $\sqrt{\chi^2/(N-2)}$. In doing this we loose the estimate of the goodness of the fit, Q, but we obtain a better estimate of the errors.

5.2.1 Star-formation history and IMF at the core of the Tarantula

Figure 5.5 shows the regions analyzed in Paper III. The outer region defined in that paper, in which the effects of crowding are minimized, is shown between the 15″ radius inner circle and the slightly off-center box. The stars in this region will serve as the basis for the comparison with our previous work. Several star-formation phases have been described by Walborn and Blades (1997) in the region covered by the

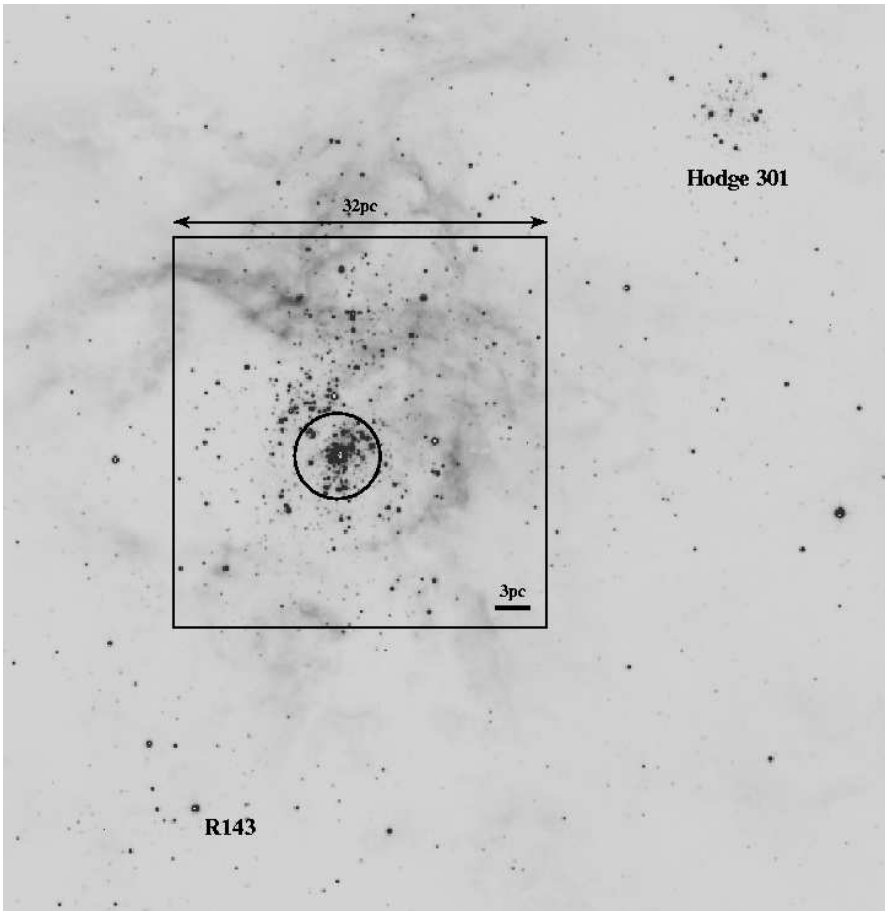

Figure 5.5: Image of the area around the core-ionizing cluster NGC2070. The image covers an area similar to that of Figure 2 of Walborn and Blades (1997). The inner circle delineates the central areas of the cluster to be excluded from our comparison with the results from Paper III. The box delineates the boundary of the region studied in that paper.

whole of Figure 5.5: (1) an Orion Nebula phase characterized by IR sources with ages $< 10^6$y found embedded in the bright nebulosity (one group lies near the upper left corner of the box and the other in the arc-like nebulosity to the right of the core of the cluster); (2) a Carina Nebula phase with very early O and WN stars ages$\sim 3 \times 10^6$y found across the cluster; (3) a Scorpius OB1 phase with late O and early B supergiants ages$\sim 5 \times 10^6$ y, also found across the cluster and near the star marked R143; and (4) a h and χ Persei phase,with mid-B, A, and M supergiants ages $\sim 10^7$ y near Hodge 301 to the north-west of the Tarantula.

In Figure 5.6 we have plotted the histogram of ages determined in the present work. The larger histogram includes all stars with $M_{bol} < -4.6$ of any mass still in the main sequence. All $12M_\odot$ stars younger than 17.8 My should be present in this

sample. The lighter histogram (yellow) contains only stars less massive than $15M_{\odot}$. We can distinguish all but the first of the Walborn and Blades phases: (1) stars in and around peak B belong to the Carina and Scorpius OB1 phases (we have removed from peak B the seven B-type supergiants which migrated there due to the Be effect); (2) stars in and around the peaks C and D belong to the Scorpius OB1 and h and χ Persei phases (we have not added the supergiants to these peaks as they should go into peak D); stars in peak C migrated there from peak D due to the Be effect; and (3) stars in peaks E and F correspond to the h and χ Persei and older phases of star formation. We have eliminated from the histogram a single bin peak at zero age which contains approximately 30% of the stars.

We can see in our data *evidence for two separate star formation events one between 0 and 4 My and another between 7 and 12 My.* Our data also show the presence of the oldest three phases of Walborn and Blades in a much smaller region of the cluster. The result from Paper III showing three peaks in the star-formation history needs to be modified: the peak with ages $< 10^6$ y is believed now to be an artifact of the conversion to ages that widened the single bin peak at zero age. The peaks at 2.5 My and 5 My correspond to peaks B and C in Figure 5.6. We have seen now that peak B is a real age peak containing most of the early O dwarfs and supergiants born in the last 5 My. Peak C corresponding to the 5 My burst of Paper III, can now be seen to be an artifact caused by the Be stars, *albeit a very important one: it hints to the presence of Be stars in this cluster, stars that really belongs to peak D,* This is an important observation that needs to be confirmed spectroscopically. Even at these small scales the star-formation history appears to be characterized by two major bursts.

The identification of at least some of the peaks in the age histogram with previously described phases of star formation in 30 Doradus is satisfying but does not prove that the parameter we have been calling "age" is an actual measure of time. Several reasons lead us to believe that the spatial distribution of stars in the various age groups should differ. First, the differences could be implanted at birth: the star formation in the region might be characterized by a constant star-formation rate in the field punctuated by recent formation of a few compact clusters and associations; or the size of the cloud complexes out of which the stars form might be changing with time. Star groups separated by age will reflect these different spatial arrangements. Second, even if stars of different ages are born with the same spatial distribution, this

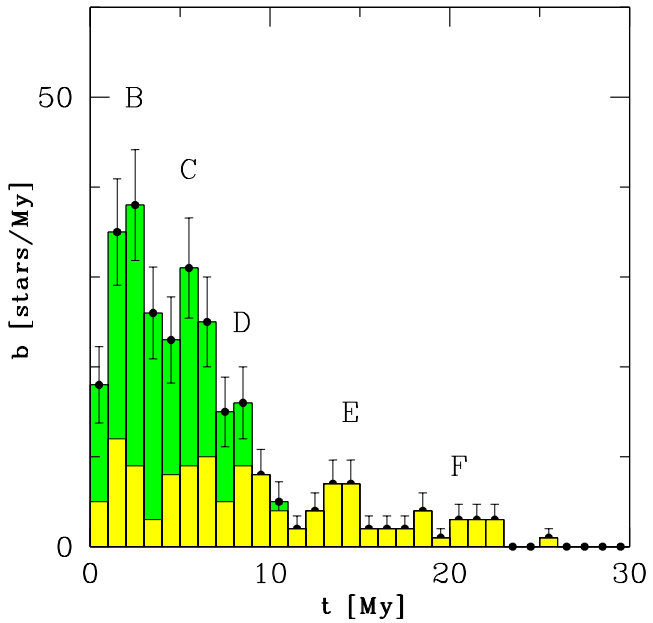

Figure 5.6: The star-formation history of the region analyzed in Paper III. The darker histogram shows the sample with $M > 12\ M_{\odot}$, and ages ≥ 30 My, while the lighter one has the additional restriction $M < 15\ M_{\odot}$. Only stars on the main sequence were used to construct the histograms.

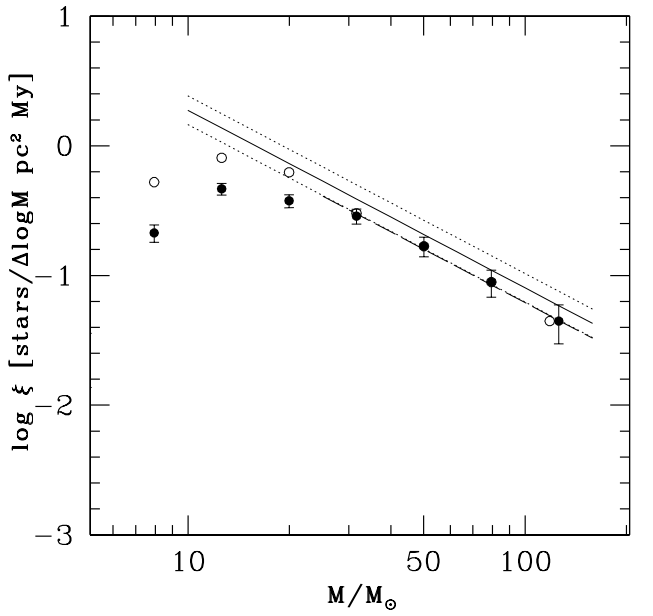

Figure 5.7: The IMF of the central cluster of 30 Doradus. The open squares show the PDMF. The filled circles show the IMF determined using all stars younger than 5 My. The solid and dotted lines represent the best fit solution of the PDMF from Paper III, with $\Gamma = -1.37 \pm 0.08$, together with the 1σ uncertainties.

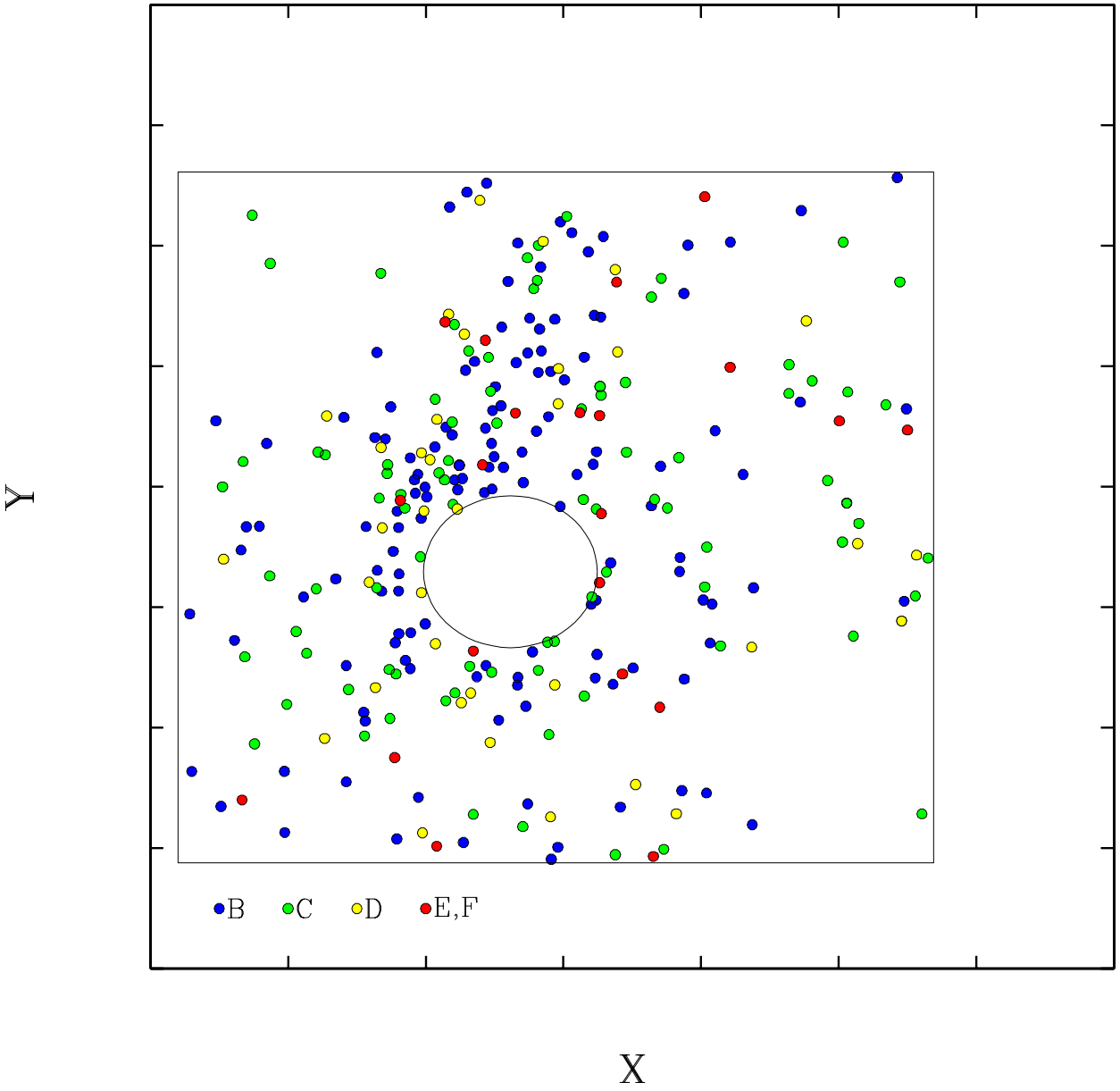

Figure 5.8: Positions of the stars in the five age groups identified in Figure 5.6.

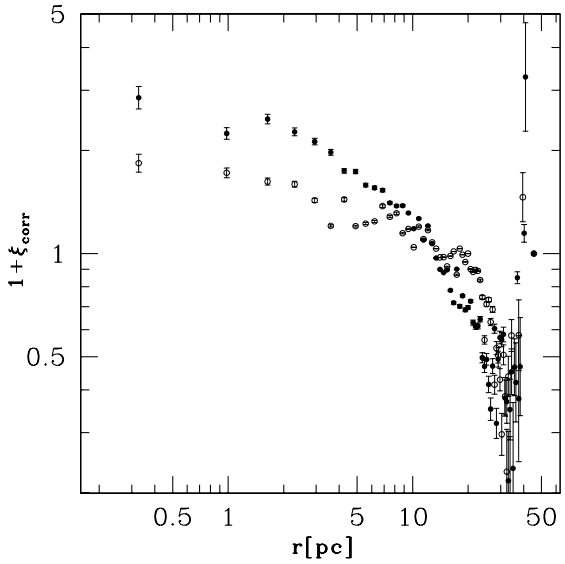

Figure 5.9: The two-point projected correlation function for the stars in the NGC2070 region. The filled circles show the two-point correlation function for the stars in peak B and the open circles show the correlation function for the stars in peaks C and D.

can be modified by processes acting for a longer time on the older population. For example, after they are born we expect the stars to diffuse away from their formation sites with speeds ~ 3 km/s[1]. Thus, the older a population is, the more its spatial distribution will differ from its distribution at birth.

Figure 5.8 shows the spatial distribution of the stars in the different age peaks. From this figure we conclude, in agreement with Paper III, that the star formation events associated with each of the peaks appear to have occurred across the face of the cluster. However, this figure also shows that the stars in the younger peak appear to be slightly more clustered than the older stars, an effect that we will quantify below.

Figure 5.9 shows the two point correlation functions for the stars in peak B, and for peaks C and D. This function was calculated with the Monte Carlo method of Davis et al. (1988) which minimizes boundary effects (do not confuse the symbol ξ_{corr}, which represent the two-point correlation function, with the initial mass function represented

[1]It is believed that many OB associations and young open clusters do not have enough mass to be bound, probably as a result of the winds from recently born massive stars blowing a considerable fraction of the mass of the clouds whence they form (Blaauw 1991). The small-scale over-densities will tend to be erased first. Zuckerman (1973) found in Orion that 3 km/s is the typical stellar velocity with respect to the parental molecular clouds (a more recent proper motion study finds 2 km/s (Tian et al. 1996)). If stars born in 30 Doradus acquire similar velocities after they are born, then a star would travel ~ 6 pc in 3 My corresponding to an average projected distance of ~ 4.2 pc, or $16''$, a detectable quantity.

by ξ). Several features are apparent in that figure. First, there are two artifacts, one associated with the inner circular boundary which causes a depression around 7 pc, and the other associated to the outside boundary of the region analyzed which causes a change in slope at around 20 pc. The plot also shows that for spatial scales < 10 pc stars of all ages are more clustered than if they were randomly distributed ($\xi_{corr} = 0$) with the younger ones with a higher correlation. At large scales the older group is more correlated than the younger one. Thus, the parameter that we call "age" is indeed separating the stars in spatially segregated groups. The full significance of this, as far as can be told with these data, will be discussed in Section 5.3.

In Paper III we obtained an IMF for the core of the Tarantula nebula excluding the very central regions closer than 15″ from the cluster center. We assumed that the bulk of the stars were formed by a few bursts whose ages were smaller than the lifetime of the most massive stars. Figure 5.6 shows that if we assign the stars in the zero age bin to the first peak, then more than 50% of all stars have ages smaller than the lifetimes of the moss massive main sequence stars. We used this to support the use of the single burst assumption in Paper III. Table 5.1 and Figure 5.7 show the PDMF and IMF determined in this thesis. In the mass range $M > 15\ M_{\odot}$, the PDMF is best fit with a line of slope $\Gamma = -1.43 \pm 0.04$[2]. Also plotted is the best fit line from Paper III. We can see that both determinations agree to within 1σ as shown by the dotted lines. Not only the slope, but also the absolute values of the PDMFs agree to within 10%. Considering that the two results come from studies with different telescopes, filters, and detectors, and different spatial resolutions, this agreement is indeed excellent.

Although the star-formation history from Figure 5.6 appears quite complex, this is not so for stars more massive than $30 M_{\odot}$ for which it reduces to a single star formation burst younger than 5 My as these stars do not live much longer than that. This is fortunate because the peak associated with the Be stars is at 7 My. Also, due to the youth of the cluster, we can use stars with all masses for the fit, from the lowest cut-off up to the most massive without including stars with non-linear photometry (see Section 4.3). The IMF, determined with the stars younger than 5 My, is tabulated in Table 5.1 and shown as the filled circles with error bars in Figure 5.7. The best fit line for $M > 25\ M_{\odot}$ has slope $\Gamma = -1.37 \pm 0.06$, consistent with a Salpeter value.

[2] Following the suggestion in Press et al. (1992), for all the values presented in the main text we will multiply the errors by the appropriate factor to obtain $\chi^2 = 1$.

Table 5.1: Mass functions in NGC2070.

		PDMF[a]			IMF[b]	
M	Age	N	$\log\xi$	$\Delta\log\xi$	N	$\log\xi$	$\Delta\log\xi$
5.01	95.6	17	-1.08	0.19	5	-1.61	0.19
7.94	37.0	106	-0.28	0.07	43	-0.67	0.07
12.6	16.8	163	-0.09	0.04	94	-0.33	0.13
20.0	9.1	126	-0.21	0.05	76	-0.42	0.05
31.6	5.9	61	-0.52	0.06	58	-0.54	0.06
50.1	4.2	34	-0.77	0.07	34	-0.77	0.08
79.4	3.3	18	-1.05	0.10	18	-1.05	0.11
118.03	2.9	9	-1.35	0.14	9	-1.35	0.16

[a] PDMF: $1.65 \pm 0.52 - (1.43 \pm 0.30)\log$ M
($15M_\odot \leq$ M ≤ 120 $M_\odot$, $\chi^2 = 0.05$, N = 5, $Q = 0.996$)
[b] IMF: $1.53 \pm 0.84 - (1.37 \pm 0.44)\log$ M
($25M_\odot \leq$ M ≤ 120 $M_\odot$, $\chi^2 = 0.08$, N = 4, $Q = 0.96$)

The slightly steeper slope of the PDMF is probably due to the contamination of the $M < 30$ $M_\odot$ bins by older stars. We thus confirm the Salpeter character for the IMF of the NGC2070 cluster.

A final pending point can be addressed with the help of Figure 5.7. In Section 2.2 we mentioned that the completeness limit of the present study was going to be determined when comparing the IMFs determined in this thesis with that from Paper III where we did a full set of Monte Carlo simulations adding artificial stars of varying magnitude, color. One of the results of that work was that the completeness of the catalog was very much influenced by differential reddening. The area of the cluster under study here suffers from one of the largest amount of differential reddening of the region. Thus, the completeness limit in this zone will apply to all other areas. Comparing the IMF in Figure 5.7 with that from Paper III implies that the current work is complete down to $\sim 10 - 20$ $M_\odot$, corresponding to a main sequence age of 10 to 20 My: denser areas will be complete only to $20M_\odot$, and sparser areas will be complete down to $10M_\odot$.

5.2.2 Star-formation history and IMF of LH104

The OB association LH104 provides an excellent laboratory for the study of clustered star-formation in a low density environment. The star-formation history and IMF of LH104 has been previously studied by Testor and Niemela (1998) using a small number of stars with spectroscopy (although the number, 57 stars, was large for that kind of spectroscopic studies). They found a star-formation history characterized by a young population with ages spread between 2 My and 6 My, and an older group

Table 5.2: Mass functions for stars in LH104.

		PDMF[a]			IMF[b]		
M	Age	N	$\log \xi$	$\Delta \log \xi$	N	$\log \xi$	$\Delta \log \xi$
5.01	95.6	39	-0.99	0.07	39	-2.97	0.07
7.94	37.0	96	-0.60	0.04	96	-2.17	0.04
12.59	16.8	65	-0.77	0.05	65	-1.99	0.05
19.95	9.1	21	-1.26	0.09	21	-2.22	0.09
31.62	5.9	5	-1.88	0.19	5	-2.65	0.19
50.12	4.2	6	-1.80	0.18	6	-2.43	0.18
79.43	3.3	1	-2.58	0.43	1	-3.10	0.43
118.30	2.9	1	-2.58	0.43	1	-3.04	0.43

[a] PDMF: $2.14 \pm 0.49 - (2.64 \pm 0.41) \log \mathrm{M}$
$(10\mathrm{M}_\odot \leq \mathrm{M} \leq 40\ \mathrm{M}_\odot,\ \chi^2 = 0.22,\ \mathrm{N} = 3,\ Q = 0.64)$
[b] IMF: $-0.43 \pm 0.47 - (1.41 \pm 0.41) \log \mathrm{M}$
$(10\mathrm{M}_\odot \leq \mathrm{M} \leq 40\ \mathrm{M}_\odot,\ \chi^2 = 0.57,\ \mathrm{N} = 3,\ Q = 0.45)$

of less massive stars. They nevertheless assumed a single burst and presented the PDMF as the IMF. For $10\ \mathrm{M}_\odot < \mathrm{M} < 60\ \mathrm{M}_\odot$, they derived a PDMF with a slope $\Gamma = -1.05 \pm 0.12$.

Figure 5.10 shows the histogram of ages for the stars in LH104. This diagram should be examined in conjunction with the HR diagram for this association in Figure 5.1. We can see evidence for both the young burst and the older group of stars. The older burst is characterized by the presence of a few red supergiant stars, with ages set at 10 My, together with many B1 and B2 stars of luminosity classes V and III, delineating a turn-off at 7-10 My. We can also see in Figure 5.10 the counterpart of the C peak found in 30 Doradus, evidence for the presence of Be stars. The younger burst is spectroscopically characterized by the presence of stars of type O5 If, O6.5 III((f)), O8 I(f), MS stars of types O7 to O8, together with three Wolf-Rayet stars. We see the burst in the peak at 2-5 My.

Because stars of larger masses live a shorter time, Figure 5.10 is not an unbiased view of the star-formation history. To reduce the effect of the different lifetimes as a function of age, we have also plotted the histogram of ages for stars with masses in the range $10\mathrm{M}_\odot < \mathrm{M} < 12\mathrm{M}_\odot$. Such a sample contains stars that live ~ 17 My. We can see the hints of a burst between 10-15 My, plus a reduced constant formation rate after that. The few red supergiants in the smallest (red) histogram in Figure 5.10 supports such a view. Thus, in analogy of what was observed in 30 Doradus, we have evidence of a complex star-formation history at the small spatial scales of this OB association. Thus, for the determination of the IMF of this association, and following the recommendations from Section 4.3, we will restrict the fit to the mass range $10\mathrm{M}_\odot \leq \mathrm{M} \leq 40\mathrm{M}_\odot$.

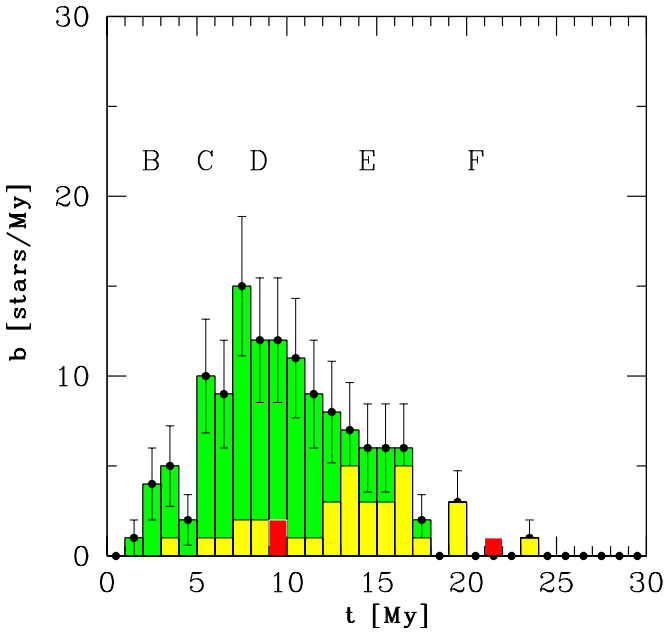

Figure 5.10: Star-formation history of LH104. The larger histogram (green) contains all stars more massive than $10M_{\odot}$ still in the main sequence. The smaller histogram (yellow) shows all stars whose masses are in the range $10\mathrm{M}_{\odot} < \mathrm{M} < 12\mathrm{M}_{\odot}$. The few red supergiants are also plotted as the smallest histogram (red).

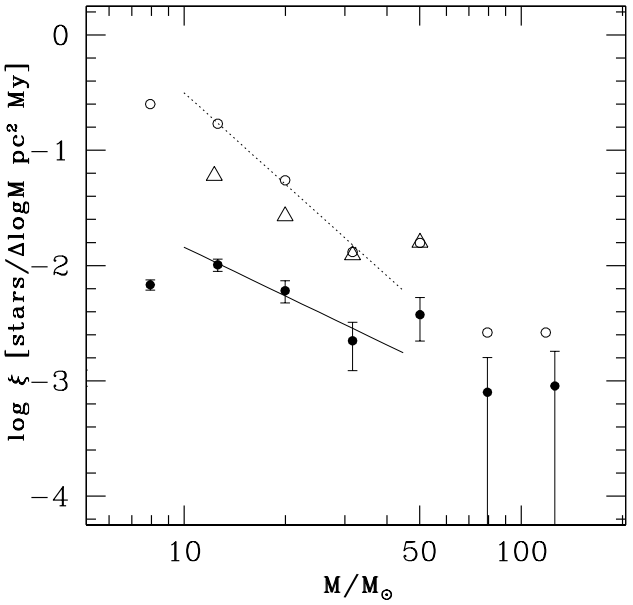

Figure 5.11: Initial mass function of LH104. The open circles represent the PDMF. The filled circles represent the IMF. The large open triangles is the IMF from Testor and Niemela (1998).

The PDMF and the IMF are shown in Figure 5.11, and Table 5.2. We counted stars in the area of our catalog defined by $4800 < \mathrm{xc} < 5650$ and $1376 < \mathrm{yc} < 2047$ corresponding approximately to the area of the finding chart in Figure 5 of Schild and Testor (1992). The best fit line for the PDMF has a slope $\Gamma = -2.6 \pm 0.2$ approximately 6σ away from the Salpeter value. The PDMFs have the same normalization used by Testor and Niemela (1998), so, not only the slopes, but also the absolute counts should be comparable as well. We can see that the flatter slope derived by Testor and Niemela (1998) is mainly due to the 50 $M_\odot$ mass bin, affected by non-linearity, and to a lesser extent to fewer stars in the range $10M_\odot < M < 20M_\odot$ in their counts. We believe this difference to be due to the different observational material: their images had $0.63''$/pixel, and were obtained under a seeing of $1.3''$, considerably worse than for our images. The two top mass bins in our counts, absent in Testor and Niemela, are affected by small number statistics; they contain only two stars, a Wolf-Rayet star and an O8 I((f)) star which these authors assign 40 $M_\odot$, while we assign 66 $M_\odot$. Despite these differences we believe that the agreement shown in Figure 5.11 is good (even the deviation from power law at $M \sim 50M_\odot$ is reproduced in both works). The IMF obtained by dividing by the main-sequence lifetimes has in the same mass range the slope $\Gamma = -1.4 \pm 0.3$. Both the IMF and the PDMF are only slightly flatter than the corresponding functions of the field. *This is consistent with a Salpeter slope for this association only if the star-formation occurred at a nearly constant rate, otherwise our data are consistent with a steeper slope.*

5.2.3 Star-formation history and IMF of the field population

One of the original goals of this research was the determination of the IMF for the field population. Massey et al. (1995, 2000) defined the field population as the set of stars at least $2'$ from the boundary of any Lucke and Hodge (1970) OB association. This distance is the product of 3 km/s, the assumed typical velocity of recently born stars, and 10 My, the approximate lifetime of a 20 $M_\odot$ star. They used circular boundaries with radii equal to the largest of the two dimensions listed by Lucke and Hodge. Being much shallower and covering a much larger area than the present work, Massey et al.'s results are not directly comparable with ours. However, we are still probing a representative fraction of the area in the LMC that these authors classified as *"field."* This region, shown in Figures 5.12, is characterized by a vastly smaller stellar density than that around N2070, and its study can give us important

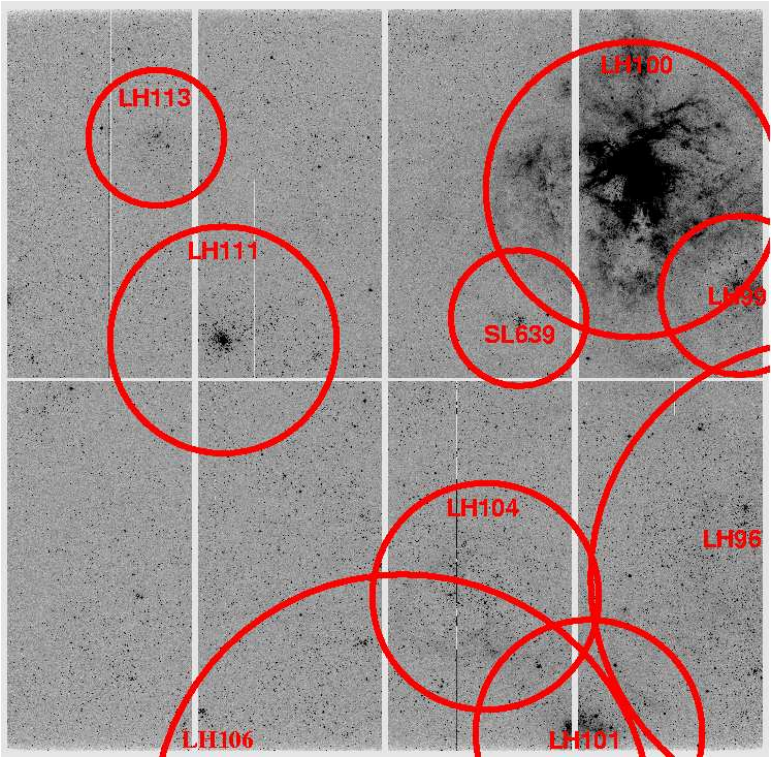

Figure 5.12: The stars outside of the circles were included in the much larger area sample used by Massey et al. (1995,2000) to study the IMF of the field population.

clues about the environmental dependence of the IMF. For the larger field of the LMC Massey et al. found an IMF with a very steep slope, $\Gamma = -3.8 \pm 0.6$, for $M \geq 25\ M_{\odot}$. This result, one of the cornerstones in the case against the universality of the IMF, deserves further study.

Figure 5.13 shows the histogram of ages of the field population defined above. This diagram should be examined in conjunction with the HR diagram for the field in Figure 4.10. The complete sample, defined by M > 10 $M_{\odot}$, and ages $\leq$ 24 My, corresponds to the larger (green) histogram; a low-mass sample with the additional constraint M < 12 $M_{\odot}$ (plotted in yellow) should be closer to the actual SFH of the field; the red super giants are shown in the smallest histogram (red). We can still see here evidence for a burst at 10 My-20 My, followed by star formation at a lower constant rate. Recent formation events are also present in the field as revealed by the hint of a peak at 3 My. Evidence for the Be effect can also be seen in the small peak at 7 My consistent with previous findings that the fraction of Be stars in the field population of the LMC is smaller than in the cluster population (Keller et al. 1999). Thus, *the SFH history of the field appears to be characterized by a*

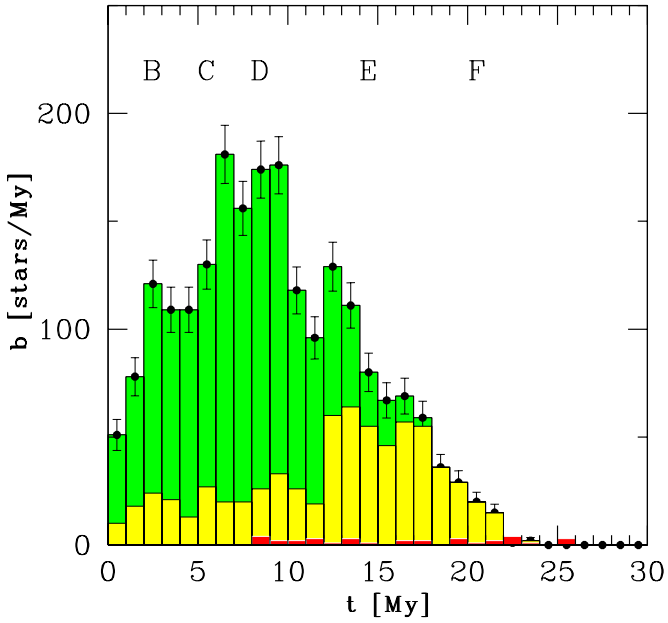

Figure 5.13: The star-formation history of the field population as defined in the text. The darker, larger, histogram shows the sample with M > 10 $M_\odot$ and ages $\geq$ 24 My. The lighter one has the additional restriction M < 15 $M_\odot$, both also restricted to main sequence stars. The histogram of ages for the red supergiants satisfying the first mass and age constraints is also shown.

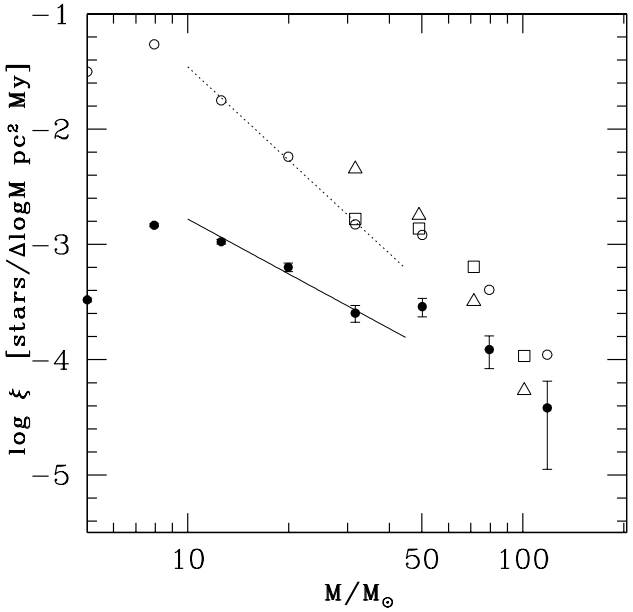

Figure 5.14: The IMF of the field population of 30 Doradus. Open circles show the PDMF. The filled circles show the IMF calculated by dividing the PDMF by the lifetime of the main sequence stars of the corresponding mass. The open triangles show the PDMF in this field from Massey's data (Massey 2002) and the open squares represent the PDMF derived from our data.

Table 5.3: Mass functions for the fiels stars.

		PDMF[a]			IMF[b]		
M	Age	N	$\log\xi$	$\Delta\log\xi$	N	$\log\xi$	$\Delta\log\xi$
5.01	95.6	782	-1.50	0.02	782	-3.48	0.02
7.94	37.0	1346	-1.27	0.01	1346	-2.83	0.01
12.59	16.8	440	-1.75	0.02	440	-2.98	0.02
19.95	9.1	143	-2.24	0.04	143	-3.20	0.04
31.62	5.9	37	-2.83	0.07	37	-3.60	0.07
50.12	4.2	30	-2.92	0.08	30	-3.54	0.08
79.43	3.3	10	-3.39	0.14	10	-3.91	0.14
118.03	2.9	2	-3.96	0.31	2	-4.42	0.31

[a] PDMF: $1.23 \pm 1.53 - (2.69 \pm 1.00)\log M$
($10M_\odot \leq M \leq 40\ M_\odot$, $\chi^2 = 0.022$, N = 3, $Q = 0.88$)
[b] IMF: $-1.20 \pm 0.94 - (1.58 \pm 0.62)\log M$
($10M_\odot \leq M \leq 40\ M_\odot$, $\chi^2 = 0.20$, N = 3, $Q = 0.65$)

burst some 10-20 My ago after which star formation did not stop completely, and continued at a nearly constant rate. For the determination of the IMF of the field, following the recommendations from Section 4.3, we will restrict the fit to the mass range $10M_\odot \leq M \leq 40M_\odot$.

To ascertain whether these peaks show spatial segregation effects we have plotted in Figure 5.15 the positions of the stars in various age groups. As was the case with NGC2070, we can also notice some differences in the spatial distribution. Figure 5.16 shows the two-point correlation function, ξ_{corr}, of the stars in peak B, filled circles; and for the stars in peaks C and D, open circles. We can see that at smaller-scales the older stars are slightly less correlated than the younger ones. The older ones appear to reach a uniform distribution above a scale of 100 pc, while the younger ones do it at 200 pc. This is probably the signature of an extended field with stars of varying ages, perhaps dominated at lower masses by stars from a burst 10-20 My ago, punctuated by a few compact associations not in the Lucke and Hodge (1970) compilation.

Figure 5.14 and Table 5.3 show the PDMF and IMF for the field population. The slope of the best fit line (in the range $10M_\odot \leq M \leq 40M_\odot$) corresponds to $\Gamma = -2.7 \pm 0.2$. Correcting our counts by the lifetime function, as Massey (1992) did, we get $\Gamma = -1.6 \pm 0.3$, significantly flatter than $\Gamma = -3.8 \pm 0.6$ determined by Massey for $M > 25\ M_\odot$.

Figure 5.17 shows the HR diagram from Massey's (2000) catalog. The data was filtered according to the prescription defined above *and restricted to the boundaries of our field.* One can see that not all stars can be assigned to mass bins in an unambiguous manner. Massey does not specify what he does with those stars, but

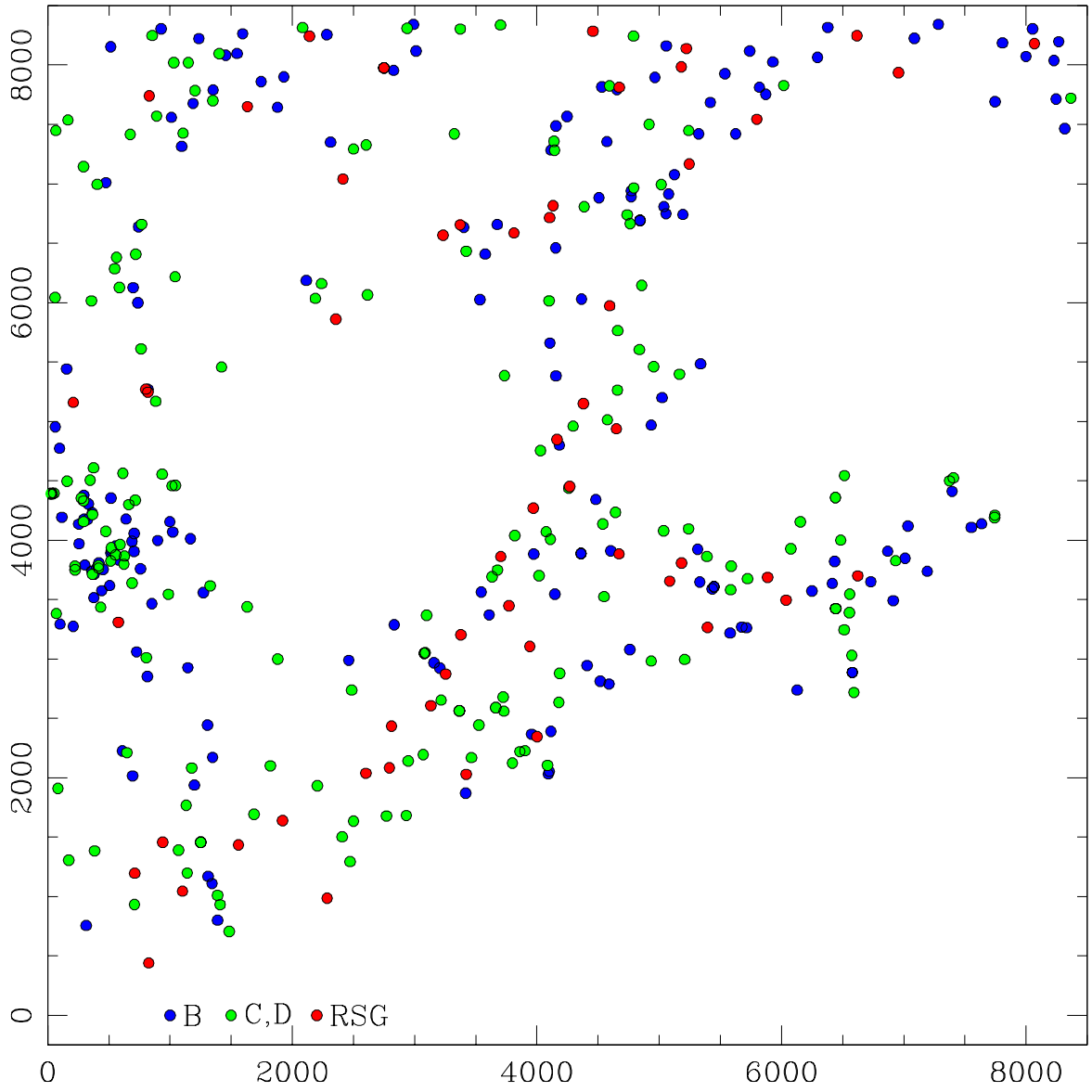

Figure 5.15: Spatial distribution of the stars in the "field". The age group B is marked dark blue, C and D in a lighter shade of green, and E and F in red. The "voids" marks the boundaries (plus 2') of the Lucke and Hodge (1970) associations.

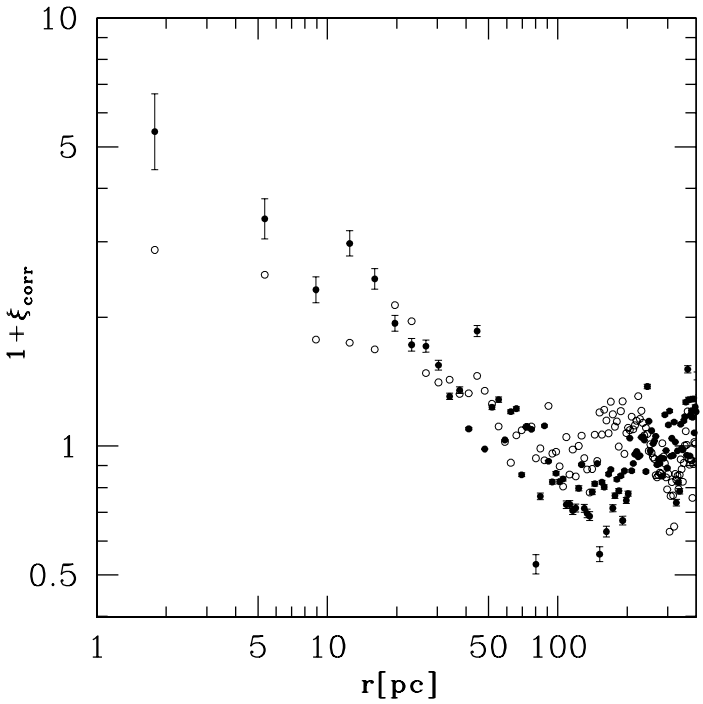

Figure 5.16: The two-point correlation function for the field stars, calculated using the Monte Carlo method of Davis et al. (1988), which is robust to the shape of the sampled "volume." Filled circles are used for stars in the B peak, while open circles are used for the stars in the C and D peaks.

the change in the derived slope caused by the stars in the *blue plume* is minor if we ignore them or move them to the right (but not so if we move them up!): $\Gamma = -4.50$ if we move them to the right and $\Gamma = -4.1$ if we ignore them. Thus, the difference in the derived slope in this thesis is not an effect of the different field we cover. Massey derives the slope of the IMF by using four mass bins: 25-40 $M_\odot$, 40-60 $M_\odot$, 60-85 $M_\odot$, and 85-120 $M_\odot$. From Figure 5.17 we derive the following counts, with the values from this thesis in parentheses: 1 (2), 6 (12), 39 (30), and 114 (42). Figure 5.14 shows the PDMF associated with these counts: large open triangles for Massey, large open squares for this thesis. Massey's work was based on observational material from the Curtis Schmidt 0.6-m telescope at CTIO. The pixel size is 2.32″. The effective area of a single pixel in the CTIO instrument is 9 times larger than in the WFI. Massey does not mention the integration time in his images, but he mentions his saturation limit at $V \sim 12.0$, thus, out of his four mass bins, only the lowest one is partially out of the non-linear regime. Therefore, the difference in slopes between this and Massey's work is most likely due to a larger number of stars discarded for having non-linear photometry by Massey. Also, Massey did aperture photometry with an aperture of 16″ diameter. Given the clustering present even in the field, we believe that the lowest mass bin can be affected by crowding for which aperture photometry is notoriously bad. At the distance of the LMC, 16″ corresponds to 4 pc and we can see in Figure 5.16 that there is an excess of pairs of stars with separations below this value. We conclude therefore that Massey's steep slope is due to systematic errors, and that in the range $10M_\odot \leq M \leq 40M_\odot$, *the IMF of the field population is consistent with Salpeter, given that the star formation proceeded at a nearly constant rate.*

5.3 Discussion

One of the original intentions of this research was to study the existence of age gradients in the super-association. This was motivated by the presence of peaks in the histograms of ages of the stars in NGC2070 studied in Paper III. We have seen in this thesis that at least one of those peaks was an artifact produced by what we have called the *Be-effect.* We believe the other peaks to be real. The one at $\sim$ 4My marks the age of the cluster itself. The second, at $\sim$ 10My, is the contribution from stars in the field. If we use the estimate of the age of the cluster core (R136) by Massey and

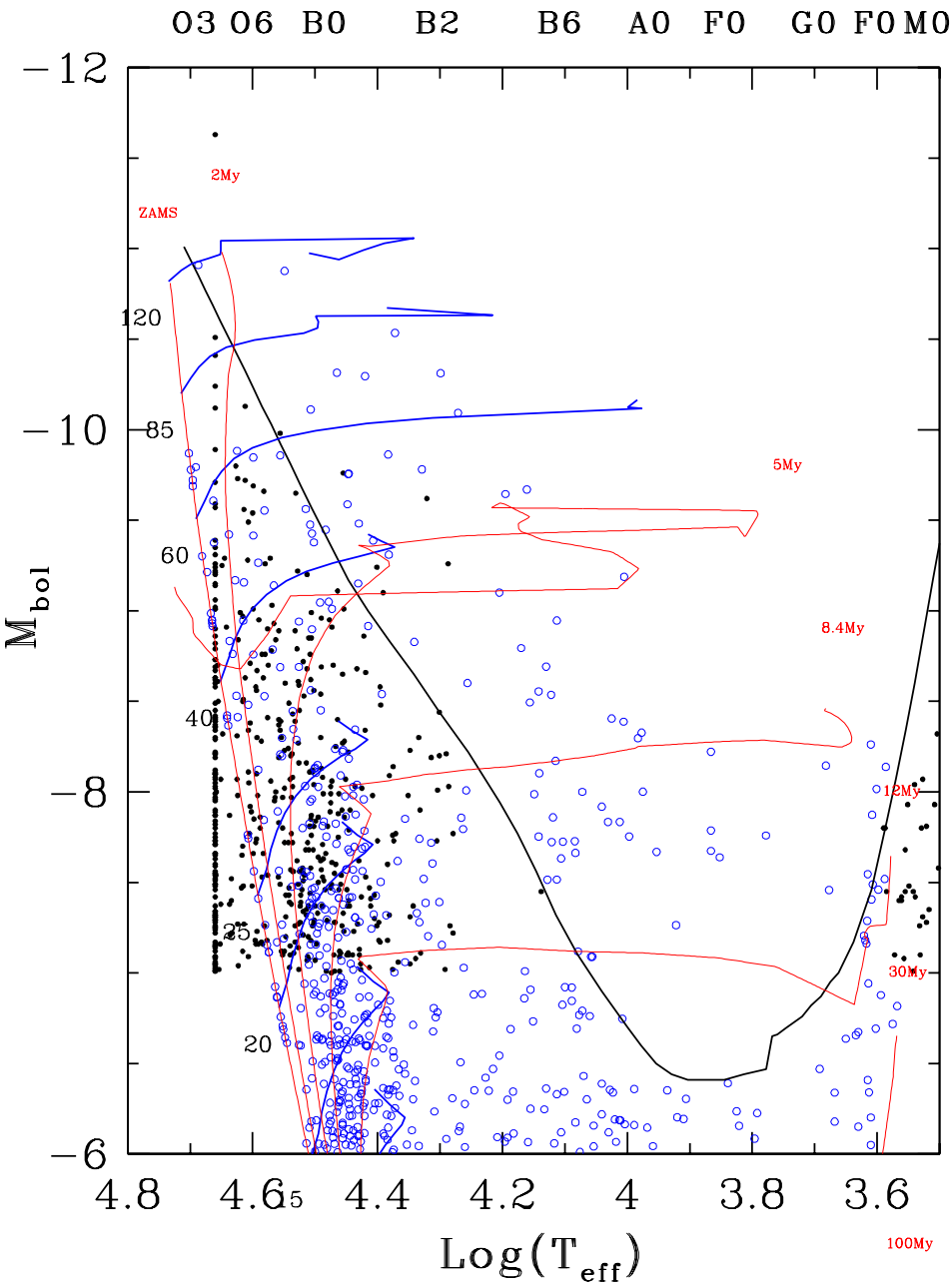

Figure 5.17: The filled dots correspond to the stars from Massey's (2000) catalog restricted to our field and outside the OB associations. Open circles correspond to our sample. The thick line corresponds to V=12.0.

Hunter (1998), we find a progression of older to younger stars as we move from the field to the center of the cluster. Although the formation episode in NGC2070 was fast, it was not instantaneous.

We have uncovered evidence for a large-scale burst of star-formation in the field, 10-20 My ago. What is more remarkable is that this burst has its counterparts in other areas of the LMC separated from 30 Doradus by up to a few kpc. Braun et al. (1997) studying LMC SGS 4 (Shapley Constellation III) find that there are no age gradients in the region with stars bursting into existence 7-15 My ago across the entire region. Previous ideas of self-propagating star formation (Dopita et al. 1985) are refuted by their data. In their study they conclude that the origin of the large-scale star formation is a bow shock produced by the motion of the LMC in the halo of the Milky Way (de Boer et al. 1998). In their study of the LMC SGS 2, Kim et al. (1999) do a census of the clusters within the SGS to find that almost all are younger than 20 My.

Another area of the 30 Doradus super-association that has been studied intensively is the neighborhood of SN 1987A. Efremov (1991) points out that SN 1987A is in the outskirts of a young loose cluster, KMK80, cataloged by Kontizas et al. (1988). Based on the photometry by Walker and Suntzeff (1990) for 38 stars within 30″ from the supernova, Efremov (1991) derives an age of 10My and Walborn et al. (1993) derives an age of 12 ± 4My. These values agree with the lifetime of the precursor star estimated at 12.7My by Wood and Faulkner (1987). A more recent study by Panagia et al. (2000) using HST photometry in nine different filters finds an age of 12 ± 2My for KMK80. Panagia et al. (2000) study both stars evolving away from the main-sequence and stars in the pre-main sequence (PMS) tracks. They find a population of PMS stars, sparsely distributed across the area studied. These stars "appear to cluster around the 20 My isochrone" by Siess et al. (1997). There is also evidence in Figure 3b of Panagia et al. (2000) of a burst 100 to 500 My ago.

Do more extensive studies of the cluster population of the LMC confirm such a burst? The cluster population of the LMC numbers upward of 4000 clusters. The studies of such an extensive data set are based on the integrated properties of the clusters (van den Bergh 1991; Sagar and Pandey 1989; Girardi et al. 1995; Bica et al. 1994). The study of Girardi et al. (1995), discussed in Appendix A, presents a histogram of ages for LMC clusters. Figure A.4 shows the presence of four clear age peaks: (1) the peak at 13 Gy; (2) the peak at 10^9y, right after the age gap; (3)

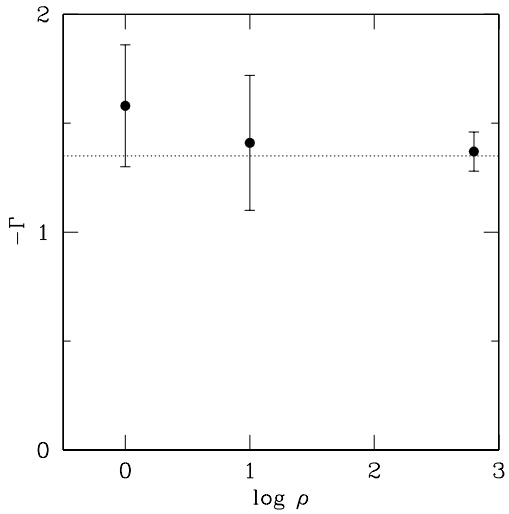

Figure 5.18: The slopes of the IMF are plotted for the field, LH104, and NGC2070, as a function of a parameter proportional to the log of the stellar density. The field density was arbitrarily set to 1.

a peak a 10^8y; and (4) a peak at 10^7y. Girardi et al. (1995) claimed that all but the youngest peaks represented periods of enhanced cluster formation. They believed that such a claim could not be made for the youngest peaks due to the fact that at these ages the sample contained objects that "probably are not clusters." With our new data we believe it is safe to conclude that the recent SFH of the region can be characterized by a burst occurring some 20 My ago followed by a period of constant, low level, star-forming activity in the field punctuated by isolated regions of enhanced star-formation such as clusters and OB associations. We do see in the data evidence for rapid, burst-like, star formation in clusters while associations appear to have a more constant rate—although the evidence is somewhat ambiguous.

We have seen in this study that the IMF and the assumed SFH are closely related. We can draw a picture in which the IMFs for the field, the OB association LH104, and the starburst cluster NGC2070, are all the same power law with a Salpeter slope. To accomplish this we need to assume that the star formation in the cluster was a single, instantaneous burst episode, while that for the low density OB association and field proceeded at a nearly constant rate: *if there are no differences in the SFH of these systems all the IMFs would differ.* Nevertheless, the age histograms of the stars with masses in the range 10 $M_\odot$ < M < 12 $M_\odot$ for the field and for LH104 are extremely similar, both showing evidence for a burst at 10-20 My ago, followed by a period of reduced, nearly constant, star-formation rate. The HST study of Massey and Hunter

(1998) shows that the population in the inner core of NGC2070 is extremely young: no traces there of the equivalent to the red super-giants found by HST in the core of NGC2100. Thus, all these facts support the conclusion that although star-formation proceeds differently in clusters and in the field, the resulting mass spectrum is, within the uncertainties, the same. Figure 5.18 show that the slope of the IMF has, within the errors, the Salpeter value over three orders of magnitude in star-formation density. This could be extended even further were we to include in this graph the slope found with HST for the core of the cluster.

In Paper III we show that the presence of variable reddening, if ignored during the analysis, could lead to the derivation of a flatter IMF. Crowded areas, or areas with bright nebulosity where the magnitude limit of the photometry is reduced are particularly affected by the flattening induced by variable reddening. We believe that many regions with claimed flattening are affected by this effect (e.g., the Arches cluster in the Milky Way). We have uncovered in this thesis another source of systematic flattening in the form of what we call the *Be effect:* the spectral energy distribution of Be stars leads to an overestimate of their effective temperatures. Such a systematic effect was already studied by Grebel et al. (1996) who found that it would result in a decrease of 0.1-0.3 in the IMF slope depending on the fraction of Be stars and the age of the stars.

In Paper III we found evidence for a flattening of the IMF in what we called the 6-pc "ring," an enhancement of the stellar density at ∼6 pc from the cluster center. This feature, easily recognized in the images of NGC2070, is populated by several B-type supergiants and WR stars. We can see now that the excess of massive stars there is an artifact produced partly by the Be effect and partly by these stars being in the non-linear regime of the photometry. *Our data is consistent with a universal IMF with a near Salpeter exponent.*

One of the original motivations of this research was to study the possible existence of age gradients: a direction of propagation of star-formation activity could contain information about what triggered the intense star-formation episode we are witnessing. *Instead of age gradients we have evidence for an almost instantaneous burst on scales of kpc.* What is the origin of this large-scale burst? Is this evidence for a large-scale triggering mechanism, or is it just coincidence? We saw in Section A that there are several timescales of interest associated with the LMC-SMC system: (1) It suffered its last close encounter with the SMC 200 My ago (Gardiner and Noguchi

1996). (2) The last passage through the plane defined by the disk of the Milky Way was 500 My ago (Moore and Davis 1994). (3) The timescale of separation of the HI L-component from the HI D-component is approximately 20 My (Luks and Rohlfs 1992). From all these timescales it appears that the only one that could be related to a burst of star-formation 10-20 My ago is the last one. Could a violent event ~ 20 My ago be able to induce the separation between the two HI components and to trigger star-formation across the face of the LMC? If so, what could such an event be? There is always a large ambiguity in the searches of triggering mechanisms for star formation. Without a successful theory of star formation the evidence for a trigger can only be circumstantial. For example, tidal interactions of late-type galaxies is almost always accompanied by enhanced star-formation (Holtzmann et al. 1992; Whitmore and Schweizer 1995). Can we assume that galactic-scale tides *induce* star formation? Although this type of argument is not logically consistent,[3] we believe that they are at least useful as they could guide further observational inquiries. Studies of HII galaxies (Taylor 1997) and of star-forming magellanic irregulars (Odewahn 1994; Willcots et al. 1996) show that they have a larger than average rate of close companions. Perhaps the most impresive case was that of NGC6822, Barnard's galaxy, which is a very isolated Local Group galaxy going through a burst of star formation. A recent HI observations with ATCA have shown this galaxy to be interacting with an HI cloud (de Blok and Walter 2003). Thus, it appear not unreasonable to seek a trigger when a starburst is observed.

We have not been able to come up with a totally satisfactory trigger candidate for this burst. One possibility is given by the More and Davies, (1994) explanation of the origin of the Magellanic Stream. They postulated the extension of the gas disk up to 100 kpc from the center of the MW. This disk would be totally ionized by the extragalactic UV field, and thus invisible to the HI surveys. We conjecture that the entrance of the LMC into such a gaseous disk, $\sim$20 My ago, could be the triggering mechanism. With the LMC currently at $\sim$25 kpc from the plane of the Milky Way, approaching it at approximately 300 km/s, such a disk would need to be extremely thick or strongly warped[4].

[3]It is such a well known logical fallacy that it even has a name: the *post hoc, ergo procter hoc* fallacy ("after this therefore because of this"), specially troublesome in the social sciences.

[4] Wouterloot et al. (1990) have studied the geometrical properties of the Milky Way disk up to a galactocentric distance of 24 kpc. The disk traced by the HI and the molecular gas (CO), shows a warp and a thickening that increases with galactocentric distance, the so called flaring of the disk. The direction of maximum warp is only 20^o away from the LMC. However, this warp

reaches a maximum excursion of 3 kpc at 15 kpc from the galactic center and then it falls back to the galactic equatorial plane. The flaring of the disk, on the other hand, increases by almost an order of magnitude from 150 pc at 9 kpc from the galactic center to 1.2 kpc at 24 kpc from the center. The data between 9 kpc and 24 kpc is well fitted by $z \sim 32 \times \exp(R/7\text{kpc})$, where R is the galactocentric distance, and z is the disk scale-height. At a projected galactocentric distance of 42 kpc, extrapolating the above relation almost a factor of 2 in distance from where it was determined, we get $z \sim 13$ kpc.

Bibliography

[1] Andersen M. I., Freyhammer L., Storm J. 1995, in: ESO-STScI workshop *Calibrating and understanding HST and ESO instruments,* ed. Benvenuti P., p.85

[2] Ardeberg A., and Virdefors B. 1980, A&AS 40, 307

[3] Azusienis A., and Straizys V. 1969, Soviet Astron. A. J. 13, 316

[4] Baade D., 2002, personal communication, from a report by Delabre B.

[5] Baade, D. 2000, *Wide Field Imager User Manual*, ESO Doc. No. LSO-MAN-ESO-22100-00001

[6] Bertelli, G., Bressan, A., Chiosi, C., Fagotto, F., and Nasi, E. 1994, A&AS 106, 275

[7] Bica, E., Clriá, J. J., Dottori, H., Santos, J. F. C., and Piatti, A. E. 1996, ApJ 102, 57

[8] Bohannan B., Abbott D. C., Voels S. A., and Hummer D. G. 1986, ApJ 308, 728

[9] Bosch G., Selman F. J., Melnick J., and Terlevich R. 2001, A&A 380, 137 (Paper IV)

[10] Bosch G., Terlevich R., Melnick J., and Selman F. J. 1999, A&AS 137, 21 (Paper II)

[11] Brandt S. 1998, *Data Analysis: statistical and computational methods for scientists and engineers*, 3rd ed., Springer-Verlag, New York

[12] Braun, J. M., Bomans, D. J., Will, J.-M., and de Boer, K. S. 1997, A&A 328, 167

[13] Breger M. 1976a, A&A 32, 1

[14] Breger M. 1976b, A&A 32, 7

[15] Breysacher, J. 1988, *Ètudes des Étoiles du type Wolf-Rayet dans Les Nuages de Magellan (Thesis) Université de Paris*

[16] Buser, R. 1978, A&A 62, 411

[17] Buser, T., Kurucz, R. L. 1978, A&A 70, 555

[18] Capaccioli et al. 2002, http://www.na.astro.it/oacdf/OACDFPAP

[19] Castelli F., Kurucz R. L. 1994, A&A 281, 817

[20] Caughlan, G. R., and Fowler, W. A. 1988, Atomic Data and Nuclear Tables, 40, 283

[21] Caughlan, G. R., Fowler, W. A., Harris, M. J., and Zimmerman, B. A. 1985, Atomic Data and Nuclear Tables, 32, 197

[22] Chlebowski T., and Garmany C. D. 1991, ApJ 368, 241

[23] Chu Y., and Kennicutt R. C. Jr 1994, ApJ 425, 720

[24] Code A. D., Davis J., Bless R. C., and Hanbury Brown R. 1976, ApJ 203, 417

[25] Cohen, R. S., Dame, T. M., Garay, G., Montani, J., Rubio, M., and Thaddeus, P. 1988, ApJ 331, L95

[26] Collins, G. W. II, Truax, R. J., and Cranmer, S. R. 1991, ApJS 77, 541

[27] Conti P. S. 1975, in: *HII Regions and Related Topics,* Wilson T. L., and Downes F. eds., Springer-Verlag, p. 207

[28] Da Costa, G. 1991, in: *The Magellanic Clouds,* IAU Symp. K/8, ed. K. Hanes and D. Milne (Dordrecht: Kluwer), p. 183

[29] Davies, R. D., Elliott K. H., and Meburn, J. 1976, Mem. RAS 81, 89 (DEM)

[30] Davis, L. E. 1994, *A Reference Guide to the IRAF/DAOPHOT Package*, NOAO

[31] Davis, M., Meiksin A., Strauss, M. A., da Costa, L. N., and Yahil, A. 1988, ApJ 333, L9

[32] Davis R. J. 1977, ApJ 213, 105

[33] de Blok, W. J. G., and Walter, F. 2003, MNRAS 341, L39

[34] de Boer, K. S., Braun, J. M., Vallenari, A., and Mebold, U. 1998, A&A 329, L49

[35] de Jager, C., Nieuwenhuijzen, H., and van der Hucht, K. A. 1988, A&AS 72, 259

[36] Descouvemont, P. 1989, PhD Thesis, Université Libre de Bruxelles

[37] Deutschmann W. A., Davis R. J., and Schild R. E. 1976, ApJS 30, 97

[38] Dickey et al. 1994, A&A 289, 357

[39] Dirsch, B., Richtler, T., Gieren, W. P., and Hilker, M. 2000, A&A 360, 133

[40] Dopita, M.A.,Mathewson, D. S., Ford, V. L., 1985, ApJ 297, 599

[41] Dunne, B. C., Points, S. D., and Chu, Y-H. 2001, ApJS 136, 119

[42] Efremov, Yu. N. 1991, Soviet Astron. Lett. 17, 173

[43] Elmegreen, B. G. 1997, ApJ 486, 944

[44] Elmegreen B. G., and Efremov Y. N. 1996, ApJ 466, 802

[45] Elson, R. A. W., and Fall, S. M. 1985, ApJ 299, 211

[46] ESO-EIS Pilot Public Survey 2000, http://www.eso.org/science/eis/eis_proj/pilot/pilot_calib.h

[47] ESO-LIN La Silla Optics Group 2002, http://www.ls.eso.org/lasilla/support/instrumentation/c

[48] ESO-ODT Optical Detectors team 2002, http://www.eso.org/projects/odt

[49] Fagotto, F., Bressan, A., Bertelli, G., and Chiosi, C. 1994, A&AS 105, 29

[50] Feast, M. W., Thackeray, A. D., and Wesselink, A. J. 1960, MNRAS 121, 25

[51] FitzGerald M. P. 1970, A&A 4, 234

[52] Fitzpatrick E. 1999, PASP 111, 63

[53] Frenk, C. S., and Fall, S. M. 1982, MNRAS 199, 565

[54] Fukuda, I. 1982, PASP 94, 271

[55] Gardiner, L.T., Noguchi, M. 1996, MNRAS 278, 191

[56] Gardiner, L.T., Sawa, T., and Fujimoto, M. 1994, MNRAS 266, 567

[57] Garmany C. D. 1992, in: *The Astronomy and Astrophysics Encyclopedia* ed. Maran S. P., Van Nostrand Reinhold, New York. p. 825

[58] Gilliote A. 2002, http://ww.eso.org/lasilla/sciops/2p2/E2p2M/WFI/filters

[59] Girardi, L., Chiosi, C., Bertelli, G., and Bressan, A. 1995, A&A 298, 87

[60] Grebel, E. K., and Chu, Y-H 2000, AJ 119, 787

[61] Grebel, E. K., Roberts, W. J., Brandner, W., 1996, A&A 311, 470

[62] Heck et al. 1984, *IUE Low Dispersion Spectra Reference Atlas, Part 1: Normal Stars,* ESA-SP-1052

[63] Henize K. G. 1956, ApJS 2, 315

[64] Herrero A. 1994, Space Sci. Rev 66, 137

[65] Herrero A., Kudritzki R. P., Vilchez J. M., Kunze D., Butler K., and Haser S. 1992, A&A 261, 209

[66] Hodge, P. 1988, PASP 100, 1051

[67] Holtzman, J., Faber, S. M., Shaya, E. J., and Lauer, T. R. et al. 1992, AJ 103, 691

[68] Hunter, D. A., Elmegreen, B. G., Dupuy, T. J., and Mortonson, M. 2003, astro-ph/0306528

[69] Hyland, A. R., Straw, S., Jones, T. J., and Gatley, I. 1992, MNRAS 257, 391

[70] Jaschek M. 1978, *Catalogue of Selected Spectral Types in the MK System* (Centre de Données Stellaires de Strasbourg)

[71] Jensen, J., Mould, J., and Reid, I. N. 1988, ApJS 67, 77

[72] Johnson H. L., Iriarte B. 1958, *Lowell Bull.* 4, 47

[73] Keller, S. C., Bessell, M. S., and Da Costa, G. S. 2000, AJ 119, 1748

[74] Keller, S. C., Wood, P. R., and Bessell, M. S. 1999, A&AS 134, 489

[75] Kennicutt R. C. Jr, and Hodge P. W. 1986, ApJ 306, 130

[76] Kennicutt, R. C., Bresolin, F., Bomans, D. J., Bothum, G. D., and Thompson, I. B. 1995, AJ 109, 594

[77] Kim, S., Dopita, M. A., Staveley-Smith, L., and Bessell, M. S. 1999, AJ 118, 2797

[78] Kim, S., Staveley-Smith, L., Dopita, M. A., Freeman, K. C., Sault, R. J., Kesteven, M. J., and McDowell, D. 1998b, ApJ 503, 674

[79] Kobulnicky, H. A. 1998, in: ASP Conf. Ser. 147, eds.: D. Friedli, M. Edmunds, C. Roberts, and L. Drissen, (San Francisco: ASP), p. 108

[80] Kolb M., 1991, Diplomarbeit, Univ. Munich, Germany

[81] Kontizas, E., Metaxa, M., and Kontizas, M. 1988, AJ 96, 1625

[82] Kroupa, P. 2002, Science 295, 82

[83] Kudritzki R. P. 1980, A&A 85, 174

[84] Kudritzki R. P., and Hummer D. G. 1990, ARA&A 28, 303

[85] Kudritzki R. P., Simon K. P., and Hamann W. R. 1983, A&A 118, 245

[86] Kurucz R. L. 1979, ApJS 40, 1

[87] Kurucz R. L. 2002, http://cfaku5.harvard.edu/grids.html

[88] Landolt, A. 1992, AJ 104, 340

[89] Langer, N. 1989, A&A 220, 135

[90] Lennon D. J., Dufton P. L., Keenean F. P., and Holmgren D. E. 1991a, A&A 246, 175

[91] Lennon D. J., Kudritzki R. P., Becker S. T., Eber F., Groth H. G., and Kunze D. 1991b, A&A 252, 498

[92] Loredo, T. J. 1992, in: *Statistical Challenges in Modern Astrophysics,* Eds. E. D. Feigelson, and G. J. Babu (New York: Springer-Verlag) p. 275

[93] Lortet M. C., and Testor G. 1984, A&A 139, 330

[94] Lucke P. B. 1974, ApJS 28, 73

[95] Lucke P. B., and Hodge P. W. 1970, AJ 75, 171 (LH)

[96] Luks Th., and Rohlfs K. 1992, A&A 263, 41

[97] Maeder, A. 1986, Hilights of Astronomy 7, 475

[98] Maeder, A., and Conti, P. S. 1994, ARA&A 32, 227

[99] Maeder, A., and Meynet, G. 2000, ARA&A 38, 143

[100] Malagnini M. L., Morossi C., Rossi L., and Kurucz R. L. 1986, A&A 162, 140

[101] Malagnini M. L., Morossi C., Rossi L., and Kurucz R. L. 1985, A&A 152, 117

[102] Manfroid J., Selman F., Jones H. 2001, Messenger 104, 16

[103] Massey, P. 2002, ApJS 141, 81

[104] Massey, Ph., and Davis, L. E. 1992, *A User's Guide to Stellar CCD Photometry with IRAF,* NOAO

[105] Massey, P., Lang, C. C., Degioia-Eastwood, K., and Garmany, C. D. 1995, ApJ 438, 188

[106] Mathewson D. S., Ford V. L., Dopita M. A., Tuohy I. R., Long K. S., and Helfand D. J. 1983, ApJS 51, 345

[107] Meaburn, J. 1980, MNRAS 192, 365

[108] Melnick J. 1986, in: *Proceedings of the 121st Symposium of the IAU: Observational Evidence of Activity in Galaxies*, ed. Khachikian E. Ye, Fricke K. J., and Melnick J.. Reidel, Dordrecht. p.545

[109] Melnick J. 1985. A&A 153, 235

[110] Melnick J., Tenorio-Tagle G., and Terlevich R. 1999, MNRAS 302, 677

[111] Mendoza, E. E. 1958, ApJ 128, 207

[112] Mermilliod, J.-C., and Maeder, A. 1986, A&A 158, 45

[113] Meynet, G., Mermilliod, J.-C., and Maeder, A. 1993, A&AS 98, 477

[114] Moore, B., and Davis, M. 1994, MNRAS 270, 209

[115] Nicolet B. 1978, A&AS 34, 1

[116] Odewahn, S. C. 1994, AJ 107, 1320

[117] Olszewski, E. O., Schommer, R. A., Suntzeff, N. B., and Harris, H. C. 1991, AJ 101, 505

[118] Paquin R. 1995, in *Handbook of Optics. Volume II.: Devices, Measurements, and Properties.* eds. Bass M., Van Stryland E. W., Williams D. R., Wolfe W. L., McGraw-Hill, p.35.29

[119] Panagia, N., Romaniello, M., Scuderi, S., and Kirshner, R. P. 2000, ApJ 539, 197

[120] Parker, J. W. 1993, AJ 106, 560

[121] Parker, J. W., and Garmany, C. D. 1993, AJ 106, 1471

[122] Peimbert, A. 2003, ApJ 584, 735

[123] Penny, L. 1996, ApJ 463, 737

[124] Points, S. D., Chu, Y.-H., Snowden, S. L., and Staveley-Smith, L. 2000, ApJ 545, 827

[125] Points et al. 1999, ApJ 518, 298

[126] Press, W. H., teukolsky, S. A., Vetterling, W. T., and Flannery, B. P. 1992, *Numerical Recipes in C*, 2nd Edition, (Cambridge: CUP)

[127] Putnam et al. 1998, Nature 394, 752

[128] Rich, R. M., Shara, M. M., and Zurek, D. 2001, ApJ 122, 842

[129] Sagar, R., and Pandey, A. K. 1989, A&AS 79, 407

[130] Salpeter, E. E. 1955, ApJ 121, 161

[131] Scalo, J. 1998, in: *The Stellar Initial Mass Function,* ASP Conference Series, 142, (San Francisco: ASP), p. 201

[132] Scalo, J. 1986, *Fundamentals of Cosm. Phys. 11, 1-278*

[133] Schaerer D., Meynet G., Maeder A., and Schaller G. 1993, A&AS 98, 523

[134] Schaller, G., Schaerer, D., Meynet, G., and Maeder, A. 1992, A&AS 96, 269

[135] Schild, H., and Testor, G. 1992, A&AS 92, 729

[136] Schild, R. E. 1966, ApJ 146, 142

[137] Schmidt-Kaler Th. 1982, In: Schaifers K., and Voigt H. H. (eds.) *Stars and Star Clusters.* Volume 2b, part of the Landolt-Borstein series on Numerical Data and Functional Relationships in Science and Technology, chief ed. Hellwege K. H., Springer-Verlag, Berlin-Heidelberg, p. 1 (SchK)

[138] Searle, L., Wilkinson, A., and Bagnuolo, W. G. 1980, ApJ 239, 803

[139] Selman F. J., and Melnick J. 2000, ApJ 534, 703

[140] Selman F.J., Melnick J., Bosch G., Terlevich R. 1999b, A&A 347, 532 (Paper III)

[141] Selman F.J., Melnick J., Bosch G., Terlevich R. 1999, A&A 341, 98 (Paper I)

[142] Serkowski K. 1963, ApJ 138, 1035

[143] Shapley, H., and Nail, V. McK. 1953, PNAS 39, 358

[144] Simon K. P., Jonas G., Kudritzki R. P., and Rahe J. 1983, A&A 125, 34

[145] Siess, L., Forestini, M, and Dougados, C. 1997, A&A 324, 556

[146] Staveley-Smith, L., Kim, S., Calabretta, M. R., Haynes, R. F., and Kesteven, M. J. 2003, MNRAS 339, 87

[147] Stetson, P. B. 1987, PASP 99, 191

[148] Stetson, P. B. 1991, in: *3rd ESO/ST-ECF Data Analysis Software,* Eds. P. J. Grosbol, R. H. Warmels, ESO Conference Proceedings No. 38, p. 187

[149] Stetson, P. B. 1993, in: *Stellar Photometry-Current Techniques and Future Developments,* IAU Colloquium No. 136, Eds. C. J. Butler, and I. Elliot, p. 291

[150] Stetson, P. B. 1997, *The DAOPHOT II User's Manual*

[151] Taylor, C. L. 1997, ApJ 480, 524

[152] Testor, G., and Niemela, V. 1998, A&AS 130, 527

[153] Tian, K. P., van Leeuwen, F., Zhao, J. L., and Su, C. G. 1996, A&AS 118, 503

[154] Vacca W. D., Garmany C. D., and Shull J. M. 1996, ApJ 460, 914

[155] van den Bergh, S. 1991, ApJ 369, 1

[156] Voels S. 1988, Ph.D. thesis, University of Colorado, USA

[157] Voels S., Bohannan B., Abbott D. C., and Hummer D. G. 1989, ApJ 340, 1073

[158] Walborn N. R. 1973, AJ 78, 1067

[159] Walborn N. R. 1972, AJ 77, 312

[160] Walborn, N. R., and Blades, J. C. 1997, ApJS 112, 457

[161] Walborn, N. R., Phillips, M. M., Walker, A. R., and Elias, J. H. 1993, PASP 105, 1240

[162] Walker, A. R., and Suntzeff, N. B. 1990, PASP 102, 131

[163] Westerlund, B. E. 1997, *The Magellanic Clouds*, Cambridge University Press, Cambridge, UK.

[164] Whitmore, B. C., and Schweizer, F. 1995, AJ 109, 960

[165] Wilcots, E. M., Lehman, C., and Miller, B. 1996, AJ 111, 1575

[166] Wood, P. R., and Faulkner, D. J. 1987, Proc. Astr. Soc. Australia 7, 75

[167] Wouterloot, J. G. A., Brand, J., Burton, W. B., and Kwee, K. K. 1990, A&A 230, 21

[168] Wu et al. 1983, *The IUE Ultraviolet Spectral Atlas,* NASA IUE Newsletter 22

[169] Ziólkowski, J. 1972, Acta Astr. 22, 327

[170] Zuckerman, B. 1973, ApJ 183, 863

Appendix A

Overview of the Magellanic Clouds system

Figure A.1 shows a projection in galactic coordinates of what is called the Magellanic Stream. This is a long and narrow HI filament, 10^o wide, that extends approximately 100^o away from the inter-cloud region. Viewed from the earth it appears as a band along a *small circle* parallel to the $\ell = 280^o$ large circle, 7^o away from the south galactic pole.

Several sub-condensations can be seen in the stream labeled MS I up to MS VI in the figure. The mean column density of gas decreases from 2×10^{20} atoms cm^{-2} near the Magellanic Clouds, down to 1×10^{19} atoms cm^{-2} near MS VI. The galacto-centric radial velocity of the Stream decreases from 0 km/s at MS I, to -200 km/s at MS VI. This velocity gradient is not shared by the internal motion of each of the sub-condensations, which appear to have constant velocity. No stars have been found associated with the Stream. Several models have been proposed to explain the origin of the Stream, but two are most probable: ram pressure stripping of weakly bound material, and a tidal tail from a LMC-SMC collision.

In the diffuse pressure model of Moore and Davis (1994), the Stream consists of material stripped from the LMC-SMC system during its last passage through an extended *disk of ionized gas* of the Milky Way. The *encounter* with this disk of ionized material occurred 500 My ago at a galacto-centric distance of $\sim$ 65 kpc. The gas with lowest column density, near the tip of the stream, has lost the most angular momentum and has fallen to a distance of ~ 20 kpc from the Milky Way. In the process it has attained a velocity of -200 km/s. To explain such small velocity after such a large infall the model requires the existence of an extended halo of diffuse

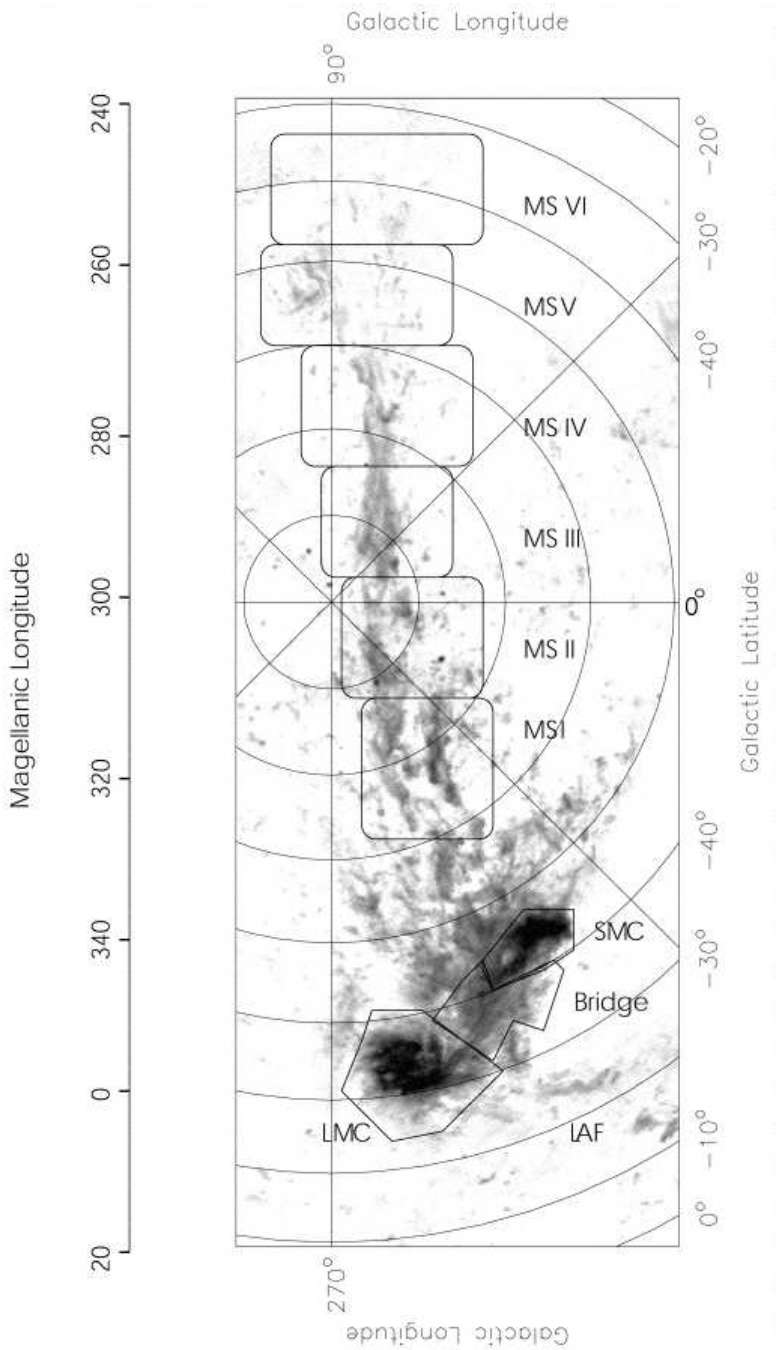

Figure A.1: HI in the Magellanic Stream seen in galactic coordinates, from Putnam et al. (2003).

ionized gas surrounding the Milky Way[1].

In the tidal tail model the LMC and the SMC form a gravitationally bound system. In a close approach 1.5 Gy ago the tidal field of the LMC pulled gas out from the SMC creating the Magellanic Stream (Gardiner et al. 1994; Gardiner and Noguchi 1996). While in their most recent closest approach 200 My ago the tidal bridge between the Clouds was generated. In Figure A.1 the tidal bridge is seen as the filament extending from the SMC toward the LMC together with the Leading Arm (LA), a tenuous HI gas feature extending some 10^o to the south.

Homing in on the LMC Figure A.2 (left) shows schematically several of the most important features while Figure A.2 (right) shows the H_α image of the LMC, from Davies, Elliott, and Meaburn (DEM, 1976). The nomenclature in Figure A.2: (1) the elongated feature delineated by the dashed line near the center marks the approximate position of the bar of the LMC; (2) the Arabic numerals identify the super-giant shells identified in the LMC (Meaburn 1980); (3) the Roman numbers identify the Shapley *Constellations* (Shapley and McKibben Nail 1953). The Shapley Constellations can be easily recognized in the H_α image in Figure A.2. Notice that these two figures are in equatorial coordinates, with North up, and East to the left, while the previous figure was in galactic coordinates: there is almost a 90^o rotation between them. Perhaps the most striking feature in Figure A.2(b) is the spatial extent of current star-formation activity, indicating that if there is some triggering mechanism, it must be acting across the face of the LMC. The paper of Davies et al. (1976) catalogs 329 emission nebulae commonly referred to by their DEM-number. DEM complements the previous work by Henize (1956) in which 415 emission nebulae are cataloged commonly referred to with an N-number. There are nine super-giant shells identified by Meaburn (1980), and referred to as LMC SGS X, where X goes from 1 to 9. Numbers larger than 9 indicate a reference to the recent catalog by Kim et al. (1999).

The stellar disk of the LMC has been observed using the data from the 2MASS and DENIS near infrared surveys (van der Marel 2001). Figure A.3(a) shows a color coded image of the near-IR star counts (AGB and RGB stars). The outermost contour with PA $= 189.3^o \pm 1.4^o$ is almost perfectly aligned with the direction of the Galactic center (PA $= 183.7^o$) hinting to a tidal origin. It points within 26^o away from the direction of the SMC (PA $= 228.7^o$). Since the LMC feels at present a Galactic tidal

[1]The properties of this halo were shown to be consistent with the constraints imposed by the ROSAT measurements of the diffuse X-ray background.

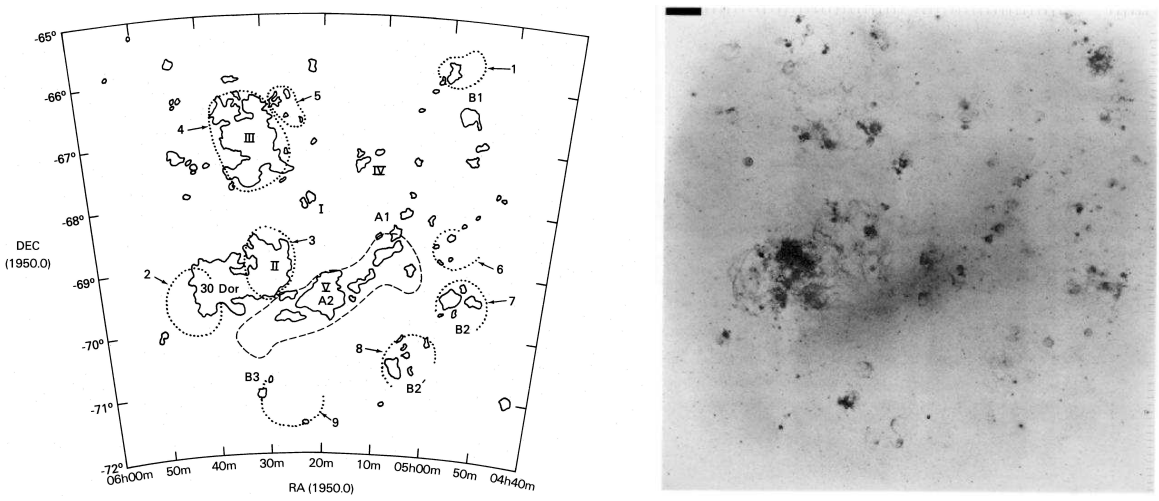

Figure A.2: The left panel shows some of the most important features of the LMC. The elongated dashed line near the center marks the position of the bar. Shapley's constellations are identified with the corresponding Roman numbers. The super-giant shells are identified with Arabic numerals. The right panel shows an H_α image of the LMC, from Davies et al. (1976).

field ~ 10 times stronger than that from the SMC, van der Marel concludes that the Galactic tidal field is the origin of the elongation. These conclusions are in agreement with the distribution of star clusters from Irwin (1991) shown in Figure A.3(b).

The LMC contains upward of 4000 clusters. To study the whole sample it is necessary to use their integrated properties. The pioneer work of Searle, Wilkinson, and Bagnuolo (1980) placed the clusters in a sequence in their Q(ugr) − Q(vgr) diagram, the so called SWB diagram. This sequence was shown to have its equivalent in the UBV color-color diagram by Frenk and Fall (1982) now known as the "equivalent" SWB sequence, E-SWB. One of the first calibrations of this sequence in terms of ages and metallicities was that of Elson and Fall (1985). More recently, Girardi et al.(1995), using the single stellar population models of Bertelli et al. (1994), and the catalog of cluster UBV colors of Bica et al. (1994), have produced an age distribution function for LMC clusters. Figure A.4 shows both the age histogram and the age distribution function corrected for the fact that clusters fade as they age. Girardi et al. (1995) interpret the peaks at 10^8y and 10^9y as periods of enhanced cluster formation while they do not make such a claim for the peak at 10^7y because "at these ages the sample contains many objects that probably are not clusters."

A most important property of the LMC clusters is the existence of an "age gap" between 4-12 Gy in which almost no clusters are found (Jensen, Mould, and Reid 1988; Da Costa 1991; van den Bergh 1991). Olszewski et al. (1991) showed that a gap is

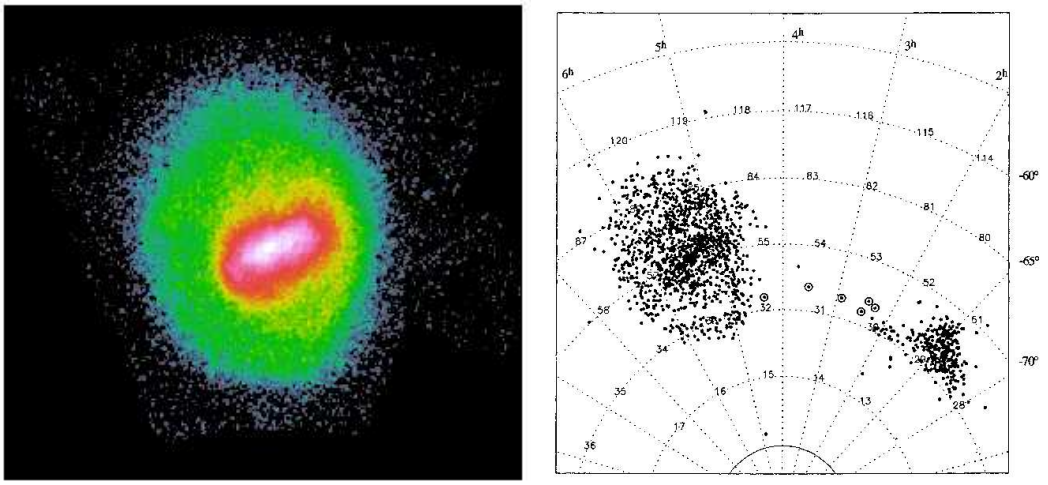

Figure A.3: (a, left) This figure plots the stellar number density in the LMC for AGB and RGB stars (van der Marel 2001). The data comes from the DENIS and 2MASS surveys combined. The field of view is approximately 22^o in each direction, North is up, East to the left. (b,right) The distribution of star clusters in the Magellanic Clouds according to Irwin (1991).

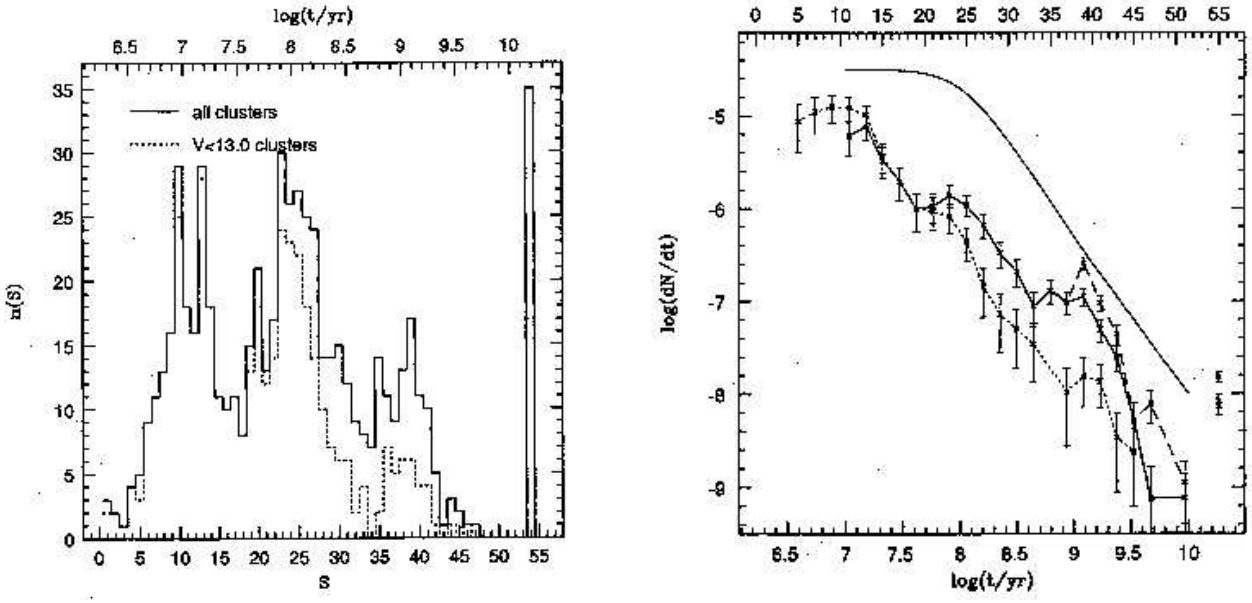

Figure A.4: (a, left) Age histogram for LMC clusters, and (right, b) the age distribution function, from integrated UBV colors. Taken from Girardi et al. (1995).

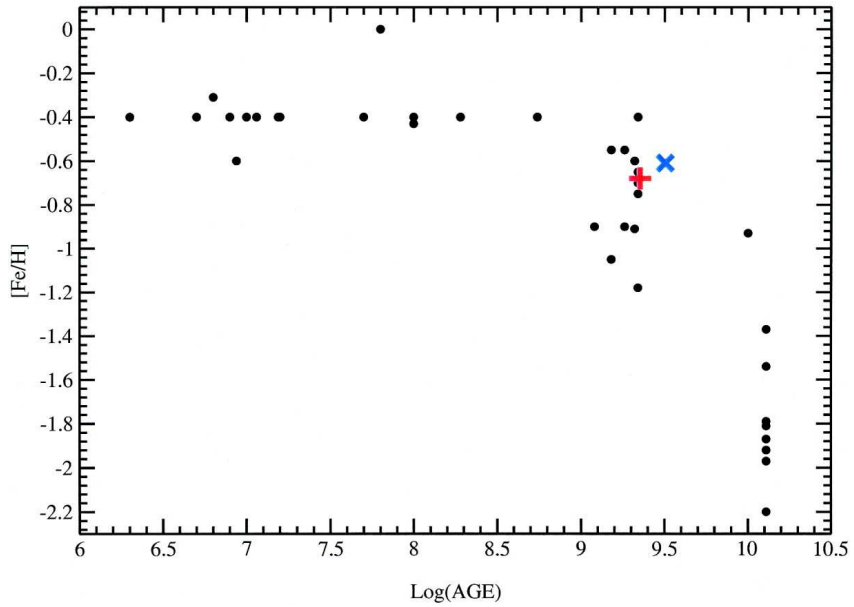

Figure A.5: Age-abundance relation for the LMC showing the gap at 3-12 My (from Rich et al. 2001).

also present in metallicity: the younger group of clusters have [Fe/H]$\sim 0.7 \pm 0.3$ dex, while the oldest LMC clusters have [Fe/H]~ -2 dex. Figure A.5 from Rich, Shara, and Zurek (2001) shows the age-abundance relation for a set of clusters they studied together with data from the compilation by Dirsch et al. (2000). We would like to point out two features. First, the age gap previously mentioned; and second, the fact that if we consider the number of clusters per unit time we have a large burst 13 Gy ago, followed by the gap, and then another burst some 3 Gy ago followed by a period of reduced activity, and by what appears to be another burst some 20 My ago which continues until now. Many systematic effects, such as cluster fading and destruction, affect the data (Hunter et al. 2003). Nevertheless, both the 3-12 Gy gap and the current "burst" that started some 20 My ago, appear to be real (see Figure 10 of Hunter et al. (2003)).

Another important property of the LMC is its chemical abundance. Chemical abundances have been obtained from many types of objects, among them star clusters, HII regions, supergiant stars, and planetary nebula (Westerlund 1997). We are mainly interested in the abundances of young clusters and HII regions that should reflect the abundances of the gas out of which the most recent generation of stars formed[2].

[2]Although one could expect strong inhomogeneities in the interstellar medium due to SN explosions injecting locally gas of very high metallicity, this is not observed (Kobulnicky 1998). Kobulnicky (1998) has shown that the timescale for chemical enrichment in galaxies is longer than the typical

The abundance of the youngest clusters in the LMC have been usually measured at $\sim$1/3 solar, or $Z \sim 0.008$. This is the value that we will assume in this thesis consistent with the recent HII gas abundance determination using UVES in the VLT that found $Z \sim 0.0099$ (Peimbert 2003).

The HI gas in the LMC has been recently shown to have a surprisingly uniform large-scale disk structure and to be highly turbulent at small scales (Kim et al. 1998). Figure A.6(a) shows this turbulent structure while Figure A.6(b) shows the velocity field of the LMC. This velocity field has been corrected by the transverse motion of the LMC as determined with HIPPARCOS by Kroupa and Bastian (1997). There is a clear signature of rotation, but also of non-circular motions (e.g., the S-shaped 0-velocity line). The above work has been recently complemented by a Nyquist sampled study (5.7′) of the LMC using a multi-beam receiver at the Parkes telescope (Staveley-Smith et al. 2003). Figure A.7(a) is a schematics view of several components of the LMC (from Staveley-Smith et al. 2003) showing: (1) Kroupa and Bastian's transverse motion vector pointing almost directly to the Milky Way plane and away from the Magellanic Stream; (2) arm E, which starts from 30 Doradus to the north and extends to the south for a couple of kilo-parsecs, in the direction of the Leading Arm mapped by Putnam et al. (1998), almost perpendicular to the Magellanic Stream, and parallel to the galactic plane; (3) arm B, pointing in the direction of the tidal bridge with the SMC.

Staveley-Smith et al. (2003) do not discuss or contrast their findings with those of the previous extensive HI study by Luks and Rohlfs (1992). They limit themselves to comment that both works show the complex structure of the interstellar medium in that area of the LMC. The latter authors divide the 21 cm lines into two components (Staveley-Smith et al. did not). The first, or D-component, has a rather uniform disk-like distribution from which they derive the rotation curve of the galaxy. The second, or L-component, for *low velocity*, appears as an almost parallel velocity component subdivided into two large HI cloud complexes. The first extends almost 2 kpc to the south and can be identified with Staveley-Smith et al.'s E-arm; the second is located to the west and north separated by a gap from the first with no clear counterpart in the Staveley-Smith et al.'s maps.

The 30 Doradus nebula lies right in the gap of these two clouds. Luks and Rohlfs

lifetimes of HII regions (10^7y). He proposes a scenario in which the freshly synthesized metals are expeled into the halos of galaxies in a hot 10^6 K phase and later "rain" down as they cool creating a gradual enrichment on spatial scales > 1 kpc.

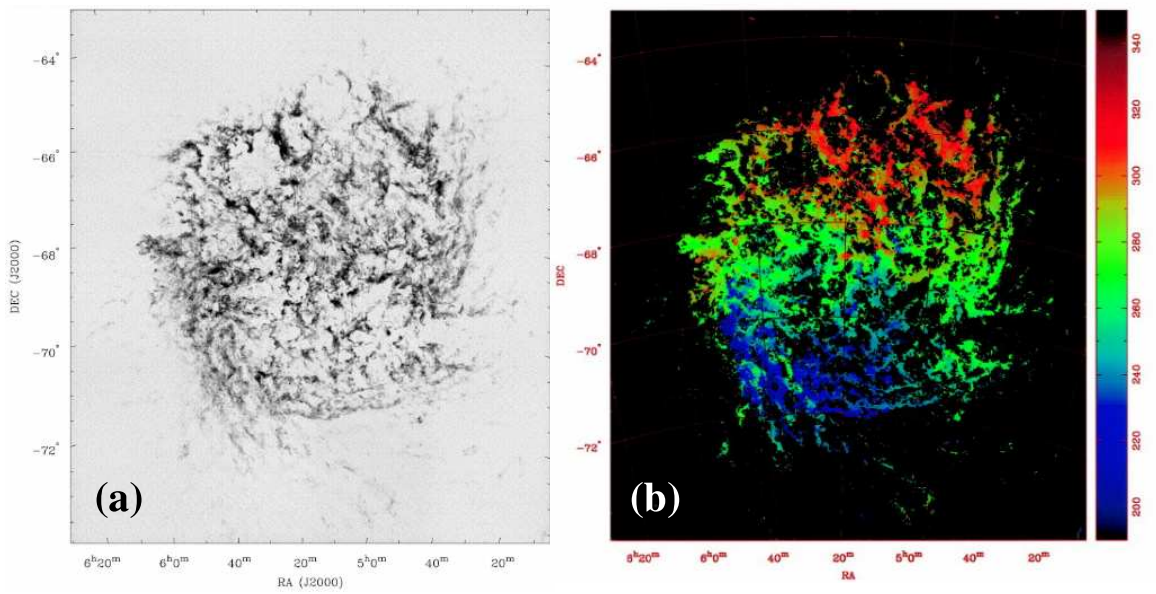

Figure A.6: (a) Integrated HI distribution, and (b), the velocity field of the LMC, according to Kim et al. (1998).

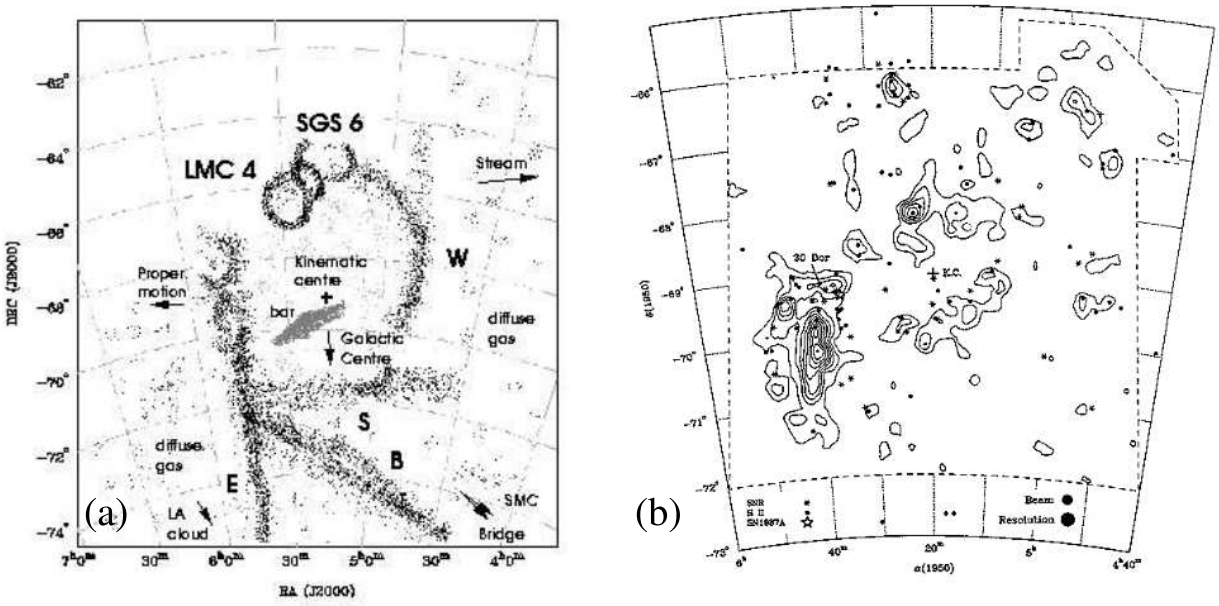

Figure A.7: (a) Schematic view of the LMC components and kinematics, from Staveley-Smith et al. (2003). (b) CO J=1-0 map of Cohen et al. (1988), with a resolution of 12′.

(1992) give good reasons to believe that 30 Doradus is indeed associated with the L-component: first, the spatial coincidence of 30 Doradus with the gap between the clouds; by virtue of the strong UV flux any gas within approximately 500 pc should be ionized; second, if 30 Doradus were to be located in the D-component, one would expect a hole of a similar diameter in the HI distribution, and none is observed. Also, the observed radial velocity of the HI gas in the L-component coincides with the radial velocity measured in the H_α gas in 30 Doradus (Westerlund 1997).

Using the absence of a hole in the D-component they estimate a minimum distance of 200-400 pc between the components (this distance depends on the assumed gas density). Furthermore, Luks and Rohlfs use a thermal source of continuum radiation in 30 Doradus as a background source to search for absorption from the D-component, but found none. They conclude that the L-component and 30 Doradus lie in front of the D-component[3]. For a typical radial velocity difference of $\Delta v = 18 \pm 5$ km/s Luks and Rohlfs estimate a timescale of separation of 14-22 My.

Important for the history of star-formation in the Clouds is the distribution of molecular clouds. Figure A.7(b) is the map by Cohen et al. (1988) made with the 1.2-m Columbia Millimeter-Wave telescope at CTIO. They find that the LMC molecular clouds are generally much less luminous for a given line-width than their galactic counterparts implying that the ratio $X = N(H_2)/W_{CO}$ of molecular column density to velocity-integrated CO intensity is 6 times larger in the LMC than in the Milky Way[4]. They catalog 40 molecular clouds, all but one with the same radial velocity than the HI L-component. There are two important features in their map. First, there is a large complex of molecular clouds extending south of 30 Doradus for 2.4 kpc with a total molecular mass estimated at 6×10^7 $M_\odot$. This feature corresponds to the E-arm in HI. Second, there is a 500 pc diameter clumpy ring of expanding molecular clouds centered in 30 Doradus with a mass estimated in 3.8×10^6 $M_\odot$ and an expansion velocity of 17 km/s. They derive a kinetic energy of 3×10^{52} ergs, comparable with the kinetic energy of expansion of the LMC SGS 4 in Shapley's Constellation III (7×10^{51} ergs).

[3]Although this was questioned by Dickey et al. (1994), who found absorption by cool HI gas in the direction of a few background sources, later work by Points et al. (1999) using the X-ray data in their multi-wavelength study of the LMC SGS 2, confirms the original conclusions by Luks and Rohlfs.

[4]Thus, to be visible in CO, a molecular cloud has to have a very large $N(H_2)$ column density. This has the ineteresting consequence that most molecular clouds are seen as dark nebula (Cohen 1988).

Appendix B

Software

The software used in the data reduction and analysis will be available on the Web for examination.

Appendix C

Published papers

Paper I

The ionizing cluster of 30 Doradus I. Internal reddening from NTT photometry and multi-object spectroscopy

A&A 341, 98 (1999)

F. Selman, J. Melnick, G. Bosch, and R. Terlevich

.

Astron. Astrophys. 341, 98–109 (1999)

ASTRONOMY
AND
ASTROPHYSICS

The ionizing cluster of 30 Doradus

I. Internal reddening from NTT photometry and multi–object spectroscopy⋆

F. Selman[1], **J. Melnick**[1], **G. Bosch**[2], **and R. Terlevich**[2]

[1] European Southern Observatory, Alonso de Córdova 3107, Santiago, Chile
[2] Institute of Astronomy, Madingley Road, Cambridge CB3 0HA, UK

Received 8 April 1998 / Accepted 7 September 1998

Abstract. UBV profile fitting photometry is presented for 1469 stars within 90″ of the center of the ionizing cluster of 30 Doradus (NGC 2070). A value of 0.82 ± 0.03 is found for the extinction parameter S = E(U-B)/E(B-V), constant over almost the whole area covered by this research, with some evidence for local variations. Two reddening components can be identified: a smooth and moderate one that increases towards R136, and a clumpy one varying widely across the face of the cluster. The total–to–selective extinction parameter, $R_V = A_V/E(B-V)$, is found to be in the range of 3.0 to 3.7, consistent with previous determinations. A new visualization tool, the colour-magnitude stereogram, is introduced and used to argue that: (1) the observations imply mass segregation in a dust filled cluster; (2) that there has been continuous dust formation near the cluster core up to the present; and (3) that an insidious systematic error has plagued previous determinations of IMF slopes. A method to obtain an unbiased estimate of the slope is discussed.

Key words: stars: early-type – stars: luminosity function, mass function – ISM: dust, extinction – Galaxy: open clusters and associations: general – galaxies: Magellanic Clouds

1. Introduction

Owing to their strong and narrow emission lines, star-forming dwarf galaxies (or HII galaxies as they are now commonly known in the literature) are interesting cosmological probes. Using 4m class telescopes and optical spectrographs, it is now possible to obtain accurate determinations of elemental abundances out to redshifts $z \sim 1$ (Terlevich & Terlevich 1998). With 8m telescopes and the new generation of infrared spectrometers, it will be possible to extend this range, at least in principle, to $z \sim 3$. Thus, it will become possible to study the evolution of "primordial" He abundance with look-back time, and the chemical evolution history of the Universe with unprecedented accuracy. Moreover, owing to the strong correlation between luminosity and emission line-profile widths in HII galaxies (Melnick et al. 1987, 1988), it is also possible to obtain distances to objects out to $z \sim 1$ and, again, with the new generation of instruments we will be able to extend this range perhaps out to $z \sim 3$ (Steidel et al. 1998; Terlevich & Terlevich 1998). In order to understand the evolution of HII galaxies, and to bootstrap from the nearest to the most distant objects, it is crucial to understand the IMF of the starburst clusters that power the nebular emission. In particular, we need to understand whether the IMF changes systematically with environment, metallicity, or position within the clusters (i.e. mass segregation). Despite theoretical and observational support for a universal IMF, variations have been claimed in various environments and mass ranges. At this moment there is considerable debate about the significance of these claims (Elmegreen 1997; Hunter et al. 1997b; Scalo 1998 and references therein).

This is the first of a series of papers aiming at an accurate determination of the IMF of the 30 Doradus cluster in the LMC which is one of the few starburst clusters that can be studied in detail from the ground or space. We combine new CCD photometry with an improved catalogue of spectral types for 265 stars, compiled from published and newly obtained spectroscopy, to investigate the properties of the ionizing cluster of the Tarantula nebula. The photometry was obtained under excellent seeing conditions with the SUperb Seeing Imager (SUSI), attached to ESO's New Technology Telescope (NTT). The spectroscopy was performed with ESO's Multi–Mode Instrument (EMMI) at the NTT.

Our interest is to obtain a reliable determination of the total photometric mass of the cluster, through the IMF, and to compare this mass with the value determined dynamically through measurements of the stellar velocity dispersion. A related problem is that of mass segregation, and we intend to use these new data to investigate whether the slope of the IMF changes with distance to the core of the cluster, as has been claimed by some authors (Brandl et al. 1996; Malumuth and Heap 1994), observations which have not been confirmed by more recent data from the un–aberrated Hubble Space Telescope (HST) (Hunter et al. 1995; Hunter et al. 1996; Massey and Hunter 1998).

Here we present the photometry and a detailed investigation of the reddening law within the cluster. We show, using a new tool which we call the *colour-magnitude stereogram*, that any

Send offprint requests to: fselman@ESO.org

⋆ Based on observations collected with the NTT ESO telescope. Table 2 is only available in electronic form at the CDS via anonymous ftp to cdsarc.u-strasbg.fr (130.79.128.5) or via http://cdsweb.u-strasbg.fr/Abstract.html

Table 1. Observing Log.

Object	U.T.	Filter	Exposure	Airmass	Seeing
30 Doradus	4 : 02 : 16	V	10	1.3173	0.62
30 Doradus	4 : 04 : 53	V	20	1.3189	0.74
30 Doradus	4 : 07 : 46	B	15	1.3207	0.91
30 Doradus	4 : 10 : 34	B	30	1.3225	0.86
30 Doradus	4 : 13 : 39	U	300	1.3262	0.90
Rubin 149	5 : 22 : 50	V	20	1.1509	
Rubin 149	5 : 29 : 12	B	45	1.1560	
Rubin 149	5 : 32 : 33	U	120	1.1595	

determination of the IMF from UBV photometry in clusters with variable internal extinction, requires a thorough control on all systematic effects, and we propose means to achieve this in a star–by–star fashion.

2. The photometry

2.1. Observations

The observations were obtained by Stefano Benetti using SUSI at the NTT telescope in La Silla on the night of 9/10 January 1995. The night was photometric, with subarcsecond seeing conditions. The observing log is as shown in Table 1.

The instrument used a Tektronix 1024×1024 CCD (Tek#25) with 24μ pixels which gives an image scale of $0.13''$/pix thus ensuring Nyquist sampling even for the best seeing conditions at La Silla. The CCD was read in slow mode (15 kpixel/sec), giving a readout noise of 5.9 electrons, and a conversion factor of 3.4 electrons per ADU. The detector system is linear to 0.4% over the full dynamic range of the 16 bit ADC. The upper limit of linearity is $\sim 160,000\mathrm{e}^-/\mathrm{pixel}$ or about 47kADU and the maximum pixel rates in our data (excluding the cluster core R136) are: 57750 ADU for the 20s V frame, 40600 ADU for the 10s V frame, 23000 ADU for the 30s B frame, 10730 ADU for the 15s B frame, and 24550 ADU for the U frame. The dark current ($\sim 2.8e^-/pixel/hour$) is negligible for the present purposes. All relevant CCD parameters are measured periodically by the NTT team and the results of the tests are distributed through the ESO web site (http://www.eso.org/). Therefore, we are certain that the values quoted are valid for our observations.

2.2. Photometric calibration

The standard CCD operations of trimming and calibration (bias level subtraction and flat fielding) were carried out using the IRAF package CCDPROC in the standard way. Dark current subtraction was not necessary because of the short duration of the exposures. Twilight sky flats were obtained for all filters. Several frames were added for each filter and normalized to unit mean. We used only the best frames to produce the final catalogue of stellar magnitudes. These are the 10s V frame, that despite being of half the exposure of the 20s frame has a better seeing and thus similar intensities, but still low enough not to have saturated stars. For the B frame we used the 30s exposure which does not show saturated stars but goes deeper than the 15s frame. The three frames are combined in a single three–colour image presented in Fig. 1.

The instrumental ubv magnitudes and the standard UBV magnitudes are related to first order by the equations (Stetson 1992),

$$u = \mathrm{U} + a_0 + k_U X + a_1(\mathrm{U}-\mathrm{B}) \quad (1)$$

$$b = \mathrm{B} + b_0 + k_B X + b_1(\mathrm{B}-\mathrm{V}) \quad (2)$$

$$v = \mathrm{V} + c_0 + k_V X + c_1(\mathrm{B}-\mathrm{V}) \quad (3)$$

where k_{UBV} are the atmospheric extinction coefficients in each band and X is the airmass[1].

The photometric calibration was done in two steps. We observed the Landolt field near Rubin 149 (Landolt 1992) to derive the colour terms (a_1, b_1, c_1). Linear fits to six stars in this field having a wide range in colour were used to determine the colour terms. We then used the colour corrected instrumental magnitudes of all stars in the 30 Doradus field in common to the observations of Parker (1993) to determine the photometric zero points. This procedure avoids the need to determine atmospheric extinction and ensures that our photometry and Parker's are in the same photometric system. Fig. 2 shows the fits to the colour equations.

In principle, Parker's photometry could also have been used to determine the colour terms. In practice, however, this was not possible because most 30 Dor stars have similar colours and because, as can be seen in Figs. 3 and 9, Parker's photometry is rather noisy. We remark, however, that since most 30 Dor stars have similar colours implies that any systematic errors in the colour coefficients would translate into zero point shifts which are taken out by our calibration procedure.

In order to have an external check on the zero points derived from Parker's photometry we also reduced the data from beginning to end using the atmospheric extinction parameters published by the Geneva Observatory[2]. The final zero points (shown in Fig. 2) agree within 2% in V, U-B, and B-V with the values derived from the 30 Dor stars. For the rest of the paper, therefore, we will only use the zero points referred to Parker's photometry. Fig. 9 shows that the overall agreement between the two photometries is excellent although the noise in Parker's data is larger, specially for $\mathrm{V} > 16.0$. This is not surprising

[1] There is also a nonlinear, colour dependent, correction that should be applied to the U data due to the effect of the Balmer discontinuity in the U band. If non-negligible it would force us to include a (B-V) term in the equation for U (Gutierrez-Moreno et al. 1966; Moffat and Vogt 1977). We can estimate this effect using the data from Moffat and Vogt: the correction in (U-B) is given by (using their notation): $\gamma_1\beta\Delta X$, where β is a constant equal to -0.27, and γ_1 varies between +0.2 and -0.1 for stars of spectral types between O5 and A0. For the airmasses of our observations, $\Delta X \approx 0.18$, this non–linear term implies an uncertainty of approximately ±0.007 magnitudes. The danger of this effect is that it is systematic, that is, the correction would be -0.007 mags for an O5 star and +0.007 for an A0.

[2] The whole database can be found in the WWW at http://www.ls.eso.org/lasilla/atm_ext/extintion.html.

Fig. 1. Three–colour composite image of 30 Doradus showing the large number of hot blue stars. The V drives the red channel, the B drives the green channel, and the U drives the blue channel. The size of the field is 130″each side, corresponding to 35 pc for an adopted distance to the LMC of 55 kpc (Feast & Walker 1987). North is up, east to the left.

given the difference in seeing, the most important factor when doing profile fitting photometry in crowded areas.

2.3. Crowded field photometry

The nature of 30 Doradus is such that it taxes even the most sophisticated crowded field photometry packages. Not only it is a crowded cluster, but it is also embedded in a bright and clumpy emission nebula. Among the available photometry packages, only Daophot II (Stetson 1987, 1991, 1997), has an algorithm that determines the sky locally, which is the most important consideration for this field. Daophot II also allows a mixture of analytical and empirical spatially variable PSFs to be used. The particular version of Daophot II we used is the one within the IRAF environment which is available for the Linux workstation used for this research (Massey & Davis 1992; Davis 1994).

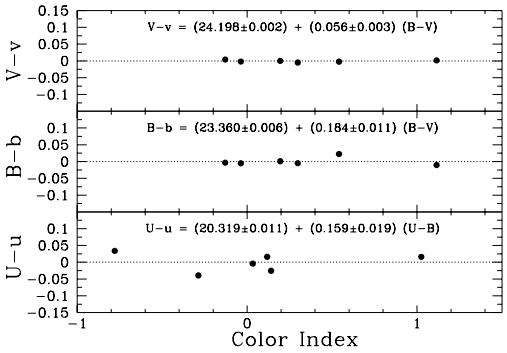

Fig. 2. Transformation equations and residuals. For V and B the colour index is (B-V), and for U is (U-B).

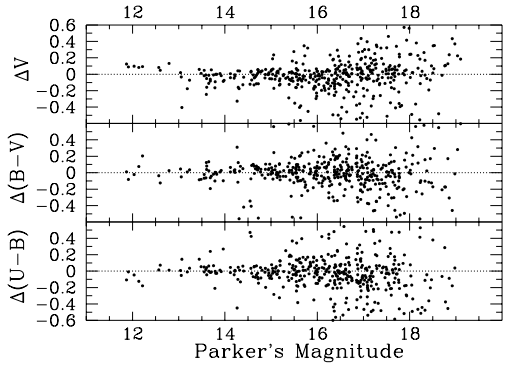

Fig. 3. Parker's magnitudes minus this paper's magnitudes as a function of Parker's magnitude.

2.3.1. Method of analysis

The profile fitting process is a variation of the one described by Stetson and Harris (1988). The first step in the process is star detection using `daofind`. This step was carried out three times for each frame. First with the standard parameters on the original image. Then, after the PSF has been determined and after a first run of *allstar*, *daofind* is ran on the subtracted image with the original convolving core but a somewhat larger value of the threshold (second pass), and with twice the initial convolving core and the same threshold as the second pass (third pass). The three lists of stars thus created are appended and renumbered. We run `allstar` and re-determine the PSF again and do the final pass of `allstar` which produces the semi–final list of stars in each filter. In order to determine incompleteness corrections for the IMF it is crucial to have an automated repeatable process. For this reason, no stars were added to the list by searching the residual star–subtracted images by eye.

As a final step, the program `daogrow` was run on the PSF stars in order to determine the aperture correction for each frame required to bring all frames to a common reference aperture (Stetson 1990).

2.4. The catalogue

The final list of magnitudes and colours was produced using the programs `daomatch` and `daomaster` (Stetson 1993) which automatically match objects in a set of different frames finding the coordinate transformations between frames and produce a list with matching objects. Therefore, the final list contains only the stars detected in all three filters. It was decided not to pass this list through `allstar` again because a few real detections are removed when we match the different filters. The transformation equations are then applied to obtain the final standard magnitudes. Table 2, published electronically, contains the photometry for the 1469 stars with UBV magnitudes.

The profile fitting photometry gives us a goodness of fit parameter, χ, which is a measure of the average rms deviations to the PSF fit normalized to the expected errors. For a good fit $\chi = 1$. Daophot also gives a shape parameter, *sharpness*, which measures how well the PSF fits the object. For a perfect fit $sharpness = 0$; for an extended object (e.g. an extended nebulosity) *sharpness* > 0, and for a *narrower* object (e.g. a cosmic ray) *sharpness* < 0. Fig. 4 shows the values for the whole sample as a function of V magnitude, colours, and distance to the center of the cluster (r). Fig. 4e shows a large number of objects with large positive values of the sharpness parameter. The expected values for stellar objects lie within the solid lines drawn in this figure (Stetson & 0Harris 1988). All points lying above this envelope are extended. Restricting our sample to $r > 100$ pixels reduces the number of stars with poor photometry without introducing systematic selection effects. Using conditions on the *sharpness* parameter, however, is not as harmless. Fig. 4 shows that the average B-V value for objects with a $sharpness > 1$ is about 0.3 magnitudes redder than those with $sharpness \sim 0$. Notice also the dependence of the point spread function on the colour of the star: the reddest stars show negative *sharpness* values indicating narrower PSFs. We conclude that restricting our sample to $\chi < 2.0$ and $r > 100$ pixels is rather harmless in the sense of not introducing serious systematic effects. However, we should be warned against using the *sharpness* in order to extract photometric sub-samples.

2.4.1. Artificial stars experiments

In order to determine systematic errors in the photometry we have performed Monte Carlo simulations by *adding* stars with known magnitudes, colours, and positions to the frames and measuring the colours with which they are recovered and the fraction of stars missed by the process. The method of choice was proposed by Stetson and Harris (1988). Several discussions and variations of the method can be found in the literature (Mateo 1988; Drukier et al. 1988; Vallenari et al. 1992; Mateo 1993; Vallenari and Ortolani 1993).

A series of 15 Monte Carlo experiments were performed for each frame. Each experiment consisted in adding 100 stars randomly distributed in the frames, with magnitudes in the range $11 <$ V < 20, $-1 <$ (B-V) < 2, and $-2 <$ (U-B) < 1. The stars were produced with a custom made program that cre-

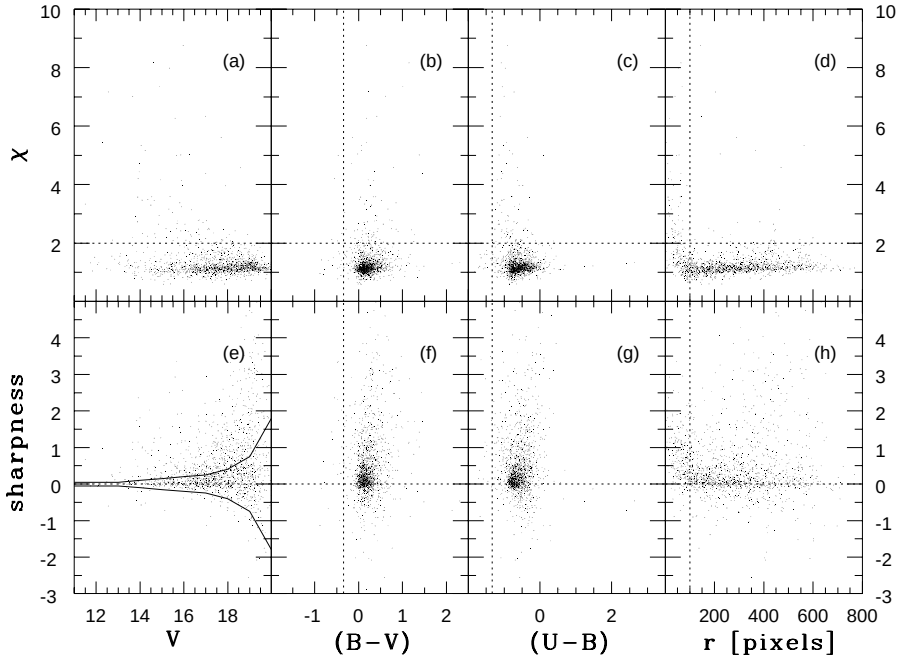

Fig. 4a–h χ and *sharpness* vs V, colours, and distance to the cluster center, r, for the whole sample. The vertical dotted lines show the colours of an O3 star and the minimum radius for which our photometry is reliable. The solid lines in panel **e** encompass the acceptable range of sharpness values for stellar objects.

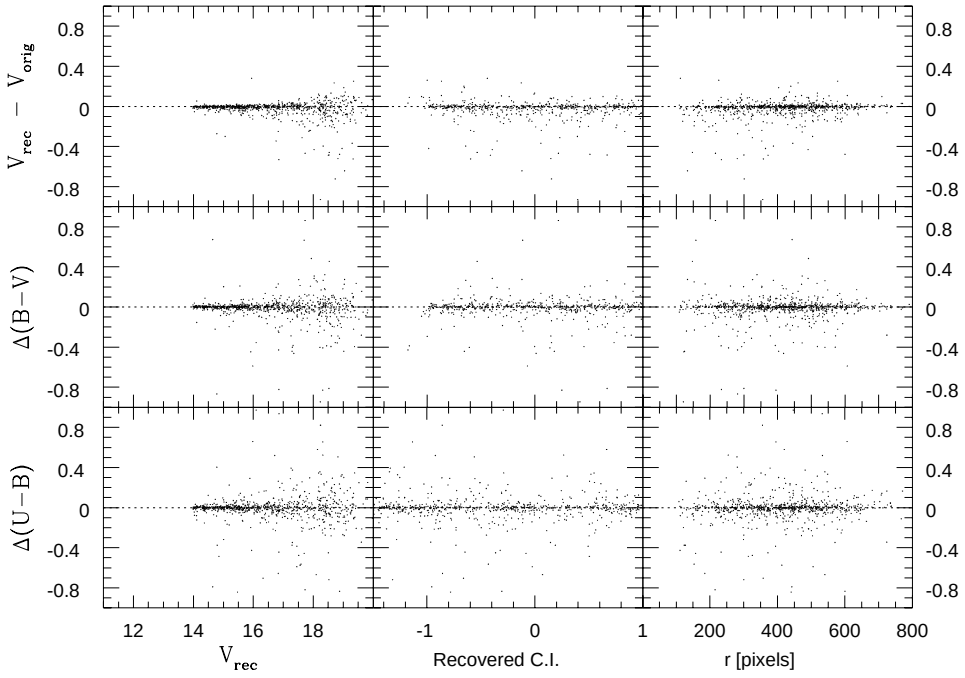

Fig. 5. Differences in magnitudes determined with Daophot II for the artificial stars. The ordinates show recovered minus original values, plotted against the recovered V magnitude, the recovered colour indexes, and the distance from the cluster center in pixels, r.

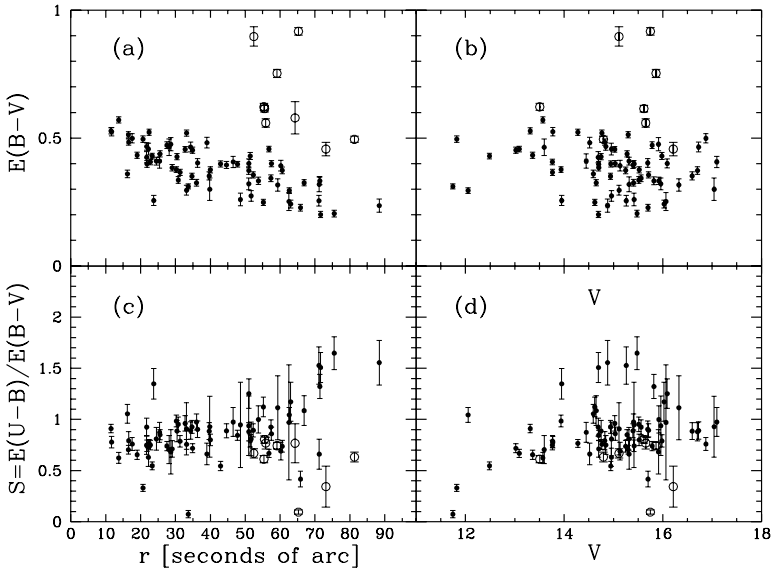

Fig. 6a–d. Reddening as a function of distance to R136 (**a**, **c**) and as a function of apparent magnitude (**b**, **d**) for stars with known spectral types. The stars with large reddening variance have been identified with open circles. Only stars with accurate photometry ($\chi < 2.0$) have been included in these plots.

ated a single large list of positions, magnitudes, and colours, which was later stored in 15×3 files for input to Daophot II's ADDSTAR routine. The simulation calculated the instrumental colours using the transformations given in Fig. 2. The frames were then processed in the standard way, and the resulting list matched with the input lists using `daomaster`. The resulting instrumental colours were converted back to standard colours with the same transformations.

The results of these experiments are shown in Fig. 5. There is no evidence of major systematic trends in the difference of the recovered and original magnitudes and colours, but there is a population of bright outliers, stars that are recovered with brighter magnitudes as a result of crowding (Stetson and Harris 1988). This trend cancels out when we use colours, even for (B-V) despite the large seeing difference between the B and V frames. From these experiments we find the overall completeness limit, defined as the magnitude at which the probability of detection in all three filters equals 50%, to be $\mathrm{V} = 19.2$.

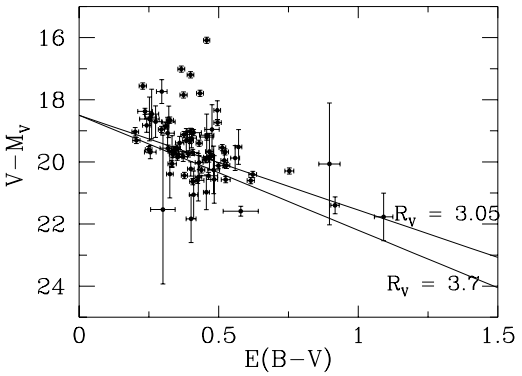

Fig. 7. Determination of total–to–selective extinction $\mathrm{R}_V = \mathrm{A}_V/\mathrm{E(B\text{-}V)}$ using stars with spectral types for which $\chi < 2.0$. The distance modulus has been fixed at $(m - M)_0 = 18.5$. The lines show $\mathrm{R}_V = 3.05$ and $\mathrm{R}_V = 3.7$. See text for details.

3. Results

The first step in the interpretation of the results is to correct the colours and magnitudes for interstellar reddening. For the LMC, and for 30 Doradus in particular, this is not a straightforward process for two reasons. First, the 30 Dor extinction law which has been shown to be quite different from the standard Galactic law in the far–UV, is somewhat dissimilar even in the near–UV (Fitzpatrick 1985). The latter variation is manifested as an anomalous value of the slope $\mathrm{S} = \mathrm{E(U-B)/E(B-V)}$. Second, most of the reddening to NGC2070 is internal to the nebula and varies from star to star (Melnick 1985; Parker & Garmany 1993; also seen in Figs. 6a and 12a, below). In order to apply the reddening corrections one needs, in addition to the slope, the ratio of total to selective absorption, $R_{\mathrm{V}} = \mathrm{A_V/E(B-V)}$. R_V was found by Melnick (1985) to be about the same as the standard galactic value $R_V = 3$, not surprisingly since most of the difference in the reddening law found by Fitzpatrick occurs in the near and far ultraviolet region of the spectrum.

To refine the determination of the critical reddening parameters, and to check whether they change from point to point within the nebula, we have carried out a programme of slit spectroscopy using the multi-object mode of EMMI at the NTT. The results of that research will be presented in a forthcoming paper (Bosch et al. 1998). For the present study we have selected the 85 stars in the frames that were not classified as either Wolf-Rayet or Of types.

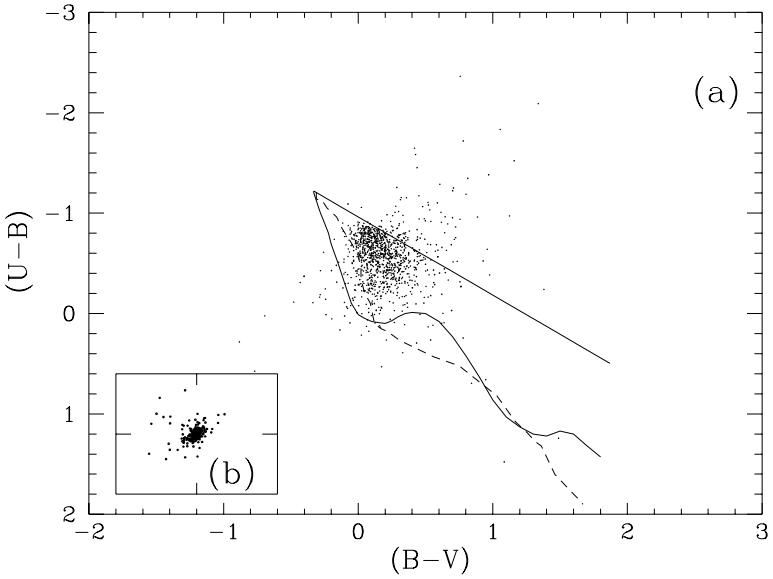

Fig. 8. a Colour-colour diagram for the stars in 30 Doradus with goodness of fit parameter $\chi < 2.0$, and distance to cluster center $r > 10''$. See text for details. **b** The difference in recovered and original (U-B) vs the same for (B-V), for the sample of 1000 artificial stars. The plotted range in the box is the same as for the larger graph.

Fig. 6a presents a plot of colour excess versus radial distance to the cluster center for the stars with spectroscopy. The intrinsic colours for these stars were determined using the spectral type to colour calibration of Schmidt-Kaler (1982), and the spectral types from (Bosch et al. 1998). We used the Kurucz (1993) model atmosphere atlas to check that the effective temperature to colour calibration does not change by more than 1% if we change the metallicity from Solar to LMC[3]. There is a clear trend showing that the average colour excess decreases outwards, from 0.55 mags at $r = 10''$ to half this value at $r = 70''$. This is the trend that we expect to see if the dust is well mixed with the stars. If the dust was distributed uniformly in a thick spherical shell we would observe a central plateau plus an increase of extinction outwards. Also evident in Fig. 6 is a region with a large variance in reddening, reaching values approaching E(B-V)=1 at radii between $50''$ and $70''$. Fig. 12a shows E(B-V) as a function of radius for the full *photometric* sample (with $\chi < 2.0$) where the increase in reddening towards the cluster center is also seen.

We conclude that the mean extinction increases towards the center of the cluster probably due to the presence of a smooth component of dust internal to the cluster itself, although the possibility that the reddening increase might be due to additional foreground extinction cannot be excluded since the amplitude of the effect seems marginally consistent with the distribution of line of sight reddening values towards the LMC (e.g. Harris et al. 1997). This would favor the idea that the 30 Doradus region lies behind the disk of the LMC as suggested by some authors (e.g. Vladilo et al. 1993, and references therein).

[3] We have used Z=0.008 for the stars in 30 Doradus (Kontizas et al. 1993). This corresponds to an scaled solar abundance of $[-0.4]$, which is then approximated with the $[-0.5]$ Kurucz's table.

Fig. 6c shows the run of S versus radius. Within $70''$ from the center there is no evidence of a radial variation of S. Notice that the values of S in the region of large E(B-V) variance are well behaved lending support to the reality of the observed variance. Further indication that the observed changes in E(B-V) are not due to photometric errors is provided by the artificial stars experiments, Fig. 5, where no systematic colour shift as a function of radius is observed. Finally, Figs. 6b and d show that S and E(B-V) do not change in any systematic way as a function of apparent magnitude. Therefore we use the 81 stars in this figure to determine a mean value of $\mathrm{S} = 0.82 \pm 0.03$. If we eliminate the 10 outliers in Fig. 6c–d we obtain $\mathrm{S} = 0.81 \pm 0.02$, but good arguments exist to eliminate only 5 of these stars because they are either crowded, lie in bad columns of the CCD, or are embedded in bright emission knots. We find no convincing reasons to exclude the remaining five stars. Therefore we retain the value of $\mathrm{S} = 0.82 \pm 0.03$ as our final determination. This is in good agreement with the values of 0.79 derived by Melnick (1985), 0.89 ± 0.08 found by Fitzpatrick (1985), and 0.86 ± 0.06 obtained by Koornneef (1982). It disagrees by 2σ from the value of 0.75 ± 0.03 quoted by Parker (1993). This marginal disagreement can be attributed to the different and larger area covered by Parker's study. Because Parker & Garmany (1993) just quote the value they derive, without giving any details on its determination, further comments are unwarranted.

Fig. 7 shows a plot of V-M_V vs E(B-V) for the stars with spectroscopy. We have used the tabulation of Schmidt-Kaler (1982) to assign absolute visual magnitudes (M_V) to spectral types and assumed a distance modulus to the LMC of $(m - M)_0 = 18.50$. The solid lines are for the values of $R_V \lesssim 3.7$ found by Fitzpatrick & Savage (1984) for the LMC, and the galactic mean value $R_V = 3.05$ (Martin & Whittet 1990). Given the considerable scatter in the data we will not attempt to fit a

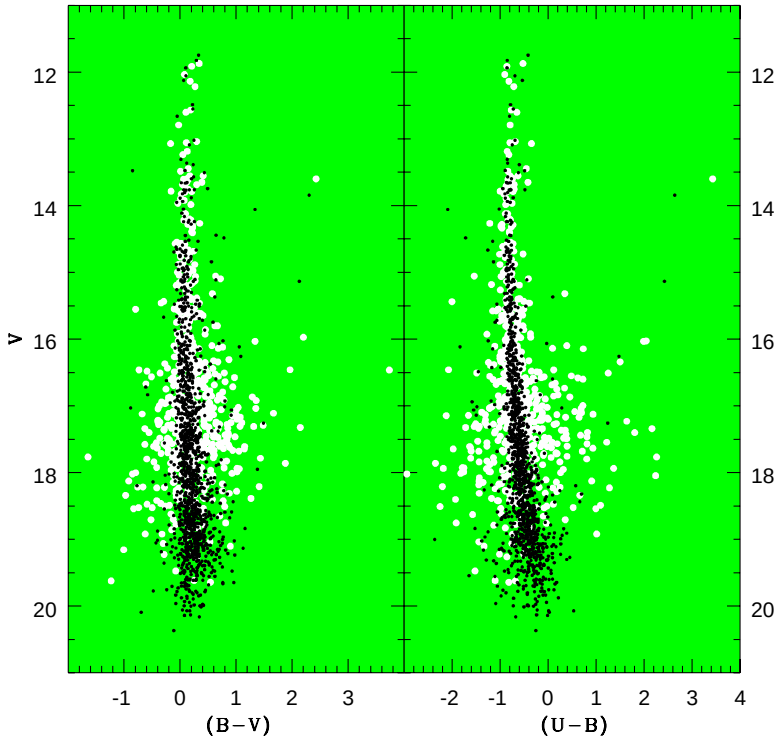

Fig. 9. Colour-magnitude diagrams for the stars at a distance $r > 10''$ from the cluster center (black dots). White dots are the data from Parker (1993) for the stars in the area covered by our photometry (same radial restriction). Notice the excellent overall agreement and the much larger random errors in Parker's data, due to the poor seeing of his frames. Notice also the presence of a few red stars.

value for R_V, but we will adopt $R_V = 3.05$ that seems to fit the data better.

Fig. 8a shows the UBV colour-colour diagram that obtains from our photometry. Also plotted are the loci for dwarfs and supergiants from Schmidt-Kaler (1982) and the reddening vector for an O3 star (S=0.82). As will be discussed below, this diagram looks deceptively simple as it hides a serious systematic effect induced by the random photometric errors.

Fig. 9 shows the colour–magnitude diagrams for the sample outside the core region where crowding is most critical. The restriction in radius ($r > 10''$) eliminates 152 out of the 1469 stars. Notice that even before applying reddening corrections our colour-magnitude diagrams show significantly less scatter than Parker's (1993) photometry. The good overall agreement should be stressed, indicating that there are no detectable systematic differences between the two photometries. Comparison with Fig. 1 shows that the reddest stars seen in these diagrams are real and not an artifact of photometric errors. We can also see from these diagrams that for $V > 16.0$ Parker's data show a much larger scatter, presumably due to the poor seeing of the observations his work is based upon. For $V < 16$ most of the scatter is probably due to the intrinsic variations in reddening.

3.1. The colour-magnitude stereogram

To help in visualizing the data we designed a new tool that we call the colour-magnitude *stereogram* (Figs. 10 and 11.) To "see" this diagram in three dimensions the reader should look at the diagram with the eyes focussed to infinity (i.e. parallel) so that each eye focus only in the diagram in front of it, the brain will do the rest! [4]

The stereogram plots the two colours at the base and the magnitude in the vertical axis. Also plotted is the locus for MS stars and the reddening vectors for main sequence O3, B1, and B5 stars. This diagram is useful because it permits the visualization of how well the stellar-theory/reddening-models fit the data. For perfect fits we expect to see the following: in the absence of reddening all main sequence stars should lie on the curve defined by the points [(B-V)$_0$, (U-B)$_0$, V_0] and parametrized by spectral type. Reddening complicates this picture by dis-

[4] These are parallel mode stereograms. Some people might find it easier to visualize the 3 dimensions if they use a crossed eyes mode. For this just photocopy the figures and cut and paste interchanging the left and right images. This will have the effect of making the 3D rendition appear smaller. Parallel mode requires the distance between the left and right image to be the same or smaller than the inter–pupil distance. In both cases the technique to visualize the three dimensions is the same: each eye sees both the left and right diagram, thus at some stage four images will be seen; one should strive then to make the two inner images merge by changing the angle between the eyes; once the images merge a final effort should be made to get the proper focus at which time the 3Ds will be visible. This last condition is probably the most difficult to achieve because the eyes adapt together their focus and the angle between them in a natural relation, and for 3D visualization this natural relation does not work.

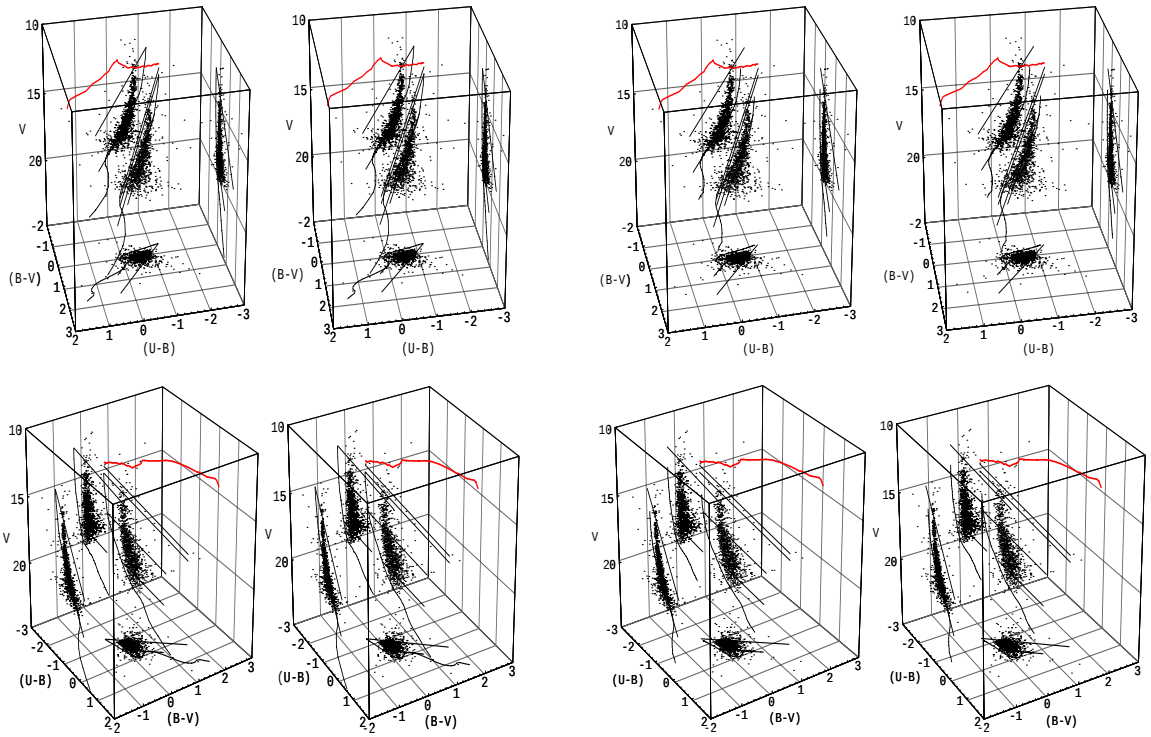

Fig. 10. Stereogram of the (B-V)–(U-B)–V space showing the locus for all the stars measured in this work. The locus for unreddened main sequence and supergiant stars taken from Schmidt-Kaler (1982) is also shown for reference. The reddening vectors for an O3f, O3, B0, and B6 stars are shown (only O3 and B6 in the projections). The diagram assumes a distance modulus of 18.50, $R_V = 3.05$, and $S = 0.82$. To see the three dimensions the reader should look at the diagram with his eyes parallel so that each eye focus only in the diagram in front of it, his brain will do the rest!

Fig. 11. Same as Fig. 10 but using the ZAMS of Mermilliod (1981). The viewpoints are the same as before. Notice the better fit for the bottom of the diagram.

placing the stars along a spatial straight line whose projection on the [(B-V)–(U-B)] plane is the classical reddening line of slope S. The projection on the [(B-V)–V] plane is a straight line with slope R_V, and the projection on the [(U-B)–V] plane is a straight line of slope R_V/S (we use the convention that the line $y = ax$ has slope a in the [x–y] plane). If the stars were behind a screen of constant reddening, the whole curve would shift along the 3D reddening vector defined by the slopes above. In the more realistic case of variable reddening we find stars at various positions along the reddening vector, and the set of stars of different spectral classes traces the *theoretical surface* in the three dimensional colour–colour–magnitude diagram.

Fig. 10 shows the stereogram for our data together with the ZAMS of Schmidt-Kaler (1982). The perspective for the upper stereogram was designed to show that the theoretical curve, when displaced along the reddening vector, does indeed go through the middle of the cloud of points as it should if the ZAMS is appropriate and there are no systematic errors. The second perspective was chosen to show better the displacement along the reddening lines by adopting a view at almost right angles to the line of slope S in the [(B-V)–(U-B)] plane. With this perspective we can see better the broadening due to the variable extinction in the cluster. Fig. 11 shows the same data but plotted with the ZAMS of Mermilliod (1981). Because the theoretical surface now *cuts* the cloud of points more symmetrically this curve appears to model the data better than the Schmidt-Kaler one. This is particularly noticeable near the bottom of the observed MS (spectral classes around B6).

The stereograms also show three effects perhaps related to mass segregation. The first is an increase of the mean reddening for brighter stars visible in the bottom stereograms as an increase in the distance between the ZAMS and the centroid of the cloud of points. The second effect, also appreciated in the bottom stereograms, is a widening of the gap between the ZAMS and the cloud of points, showing that there are fewer bright stars with smaller reddenings than fainter ones (although it should be mentioned that the increased photometric errors for the fainter stars also contribute to this effect). The third (less pronounced) effect is a narrowing of the range of reddenings as we go from fainter to brighter stars, an effect already visible in the spectroscopic data (Fig. 6b). That these effects might be a consequence of mass segregation in a dusty cluster can be seen in Fig. 12b, which plots absolute magnitude versus distance to

the cluster center for stars with $\chi < 2.0$. The big dots show the median distance for the stars in each rectangular bin. There is a sloping upper envelope in this graph showing that brighter stars populate a narrower range of radii than fainter ones. The problem of mass segregation in 30 Doradus, however, is beyond the scope of this paper and will be explored in detail in the next two papers of this series (Bosch et al. 1998; Selman et al. 1998).

4. Discussion

4.1. The reddening associated with NGC2070

Brandl et al. (1996) claim that there is a $3''$–diameter extinction *hole* in the core of the cluster. This is only possible in the unlikely case that the distribution of matter itself has a small hole right in our line of sight to R136, since a hollow cavity carved by winds would result in a flat reddening distribution near the center. These authors also claim that the stars surrounding the core "... show correlated, *enhanced* extinction", result that can be interpreted to be similar to what we have found. Brandl et al. use a complex procedure to analyze and interpret their IR adaptive optics observations, but they do not provide enough details in their paper for us to be able to understand the systematics. In particular, they use the two-channel PLUCY deconvolution package (Lucy 1994; Hook and Lucy 1994) for their photometry which may introduce systematic effects correlated with distance to the center, but they did not perform artificial star experiments to quantify this effect. Therefore, we consider their results to be consistent with the increase of reddening towards R136 we find, but we think that their extinction hole for $r < 3''$ is an artifact of their data reduction techniques, although our own data does not allow a direct check of this conjecture.

Hill et al. (1993) also claim that the average extinction decreases closer to the center of the cluster, but their data refers to a much wider area and are not relevant for the center of NGC2070 which is beyond the resolving power of the UIT with its $> 2.5''$ FWHM spatial resolution.

De Marchi et al. (1993) present observations of the central $20''$ of R136 taken using the FOC with the aberrated HST through filters F130M and F346M. They adopted a Milky Way foreground reddening of 0.07 mag, an LMC foreground reddening of 0.16 mag, and a 30 Doradus *constant* reddening of 0.18 mag adding to a total reddening E(B-V)=0.41 magnitudes for the region. They detect a larger dispersion in the UV colour–magnitude diagram than expected and correctly attribute this to variable extinction. They also appear to detect a trend of larger extinction towards the center ($r < 0.3''$), but they dismiss this effect because it would imply E(B-V) values of 0.73 and 0.65 for R136a$_1$ and R136a$_2$ which translate to $(\mathrm{B-V})_0 = -0.59$ and $(\mathrm{B-V})_0 = -0.51$ for these stars, which they considered unphysical. They therefore assume the colour differences to be due to evolutionary effects. The problem with this argument is that their estimates of E(B-V) come from the azimuthally averaged light profiles and thus correspond to an average reddening as a function of distance to the cluster center. Since the reddening has a large intrinsic scatter, the "unphysical" colours of R136a$_1$ and R136a$_2$ can be attributed to reddening fluctuations.

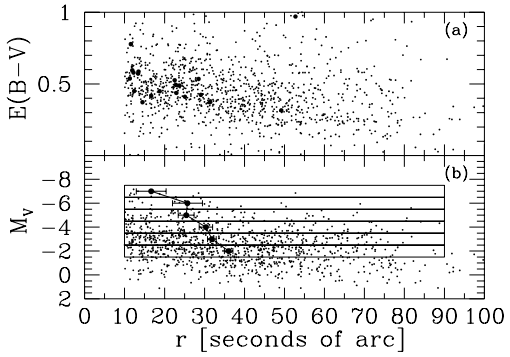

Fig. 12. **a** Colour excess, E(B-V), as a function of radius for the photometric sample of main sequence stars with $\chi < 2.0$. The intrinsic colours for all the stars were computed *photometrically* according to the standard prescription outlined in the text. The big dots mark stars with absolute magnitudes greater that -6.0. **b** Absolute magnitude versus distance to the cluster center for the same sample. The big dots mark the median distances to the cluster center for the stars in the appropriate bins.

Using data from WFPC2, Hunter et al. (1997a) find a value of E(B-V)$\lesssim 0.5$ for the inner $34''$ of the cluster. They find that the width of the MS in the F170W–(F170W−F555W) colour magnitude diagram is larger than can be accounted for by photometric errors and also conclude that most of the spread is due to variations in reddening. They find the bright stars in their outer sample ($r > 3''$) to extend further to the blue in the colour magnitude diagram than those within $r < 3''$ (the inner sample), and that inner bright stars are redder than fainter inner and outer stars. They interpret these observations as due to a combination of a larger range in reddening for $r > 3''$ with mild evolution for the inner stars (although mild evolution has an almost negligible colour effect, as can be appreciated in their Fig. 4). Our observations suggest that the reason for the colour difference between their inner and outer bright samples is the smooth increase in extinction towards the center of the cluster.

We conclude that all previous observations are consistent with our finding of a smooth dust component in NGC 2070, although the existence of this component is somewhat puzzling as it indicates the presence of dust close to the core of the cluster (about 30 to 60 $M_\odot$ within $15\,pc$). In principle we would expect dust in the central regions of the cluster to be destroyed by the strong UV radiation field, or swept away by the winds from the massive stars. Therefore, dust must be replenished in this region at least at the same rate as it is being destroyed. A possible mechanism for this replenishment is dust formation in colliding winds (Usov 1991; Beck & Sedlmayr 1998).

4.2. Application of the colour–magnitude stereogram: a systematic flattening of the IMF

The standard process of determining the IMF for massive stars from UBV photometry is as follows: by measuring the apparent magnitude and colours each star is placed on reddening lines in

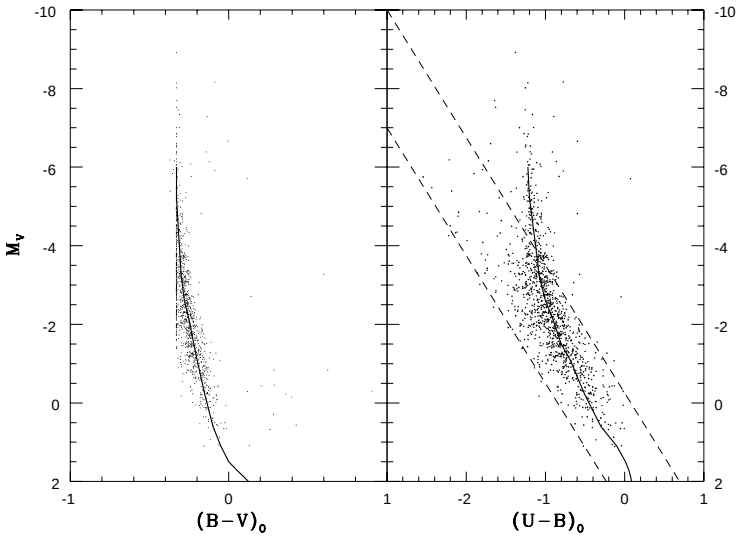

Fig. 13. Derredened colour-magnitude diagrams for the subsample with $\chi < 2.0$, and $r > 10''$. The solid line represents the Schmidt-Kaler (1982) ZAMS. The two diagonal dashed lines in the $(U\text{-}B)_0$ diagram mark the position of the *hot plume* discussed in the text.

the colour-colour diagram. By displacing each star along these lines to the theoretical ZAMS, the intrinsic colours, and with them, the colour excess and absolute magnitude (assuming a known distance modulus) are obtained. The intrinsic colours translate into effective temperatures and bolometric corrections. Each star is then placed in mass bins using theoretical evolutionary tracks (e.g. Schaerer et al. 1993), and the IMF is determined by counting stars in different mass bins.

There are many practical problems when actually carrying out this program (see Melnick 1992), but there is a particularly insidious one that becomes evident looking at the colour–magnitude stereogram. Because of random measurement errors, the colours have an uncertainty that increases for fainter stars. By displacing faint stars to the ZAMS we will determine intrinsic colours that are either too blue or too red, depending on whether we are above or below the *theoretical surface*. Thus, every mass bin will have contributions from stars of both lower and higher masses. But two additional ingredients contrive to corrupt the IMF: first, because the IMF is a decreasing function of mass, more stars migrate from lower mass bins up than from higher mass bins down. Second, because the errors in the colours for lower mass stars are larger, the lower mass stars can *migrate* a larger distance in mass. This is evident in the upper stereograms of Figs. 10-11 where we can appreciate that stars of all apparent magnitudes end up at the location of an O3 star in the ZAMS. These effects were discussed by Mateo (1988), who refers to Butcher (1977), but none of these authors apply any correction. These effects are also apparent in the derredened colour–magnitude diagram in Fig. 13 as a *stream* of stars that seem to *shoot* to the upper left hand corner of the diagram. These are the stars that produce the *hot plume* of the HR diagram found by other authors (e.g Parker & Garmany 1993 and references therein).

The two ingredients discussed above distort the IMF in the same way making it *shallower*. We can correct this effect by designing a method to determine the most likely spot on the *theoretical surface* where a given star should be located given its magnitude and colours. One obvious possibility is to *move* the star to the closest spot on the surface before we derreden it. This method will be developed and applied in Selman et al. (1998).

5. Conclusions

Using a combination of CCD photometry taken with the NTT under excellent seeing conditions together with a new improved catalogue of spectral classifications we have investigated the properties of the central cluster of the 30 Doradus nebula. The main conclusions of this work are the following;

1. The mean slope of the reddening law in the UBV system is S$= 0.82 \pm 0.03$ consistent within the errors with previous determinations. We find S to be almost constant for distances between $10''$ and $70''$ from the cluster center. This does not mean that the same extinction law applies in the core of the cluster (R136) where, due to the strong UV radiation field, the properties of the dust may differ from the rest of the cluster.

2. The ratio of total to selective extinction is found to be constant and close to the normal value. Again, this result only applies to distances larger than $10''$ from the core of the cluster.

3. The extinction varies widely within the cluster. It is apparent from the three colour image of the cluster that the reddening is associated with the clumpy structure of the dust. What it is not apparent from this image is the existence of a moderate, smooth component, most likely associated with NGC2070, that decreases from the center outwards.

4. In order to study how well the combined extinction and stellar theory models the 30 Doradus cluster we have introduced a new tool, the *colour-magnitude stereogram*, which is a pseudo 3D rendition of the position of the stars in the (B-V), (U-B),

V space. Using this tool we find that systematic and/or modeling errors are below the random measurement errors. We have shown that random measurement errors combined with a luminosity function which increases for lower luminosities lead to a systematic underestimation of the IMF slope. This effect needs to be quantified before using the data to determine the IMF of the cluster and, in particular, the change of IMF with radius, if any.

Acknowledgements. The authors would like to thank S. Bennetti for obtaining the UBV frames on which part of this research was based. We would also like to thank Peter Stetson for making his programs **daophot ii**, **daomatch**, and **daomaster** available to us, and an anonymous referee for many valuable suggestions.

References

Beck H., Sedlmayr E., 1998, in: *The Molecular Astrophysics of Stars and Galaxies* ed. by T.W. Hartquist & D.A. Williams, Oxford: OUP, p.5
Bosch G., Terlevich R., Melnick J., Selman F.J., 1998, in preparation
Brandl B., Bertoldi F., Sams B.J., Eckart A., Genzel R., 1996, in: *Starburst Activity in Galaxies*, ed. J. Franco, R. Terlevich, and A. Serrano, Revista Mexicana de Astronomía, Serie de Conferencias, Vol. 6, p.126
Butcher H., 1997, ApJ 216, 372
Davis L.E., 1994, A Reference Guide to the IRAF/DAOPHOT Package, NOAO
De Marchi G., Nota A., Leitherer C., Ragazzoni R., Barbieri C., 1993, ApJ 419, 658
Drukier G.A., Fahlman G.G., Richer H.B., VandenBerg D.A., 1988, AJ 95, 1415
Elmegreen B.G., 1997, ApJ 486, 944
Feast M.W., Walker A.R., 1987, ARA&A 25, 345
Fitzpatrick E.L., 1985, ApJ 299, 219
Fitzpatrick E.L., Savage B.D., 1984, ApJ 279, 578
Gutierrez–Moreno A., Moreno H., Stock J., Torres C., Wroblewski H., 1966, Pub. Observatorio Astronómico Nacional No 1, Santiago de Chile.
Harris J., Zaritsky D., Thompson I., 1997, AJ 114, 1933
Hill J.K., Bohlin R.C., Cheng K., Fanelli M.N., Hintzen P., et al., 1993, ApJ 413, 604
Hook R.N., Lucy L.B. 1994, in: *The Restoration of HST Images and Spectra II*, ed. R. J. Hanish and R.L. White (Baltimore: STScI), 86
Hunter D.A., Shaya E.J., Holtzman J.A., Light R.M., O'Neil E.J., Lynds R., 1995, ApJ 448, 179
Hunter D.A., O'Neil E.J., Lynds R., Shaya E.J., Groth E.J., Holtzman J.A., 1996, ApJ 459, L27
Hunter D.A., Vacca W.D., Massey P., Lynds R., O'Neil E.J., 1997a, AJ 113, 1691
Hunter D.A., Light R.M., Holtzman J.A., Lynds R., O'Neil E.J., Grillmair C.J., 1997b, ApJ 478, 124
Kontizas M., Kontizas E., Michalitsianos A.G., 1993, A&A 269, 107
Koorneef J., 1982, A&A 107, 247
Kurucz R.L., 1993, ATLAS9 Stellar Atmospheres Programs and 2km/s Grid, CDROM13.COLORS, August 22, 1993, SAO
Landolt A., 1992, AJ 104, 340
Lucy L.B., 1994, in: *The Restoration of HST Images and Spectra II*, ed. R. J. Hanish and R.L. White (Baltimore: STScI), 79
Malumuth E., Heap S. 1994, AJ 107, 1054
Martin P.G., Whittet D.C.B., 1990, ApJ 357, 113
Massey Ph., Davis L.E., 1992, *A User's Guide to Stellar CCD Photometry with IRAF*, NOAO.
Massey Ph., Hunter D., 1998, ApJ 493, 180
Mateo M., 1988, ApJ 331, 261
Mateo M., 1993, in: *The Globular Cluster–Galaxy Connection*, eds. G. H. Smith, J. P. Brodie, Eleventh Santa Cruz Workshop, ASP Conference Series, Vol. 48, San Francisco: ASP, p.387
Melnick J., 1985, A&A 153, 235
Melnick J., 1992, in: *Star Formation in Stellar Systems*, eds. G. Tenorio–Tagle, M. Prieto, F. Sánchez, (Cambridge: CUP), p.253
Melnick J., Moles M., Terlevich R., Garcia-Pelayo J.M., 1987, MNRAS 226, 849.
Melnick J., Terlevich R., Moles M., 1988, MNRAS 235, 313.
Mermilliod J.C. 1981, A&A 97, 235
Moffat A.F.J., Vogt N., 1977, PASP 89, 323
Parker J.Wm., 1993, AJ 106, 360
Parker J.Wm., Garmany C.D., 1993, AJ 106, 1471
Scalo J., 1998, in: *The Stellar Initial Mass Function*, eds. G. Gilmore, D. Howie, 38th Herstmonceux Conference, ASP Conference Series, Vol. 142, San Francisco: ASP, p.201
Schaerer D., Meynet G., Maeder A., Schaller G., 1993, A&AS 98, 523
Schmidt-Kaler Th., 1982, in: *Stars and Star Clusters*, Volume 2b, ed. K. Schaifers & H. H. Voigt, part of the Landolt-Börstein series on Numerical Data & Functional Relationships in Science and Technology, chief ed. K.-H. Hellwege, Springer-Verlag, Berlin–Heidelberg, p1
Selman F.J., Melnick J., Bosch G., Terlevich R., 1998, in preparation
Steidel C.C., Adelberger K.L., Dickinson M., Giavalisco M., Pettini M., Kellog M., 1998, ApJ 492, 428
Stetson P.B., 1987, PASP 99, 191
Stetson P.B., 1990, PASP 102, 932
Stetson P.B., 1991, in: *3rd ESO/ST-ECF Data Analysis Software*, eds P. J. Grosbøl, R. H. Warmels, ESO Conference Proceedings No 38, p. 187
Stetson P.B., 1992, J. Roy. Astron. Soc. Can., Vol. 86, No. 2, p. 71
Stetson P.B., 1993, in: *IAU Colloquium No. 136, Stellar Photometry – Current Techniques and Future Developments*, eds. C. J. Butler, I. Elliot, p.291
Stetson P.B., 1997, The DAOPHOT II Users's Manual
Stetson P.B., Harris, W.E., 1988, AJ 96, 909
Terlevich E., Terlevich R., 1998, in: *Proceedings of the La Plata conference: Hot Stars in Open Clusters*, to be published by Rev. Mex. Astron. Astrofis.
Usov V.V., 1991, MNRAS 252, 49
Vallenari A., Ortolani S., 1993, in: *5th ESO/ST-ECF Data Analysis Workshop*, eds. P. J. Grosbøl, R. C. E. Ruijsscher, ESO Conference Proceedings No 47, p. 125
Vallenari A., Chiosi C., Bertelli G., Meylan G., Ortolani S., 1992, AJ 104, 1100
Vladilo G., Molaro P., Monai S., D'Odorico S., Ferlet R., Vidal–Madjar A., Dennefeld M., 1993, A&A 274, 37

Paper II

The ionizing cluster of 30 Doradus II. Spectral classification for 175 stars

A&AS 137, 21 (1999)

G. Bosch, R. Terlevich, J. Melnick, and F. Selman

.

ASTRONOMY & ASTROPHYSICS
SUPPLEMENT SERIES
Astron. Astrophys. Suppl. Ser. **137**, 21–41 (1999)

MAY II **1999**, PAGE 21

The ionising cluster of 30 Doradus⋆

II. Spectral classification for 175 stars

G. Bosch[1,⋆⋆], **R. Terlevich**[1,⋆⋆⋆], **J. Melnick**[2], **and F. Selman**[2]

[1] Institute of Astronomy, Madingley Road, Cambridge CB3 0HA, UK
[2] European Southern Observatory, Alonso de Córdova 3107, Santiago, Chile

Received September 16, 1998; accepted February 5, 1999

Abstract. We present spectral types for 175 stars in the ionising cluster of 30 Doradus derived from multislit observations of 231 stars. Comparison with published classifications for 70 stars in common with other authors reveals excellent agreement with the exception of a few cases which are discussed in detail. Our new observations raise to 261 the total number of stars in 30 Dor with known spectral types, outside R136. We analyse the spatial distribution of these stars according to their spectral types, and find evidence for mass segregation.

Key words: stars: Hertzsprung Russell (HR) diagram — stars: luminosity function, mass function — stars: early-type — ISM: dust, extinction — galaxy: open clusters and associations: general — galaxies: Magellanic Clouds

1. Introduction

Starbursts play an important role in the formation and evolution of galaxies (Ellis 1997), and the IMF is the key parameter in starburst models (Stasinska & Leitherer 1996; Elmegreen 1997). One of the few starburst clusters that can be studied in detail (either from the ground or space) is the central cluster of the 30 Doradus giant HII region, which, in fact, has been called the *Rosetta Stone* for young stellar evolution by Walborn (1991).

This paper is the second of a series devoted to the determination of the IMF of the ionising cluster of 30 Doradus. This a-priory simple task is made extremely complex by a number of factors including stellar crowding, strong and variable internal extinction within the cluster, overlapping of stellar ages, and degeneracy of the relation between mass and photometric indices for the most massive stars.

In Paper I of this series (Selman et al. 1999) we combined accurate UBV photometry with spectral classifications in order to determine the extinction law of the dust, and map the distribution of reddening within the cluster. We also introduced a new technique to compare photometry with models in clusters with strong and variable internal extinction.

In this paper (Paper II of the series) we present spectral types for 175 stars in 30 Dor, of which 105 have not been published, obtained with the NTT multi-slit spectrograph. These types were used in Paper I for the study of the extinction law, and will be used in the study of the IMF in Paper III of the series (in preparation). Spectroscopy is critical for the study of the high-mass end of the IMF because it is impossible to determine masses for earliest O-type stars using only photometry (Massey 1985; Massey 1998). In addition to spectral types, the spectroscopy has also been used to determine the radial velocities of the stars. These data will be used in Paper IV of this series (in preparation) to investigate in depth the intriguing possibility of mass segregation in this extremely young cluster which was briefly discussed in Paper I, and which is also discussed in the present paper.

Section 2 describes the spectroscopic observations, Sect. 3 outlines the procedures followed for extracting the spectra, and Sect. 4 shows and discusses the spectral classification itself. The spatial distribution analysis of stars according to their spectral types is presented in Sect. 5.

Send offprint requests to: gbosch@ast.cam.ac.uk
⋆ Based on observations collected at the European Southern Observatory.
⋆⋆ On leave from Facultad de Ciencias Astronómicas y Geofísica, La Plata, Argentina.
⋆⋆⋆ Visiting Professor at I.N.A.O.E., Puebla, Mexico.

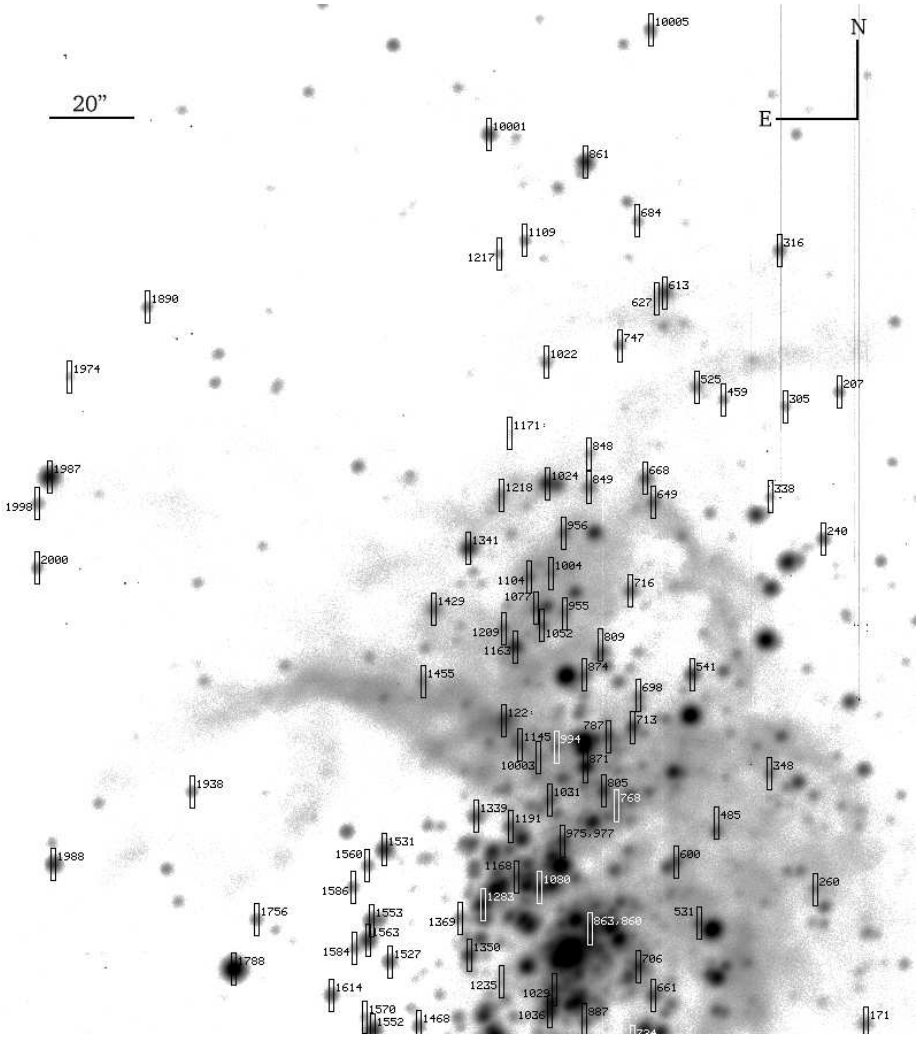

Fig. 1. Finding chart for observed stars north of R136. Stars observed are enclosed by the slit position, drawn to scale. Numbers correspond to the ones listed in Tables 1 and 2. North is to the top, East to the left

2. Observations

The observations were carried out in January 1995, at the ESO 3.5 m NTT using EMMI in its multi-object spectroscopy mode. Grism #5 was employed yielding a dispersion of 1.3 Å/pix on a Tektronix $2048 \times 2048 - 24\,\mu$ pixel CCD detector.

A total of seven starplates were produced using the punching machine mounted inside EMMI from a direct image of the region previously obtained. This provides an excellent accuracy in the slit positions without need for accurate astrometry prior to mask construction. Each starplate contained an average of 30 slitlets thus producing more than 200 spectra in total. The slitlets were 1.1″ wide and 8″ long.

The stars included in each starplate were chosen from the direct images in groups of similar brightness and minimum overlapping. Thus, the number of stars and the exposure times differ from plate to plate. Figures 1 and 2 show

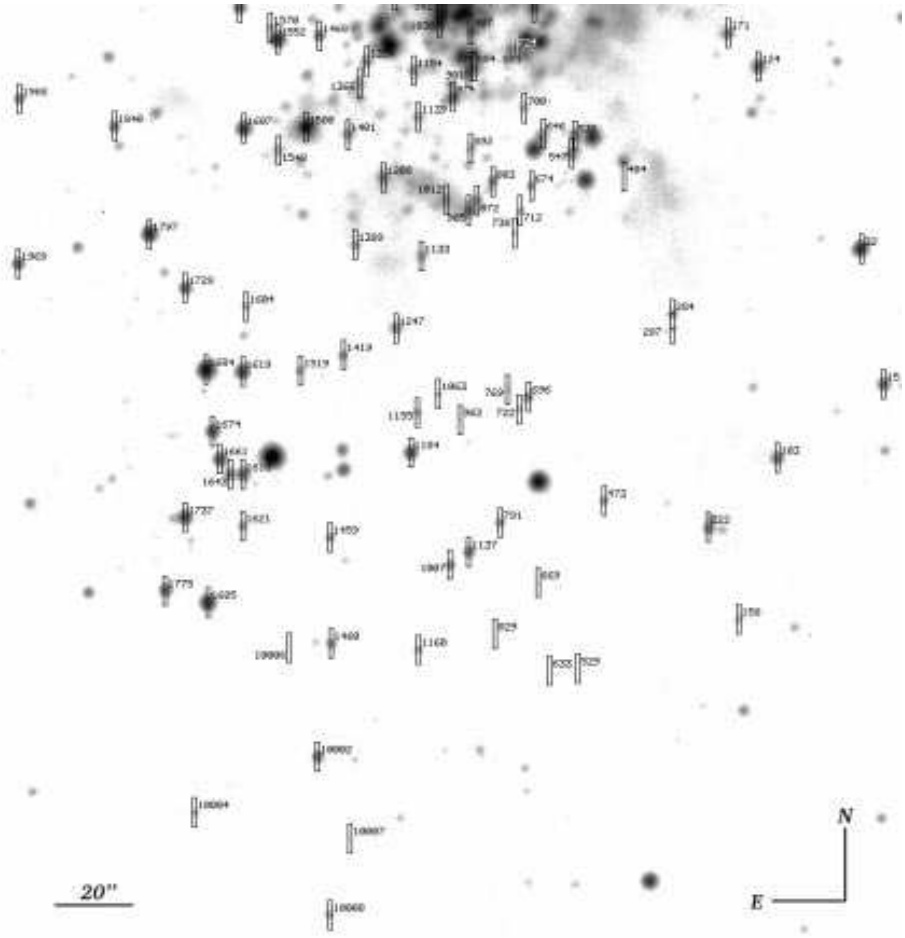

Fig. 2. Same as Fig. 1, for the region south of R136

the slit positions together with the identification numbers from Parker (1993).

He-Ar lamp exposures were taken for wavelength calibration, and halogen lamp exposures were obtained for flat-fielding the images.

3. Reductions

The spectra were reduced using a modified version of the MULTIRED package, which runs within IRAF[1], using the following procedure: (i) for each starplate the location and dimensions of each slit spectrum are determined; (ii) using these parameters, subsections of the image are trimmed to produce individual 2D spectra corresponding to each slitlet; (iii) identical trimming sections are applied to the corresponding bias, flat-field, and wavelength calibration frames; (iv) the bias and flat-field corrections are pipelined in the standard way for the whole set of stellar and arc spectra. This produced 231 individual slit spectra averaging 25 × 1700 pixels each.

3.1. Wavelength calibration

Wavelength calibration was performed on the 2-D images. This is essential in order to correct for possible distortions along the slit, which can prevent a proper nebular background subtraction. He-Ar lines were identified in

[1] IRAF is distributed by the National Optical Astronomy Observatories, operated by the Association of Universities for Research in Astronomy, Inc., under cooperative agreement with the National Science Foundation.

Table 1. Spectral types of the observed stars

Parker id.	$V_{\rm mag}$	Spectral type	Literature Sp. T	Parker id.	$V_{\rm mag}$	Spectral type	Literature Sp. T
15	15.33⋆	O8.5 V	O9: V [2]	863	13.67	O6.5 V	O3 V [4]
32	14.15⋆	O9 IV	O8.5 V [2]	871	13.31	O4 V((f*))	O3 V: [1,3]
103	15.56⋆	B0 V		872	15.98⋆	O8 V	
122	14.72⋆	O5-8 V (b)		874	15.70	B2 V	
124	14.96⋆	O8.5 V	O8-9 III [3]	880	12.66	WN5.5	WN4.5 [1]
158	16.80⋆	B0.2: III		884	15.28	O6 V	
171	15.82	O8 V	O6-8 Vz [3]	885	14.28	O5 III	
207	15.88⋆	B1 V		887	15.30	O8 V	
222	15.72⋆	O9.5-B0 V		892	17.09	B0.5 V	
240	15.48⋆	O9 V		901	15.11	O3 V((f*))	
260	16.32	B0.5: V		905	15.34⋆	O9-B0 V	O9-B0 V [3]
284	16.02⋆	B0.5 III-V		955	15.94⋆	O9: V	
287	16.61⋆	B2 V		956	15.58⋆	B1-2 V	O9-B0 III [3]
305	16.41⋆	B0-B0.5 V		962	17.17⋆	B0.5-1.5 V	
316	15.49⋆	O6.5 V		974	14.76	O5-6 III	O3-6 V [3]
338	16.61⋆	B0.5-1.5 V		975	14.48	O6-7 V((f))	
348	16.03	B0.2-0.5 V		977	15.31	O6: V	
404	15.75	O4-5 IV-V		994	15.42	B0: V	
459	15.61⋆	G V		1004	16.21⋆	B1-2 III-V	
473	16.10⋆	O5-6 V		1007	15.28⋆	G V	
485	15.39	O8-9 V	O7-9 V [3]	1012	16.14⋆	O8-9 V	O7-8 III [3]
525	16.24⋆	B0-1: I		1013	14.47	O4 V	O8: V [3]
529	17.58⋆	G V		1022	15.93⋆	O5: V	
531	15.51	O8 V		1024	13.99⋆	O9-B0 V (b)	O9:n [3], O [1]
538	15.11	B0.2 III-I	B0-1 III [3]	1029	13.40	WN 4.5-7 + abs	O3If*/WN6-A [3,4]
541	14.69	O7.5 V	O7-8 III [3]	1031	15.41	B0 V	
547	15.65	O6 V	O8-9 V [3]	1036	13.82	O3-4 V((f*)):	O4-5 V: [3], O3III(f*)
574	16.60⋆	G8 III		1052	15.30⋆	B0.2 V	O8-9 III [3]
600	15.03	O3-5 V	O3-6 V [3]	1063	16.45⋆	O6-7 V	
613	15.08⋆	O8.5 V (b)		1077	15.25⋆	O7.5: V	
627	17.14⋆	B0.2 V		1080	13.88	O3-4 V((f))	O3-4 V((f*)) [2] O3 V((f))
633	17.39⋆	G0: V		1104	15.47⋆	B0: V	O7-9 V [3]
646	15.37	Gtype		1109	15.87⋆	O9 V	
649	15.34⋆	O8-9 V		1133	16.49⋆	B0: V:	
661	14.84	O5: V	O3-6 V [3]	1137	18.52⋆	O8-9 II(f)	
668	15.31⋆	B0.2 V	B0 III [3]	1139	16.59	B0 V	
669	17.05⋆	O9: V		1145	15.40⋆	O8 III-II	
674	15.86	O7.5 V		1154	15.91	B0: V	
684	16.38⋆	B0: I		1155	16.28⋆	B0.2 III	
696	15.54⋆	O9 V	O9.7 Ib [3]	1160	16.30⋆	B1: III:	
698	16.06	B1: III		1163	14.05	O4 If*:	O3 V((f*)) [3]
700	16.37	O7: V((f))		1168	14.95⋆	O9.5 V	
706	14.59	O6 V	O3 V [3]	1171	17.38⋆	O8-B1 V:	
712	16.38⋆	O6 V		1184	14.46⋆	B1: II-I	B1 Ia [3]
713	14.62	O5 V	O3-6 V [3]	1191	15.11	B0.2-1 III-IV	
716	15.53⋆	O5.5 III(f)		1209	15.72	O9-B0 V:	
722	16.36⋆	B0.2 V		1217	16.67⋆	O9.5-B0.5 V	
724	14.45	O7 III	O6: V: [3]	1218	16.08⋆	O6: V	
738	16.75⋆	B2 Ia		1235	16.87	B0 III	
747	15.83⋆	O6-8 V		1247	15.83⋆	B0.5 IV	B2-3 III [3]
768	15.69	O9-B0 V		1283	17.65⋆	O6 V:((f*))	

Table 1. continued

Parker id.	$V_{\rm mag}$	Spectral type	Literature Sp. T	Parker id.	$V_{\rm mag}$	Spectral type	Literature Sp. T
769	17.0⋆3	B0.5-0.7 V		1288	15.56	O8.5 V	O8 V [3]
787	14.96	O9-B0 V		1339	18.46	B0-0.2 IV	
791	15.84⋆	O5 V	O3-5 V [3]	1341	14.01⋆	O3-4 III(f*)	O5 V [3]
803	15.62	O6 V	O3-5 Vz [3]	1350	14.22	O6 III(f*)	O3-6 V: [3], O3 III(f*) [4]
805	14.52	O5-6 V	O4 V [1]	1354	16.72	B0-0.2 III	
809	15.32	O8-9 V		1366	17.04	B1.5 III-I	
829	16.80⋆	K I		1369	15.78	O8.5 V (b)	
848	16.77⋆	O9-B0: V		1389	16.45⋆	B1: V::	
849	15.74⋆	O9-B0 V		1401	15.98	O8 V	
860	14.02	O7: V((f))	O5-7 V [2], O3 V [4]	1419	16.00⋆	B0-0.2 III-I	B1 III [3]
861	16.27	O7: V		1429	15.39⋆	O4-6V	O3-6 V [3]
1455	16.21	B0.2: V		1685	13.80⋆	B0.5-0.7 III-I	B0.5 Ia [3], B1 II [2]
1459	15.92⋆	O9.5 II	O9-B0 II [3]	1729	14.92⋆	B1 II-III	B0.5 III [3]
1460	15.91⋆	B0-2 V		1737	14.29⋆	B1.5 III	B1 Iab [3], B1 Iab [2]
1468	15.55	O9.5 V		1756	15.65⋆	B0.2 V (b)	
1500	13.09	B0.2 III	B0 Ib [3], B0.5 Ia [1]	1775	14.76⋆	A2-3 I	A I [3]
1519	16.22⋆	B0-0.2 V		1788	12.04⋆	WN6	WN6 [1]
1527	14.94	B1 IV	B1 III [3]	1797	13.68⋆	early Be	B3 Ia [3]
1531	14.16	O6 V((f))	O5: V [3]	1840	15.62⋆	B1 V	
1548	17.32⋆	B2 V		1890	15.86⋆	B0.2 V	
1552	13.88	B2 II-III	B2 Ib: [3]	1938	15.77⋆	O7.5 V (b)	
1553	14.70	O7 V	O3-6: V [3], O(7) V [1]	1966	15.67⋆	B0.2 V	O9:: V: [2]
1560	15.71	O8.5 V		1969	14.91⋆	B0.7 IV	O9-B0 III [3]
1563	14.24	O7.5 II-III(f)	O7.5 [3]	1974	16.19⋆	WC 7-9	
1570	16.68⋆	B0-0.2 IV	O9:: V [2]	1987	13.03⋆	B2 I	B1 Ia [1]
1584	16.70	B0-1 V	B0: V: [2]	1988	14.28⋆	B0.5 V (b)	O9 V: [3]
1586	15.92	O9: V	O9 III [2]	1998	15.81⋆	O9.5 III-IV	O8 V [2]
1604	16.34	B1 V		2000	15.67⋆	O6-7 III(f*)	
1607	14.25	O7: If	O6: III: [3], O3 V(f) [1]	10001	...	O4 V	
1614	15.03	O5-6 V((f))		10002	...	O9.5-B0.2 IV-V	
1618	15.03⋆	B0-0.2 III	B0.5 III [3]	10003	...	B1-1.5 V	
1619	14.18⋆	O8 III(f)	O8 Ib(f) [3]	10004	...	B1.5:	
1621	15.97⋆	B0.2-0.5 III	B0.5-1 III [3]	10005	...	B1-1.5 V	
1643	15.51⋆	O5 V	O3-5 Vz [3]	10006	...	G V	
1661	14.46⋆	B1 III	B0.7 Ia [3]	10007	...	G V	
1674	14.39⋆	B1 Ib	B0.5-0.7 I [3]	10008	...	G type	
1684	12.32⋆	G8V (field)	K0 V [1]				

Notes to Table 1: Columns 1 & 5 indicate identifications from Parker (1993), numbers 10001 to 10008 indicate stars not identified before; Columns 2 & 6 show visual magnitudes from Parker (1993), and Selman et al. (1999), marked with a "⋆"; Columns 3 & 7 list our spectral classification. A "(b)" after the spectral type indicates possible spectroscopic binarity according to our spectra; Columns 4 & 8 list previous classification, if any. The references are: Melnick 1985, (2) Parker (1993), (3) WB97, (4) Malumuth & Heap (1994).

a selected column of each slit, the central one in most cases, and were then traced along the direction of the slit. Unfortunately, problems with the arc lamps that occurred during the observing run imply that in some calibration frames the argon lines are not well exposed and the intense HeI 5875 Å line is saturated. Therefore, in order to avoid systematic effects within the whole sample, we used a 5th order Legendre polynomial for all the pixel-wavelength transformations, and we used the same sub-set of He-Ar lines for all spectra. This procedure is not critical for spectral classifications, but is crucial for stellar radial velocities which will be discussed in a forthcoming paper. The mean rms error of the wavelength

Table 2. Spectral types of 30 Dor stars available in the literature

Parker id.	$V_{\rm mag}$	Literature Sp. T	Parker id.	$V_{\rm mag}$	Literature Sp. T
42	12.50⋆	O8 II [3]	954	11.50	WN4.5 + OB
61	17.40⋆	B1-2: V: [2]	982	16.00⋆	O4: V((f)) [2]
75	15.9⋆3	B1:: V: [2]	987	11.82	B0.5-0.7 I [3]
76	16.74⋆	O9:: V: [2]	998	12.86⋆	WN7 + OB [1]
83	15.44⋆	O9-9.5 V [3]	1018	13.47	O3 If*/WN6-A [3]
169	14.80	O9-B0 III [3]	1035	14.73⋆	O3-6 V [3]
195	14.88	O9.7 II [3]	1120	13.77	WC5 + O4 (P,M)
246	15.25	B0.5 V [3]	1130	13.36	O7.5 II [3]
288	14.65	O3-6 V [3]	1134	13.43⋆	WN4.5 [1]
304	14.17⋆	O8 V [3]	1140	13.57	O(4) [1]
324	15.26	O7-8 V [3]	1150	13.66	O4 III(f) [3]
341	14.40⋆	O8-9 Vz [3]	1161	15.42	O9.5 V [2]
355	13.07⋆	WN6 [1]	1170	16.09	O3-6 V [3]
370	14.30⋆	O4-5: [3]	1222	14.84	O3-6 V [3]
409	15.03	O3-6 V [3]	1253	12.49	BN0.5 Ia [3]
466	15.48	O9 V [3]	1257	12.55	B0 Ia [3]
488	13.02	B0.5-0.7 Ia [3]	1260	13.94	O3 V [3]
493	13.50	BC1 Ia [3]	1267	14.70	O7: V [2]
499	11.74	A0 Ia [1,3]	1306	14.96	O8 III [3]
515	13.76	WN 8 [1]	1311	13.80	O3 III (f*) [3]
548	12.05	B0.7-1.5 I [3]	1312	13.95	O7 V [1,3]
607	13.66	O4 III(f) [3]	1317	14.69	O4 V [3]
615	15.71	O4-6 III(f) [3]	1340	14.94	O7 Vz [3], O9.5: V [2]
621	14.75	O3-6 V [3]	1416	16.55⋆	B1: V [2]
643	13.60	ON9: I [3]	1423	14.84⋆	O3-4 III(f) [3]
662	12.67⋆	BN6 Iap [3]	1445	13.60⋆	M I [1]
666	13.76	O3 If*/WN7-A [3]	1554	16.50⋆	O9: III: [2]
691	13.45 ⋆	WN7 [1]	1573	15.45⋆	O3-6 V: [2]
761	14.82	O3-6 V [3]	1575	12.01⋆	B9 Ip [3]
767	12.85	O3 If*/WN6-A [3]	1594	15.13	O7 III [2]
786	12.63⋆	WN7 [1]	1838	15.77⋆	early O [2]
830	14.16⋆	O8-9: [3]	1875	15.64⋆	B0:: V: [2]
841	15.45	O4-6(n)(f)p [3]	1892	15.63⋆	O8.5 Vz [3]
850	13.76	B0 III [3]	2022	15.39⋆	B0.5: V [2]
877	12.12	WC5+WN4 [1]	2041	15.13⋆	O4: V((f)) [2]
909	14.72⋆	O8-9 III: [3]	2104	15.69⋆	B0.5: V [2]
917	13.31	WN7-A [1]	2123	12.87⋆	B8 Ia [2]
922	12.71	O3 If*/WN6-A [3]	2186	13.58⋆	early K I [2]
925	14.96⋆	O8 Iaf [3]	2246	14.76⋆	O4 V [2]
930	13.76	OC9.7 Ib [3]	2252	15.46⋆	B1.5 Ia [2]
945	11.37⋆	WN4.5 [1]	2270	15.31⋆	O7 V [2]
949	13.44	O4 If [1]	2305	15.20⋆	B1 III [2]
952	11.94	O7 Iafp [3]	2313	15.39⋆	B0.5: V [2]

Notes to Table 2: Columns 1 & 4 indicate identifications from Parker (1993);
Columns 2 & 5 show visual magnitudes from Selman et al. (1999) and Parker (1993), marked with a "⋆";
Columns 3 & 6 list previous classification.
The references are: (1) Melnick 1985, (2) Parker (1993), (3) WB97.

calibration for the 13 lines in common to all spectra is 0.06 Å.

Notice that, since the multislit spectrograph yields different wavelength ranges for different slit positions, the reddest line available for wavelength calibration varies from star to star. This, together with the saturation problems of HeI 5875 Å, introduces different limits to the reliable wavelength interval for each object. These limits, however, are beyond the wavelength range used for spectral classification (3800 Å − 4800 Å.)

3.2. Background subtraction

3.2.1. Spectra extractions

EMMI spectra are slightly curved in the spatial direction forming an arc with up to 5 pixels transversal deviation from centre to edge. On top of that, crowding sometimes causes overlapping of information in adjacent spectra. These two effects often left only a few pixels available for background subtraction, so the usual procedure of selecting background strips in the image for subtracting the sky and nebular contamination could not be performed. On the other hand, the strength of the nebular emission lines from the HII region itself makes the background subtraction crucial for the final quality of the reduced data. Therefore, in order to minimise residuals in the nebular subtraction due to the curvature of the spectral lines, we used the IRAF APEXTRACT task to trace the nebular background as close as possible to the stellar spectra. (In order to use this procedure it is essential to eliminate distortions in the slit direction by performing the wavelength calibration in 2-D, as described above.)

Due to the large variations in the intensity of the nebular HeI emission lines within the slit length, we used – whenever possible – two background windows situated symmetrically on both sides of the stellar spectra. Each window was 3 pix-wide and 6 pix (1.7″) away from the aperture centre, and linear interpolation between the two windows was used to determine the background spectrum.

3.2.2. [OIII] scaling factor corrections

We have devised a method to improve the background subtraction which uses the [OIII]λλ4959, 5007 Å lines to minimise the residual contamination by the nebular lines.

Since the [OIII] lines are not emitted by the stars and are the strongest lines in the nebular spectrum, the presence of residual emission (or "absorption") features of [OIII] in the final stellar spectra is a sensitive indication of under (or over) subtraction of the nebular background. Although, due to the clumpiness of the ionised gas, the intensity of the nebular spectrum can change significantly on very small distance scales, the intensity ratios of the relevant nebular lines are relatively insensitive to density variations and thus remain constant within the slitlets. We have checked for the stability of the line ratios ([OIII]/Hβ, [OIII]/HeI 4471) for the slits with the strongest [OIII] nebular lines. In all cases, the observed ratios changed less than 20%. Therefore, our estimation (and correction where necessary) using the [OIII] residuals also applies to other nebular lines, and in particular to HeI 4471 Å which is critical for spectral classification of O stars.

The correction was estimated as follows:

1. The flux of the residual [OIII] features present in the stellar spectrum (after background subtraction) was measured. ($F([\mathrm{OIII}])_{\mathrm{residual}}$).
2. The flux of the same feature from the nebular spectrum used for background subtraction ($F([\mathrm{OIII}])_{\mathrm{nebular}}$) was also measured.
3. The parameter
$$\Gamma = \frac{F([\mathrm{OIII}])_{\mathrm{residual}}}{F([\mathrm{OIII}])_{\mathrm{nebular}}}$$
which measures ratio of residual to nebular fluxes was calculated for every object.
4. The nebular spectrum was then scaled by a factor $(1+\Gamma)$ and the background subtraction was performed again.

As shown in Fig. 3, this procedure allowed us to achieve excellent subtraction of the nebular lines in most cases. Where this was not possible, the procedure gave us a good estimation of the amount of contamination present. The critical diagnostic for O-type stars is the ratio of HeI 4471 to HeII 4542. As an indicator of the accuracy of the background subtraction for the former line, we used the ratio of the equivalent widths of HeI 4471 to [OIII]5007 in the nebular spectra. For the whole sample, the average ratio is $\sim$0.004, which indicates that only 0.4% of the residual in [OIII]5007 present in the stellar spectrum will be affecting the flux of the HeI 4471 line.

4. Discussion

4.1. Spectral classification

The stellar spectra were normalised and smoothed using a 3 pixel window, and classified following the criteria of Walborn & Fitzpatrick (1990). We obtained thus reliable spectral types for 175 stars. This is fewer than the 231 slit spectra mentioned in Sect. 3 because many stars were observed more than once, while a few were discarded because the signal-to-noise was too low to classify them properly. The method we have used for background subtraction allows us to estimate if the features present in the stellar spectra are undoubtedly of stellar origin.

Figures 4 to 24 show the classified spectra grouped by similar spectral type. The neutral hydrogen lines, together with the nebular lines that showed problems throughout the background subtraction, have been left out of scale

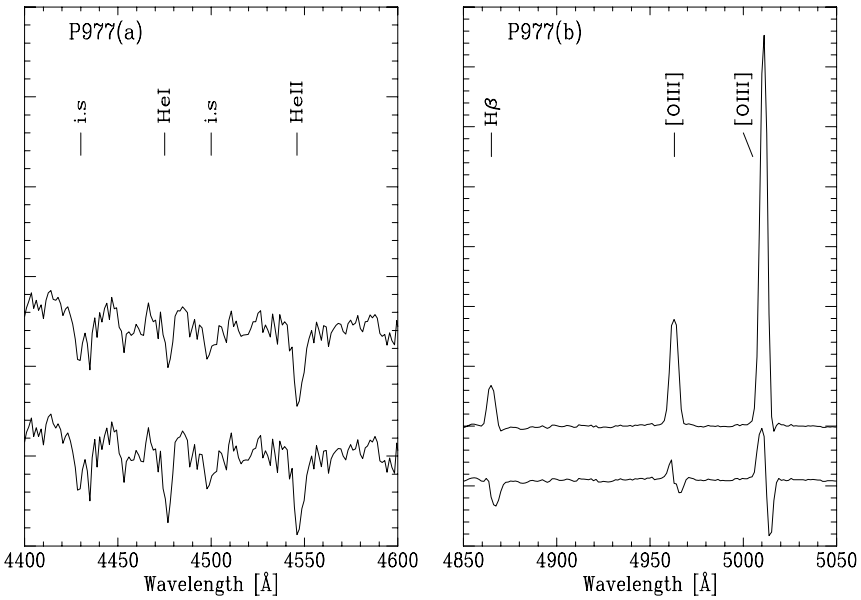

Fig. 3. Both panels show, at different wavelengths, the reduction of the nebular residual with the procedure described in the text, for the case of star 977. Within each panel both spectra, the corrected one being plotted below, are drawn at the same scale. The correction introduced from the [OIII] lines is shown in the right panel. The effects of improved background subtraction can be seen in the left panel, as the observed intensity of the HeI 4471 Å absorption changes

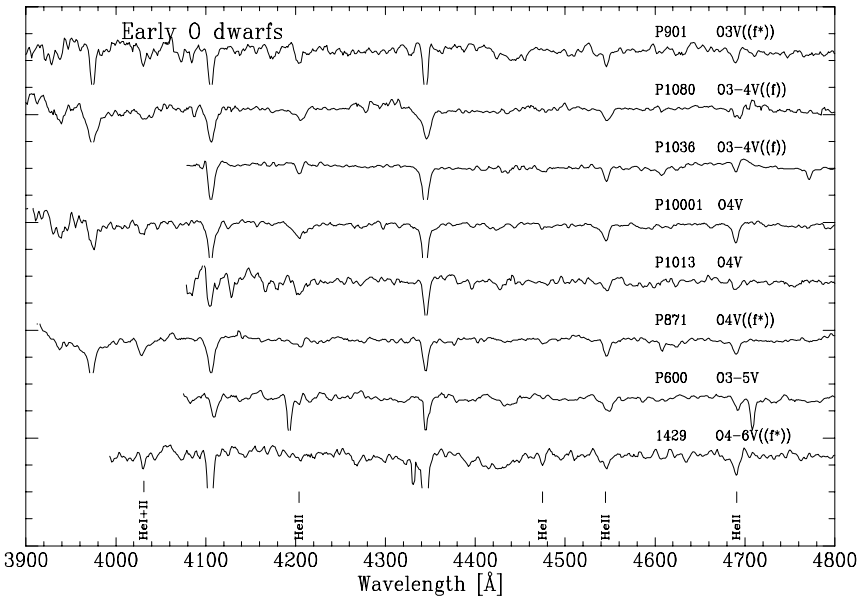

Fig. 4. Spectral classification for early O-type dwarf stars. HeII and HeI lines have been identified as a reference. The range suitable for classification is shown in this figure. The y axis scale is in arbitrary units, each spectrum being normalised to its continuum

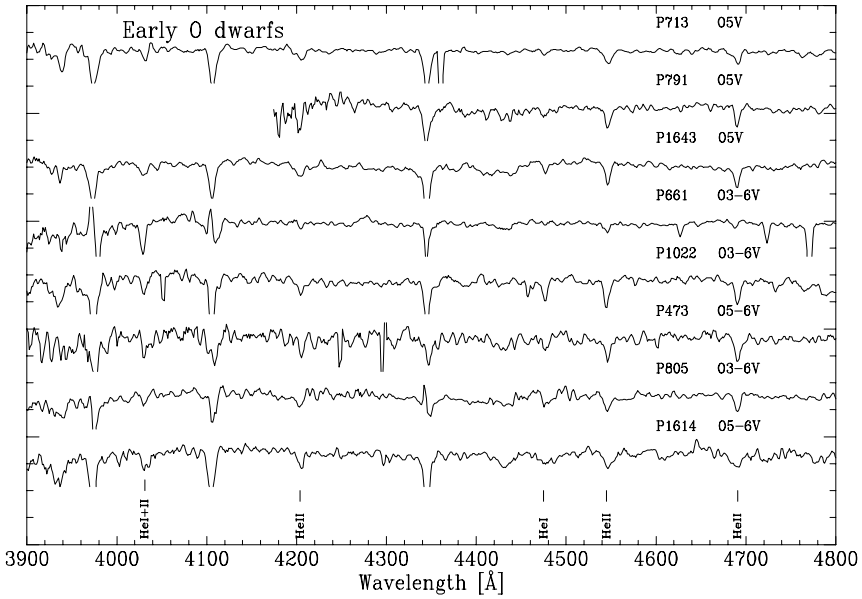

Fig. 5. Same as Fig. 4, stars classified as O3-6 are early O stars, with strong nebular contamination on HeI 4471 Å that prevents from the determination of a more accurate spectral type

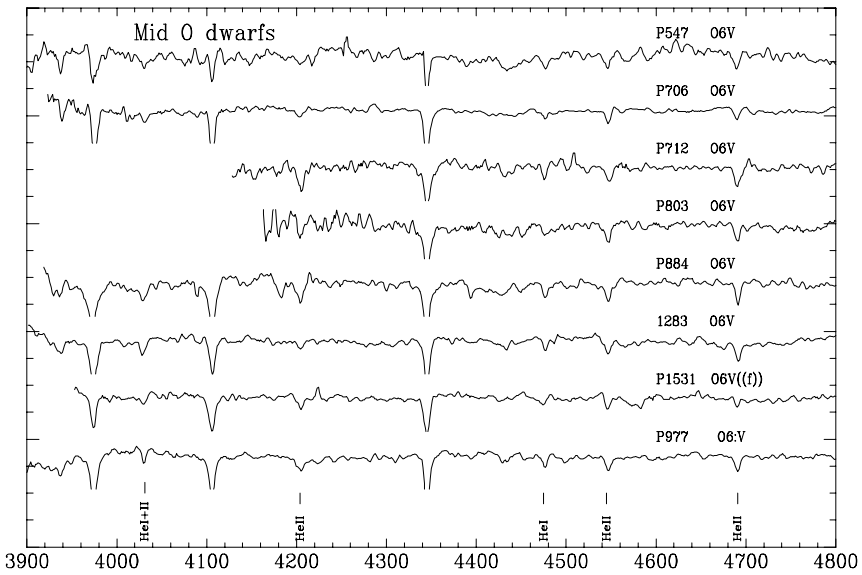

Fig. 6. Same as Fig. 4. for the mid O-type dwarfs

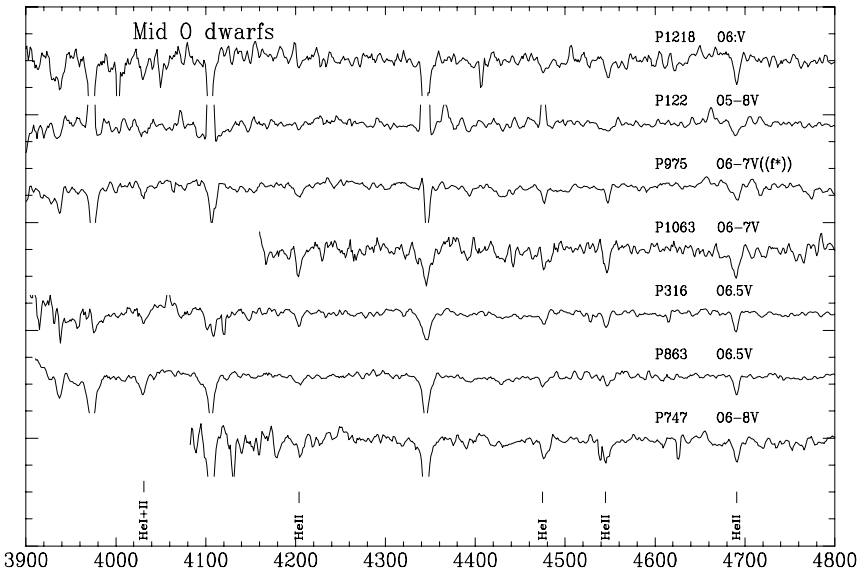

Fig. 7. Same as Fig. 4 for mid-O stars. The O6-8 type indicates weak HeII absorption lines, but with nebular contamination on HeI 4471 Å

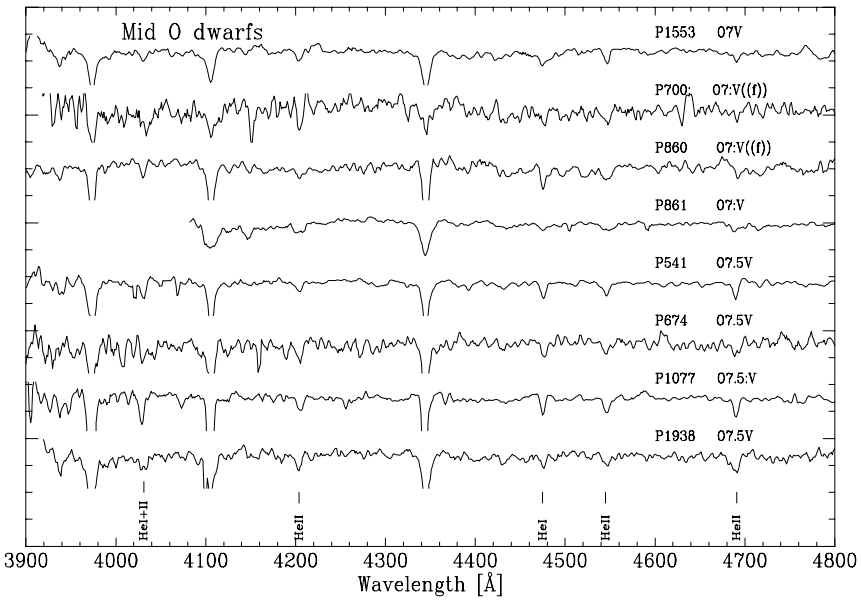

Fig. 8. Same as Fig. 7

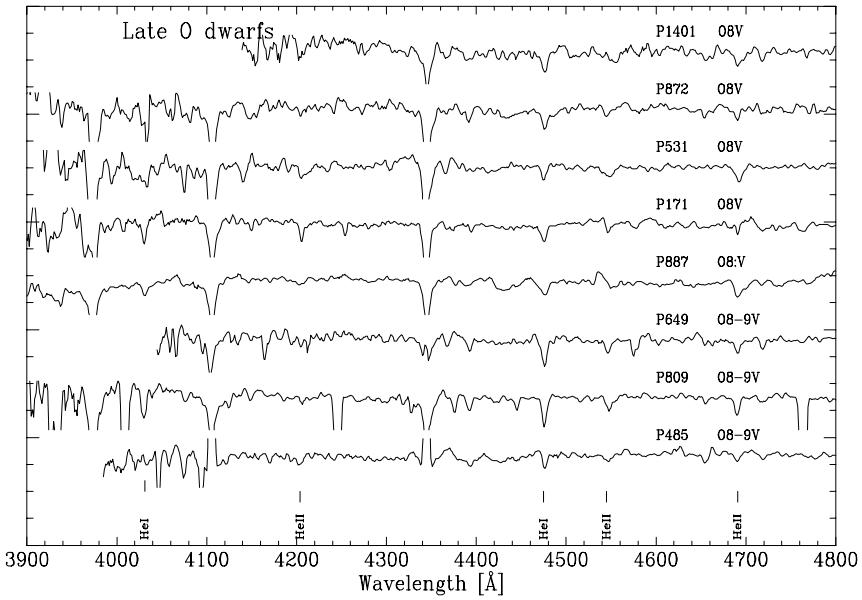

Fig. 9. Same as Fig. 4 for late O-type dwarf stars. As the intensity of the HeII absorption lines diminishes, the feature identified at 4026 Å is only due to HeI

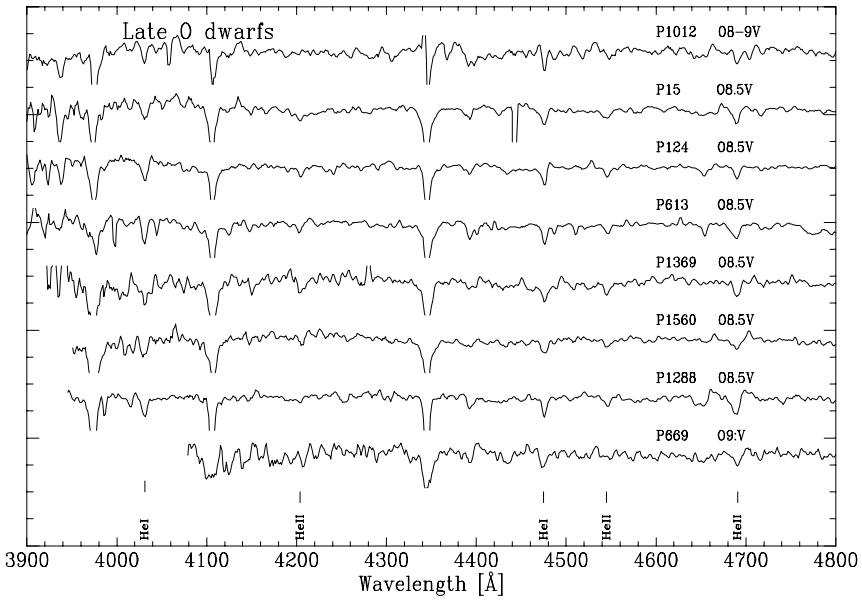

Fig. 10. Same as Fig. 9

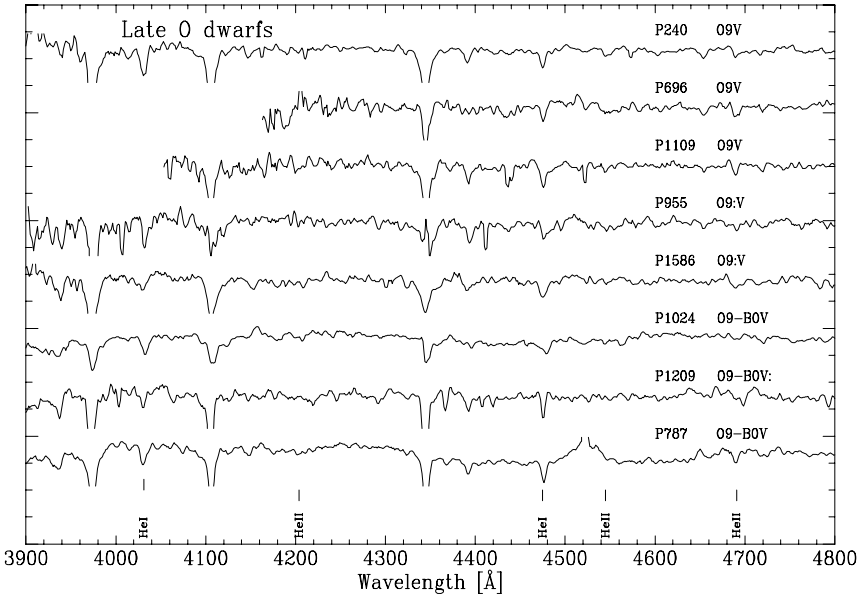

Fig. 11. Same as Fig. 9

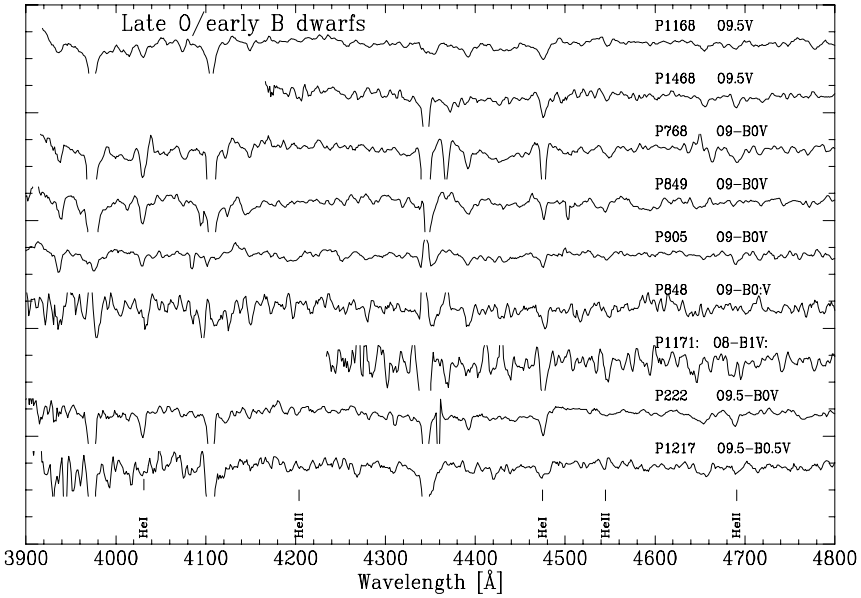

Fig. 12. Same as Fig. 9

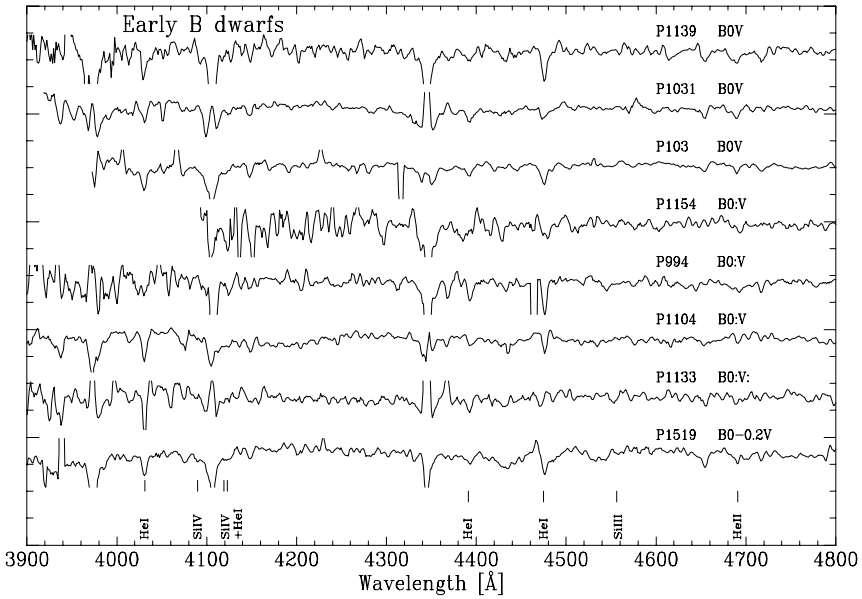

Fig. 13. Same as Fig. 4 for the early B-type dwarfs. Only traces of HeII are detected. SiIII and SiIV, used for classification, are identified here

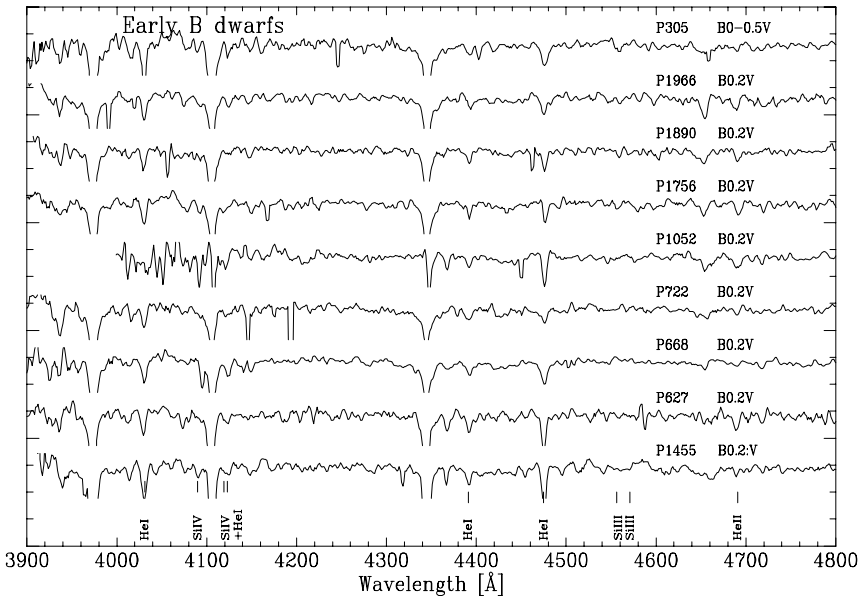

Fig. 14. Same as Fig. 13

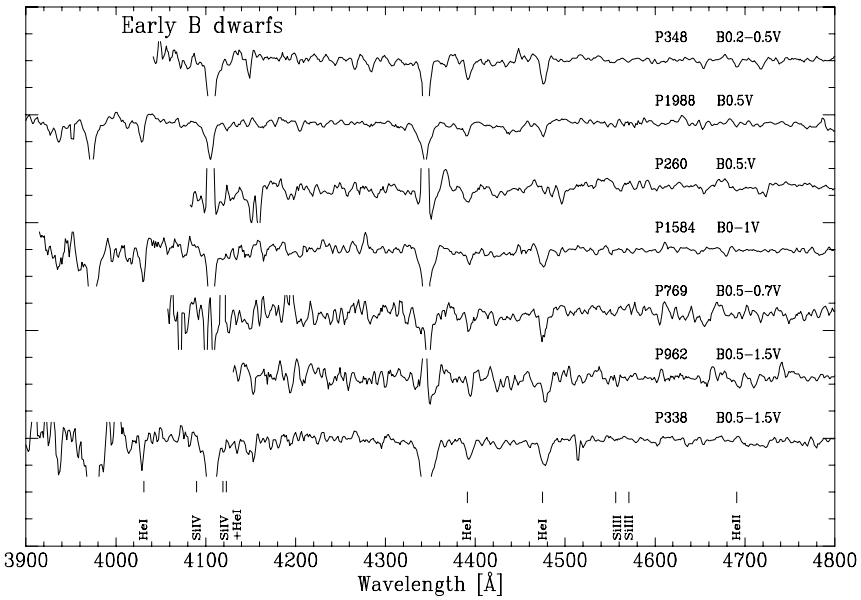

Fig. 15. Same as Fig. 13

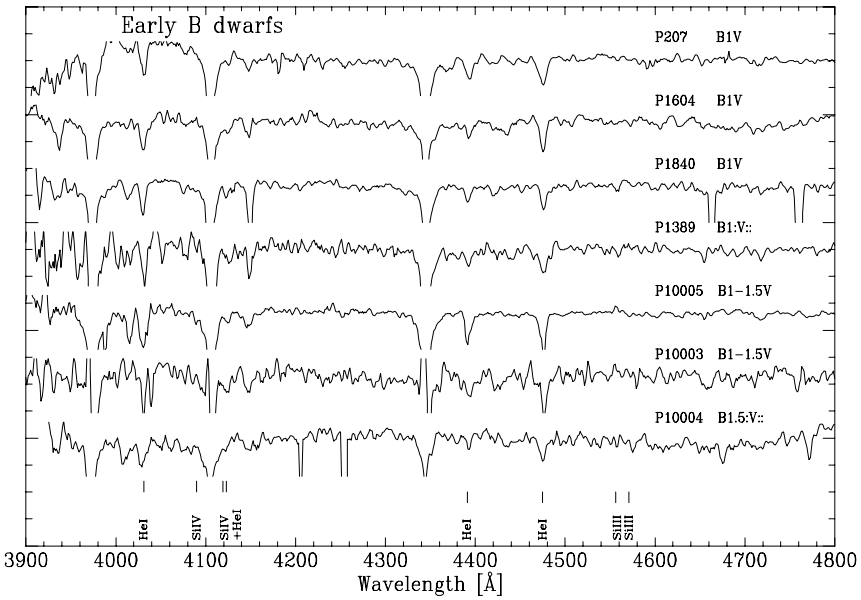

Fig. 16. Same as Fig. 13

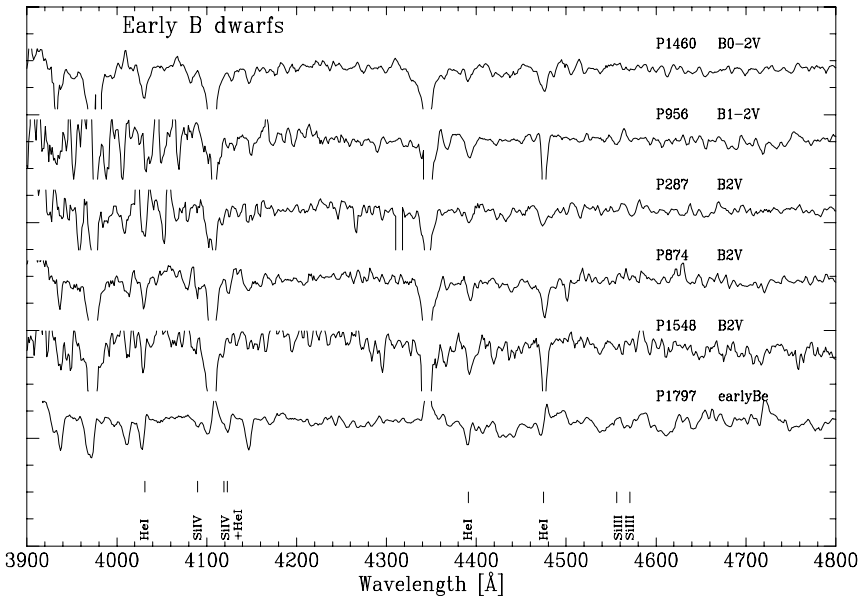

Fig. 17. Same as Fig. 13

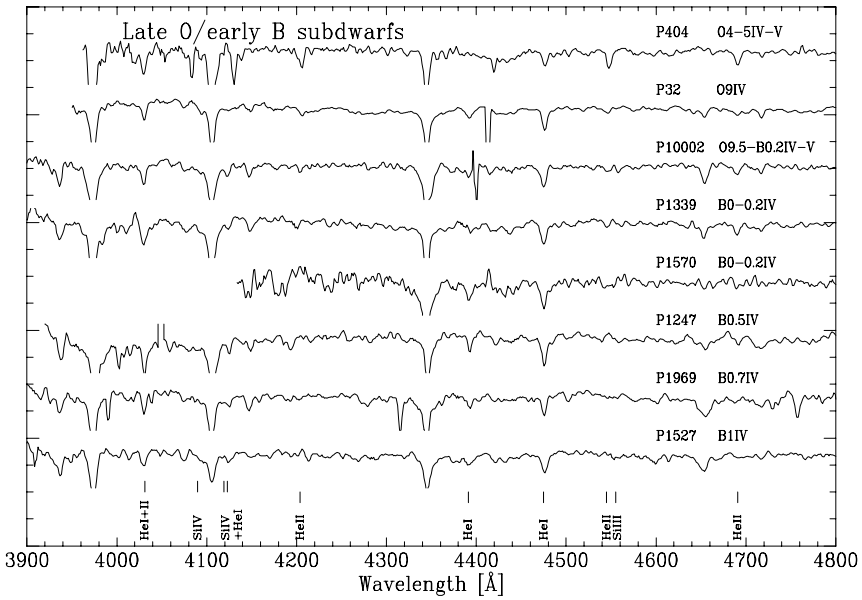

Fig. 18. Same as Fig. 4 for OB-type subdwarf stars

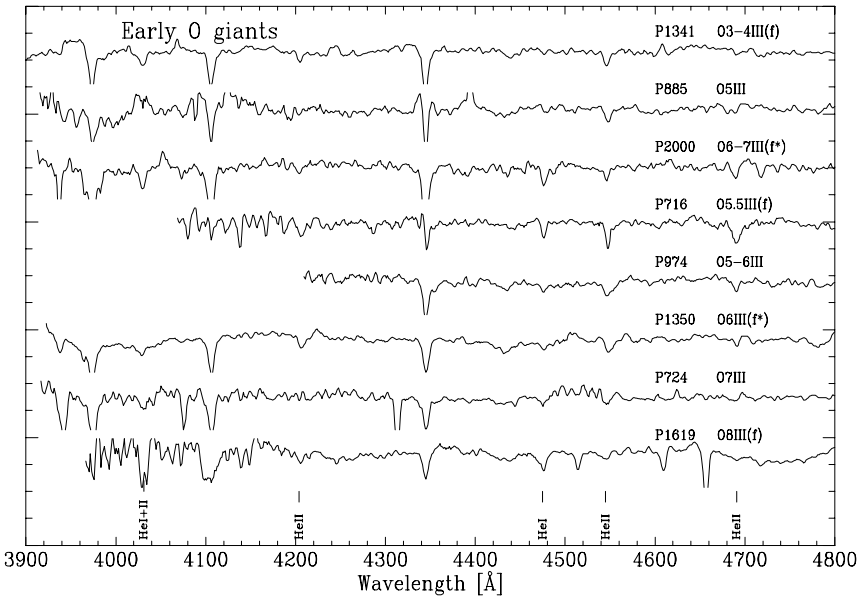

Fig. 19. Spectral classification for early O-type giant stars. HeI and HeII features are identified. The luminosity criterium used is the partial filling of the HeII 4686 Å feature

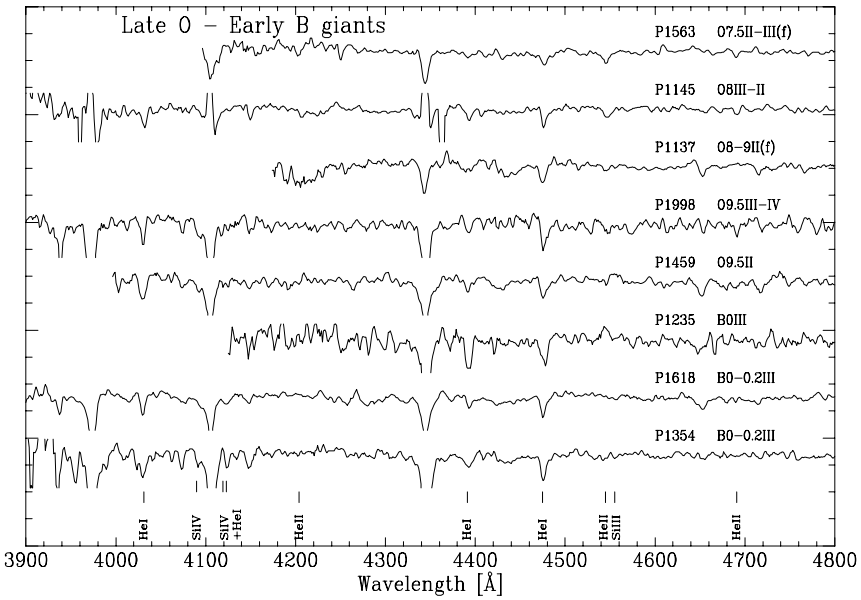

Fig. 20. Same as Fig. 19 for late O - early B type giant stars. Together with HeI and HeII, SiIII and SiIV features are identified

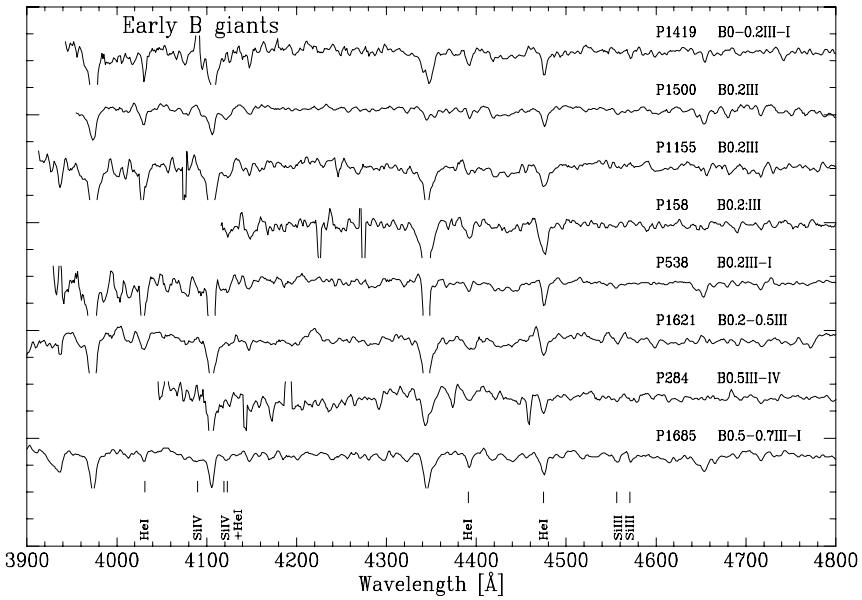

Fig. 21. Same as Fig. 20 for early B-type giant stars

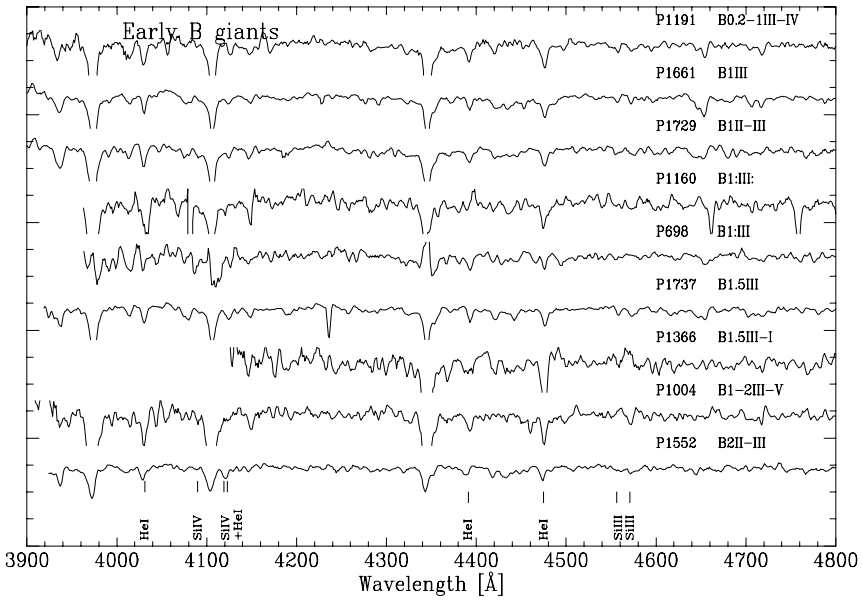

Fig. 22. Same as Fig. 20

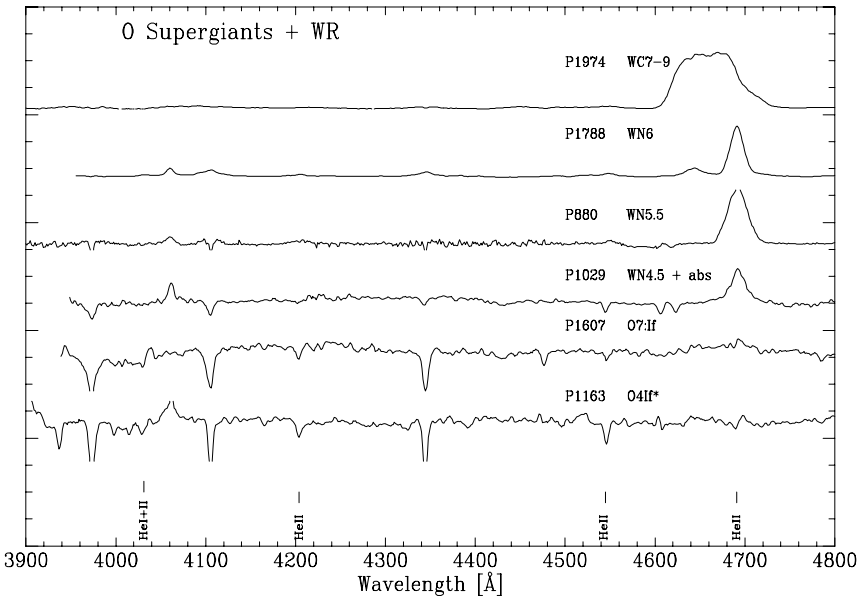

Fig. 23. Spectral classification for O giant and Wolf-Rayet stars

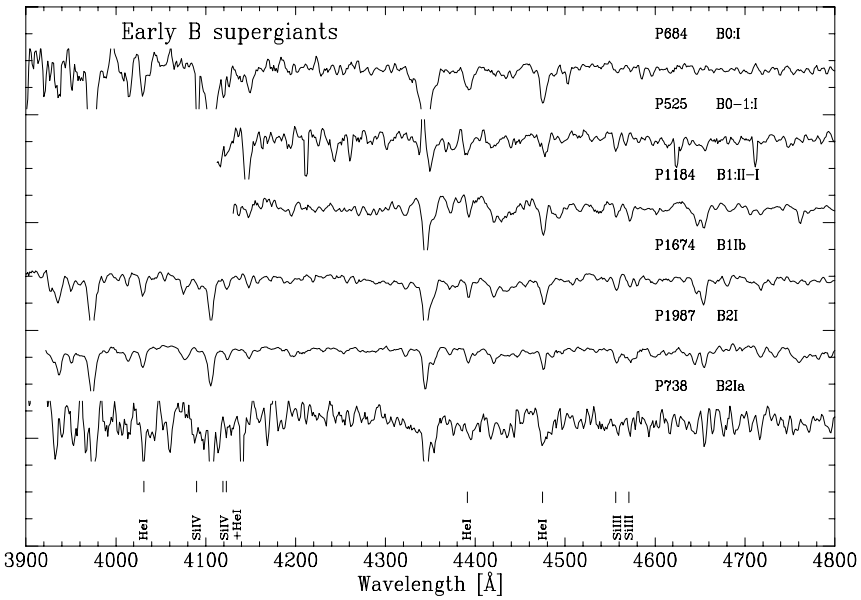

Fig. 24. Spectral classification of B supergiant stars

in order to enhance the weaker features relevant to the classification process.

The resulting spectral types are presented in Table 1. The stellar identifications in Col. 1 are those by Parker (1993) (with the exception of a few stars which lie beyond the area covered by his photometry, namely stars 10001 to 10008). Column 2 shows the visual magnitude from Paper I when available and Parker (1993). The ones from the latter are indicated with a "⋆" symbol. The discrepancies between both photometries has already been discussed in Paper I. Column 3 lists our spectral classification, and Col. 4 indicates previous classification taken mostly from the compilation of Walborn & Blades (1997) (hereafter WB). Table 2 lists the spectral types available in the literature, for stars not observed by us but which have been included in our analysis.

A finding chart for our objects is included in Figs. 1 and 2, where slits have been drawn to scale, showing the corresponding identification number.

4.2. Comparison with other spectral classifications

4.2.1. Ground based data

There are 70 stars in our sample with published spectral types, mostly from WB. A comparison plot of both classifications is presented in Fig. 25, where we plot the spectral types from the literature against our own spectral types. The bars indicate the uncertainty in the spectral classification using the following convention: an O3-6 star appears in the Fig. 25 as an O4.5 type with a ±1.5 error bar in spectral class. From the plot it can be seen that:

1. There is an excellent overall agreement between our spectral types and the ones already published.
2. The "flat" distribution of points in the early-mid O range is mostly due to a number of stars classified as "O3-6V" in WB due to strong nebular contamination, and which we have been able to classify more accurately.
3. We seem to classify late O-type and B-type stars with slightly later types, although the agreement is still quite remarkable.
4. There are 9 stars that fall well away from the diagonal line. These stars are labelled in the diagram and are discussed below.

Our O-type classification was done using better quality data than the previous observations. The improvement comes mostly from our method for subtraction of nebular contamination, and also from a better S/N ratio. However, for the B-type stars the classification is more sensible to spectral resolution, which is slightly better in WB, than to S/N. These facts are relevant in the following discussion of the 9 discrepant cases.

Parker 706: Previously classified as O3V. The spectrum presents HeI absorption lines which indicate a later type (O6V). The residual of the [OIII]5007 Å line is smaller than 4%, which indicates that the chance of HeI being due to over-subtraction is small.

Parker 1013: This star was classified as O8:V by WB, but our data shows no strong HeI absorption features. The nebular spectrum extracted close to the star indicates low probability of HeI under-subtraction. Thus, our O4V type appears more secure.

Parker 547: WB give O8-9V for this star, but our data shows no strong HeI features, although with some uncertainty because the nebular contribution had a high residual before the correction. However, the nebular scaling correction did not change our initial O6V spectral type which we retain.

Parker 1247: We detect a faint HeII 4686 Å feature together with SiIV 4089 – 4116 and SiIII 4552 – 4567. The presence of HeII is not expected in a B2-3 star, as classified in WB, so our B0.5IV type appears more secure.

Parker 1553: This is one of the clearest cases in which there is no HeI emission detected in the background, so the undoubtedly stellar absorption line HeI 4471 makes it an O7V type star.

Parker 1797: The long error bar shows our uncertainty when classifying this star. Notice, however, that according to our estimated contribution of nebular Balmer lines, the hydrogen emission lines seen in the spectrum are intrinsic to this star, so we classify it as Be.

4.2.2. HST data

There are six stars in common with the work of Massey & Hunter (1998) where they present spectral types for stars within the core of the cluster obtained using the Faint Object Spectrograph (FOS) (numbers 860, 863, 1029, 1036, 1080, 1350 in Table 1; plotted in triangles in Fig. 25.) The FOS observations were obtained through a 0.26″ diameter aperture which reduces the nebular contamination considerably, making it negligible for H and HeI lines. From the ratio of slit areas we estimate that the nebular contamination in the FOS spectra is about 40 times smaller than in our NTT observations. On the other hand, there is a big difference in the light collecting areas so, since the exposure times are slightly larger for the NTT data, the overall S/N ratio is significantly larger in our data. Furthermore, the Digicon detector of the FOS is known to introduce problems due to "dead" and noisy diodes. The observational procedure, described by MH, shifts the spectra along 5 neighbouring diodes at a step of 1/4 diode, which means that a diode turned off

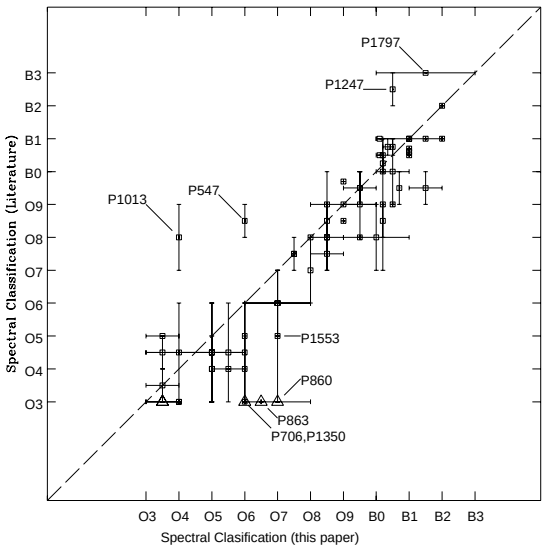

Fig. 25. Comparison between spectral classification described in this paper, and the one found in the literature. Square markers identify the comparison with Walborn & Blades (1997) (WB97) and Parker (1993). Triangle markers indicate the comparison with spectral types in MH. Labelled points are discussed in the text

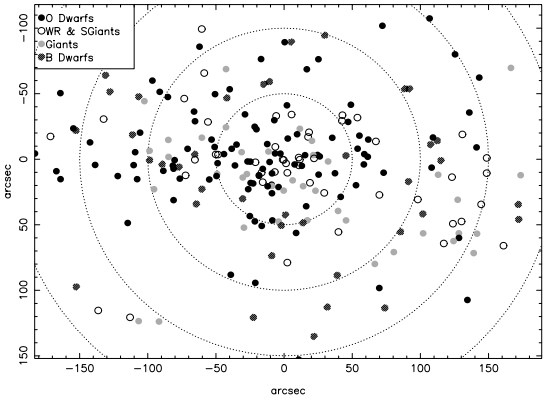

Fig. 26. Spatial distribution of stars classified in this paper. The different distribution of early and late type stars can be seen in this diagram. Coordinates are in arcsec, measured from R136. The dotted circles indicate radial distances from R136, at 50 arcsec steps

reduces the S/N ratio by a factor of $\sim 20\%$, while a noisy diode introduces spurious emission or absorption features that are 20 pixels wide. In particular, at the redshift of 30 Doradus, the HeI 4471 feature lies approximately in diode # 408. According to the information available in the FOS manual, diode # 409 is turned off and diode # 410 is reported as possibly noisy, though still turned on. This reduces considerably the S/N ratio in this region of the spectrum, which unfortunately makes the detection of weak HeI 4471 features rather difficult.

By comparing the FOS intensities of the Hδ and Hγ absorption lines, which are free from nebular contamination in the FOS data, with our NTT data, we can obtain an independent check of the goodness of our nebular subtraction method. Below we present the result of this comparison for the 3 stars for which we disagree with the classification of MH.

Parker 860 (=MH 28) We classify this star as O7:V((f)) although the [OIII] residuals indicate significant nebular contamination of the HeI lines. Comparison of the Balmer lines with the FOS data yield the same estimate, but we still consider that there is real HeI absorption in the spectrum, so the type O3V given by MH is probably not correct.

Parker 863 (=MH 29) We classify this star as O6.5V. Comparison of the Balmer lines in the FOS spectrum indicates that our nebular subtraction is good. Moreover, in this particular case we have detected the stellar HeI 4471 absorption even *without* background subtraction. So again the O3V type given by MH is probably incorrect.

Parker 1350 (=MH H96-28) We classify this star as O6III(f*) while MH give O3III(f*). The presence of NIV 4058 Å emission in the FOS spectra favours the classification of MH, but this feature is probably of instrumental origin. Although there is no report of problems in that area of the detector, the NIV emission feature is 20 pixels wide, matching the extension of a noisy diode feature. Moreover, the NIV feature is not detected in our higher S/N spectrum of the star.

5. Spatial distribution

In Paper I we detected evidence for mass segregation in the 30 Dor cluster. To further investigate this important point we have combined our spectral classification, with that available in the literature, to obtain a total of 235 stars with reliable spectral types within the 30 Dor cluster. This allows us to examine the spatial distribution of stars, grouping them in spectral class bands. The result is shown in Fig. 26 where we have split the stars in four main groups: O dwarfs, B dwarfs, OB giants and OB supergiants (including Wolf-Rayet stars).

It was pointed out by Underhill (1983) that determination of evolutionary stages from spectral types is unreliable. Still there are some clear points that come out of the distribution:

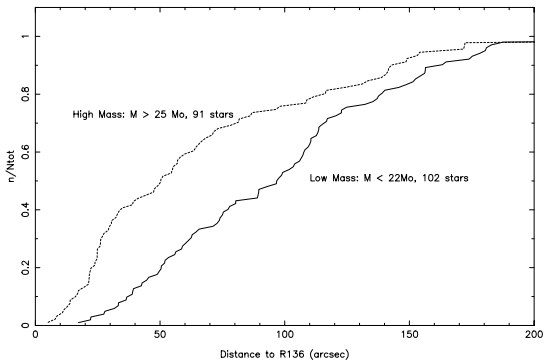

Fig. 27. Cumulative radial distribution of stars according to masses determined from their spectral types. Both distributions are plotted with dashed and continuous line styles, for the high-mass and low-mass stars respectively. The different distribution for both subsets indicates the presence of mass segregation

1. Giant and supergiant stars are evenly distributed in the sampled region (our sample is intrinsically stretched in the N-S direction).
2. O dwarfs are notoriously concentrated towards R136.
3. There is a large region, south-east of R136, where the number of late type stars is much larger than that of early type ones. These stars can be identified in the center of Fig. 2.

We have also estimated the stellar masses of stars from their spectral types interpolating from the relationship tabulated by Schmidt-Kaler (1982). With these values we analysed the radial distribution of stars according to their masses. As the determination of a star's mass from it's spectral type is not very accurate, we split the dataset in two large groups: high mass and low mass stars, with the transition at $\sim 23.5\,M_{\odot}$. Figure 27 shows the cumulative distribution of stars from the centre of the cluster. It can be readily seen that the massive stars show a concentrated distribution, while the lower mass stars have a flatter distribution, with few stars in the inner region. Thus, there is evidence for mass segregation in the 30Dor cluster, as it is also suggested from the photometric analysis of Paper I. A Kolmogorov-Smirnov test to both distributions, yields a significance level of 0.007, which indicates that the distribution of high mass stars is significantly different from the less massive ones.

In previous works, Malumuth & Heap (1994) and Brandl et al. (1996) had also found mass segregation in the inner region of 30Dor, close to R136, which agrees with our findings. Malumuth & Heap detected a difference in the slope of the IMF of stars within a 3.3 arcsec radius of R136a and of those outside this area. Brandl et al. detected changes in the IMF slope and a clear trend towards smaller core radii for brighter –more massive– stars. Thus, there is evidence for mass segregation at the core and outer regions of 30 Dor. We believe that these results are also compatible with the lack of change of the IMF slope found by Hunter et al. (1996) given the narrow mass range and the restricted radial range of their data.

A more detailed analysis of this important point will be discussed in Paper III where we combine the masses derived from our photometric and spectroscopic observations.

6. Summary

We have obtained 175 spectral types for stars in 30 Doradus of which 105 are new. The total number of stars with spectral classification is now 261, which allows a thorough spectrophotometric analysis of the region. We have used the [OIII] nebular lines to reduce the contamination effects of the ionised nebula to the stellar spectra, improving the reliability of the spectral classification from ground based spectroscopy. Our spectral classification is good to about ± 1.2 subtypes. The spatial distribution of spectral types suggests the presence of a later type group $2'$ south of R136. The radial distribution of stars according to the masses estimated from their spectral types shows a more compact distribution for the most massive stars, indicating the existence of mass segregation in the cluster.

References

Brandl B., Sams B.J., Bertoldi F., et al., 1996, ApJ 466, 254
Ellis R.S., 1997, ARA&A 35, 389
Elmegreen B.G., 1997, ApJ 486, 944
Hunter D.A., O'Neil E.J., Lynds R., et al., 1996, ApJ 459, L27
Malumuth E.M., Heap S.E., 1994, AJ 107, 1054
Massey P., 1985, PASP 97, 5
Massey P., 1998, in Stellar Astrophysics for the Local Group, Aparicio A., Herrero A. and Sánchez F. (eds.). Cambridge University Press, Cambridge, UK
Massey P., Hunter D.A., 1998, ApJ 493, 180 (MH)
Melnick J., 1985, A&A 153, 235
Parker J.Wm., 1993, AJ 106, 560
Schmidt-Kaler Th., 1982, in Stars and Star Clusters, Vol. 2b, Schaifers K. and Voigt H.H. (eds.), part of the Landolt-Börstein series on Numerical Data & Functional Relationships in Science and Technology. Springer-Verlag, Berlin-Heidelberg
Selman F.J., Melnick J., Bosch G.L., Terlevich R.J., 1999, A&A 341, 98 (Paper I)
Stasinska G., Leitherer C., 1996, ApJS 107, 661
Underhill A.B., 1983, in: Garrison R.F. (ed.), The MK Process and Stellar Classification. David Dunlap Observatory, Toronto, p. 60
Walborn N.R., 1991, in: Haynes R., Milne D. (eds.), IAU Symp. 148, The Magellanic Clouds. Kluwer, Dordrecht, p. 145
Walborn N.R., Blades J.C., 1997, ApJSS 112, 457
Walborn N.R., Fitzpatrick E.L., 1990, PASP 102, 379

Paper III

The ionizing cluster of 30 Doradus III. Star-formation history and initial mass function

A&A 347, 532 (1999)

F. Selman, J. Melnick, G. Bosch, and R. Terlevich

.

Astron. Astrophys. 347, 532–549 (1999)

ASTRONOMY AND ASTROPHYSICS

The ionizing cluster of 30 Doradus

III. Star-formation history and initial mass function⋆

F. Selman[1], **J. Melnick**[1], **G. Bosch**[2], **and R. Terlevich**[2]

[1] European Southern Observatory, Alonso de Córdova 3107, Santiago, Chile
[2] Institute of Astronomy, Madingley Road, Cambridge CB3 0HA, UK

Received 5 February 1999 / Accepted 6 May 1999

Abstract. A new method is presented and used to determine the IMF of the starburst cluster NGC2070. A new correction, the *magnitude-limit correction* is introduced, and shown to be crucial when attempting to derive the IMF in the presence of variable reddening when the photometry is not several magnitudes deeper than the fainter stars analyzed. Failure to apply this correction is responsible for the drop at the low mass end of the IMF found in previous work on this cluster, despite the proper application of incompleteness corrections. For masses between $3M_\odot \lesssim M \lesssim 120M_\odot$ and outside $15''$ the IMF of NGC2070 is shown to be consistent with being a single power law with a Salpeter exponent. In the central region ($4.6'' < r < 19.2''$) within $2.8M_\odot < M < 120M_\odot$ our data combined with HST observations yield a slope flatter than Salpeter at the 2–3σ level. Furthermore, it is shown that the number of $M > 50M_\odot$ stars near the core (Massey & Hunter 1998a, 1998b) is incompatible with the intermediate mass counts of Hunter et al. (1995, 1996) extrapolated with a Salpeter slope, so either the slope is flatter than Salpeter, or the HST spectral types are biased towards earlier types. The star-formation history is dominated by three bursts of increasing strength occurring 5My, 2.5My, and $\lesssim$1.5My ago, the latest one responsible for most of the star-formation within 6 pc from the cluster center. A spherically symmetric structure is detected at about 6 pc from the cluster center which contains predominantly massive stars and has a flatter IMF. The surface number density profile of the cluster is shown to be well modeled by a single power law, $\Sigma(R) \simeq R^{-\alpha}$, over $0.4\,\mathrm{pc} < R < 12\,\mathrm{pc}$, with $\alpha \approx 1.85$, significantly steeper than isothermal.

Key words: stars: early-type – stars: Hertzsprung–Russel (HR) and C-M diagrams – stars: luminosity function, mass function – ISM: dust, extinction – Galaxy: open clusters and associations: general – galaxies: Magellanic Clouds

Send offprint requests to: fselman@ESO.org

⋆ Based on observations collected with the NTT ESO telescope.

1. Introduction

The Initial Mass Function (IMF) of starburst clusters has become critical for our understanding of the Universe at high redshifts. Starbursts are a natural consequence of tidal interactions and merging (e.g. Mihos & Hernquist 1994, and references therein) and there are good reasons to believe that these processes were more frequent in the past (Barnes 1998): first, recent work suggests that the number of pairs of galaxies was larger in the past than it is today (Abraham 1999); second, most of the high z galaxies, as revealed for example by the *Hubble Deep Field* (HDF) can be classified as Irr/Pec/Merger (Glazebrook et al. 1995; Abraham et al. 1996). In addition, the signatures of starbursts have been actually observed at very large redshifts (Pettini et al. 1998). Thus, violent star formation and starburst clusters have gained a new status: a large fraction of the old stellar population of present day galaxies appears to have formed in starbursts. 30 Doradus, as the nearest example of a starburst cluster and the only one whose stellar population can be spatially resolved from the ground, is a natural laboratory for our studies of the IMF of these objects.

Beyond its importance in helping us decode the information contained in the light we receive from distant objects, the IMF is interesting in its own right. In what follows it will be useful to recognize, somewhat arbitrarily, three mass ranges: (1) the low mass end defined by $M < 1M_\odot$; (2) the intermediate mass range defined by $1M_\odot \lesssim M < 20M_\odot$; and the high mass end defined by $20M_\odot \lesssim M < 120M_\odot$. It has recently being proposed that the stellar IMF is the direct result of a random sampling of a fractal molecular cloud system (Elmegreen 1997). In this view the form of the IMF has its origin in the turbulent processes that give molecular clouds their fractal structure, so the intermediate and high mass range IMF is expected to be a universal power law function, $dN \propto M^{-(1+\Gamma)}dM$, with an exponent close to the Salpeter value, $\Gamma = 1.35$ (Salpeter 1955).

Notwithstanding its attractiveness, the idea of universality is contradicted by some observations of clusters in the Large Magellanic Clouds (LMC) and the Milky Way. These observations reveal a mass function subject to important regional variations in the intermediate to high mass range (Parker et al. 1992; Walborn & Parker 1992), variations that have been used to support the idea of propagating or contagious star formation. However, a

proper control over systematic effects is a pre-requisite to properly analyze this type of observations. In this paper, the third in a series of papers studying the IMF and star-formation history of the 30 Doradus superassociation, we develop a method that reduces the magnitude of systematic effects thus permitting the determination of stellar physical parameters in an unbiased way. In particular, we show that a hitherto neglected systematic effect might be responsible for some of the claims of regional variations of the IMF mentioned above.

In Paper I we used *Daophot II* (Stetson 1997; Davis 1994) to analyze a set of UBV frames of 30 Doradus obtained in subarcsecond seeing and photometric conditions. The overall completeness limit, defined as the magnitude at which the probability of detection in all three filters equals 50%, was found to be V=19.2. These observations are used, together with the spectroscopy presented in Paper II (Bosch et al. 1999), to determine the reddening law of the region. In this paper we combine the photometry and reddening determination from Paper I with the spectroscopy from Paper II to "read" the star-formation history of the region, and to determine its IMF for almost the full intermediate to high mass range. This will give us the keys to interpret other regions of star formation. Reddening is shown to play a crucial role, as the culprit of a hitherto scarcely described systematic effect, possibly responsible for some of the variations that have been found in the IMF slopes of various systems.

2. From UBV photometry to physical parameters: the colour-magnitude stereogram

The determination of the fundamental physical parameters of massive stars in young clusters from UBV photometry poses a formidable observational challenge (Melnick 1992; Massey 1998). In fact, it has been claimed that the problem is equally challenging even for photometric systems extending into the far UV (Hunter et al. 1997). In Paper I we introduced a new tool, the Color-Magnitude Stereogram (CMS) and we showed how this tool can be used to visualize the different systematic effects that complicate the problem, including the effects of zero point calibrations (especially in the U-band), the effect of variable reddening, etc. In fact, the CMS is much more than just a visualization tool; it also provides possibly the only tool to derive the fundamental stellar parameters (age, effective temperature, luminosity) from UBV magnitudes in the presence of strong and variable reddening. A detailed description of this process is presented below.

2.1. The theoretical surface

The *theoretical surface* in the CMS is the locus of all stars in a reddened cluster in the absence of observational errors. To see this better, consider a cluster of coeval stars. In the three dimensional [(B-V),(U-B),V] space (the CMS) these stars fall on a spatial curve which is the generalization of the corresponding isochrone. In the presence of reddening, these stars are shifted away from the isochrone along a vector which can be parametrized by $\mathrm{R_V} = \mathrm{A_V/E(B-V)}$ and $\mathrm{S} = \mathrm{E(B-V)/E(U-B)}$. If, as is the case for 30 Doradus, the reddening is variable and changes from star to star (see Fig. 7), all stars in the cluster fall on a surface, the *theoretical surface*, which is defined by the theoretical isochrone and the reddening vector $\mathbf{R} = (1, \mathrm{S}, \mathrm{R_V})$ times the color excess E(B-V). Thus, the position of a star on the theoretical surface univocally determines the reddening free colors of the star. Two real-life effects complicate this simple picture: the clusters stars are not necessarily coeval, and all observations are affected by measurement errors.

In order to deal with these effects we have developed a process which is in fact a generalization of the standard approach to three dimensions. We start with theoretical isochrones. We have used the Geneva tracks for Z=0.008 appropriate for the LMC as presented by Meynet et al. (1994). These models, which assume twice the standard value for the stellar mass loss rates, are chosen because they reproduce better the observed populations of massive stars in galaxies, but our results are insensitive to this parameter as we will show later. For each initial mass, $\mathrm{M_i}$, the models give effective temperatures (T_{eff}) and radius (R_{eff}) as a function of age (t) in million years. In principle, to convert these parameters to magnitudes and colors atmosphere models are needed. In practice, however, it is much simpler to use semi-empirical[1] conversions from T_{eff} to UBV colors (Schmidt-Kaler 1982, SchK) and T_{eff} to bolometric correction (Chleboswsky & Garmany 1991, ChG; Vacca et al. 1996, VGS; Malagnini et al. 1986). We have collected together these conversion tables in Fig. 1 for comparison and easy reference. Notice that the ChG temperature scale is much cooler than the VGS one. Since the temperature range spanned by the theoretical isochrones reach values much larger than those covered by ChG, their conversion produces a false turn-up in the HR-diagram. Therefore, in this paper we only consider the VGS calibration. For each age, we generate the theoretical surfaces transforming the theoretical isochrones into UBV space through these relations and applying the reddening vector over the full range of color excesses E(B-V) observed in the cluster. Examples of theoretical surfaces are presented in Fig. 2.

For each set of physical parameters we now have a unique set of observable quantities. We now need to solve the inverse problem: given a set of observations of a star, find the most probable combination of initial mass, age, and reddening that would result in that observation. The solution to this problem is well known and involves the use of Bayes theorem together with a model for the observational errors.

2.2. The Bayesian approach

In a Bayesian approach probabilities are assigned to hypothesis such as: *the star formed t years ago, with an initial mass M_i, and is presently reddened by an amount E(B-V).* Using a model of the phenomenon under study together with a model

[1] The model atmospheres of Kurucz (1993) were used to determine that, for dwarfs, metallicity effects are not important for the T_{eff}-color conversion in the mass range of interest in this research.

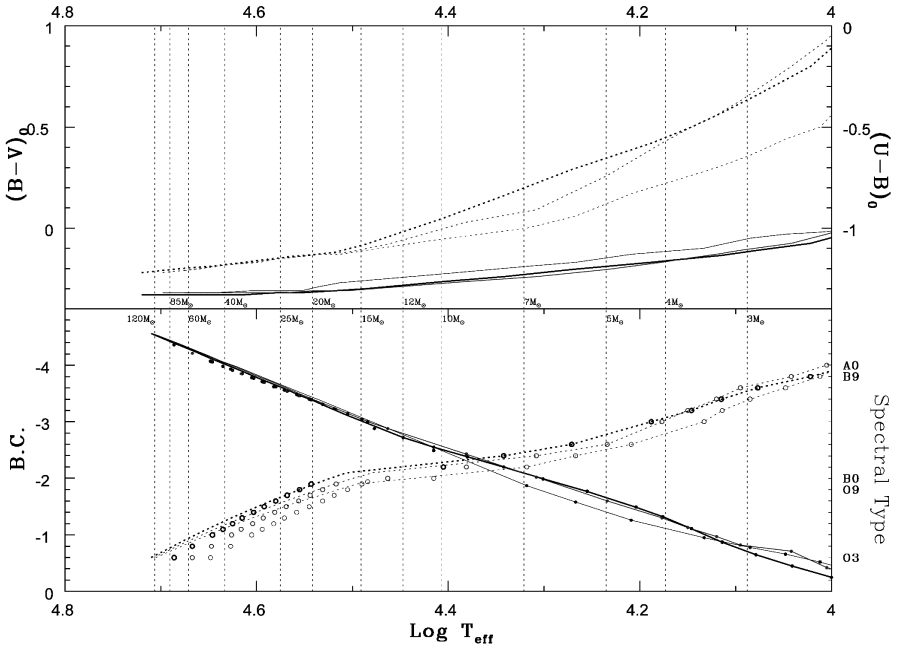

Fig. 1. Calibration relations for the conversion of observable to physical quantities. The dotted lines use the right hand axes and the solid lines use the left axes. Color transformations are from Schmidt-Kaler (1982); Bolometric Corrections (B.C.) and spectral type calibrations are and Malagnini et al. (1986) for the later spectral types merged smoothly with the calibrations for O-type stars of Vacca et al. (1996), lines, and Chlebowsky & Garmany (1991), dots. The effective temperatures of ZAMS stars of different masses have been drawn as vertical dotted lines.

of the measuring errors we can directly calculate the probability of obtaining a particular observation given a hypothesis. Then, Bayes' theorem is applied to obtain the probability of the hypothesis given the observation, once a suitable assumption about the *prior* probabilities of the hypothesis is made (see e.g. Kendall & Stuart 1977). The application of the Bayesian approach to the determination of the most probable age, initial mass, and reddening of the stars in 30 Dor given our UBV data is presented below.

2.2.1. Photometric solution

The first step is to produce a model of the observational errors. Because of error correlation effects it is simpler to work in a magnitude-magnitude space, as recently done by Tolstoy & Saha (1996), than to work in color-magnitude space. However, the additional complication of using colors is largely compensated by the fact that the CMS is conceptually simpler to interpret allowing us to better understand the data at the different stages of processing. Still, in order to model the errors it is convenient to start with the simpler magnitude-magnitude diagram generalized to three dimensions. In this space a measurement is represented by a vector $\mathbf{m}_*$ whose transpose is given by $\mathbf{m}_*^{\mathrm{T}} = (V_*, B_*, U_*)$. The components of this vector are independent[2] and therefore the covariance matrix is diagonal. A measurement will be characterized by the pair $(\mathbf{m}_*, Q^*_{\mathbf{m}})$, where $Q^*_{\mathbf{m}}$ is the *curvature matrix*, i.e. the inverse of the covariance matrix.

In the same space, a particular set of physical parameters for the star is represented, through the use of the calibrating relations (Fig. 1), by a vector $\mathbf{m}$. This value will be called the *true* magnitude of the star. The measurement process can be represented by a curvature matrix $Q_{\mathbf{m}}$. To solve the problem we have to assume that $Q_{\mathbf{m}} = Q^*_{\mathbf{m}}$.

Given that the observed value of a star's magnitude lies in a small neighborhood surrounding $\mathbf{m}_*$, let $p(\mathbf{m} \mid \mathbf{m}_*, Q^*_{\mathbf{m}})$ be the conditional probability density that the *true* value of the star's magnitudes is $\mathbf{m}$. Using Bayes theorem with equal a-priori probabilities for the true stellar magnitudes it can be shown that

$$p(\mathbf{m} \mid \mathbf{m}_*, Q^*_{\mathbf{m}}) \propto p(\mathbf{m}_* \mid \mathbf{m}, Q_{\mathbf{m}}) \qquad (1)$$

which is just the statement that, for a given model for the measuring process, the probability of the *true* value given the measurement is proportional to the probability of the measurement given the true value. Assuming independent Gaussian errors we can then write

[2] Magnitude error correlation effects can be introduced by crowding but they are much reduced if colors are used instead, as can be seen in Fig. 5 of Paper I.

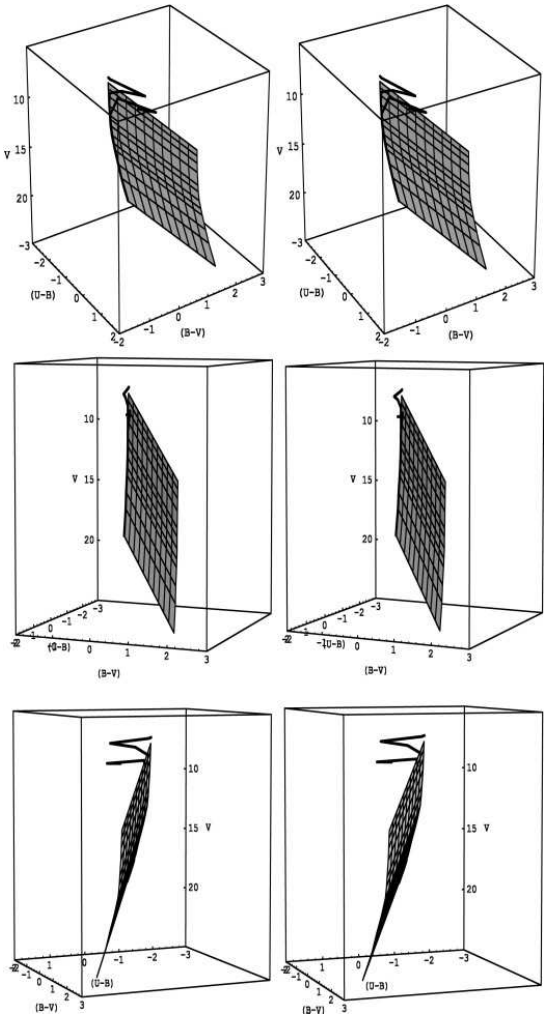

Fig. 2. The *theoretical surface*, described in the text, in the CM stereogram. The surface has been drawn for the 1 My isochrone with standard mass-loss. The reddening lines have been drawn for 120M$_\odot$, 85M$_\odot$, 60M$_\odot$, 40M$_\odot$, 25M$_\odot$, 20M$_\odot$, 15M$_\odot$, 12M$_\odot$, 10M$_\odot$, 7M$_\odot$, 5M$_\odot$, and 4M$_\odot$. A heavier line marks the 3 My isochrone. Another heavy line marks the 5 My isochrone which reaches only up to 40M$_\odot$! Notice in the upper viewpoint how evolution appears to get entangled with reddening. But the bottom perspective shows the degeneracy to be broken because evolution actually moves the star away from the reddening determined theoretical surface for a lower age isochrone.

$$p(\mathbf{m} \mid \mathbf{m}_*, Q^*_{\mathbf{m}}) \propto e^{-\frac{1}{2}[\mathbf{m}-\mathbf{m}_*]^{\mathrm{T}} Q_{\mathbf{m}} [\mathbf{m}-\mathbf{m}_*]} \propto e^{-\frac{1}{2}\chi^2(\mathbf{m})}, \quad (2)$$

where $Q^*_{\mathbf{m}} = \mathrm{Diagonal}(\sigma_V^{-2}, \sigma_B^{-2}, \sigma_U^{-2})$. It can be shown that χ^2 is indeed distributed as the standard χ^2-distribution with 3 degrees of freedom (Brandt 1970). In case of non-Gaussian errors we can keep the equation above changing to a different $\chi^2(\mathbf{m})$ function.

In the CMS space a measurement will be characterized by a vector $\mathbf{x}$ given by $\mathbf{x}^{\mathrm{T}} = (\text{B-V}, \text{U-B}, \text{V})$. Since $\mathbf{x}$ is related to $\mathbf{m}$ by a unitary transformation, the probability density of $\mathbf{x}$ is given by

$$p(\mathbf{x}) = e^{-\frac{1}{2}[\mathbf{x}-\mathbf{x}_*]^{\mathrm{T}} Q_{\mathbf{x}} [\mathbf{x}-\mathbf{x}_*]} \quad (3)$$

where $Q_{\mathbf{x}} = O^{\mathrm{T}} Q_{\mathbf{m}} O, O\mathbf{x} = \mathbf{m}$. The price paid for working in color-magnitude space is that the covariance matrix $C_{\mathbf{x}} = Q_{\mathbf{x}}^{-1}$ is no longer diagonal.

The problem to be solved for each star is: given a measurement $(\mathbf{x}_*, Q^*_{\mathbf{x}})$, find the most probable value for $\mathbf{x}$ subject to the condition that it should belong to the *theoretical surface.* Maximizing the probability is equivalent to finding the maximum of the likelihood function $L(\mathbf{x}) = \log\ p(\mathbf{x})$, or the minimum of $\chi^2(\mathbf{x}) = -2 \times L(\mathbf{x})$. Unless the matrix $Q_{\mathbf{m}}$ is singular (a situation that can not occur unless one or more of the measurement errors is equal to zero), the solution to the problem always exists. The reader can convince him/herself of this by considering χ^2 as a quadratic form, and realizing that there will always exist a value of χ^2 for which the ellipsoid thus defined touches the theoretical surface. For reasonably smooth theoretical surfaces the solution will be unique.

Let us parameterize the isochrone for time t with the initial mass M$_i$. Then, in the CMS it is represented by the equation $\mathbf{x} = \mathbf{x}_t(M_i)$. The theoretical surface is then represented by the equation

$$\mathbf{x} = \mathbf{x}_t(M_i) + \text{E(B-V)} * \mathbf{R}, \quad (4)$$

where $\mathbf{R}$ is the reddening vector $\mathbf{R} = (1, S, R_V)$, and E(B-V) is the color excess. Thus, for a given M$_i$ and t the color excess which minimizes χ^2 is given by

$$\text{E(B-V)} = \frac{[\mathbf{x}_* - \mathbf{x}_t(M_i)]^{\mathrm{T}}\, Q^*_{\mathbf{x}} \mathbf{R}}{\mathbf{R}^{\mathrm{T}} Q^*_{\mathbf{x}} \mathbf{R}}. \quad (5)$$

The actual procedure used to find the most likely values of M$_i$, t, and E(B-V) for a star is as follow: first, a library of isochrones is prepared; each isochrone in the library consists of a tabulation of M$_i$, T$_{eff}$, and M$_{bol}$, together with the calibration relations which permits the calculation of the vector $\mathbf{x}_t(M_i)$, that is, magnitude and colors. Once the library has been set up the following procedure is carried out for each star:

1. from its observed magnitudes calculate the matrix $Q^*_{\mathbf{x}}$ and the vector $\mathbf{x}_*$;
2. for each isochrone indexed by its age, t, find the mass, M_i, and E(B-V) from Eq. (5), which minimizes the χ^2 implicitly defined in Eq. (2);
3. assign the probability defined by Eq. (3) to the solution determined in the previous step;
4. calculate average values and variances of the physical parameters over the whole set of isochrones using the probabilities as weights.

Although this is not the most computationally efficient method it avoids the convergence problems introduced by the complex topology of the theoretical surfaces at high masses.

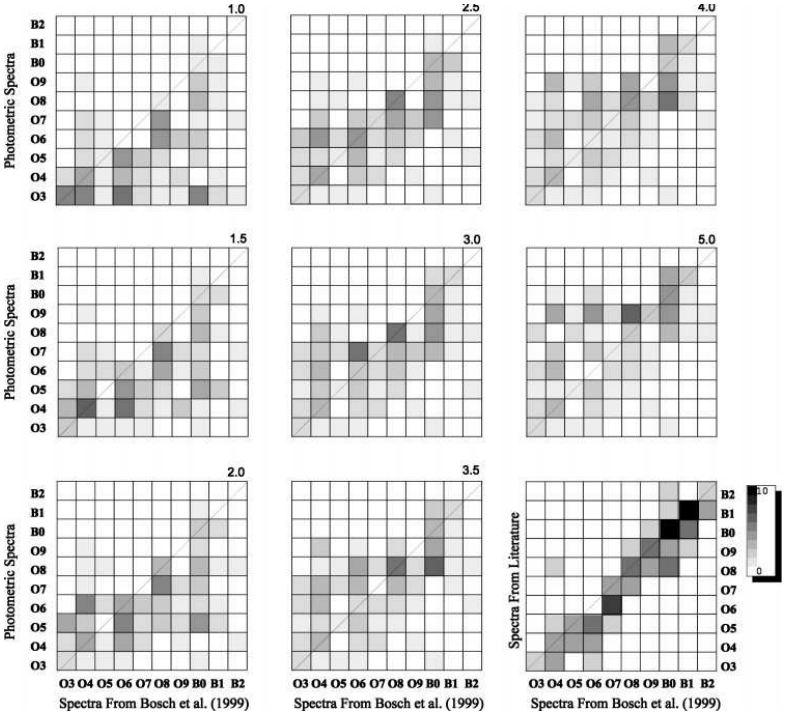

Fig. 3. Comparison of spectral types obtained photometrically as described in the text, with the "true" spectral types determined in Paper II. The comparison is done for eight libraries of isochrones (Z=0.008, twice standard mass-loss rates). The number in the upper right of each comparison indicates the age in My of the oldest isochrone employed; between 0 and the maximum age the isochrones are uniformly distributed. The plot in the lower right panel compares the spectroscopic types from Paper II to values from the literature and gives an indication of the uncertainties in the "true" spectral types (the literature types are mainly from Melnick 1985, Parker & Garmany 1993, and Walborn & Blades 1997). These diagrams show that the O3–O6 stars can be modeled with isochrones not older than 2.5My, but for the later classes it is necessary to include older isochrones.

2.2.2. Spectroscopic solution

Spectroscopic observations for 85 of the stars in the frame can be used to better constrain their physical parameters. To get a second solution as independent as possible from the photometric solution, we will disregard color information and use only spectral types and V magnitudes. The procedure is formally equivalent to the photometric one with a different χ^2 function.

The spectroscopic data can also be used to check the photometric solution. This is done by comparing the stellar types predicted photometrically with those obtained through spectroscopy. The photometric types depend on the star-formation history one assumes for the cluster. This is illustrated in Fig. 3, which compares our photometric spectral types with those measured spectroscopically. The correlation obtained when comparing spectroscopic types from different authors is shown for reference. The figure shows that the photometric method is able to predict spectral types with an accuracy of 3 subtypes approximately (0 to 3.0 My case). More importantly, this can be done without introducing a large bias towards later spectral types as is the case with the traditional method (e.g. Massey 1998).

An independent check of the method can be obtained by combining the spectroscopic solution with the photometric one. This is presented in the Appendix where a distance modulus of $(m-M)_0 = 18.45 \pm 0.15$ to the LMC is obtained, in excellent agreement with previous work (e.g. Gieren et al. 1998).

2.3. The HR diagram

Fig. 4 shows the HR diagrams determined with this method using the VGS effective temperature scale, the SchK effective temperature to color transformation, and the Geneva isochrones for standard (Schaerer et al. 1993) and twice standard (Meynet et al. 1994) mass-loss rates. The stars with spectroscopy are represented with open circles and the stars with photometry alone by small dots. The physical parameters of the stars have been determined with the Bayesian method using an uniformly populated library of isochrones from 0.1 My to 145 My.

Several points can be made from these diagrams. First, our transformation from observable to physical quantities is rather insensitive to the mass-loss rates assumed for the theoretical models. Second, the VGS calibration from colors to effective temperatures might introduce a spurious turn-off at approximately 1 My because its highest temperature is still below that of the isochrones. Third, there is a spurious concentration of data points at $\log T_{eff} \sim 4.2$ and $M_{bol} \sim -2$ which results from the photometric errors of stars with masses $M < 10 M_\odot$. Since the photometric errors are larger than the evolutionary change in colors for stars in this mass range, stars tend to cluster near the average of the isochrone library (0.1–145 My). The last point we wish to remark is that there is a group of stars that appear to have masses $M > 120 M_\odot$. This suggests that the upper mass limit of the IMF may be larger than $\sim 120 M_\odot$, although we cannot exclude that some of these stars may be massive binaries, or

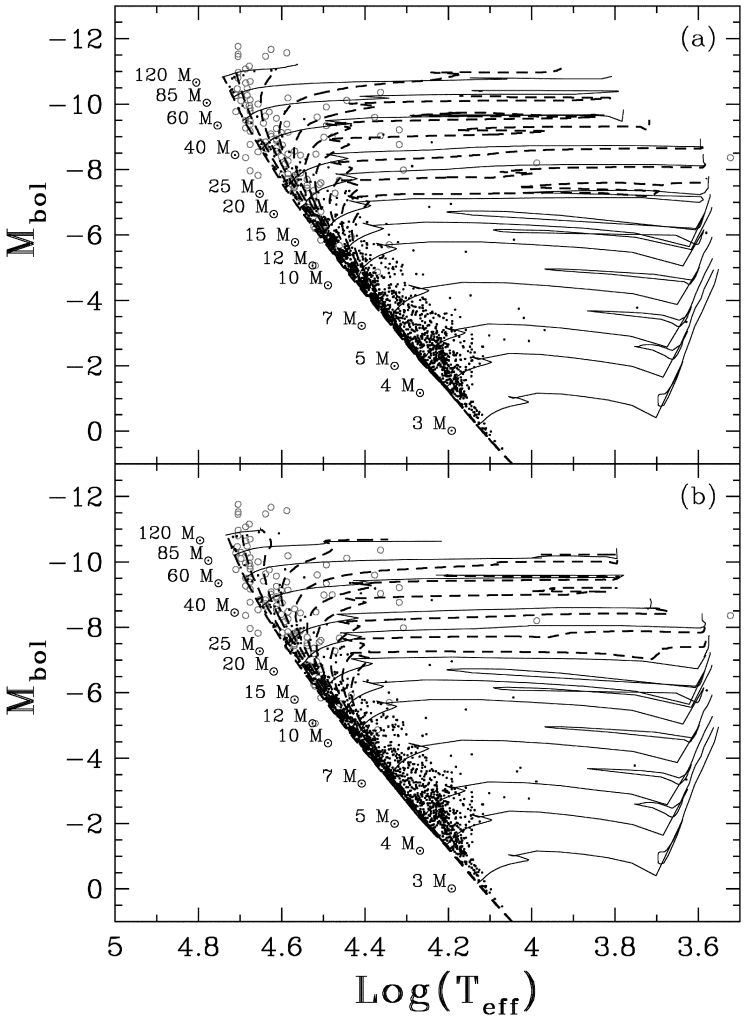

Fig. 4a and b. HR diagram of NGC 2070. The open circles represent stars with spectral types from Paper II. The dots show the positions of the stars from photometry alone. The solid lines show the Geneva tracks for Z=0.008 and the standard **a** and twice the standard **b** mass loss rates. The dashed lines plot isochrones of 0.1, 1, 2, 3, 4, 5, 6, 8, 10, and 12 My.

that physical effects such as mixing or rotation (not considered in the models) are affecting the mass determinations.

For the discussion it is important to summarize our results from the HR-diagram as follows: (1) while from photometry alone we cannot constrain the ages for the low mass and for some of the intermediate mass stars (for those with $M < 10M_{\odot}$), we can still reliably determine their masses if we know their ages (e.g by assuming that they have the same formation history as the more massive stars in the cluster); (2) the rapid rate of evolution of the high mass stars, although not accurately known because of the uncertainties in their mass-loss rate, permits us to determine their ages, and thus, study the star-formation history of the cluster.

2.4. Systematic errors

A most delicate step in the determination of the IMF of a cluster is the determination and control of systematic effects. Once a set of stellar evolutionary models and a T_{eff}-color calibration has been chosen, the process is in principle straightforward: count the number of stars that fall in each (logarithmic) mass bin.

There are two main complications when applying this procedure to real data. The first is the well known problem of determining the incompleteness corrections. The second complication is due to the *magnitude-limit correction*: for a given absolute magnitude a star will have a different probability of being included in a magnitude-limited sample depending on the amount of reddening along its line of sight. For $A_V = 3.0$, even stars with absolute magnitudes as bright as $M_V = -2.5$ are affected

by this effect in a sample with magnitude limit $V_{lim} = 19.0$. This corresponds to a zero-age main sequence mass of approximately $15 M_{\odot}$.

2.4.1. The incompleteness correction

Artificial stars were created with a uniform distribution of magnitudes and colors over the range spanned by the real stars (omitting only the very reddest stars). These stars were then added to the original frames with the appropriate instrumental magnitudes calculated using the inverse of the instrumental equations determined in Paper I to create the catalogue of real stars. Each artificial star was then added at the appropriate location in each of the frames analyzed (remembering the small frame offsets). To avoid changing the crowding by too much the artificial stars were added a few at a time in many Monte Carlo experiments, such that less than $\sim 15\%$ of the total number of stars in the frames were added at a time. *Daophot II*'s `addstar` was used within the PC/LINUX IRAF environment to actually add the stars to the frames. The frames with the artificial stars were then reanalyzed from beginning to end in exactly the same way as the final data was. In doing this it was found that the recovery probability depended not only on the magnitude of the stars, but also on their colors. In addition, the the recovery probability depends locally on the surface density of stars[3]. More than 40 000 artificial stars were added to the frames in more than 200×3 experiments. A script was written to automate the process. Each experiment took approximately 14 minutes to run on a 200MHz Pentium Pro machine.

When calculating the IMF each of the real stars will contribute not one star, but a number equal to the inverse detection probability. This number depends on the position (or rather the local stellar surface density, ρ) of the star, its magnitude, V, and its color, (U-B). To determine it star-by-star we created a table (see Table 1) with the results of the MC experiments, and use a 3-dimensional cubic splines interpolation routine (Press et al. 1994) to determine, for a given (ρ,V,(U-B)), its detection probability. For easy reference we include in Table 1 the actual number of stars added, Nadd, the number of stars recovered, Nrec, and the detection probability, p.

The maximum density for which we can determine reliable incompleteness corrections depends on the number of Monte-Carlo experiments one can perform in a reasonable amount of time. The 600 experiments performed here took approximately 140 CPU hours, and, for $V < 19.5$, permit us to correct the data up to $\log \rho \approx 3.3$, where, ρ, the local stellar surface density is measured in stars per arcmin^2 (for $r > 15''$ the surface density is smaller than this for all but one star, see Fig. 5).

Fig. 5 shows scatter plots of the data as a function of V magnitude, radial distance to the cluster center, and local stellar density. The Monte-Carlo experiments show that the apparent boundaries defined by the sharp decrease in the number density of points at high stellar densities and small radial distances are due to incompleteness effects and have no physical significance. These figures can then be used to construct "fair" samples for the study of the IMF defined as regions in these diagrams where the incompleteness corrections are well established.

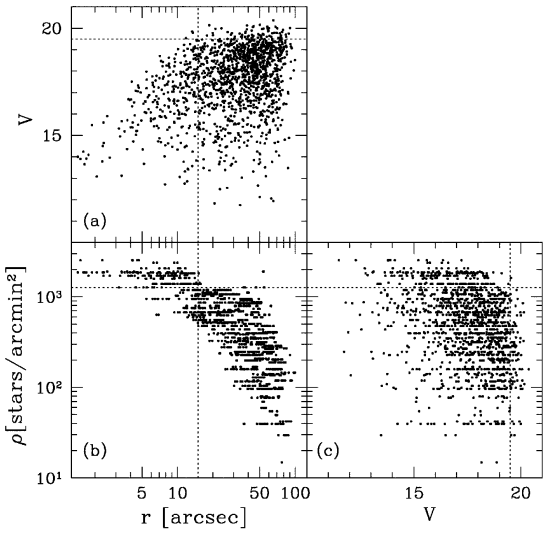

Fig. 5a–c. a V magnitudes as a function of distance to the cluster center for the whole sample of stars. The upper envelope of the cloud of points defines the magnitude limit of the photometry. **b** Log of the stellar density as a function of distance to the cluster center. **c** Same as **a** but as a function of local stellar density (with axes interchanged).

We have thus constructed two samples: an *outer* sample defined by $r > 15''$, which is "fair" down to $V \approx 19.5$, and an *inner* sample defined to correspond to the outermost sample of the HST study of Hunter et al. (1995, 1996), and which is "fair" down to $V \approx 17 (r > 4.6'')$.

2.4.2. The magnitude-limit correction

Once the incompleteness correction has been determined it becomes necessary to apply the *magnitude-limit correction*. This correction can be understood by tracing the steps for the conversion from physical parameters to observed magnitude and colors. Consider a B3 zero age main sequence star, which according to SchK has an absolute magnitude of $M_V \approx -1.1$ and a mass of $M \approx 7.6 M_{\odot}$. At zero reddening this star would have an apparent magnitude $V = 17.40$, well within the magnitude limit of the catalogue in Paper I ($V_{lim} = 19.2$). Nevertheless, this star would not be included in a photometry with a cut-off at this magnitude limit if $A_V \gtrsim 1.8$.

Correcting for incompleteness alone does a proper job for all stars whose absolute magnitude is brighter than $V_{lim} - (m - M)_0 - A_V^{max}$, where A_V^{max} is the maximum total extinction

[3] A code was written to determine the local stellar density around each of the artificial stars. This program takes each artificial star position and determines approximately the largest square that contains it and none of the real stars. The inverse of this area is used as an approximate measure of the local stellar density. The algorithm to do this is similar to that in the tree-code of Barnes & Hut (1986).

Table 1. Results of artificial stars experiments. The number in parenthesis below the density range denotes the average density for all the stars in that range; Nadd is the number of stars added; Nrec is the number of stars recovered; p is the detection probability. The total number of added stars in the table is 38646, which together with the 1500 stars used to study systematic errors in Paper I make a total of 40 146.

		$-1.5 < (U-B) < -0.5$			$-0.5 < (U-B) < 0.0$			$0.0 < (U-B) < 0.5$		
$\log\rho$ [stars/arcmin^2]	V	Nadd	Nrec	p	Nadd	Nrec	p	Nadd	Nrec	p
$\log\rho > 3.2$	$V < 15.0$	62	59	0.952	48	42	0.875	29	28	0.966
(3.23)	$15.0 < V < 16.0$	56	52	0.929	47	36	0.766	38	29	0.763
	$16.0 < V < 17.0$	85	71	0.835	52	41	0.788	32	21	0.656
	$17.0 < V < 18.0$	147	70	0.476	144	60	0.417	113	38	0.336
	$18.0 < V < 18.5$	69	23	0.333	79	21	0.266	66	13	0.197
	$18.5 < V < 19.0$	73	10	0.137	62	12	0.194	64	3	0.047
	$19.0 < V < 19.5$	79	5	0.063	76	4	0.053	72	3	0.041
	$19.5 < V < 20.0$	177	0	—	189	0	—	215	0	—
$3.0 < \log\rho < 3.2$	$V < 15.0$	60	54	0.900	49	40	0.816	42	37	0.881
(3.07)	$15.0 < V < 16.0$	79	74	0.937	51	43	0.843	40	30	0.750
	$16.0 < V < 17.0$	80	70	0.875	49	41	0.837	41	27	0.659
	$17.0 < V < 18.0$	231	164	0.710	243	151	0.621	187	102	0.545
	$18.0 < V < 18.5$	98	49	0.500	101	59	0.584	96	34	0.354
	$18.5 < V < 19.0$	96	34	0.354	103	34	0.330	102	24	0.235
	$19.0 < V < 19.5$	98	12	0.122	93	19	0.204	97	10	0.103
	$19.5 < V < 20.0$	211	11	0.052	230	4	0.017	231	0	—
$2.8 < \log\rho < 3.0$	$V < 15.0$	133	126	0.947	118	115	0.975	105	100	0.952
(2.90)	$15.0 < V < 16.0$	118	113	0.958	108	101	0.935	104	97	0.933
	$16.0 < V < 17.0$	161	153	0.950	145	128	0.883	122	110	0.902
	$17.0 < V < 18.0$	548	477	0.870	566	466	0.823	498	384	0.771
	$18.0 < V < 18.5$	271	217	0.801	240	189	0.787	238	153	0.643
	$18.5 < V < 19.0$	264	175	0.663	281	175	0.623	248	103	0.415
	$19.0 < V < 19.5$	231	112	0.485	276	109	0.395	214	58	0.271
	$19.5 < V < 20.0$	584	44	0.075	580	45	0.078	607	13	0.021
$2.6 < \log\rho < 2.8$	$V < 15.0$	75	70	0.933	62	60	0.968	55	52	0.945
(2.71)	$15.0 < V < 16.0$	66	58	0.879	45	44	0.978	47	47	1.000
	$16.0 < V < 17.0$	67	58	0.866	82	79	0.963	57	51	0.895
	$17.0 < V < 18.0$	271	238	0.878	247	221	0.895	212	179	0.844
	$18.0 < V < 18.5$	129	107	0.829	139	110	0.791	127	90	0.709
	$18.5 < V < 19.0$	128	91	0.711	158	105	0.665	122	47	0.385
	$19.0 < V < 19.5$	125	65	0.520	132	49	0.371	109	18	0.165
	$19.5 < V < 20.0$	284	18	0.063	289	14	0.048	295	8	0.027
$2.2 < \log\rho < 2.6$	$V < 15.0$	243	237	0.975	212	209	0.986	270	263	0.974
(2.41)	$15.0 < V < 16.0$	184	177	0.962	198	197	0.995	202	198	0.98
	$16.0 < V < 17.0$	238	230	0.966	220	212	0.964	206	194	0.942
	$17.0 < V < 18.0$	1086	1043	0.960	1129	1064	0.942	1034	973	0.941
	$18.0 < V < 18.5$	556	527	0.948	611	567	0.928	530	471	0.889
	$18.5 < V < 19.0$	529	476	0.900	601	489	0.814	500	339	0.678
	$19.0 < V < 19.5$	504	370	0.734	527	321	0.609	512	219	0.428
	$19.5 < V < 20.0$	1321	156	0.118	1405	125	0.089	1418	68	0.048
$\log\rho < 2.2$	$V < 15.0$	160	159	0.994	154	153	0.994	146	145	0.993
(2.05)	$15.0 < V < 16.0$	131	130	0.992	114	112	0.982	104	102	0.981
	$16.0 < V < 17.0$	137	136	0.993	123	121	0.984	121	119	0.983
	$17.0 < V < 18.0$	732	713	0.974	713	696	0.976	705	672	0.953
	$18.0 < V < 18.5$	370	357	0.965	388	371	0.956	311	283	0.910
	$18.5 < V < 19.0$	390	366	0.938	388	332	0.856	334	235	0.704
	$19.0 < V < 19.5$	389	286	0.735	381	251	0.659	349	164	0.470
	$19.5 < V < 20.0$	982	157	0.160	947	104	0.110	920	47	0.051

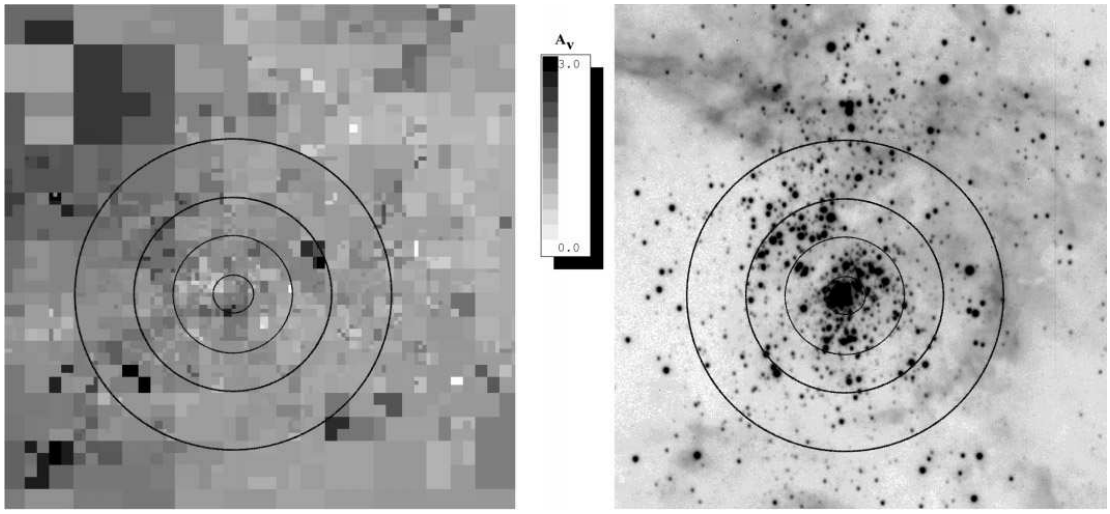

Fig. 6. The probability distribution of visual absorption Av. The top panel shows that the extinction distributions of high mass and low mass stars are virtually identical. The bottom panel separates the sample using the radial distance to the cluster center. There is a clear trend of larger extinction towards the cluster center (which can not be the result of systematic errors, as discussed in Paper I). Only stars brighter than V=16.2 have been included in the bottom panel to ensure a fair sample.

for the stars in the cluster. Fig. 6 shows that for 30 Doradus this value is given by $A_V^{max} \approx 3.0$. Thus, the catalogue can be used with incompleteness correction alone only down to $V = 16.20$, which corresponds to $M_V = -2.3$, or $13 M_\odot$. Parker & Garmany's (1993) catalogue is complete to $V = 18.0$, which would translate to $M \approx 20 M_\odot$.

Stars with $M_V = -1.1$ and $A_V \lesssim 1.8$ will be included in the catalogue with a probability given by the incompleteness correction for the appropriate apparent magnitude, color, and position in the frame. *All those stars with $A_V \gtrsim 1.8$ will be lost.* Thus, for each star of this absolute magnitude detected a further correction should be applied: the star contribution to the appropriate mass bin should be divided by the probability of inclusion, i.e. the fraction of these stars with $A_V \lesssim 1.8$. This fraction can be calculated assuming that the probability distribution A_V is independent of absolute magnitude. The probability of inclusion is then given by the area under the curve in Fig. 6 between $A_V = 0$, and $A_V = V_{lim} - V$.

This reddening induced problem has already been recognized in a few recent studies of deeply embedded clusters. The complications introduced by reddening become most severe in the study of these clusters, as recognized in the recent infrared work of Meyer (1996). Nevertheless, in order to apply the magnitude-limit correction it is necessary that A_V^{max} be well defined. Fig. 6 shows that this is indeed the case for NGC2070. For the extremely embedded clusters the situation is not as fortunate, and a limit for A_V^{max} is not evident in the data (e.g. Fig. 6 of Carpenter et al. 1997). In this case it becomes necessary to select a subsample of the data imposing an upper limit for A_V in what is called an A_V-limited sample (Meyer 1996).

For the correction to work we should be able to define a meaningful reddening distribution. First, if present, systematic differences in reddening for stars of different mass should be considered. In Fig. 6a the stars have been divided into two subsamples of different masses. Using the χ^2 test we find that the hypothesis that the two samples have been drawn from the same distribution can only be rejected at the 10% confidence level. It is then appropriate to use the same distribution of reddening for stars of different masses.

A different conclusion is reached after examining Fig. 6b, where the sample has been subdivided according to the distance of the stars to the cluster center. In this case a χ^2 test shows that the hypothesis that the two samples have been drawn from the same parent distribution can be rejected at the 99.5% confidence level. This is the photometric counterpart to the conclusion reached in Paper I, based on the spectroscopy and photometry, that there is a reddening component associated to the cluster itself, and that the average reddening due to this component increases towards the center (Fig. 5 of Paper I shows that this can not be a systematic effect due to a higher probability of blending near the center: no systematic trends with radius were uncovered by the MC experiments reported in that work).

Fig. 7 stresses the importance in determining the reddening for each star individually. It shows a reddening map, together with a reference B image. The map was created with a recursive tree algorithm specially designed to preserve the high resolution in higher stellar density areas. We can appreciate that together with the high spatial variability, there are some clear large scale trends, the most noteworthy being an east west gradient, an area of increased reddening towards the north-east, and a zone of

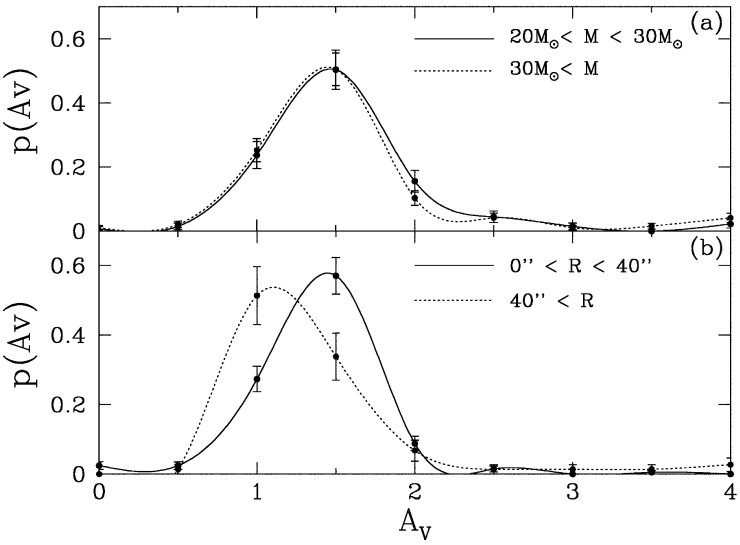

Fig. 7a and b. Reddening map of 30 Doradus calculated with an adaptive algorithm to preserve spatial resolution. The circles are centered in R136 with radii of 5″, 15″, 25″, and 40″. The image is a copy of the B frame employed for the photometry. The reddening scale goes from Av=0 to Av=3.0, calculated assuming Rv=3.05. North is up and east to the left; size is 133″or ∼30 pc.

large reddening variation with an above average mean near the cluster center[4].

3. Results and discussion

3.1. The star-formation history of 30 Doradus

The star-formation history presented by Massey & Hunter (1998a, 1998b) asserts that the massive stars formed last, in accordance with the *sequential* picture proposed by Herbig (1962). The large number of O3 stars observed by HST is thus explained as an age effect: these extremely massive stars, which do not last for more than 1My, were the last to form quenching any further star formation in the center of the cluster. An alternative picture of star formation, which has been called *contemporaneous* by Stahler (1985), proposes that the star formation rates of stars of different masses is not a function of time: at all masses the probability of formation, although fluctuating, is approximately constant since the beginning of the star formation event. When averaged over the lifetime of the cluster we find a higher average star formation rate for the less massive stars, precisely the information contained in the IMF. In contrast to the sequential star formation scenario, but also stochastically, the most massive stars can appear at any time during the lifetime of the cluster with equal probability. According to Elmegreen (1997) the presence or absence of high mass stars depends on the total number of stars formed according to a *stochastic sampling* of an universal IMF.

Fig. 8 shows the star-formation history of 30 Doradus determined using the ages and masses derived from the Bayesian method and equally likely isochrones up to 15My. The upper curve on the top panel gives the main sequence lifetime as a function of mass (defined as that point in the evolution when the surface fraction of Hydrogen falls below 40%.) The lower curve gives 1σ errors in the estimated ages[5]. For $M > 40M_{\odot}$ the photometric solution gives approximately the same star-formation history as the spectroscopic one. Below this limit there is a tendency for the photometric solution to track the mean isochrone of the library. Thus we have used both the spectroscopic and the photometric solutions to draw the high mass histogram shown in the lower panel. For the low mass histograms we have used only stars with spectroscopy. Three unresolved peaks in the star-formation rate are clearly seen in this figure: a *young* peak at $0 < t < 1.5My$, a *middle-age* peak at $1.5My < t < 3.5My$, and an *old* peak at $4My < t < 6My$. The weakness of the young peak in the lower mass bin is an artifact introduced by the incompleteness of the spectroscopy for these stars.

Fig. 9 shows the spatial distribution of the stars in the three age groups. The region within 15″ is populated almost exclusively by young stars (green dots) while the other two groups tend to avoid this region. Even outside the central region the young stars appear to be more clustered than the middle-age stars (yellow dots), which in turn appear to be significantly more clustered than the old stars (red dots). Also shown in Fig. 9 are the O3If/WN and the WR stars which appear mostly within

[4] This way of presenting the reddening data emphasizes the spatial variations while optimizing spatial resolution. Showing these variations is what we wanted to accomplish with it. The average excess reddening towards the center is only barely discernible in this picture because: (1) the effect is small (0.5 mags); and (2), the reddening of a few highly reddened stars near the outskirts of the clusters dominate a much larger area, giving them a much larger weight in our perception.

[5] The absence of stars more massive than $100M_{\odot}$ and younger than 0.5My is an artifact of using a set of evolutionary tracks with an upper mass limit apparently below the highest masses present in the cluster (see discussion on upper mass limit below).

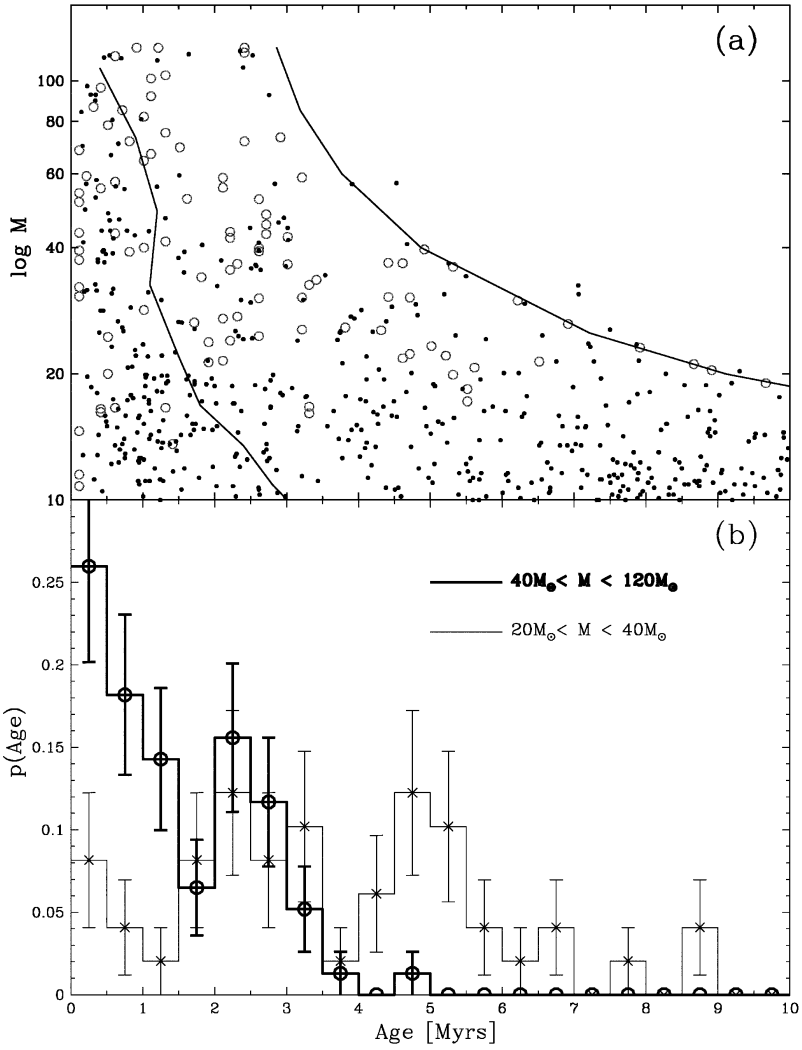

Fig. 8. **a** Star-formation history as a function of mass. The curve that envelopes the data shows the main sequence lifetime as a function of mass. The lower curve gives an estimate of the 1σ errors in the ages, determined using a weighted average of the square deviations from the determined mean ages. Solid dots represent stars placed with photometry alone; open circles represent stars placed with spectroscopy and their V magnitudes. Above $40M_{\odot}$ both sets of points reveal the same history. **b** Histograms of ages for the stars with $r > 5''$: the heavy line was drawn using spectroscopic solution if available, and photometric solution otherwise. The thin line was drawn using spectroscopic data exclusively. Three different episodes of star formation appear to be revealed by the data.

$r < 15''$, with a few of the WR stars associated with subgroups located at $r > 40''$ (Brandl et al. 1996, coined the term "ring-like structure" to refer to the spatial distribution of these stars near the core). Two of the four O3If/WN stars are associated with the middle-age peak, but both are closer to the center than typical for that age group. The WR stars, supposed to have ages between 3My and 7My, would be associated with the old peak. They also appear spatially segregated from the rest of the stars in this age group.

The star-formation history of 30 Doradus appears to be dominated by three distinct bursts of increasing strengths which took place approximately 5My, 2.5My, and $\lesssim$1.5My ago. The fact that the central parts of the cluster are populated almost exclusively by young stars, while both older and younger stars populate the periphery provides evidence that star formation propagated inwards. This appears to be contradicted by the distribution of WR stars which, being "old", are centrally concentrated. Note, however, that de Koter et al. (1997) have shown that several WR stars in the core of the cluster may, in fact, be very young. In that case their location near the center would be consistent with that of the rest of the young massive stars.

Working over a much wider area, Walborn & Blades (1997) identified five age groups in 30 Dor, three of which are similar to the ones identified here. Of particular interest are the 5My stars which appear to be uniformly spread over the face of the nebula supporting the idea that star formation propagated inwards in the cluster.

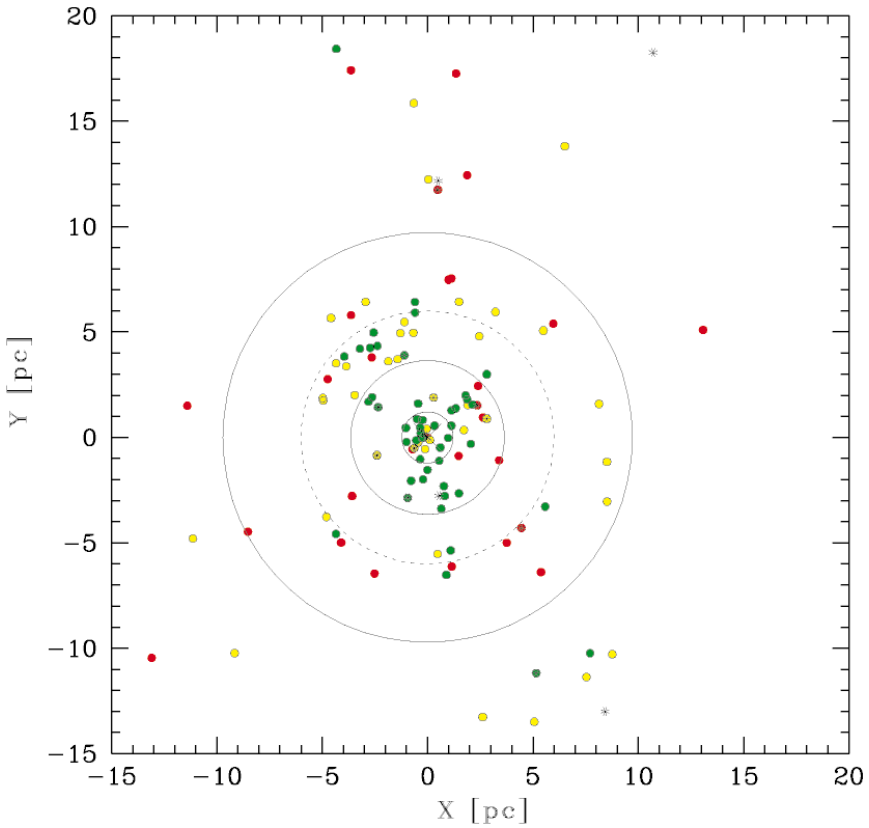

Fig. 9. Spatial distribution of stars with $M > 20M_{\odot}$ as a function of age. The color codes the position of the stars in the three episodes of star formation identified in Fig. 8: green for young peak, yellow for the middle-age peak, and red for the old peak. The O3If stars are the color dots with a superposed asterisk. The WR stars are plotted using an asterisk.

Brandl et al. (1996) combined near-infrared adaptive optics observations together with HST observations to study the star-formation history and IMF of a region 12″ by 12″ at a distance of 4″ from the cluster center. In their Fig. 13, which is the equivalent of this paper's Fig. 8b, we can see three peaks of increasing intensity, separated by approximately 2.5My. Their three peaks are approximately 1My older than the ones derived in this work, a fact that might be attributable to the known problems with the HST photometry discussed in Paper I.

Our observations suggest that the formation of massive starburst clusters, such as 30 Dor, is more complex than the relatively simple *stochastic sampling* picture presented by Elmegreen (1997). While the model correctly predicts the IMF slope and the relation between stellar-mass and age we observe, it does not consider the effects of dynamical evolution and age clustering discussed above.

The fact that star formation appears to be synchronized over very large distances is puzzling and needs to be investigated further by extending the present work over the whole face of the 30 Doradus superassociation.

3.2. Initial mass function of 30 Doradus

It is customary to define the IMF of a cluster as the number of stars per unit mass interval. The implicit assumption is that all the stars in the cluster are coeval i.e. that the age spread of the stars, Δt, is much smaller than the age of the cluster, τ_{cl}, $\Delta t << \tau_{cl}$. The IMF of coeval clusters can only be determined for stars less massive than the maximum mass still present in the cluster and more massive than the *pre-main-sequence* (PMS) cut-off: the minimum mass a star can have so that it has reached the main-sequence in the time available since the start of the starburst scenario. Thus, if $\tau_{MS}(M)$ is the main sequence lifetime for a star of mass M, the IMF can be derived up to a mass M which satisfies $\tau_{MS}(M) = \tau_{cl}$.

Since Δt cannot be arbitrarily small, for very young clusters such as 30 Doradus, $\Delta t \sim \tau_{cl}$, so the determination of the IMF is

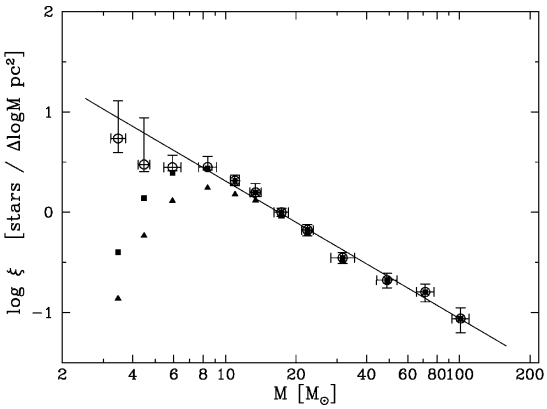

Fig. 10. The IMF of 30 Doradus for the sample of stars with $r > 15''$, calculated assuming equally likely isochrones below 3My. The line is a least squares fit to the data which gives $dN \propto M^{-2.37\pm0.08}dM$. The error bars consider counting statistics together with the errors in the incompleteness and magnitude-limit corrections.

more complicated than just counting stars in different mass bins. The present day star counts are the integration in time of the star-formation rate, so, when dealing with non-coeval populations, it is appropriate to report an average *star-formation rate* as a function of mass rather than counts as a function of mass.

In order to compute this rate, the counts must be normalized by Δt for stars with masses smaller than those given by $\tau_{MS}(M) = \Delta t + \tau_{cl}$, and by the fraction of their main sequence lifetime spent in the star-formation episode for all other masses. If the star-formation episode continues until now, as is probably the case for 30 Doradus, this fraction is 100% and the normalization is simply $\tau_{MS}(M)$. Fig. 8 shows the star-formation history of 30 Dor as a function of mass. The bulk of the stars appear to have formed three bursts of strength increasing with time, and with the most massive starts preferentially formed in the most recent burst. Thus, the simple prescription of dividing the counts by a time interval which is only a function of stellar mass is incorrect. However, since all previous determinations of the IMF of 30 Dor report star counts as a function of mass and not the star-formation rate as a function of mass (Parker & Garmany 1993; Hunter et al. 1995; Hunter et al. 1996; Massey & Hunter 1998a, 1998b), we will continue the tradition in this paper keeping in mind that the IMF thus determined may not contain all the relevant physical information available in the data. For that it is indispensable to study Fig. 8.

The IMF determined in the outer and inner regions of the cluster, using Maeder's high mass-loss models for a metallicity of Z=0.008, together with the VGS effective temperature calibration is given in Table 2 and plotted in Figs. 10 and 11. There are three sets of points in these plots corresponding to the uncorrected counts, the counts corrected only for incompleteness, and the counts corrected for incompleteness and magnitude-limit effect. Between $3M_\odot$ and $120M_\odot$, the data are very well represented by a *single* power law of Salpeter slope.

Table 2. Initial Mass Functions

Radius[a] $''$	Mass $M_\odot$	$\log \xi$[b] $(\Delta \log M)^{-1} pc^{-2}$	$\sigma^+_{\log\xi}$	$\sigma^-_{\log\xi}$
15–75	85–119	−1.06	0.11	0.14
	60–85	−0.80	0.08	0.10
	40–60	−0.68	0.07	0.08
	25–40	−0.45	0.05	0.06
	20–25	−0.18	0.05	0.06
	15–20	−0.00	0.04	0.04
	12–15	0.20	0.09	0.04
	10–12	0.31	0.05	0.05
	7–10	0.45	0.11	0.03
	5–7	0.45	0.12	0.03
	4–5	0.47	0.47	0.07
	3–4	0.74	0.37	0.14
4.6–19.2	85–119	−0.07	0.13	0.19
	60–85	0.07	0.12	0.16
	40–60	0.17	0.11	0.13
	25–40	0.58	0.07	0.07
	20–25	0.66	0.10	0.10
	15–20	0.92	0.06	0.07
	12–15	0.97	0.08	0.09
	10–12	1.24	0.14	0.16
	7–10	0.90	0.25	0.41

[a] These are non-circular boundaries and the outer radii are effective in the sense of areas. The outer boundary of the outer sample is the square boundary of the NTT frame. For the inner sample the outer boundary is defined by the rectangular frame of the HST PC as defined in the text.

[b] For the $15''$–$75''$ region the best fit has $\log \xi_0 = 1.68 \pm 0.11$ and $\Gamma = 1.37 \pm 0.08$. The inner $4.6''$–$19.2''$ region, including the H96 data, is best fitted with $\log \xi_0 = 2.29 \pm 0.05$ and $\Gamma = 1.17 \pm 0.05$.

3.2.1. Comparison with previous work

No single previous analysis of 30 Doradus, either from the ground or space, has the large coverage in mass that we present here and we are thus forced to compare our work with a combination of several published investigations.

For the outermost regions there is no correct space or ground-based determinations to compare our results with. The finding by Parker & Garmany (1993) of an IMF which is not well represented by a power law in any mass range is a result of their not recognizing the need to apply a magnitude-limit correction. Thus, our work is the only one available in this radial distance range. We can see in Fig. 10 that for $r > 15''$ the IMF is indistinguishable from Salpeter, with a slope $\Gamma = -1.37 \pm 0.05$ between $3M_\odot$ and $120M_\odot$.

For the inner region of the cluster we can compare with the HST observations of Hunter et al. (1995; H95) and Hunter et al. (1996; H96). Their outermost area extends from $4.6''$ out to the boundaries of the HST PC field. We have used their published list of coordinates to determine the transformation between our system and theirs and thus count stars in exactly the same region. This procedure is important due to the highly fluctuating stellar density distribution which would render a comparison based on counts between effective radii useless. H95 give $\Gamma = -1.17 \pm$

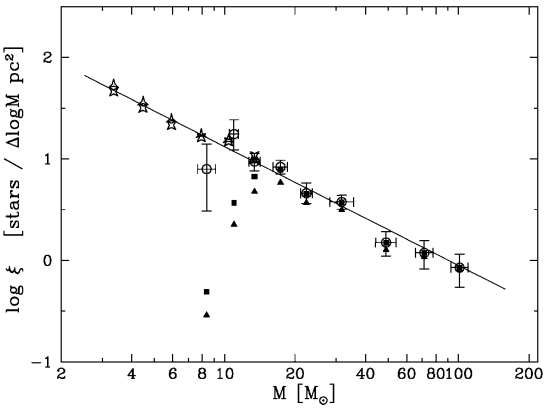

Fig. 11. The IMF of 30 Doradus for the region in common with the HST work of Hunter et al. (1995, 1996). The symbols are as in Fig. 10 with the addition of Hunter's IMF represented by the stars: 3 points H95, 4 points H96. The solid line is the best fit to this paper's data together with H96 which gives $dN \propto M^{-2.17\pm0.05}dM$. Error bars as in previous figure.

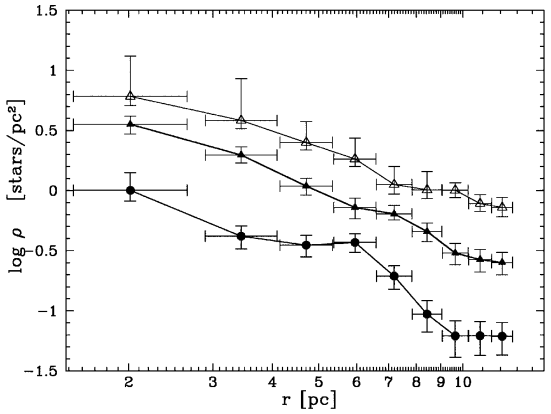

Fig. 12. Radial profile of stars of different masses. From top to bottom: open triangles, $7M_\odot < M < 10M_\odot$; filled triangles, $10M_\odot < M < 40M_\odot$; and filled circles, $M > 40M_\odot$.

0.07 while H96 quote $\Gamma = -1.01 \pm 0.07$ in the mass range $2.8M_\odot < M < 15M_\odot$ for this region, but give no explanation for the discrepant values of the slopes (see also Brandl et al. 1996, for a different analysis of the IMF and mass segregation in 30 Doradus combining a fraction of the H95 data with adaptive optics near-infrared observations).

We find $\Gamma = -1.37\pm0.10$ for $10M_\odot < M < 120M_\odot$ using only our data, in almost perfect agreement with a Salpeter slope. Fig. 11 shows the H95 and H96 counts together with ours. The IMFs merge smoothly given the errors, providing confirmation that the incompleteness and magnitude limit corrections have been properly determined. Combining our data with HST we find the slope over $2.8M_\odot < M < 120M_\odot$ to be $\Gamma = -1.17 \pm 0.05$ using the H96 data, and $\Gamma = -1.25 \pm 0.05$ using H95.

3.2.2. Mass segregation

In Papers I and II we presented evidence for mass segregation in 30 Doradus in the form of a larger median distance to the cluster center for stars of smaller absolute luminosity. In this Paper we find an inner region IMF slope flatter than in the outer one, a 2-3σ effect, confirming the result from our previous work.

For $r < 5''$ our data are inconclusive and we must rely exclusively on HST. Although H95 and H96 do find evidence for a flattening of the IMF towards the core of the cluster, in their most recent HST work Massey & Hunter (1998a) deny the existence of mass segregation and ascribe the large number of very massive stars they observe in the core of the cluster to age effects. They base their conclusion on the fact that, extrapolating the *best fit* IMF of H96 for intermediate mass stars, they were able to predict exactly the number of massive stars ($50M_\odot < M < 120M_\odot$) they observed in the cluster core (22.8 stars predicted versus 23 stars observed within 2.8″of the center). The flaw in this argument is that the *best fit* slope of H96, $\Gamma = -1.01$, is already flatter than the Salpeter slope which is observed elsewhere in the cluster, and which predicts ~ 2.5 times fewer massive stars in the core than they observed.

We conclude that mass segregation, as evidenced by a flattening of the derived IMF, is the most likely explanation for the large number of very massive stars present in the core of 30 Doradus. However, as we pointed out in Paper II, the HST spectra may be corrupted by nebular HeI lines and bad pixels which conspire to bias the data towards earlier spectral types.

Another way to investigate mass segregation is to compare the radial density profile of stars of different masses. The danger is that systematic errors due to crowding and incompleteness tend to mimic mass segregation. Figs. 10 and 11 show that for $M > 7M_\odot$ and $r > 15''$, and for $M > 10M_\odot$ and $r > 5''$ systematic errors are below 10% so we can confidently use these stars to study the density profiles. Fig. 12 gives the radial density profile, corrected for incompleteness and magnitude limit effects, for stars in 3 different mass bins. Below $40M_\odot$ the profiles are remarkably similar, while there is an excess of stars with $M > 40M_\odot$ between 4 pc and 8 pc. This excess of bright stars can be seen by eye in Fig. 7 around the $25''$ circle (6 pc shell). What cannot be seen in this figure is that the number of less massive stars in the 6 pc shell does not show an equivalent increase. A χ^2 test rejects the hypothesis that the two sets of counts are drawn from the same distribution at the 98% confidence level. In the three radial bins centered at 6 pc shell one expects about 40 stars while ∼80 are observed. There is marginal evidence that the density of massive stars increases more rapidly towards the center, but the errors are too large to make this a firm conclusion.

3.2.3. The upper mass cut-off (M_U)

It has been claimed that M_U is not well defined, but is given by the stochastic nature of the IMF (Elmegreen 1997). Other

authors claim that there are physical reasons to expect a limit for the maximum mass of a stable star (Stothers 1992 and references therein). Perhaps the two ideas are not incompatible and the IMF is set by a random sampling of a fractal cloud, while physical process trim the over massive proto-stars to stable sizes leading to an IMF with an excess of stars with masses near the physical upper mass limit. This could result in a top-heavy IMF without need to invoke mass segregation. However, it is easy to show that this effect would increase the number of the most massive stars at most by a factor of 1.4 for a Salpeter slope, still significantly less than the factor of 2.5 needed to reconcile the HST counts with a Salpeter IMF.

Stellar models (e.g. Stothers 1992) predict that the most massive stable stars should have masses around 120M$_\odot$ for solar metallicity, and 90M$_\odot$ for SMC metallicity. This would imply an upper mass cut-off of about 100M$_\odot$ for the LMC in apparent contradiction with our observations. In Fig. 4, the brightest stars are almost a whole magnitude more luminous than the 120M$_\odot$ models, indicating that either the models are not accurate for these high masses, or that there are stars with larger masses, possibly binaries. We should point out that the Geneva tracks we used do not include the effects of mixing and rotation. For a given mass, models with rotation evolve at higher luminosities (Langer 1992) and are stable for larger masses (Stothers 1974).

From our observations alone, therefore, we conclude the most probable upper mass limit in the LMC is about $130M_\odot$.

3.2.4. The lower mass cut-off (M_L)

Our data does not go deep enough to provide a direct determination of the lower mass cut-off of the IMF, but it does allow us to understand the systematic errors that may mimic a low-mass cut-off in the photometry of massive young clusters.

As discussed above, the biggest offender is the *magnitude limit effect*. Fig. 10 shows that after correcting for incompleteness only, the 30 Dor IMF drops sharply at $\sim 6M_\odot$. In the inner region (Fig. 11), the effect is even more pronounced and starts at $\sim 15M_\odot$. But, when the magnitude limit correction is applied, the data are very well fitted by a single power law over the full mass range sampled with no evidence for a turn-over.

Nota (1998) has presented an IMF based on HST data that drops below $2M_\odot$. At $2M_\odot$ we expect V=20.0 unreddened so, in order to avoid magnitude limit corrections, the photometry must be complete to *at least* V=23.0. Although they claim to reach $V = 24.7$ (Siriani et al. 1998), it is not clear to which limiting V magnitude they determined the incompleteness correction over the area and color range of their study. The magnitude-limit correction starts to be important for the same mass bins for which the incompleteness correction starts to matter. Therefore, the claimed cut-off at $2M_\odot$ is very likely to be due to the magnitude-limit effect.

3.3. The radial density profile of the cluster

Fig. 13 shows the radial surface number density profile of the cluster. It combines the H96 data together with our counts corrected for incompleteness and magnitude limit. We have restricted our counts to $10M_\odot < M < 40M_\odot$, and merged with the H96 counts by fitting a straight line to each radial bin in their Table 4 and then integrating the fitted $\xi = \xi(\log M)$. We can see that their innermost bin is highly incomplete. The line represents the relations

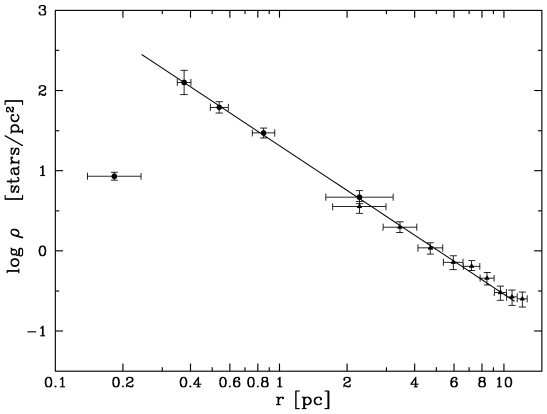

Fig. 13. Radial density profile for the stars with $10M_\odot < M < 40M_\odot$. For the innermost bins we have calculated the points using the Hunter et al. (1996) data following the procedure described in the text. The line is a power law with exponent -2.85.

$$\Sigma_n(R) \;=\; 20.6\;\frac{\text{stars}}{\text{pc}^2}\;\left(\frac{1\text{pc}}{R}\right)^{1.85},$$

$$\rho_n(r) \;=\; 9.8\;\frac{\text{stars}}{\text{pc}^3}\;\left(\frac{1\text{pc}}{r}\right)^{2.85},$$

where r is the distance to the cluster center (R136a1) in parsecs, R is the projected distance in parsecs, and Σ_n and ρ_n are the surface and spatial number densities. Integrating the appropriate relations we can estimate a total of 1350 stars with $10M_\odot < M < 40M_\odot$ interior to 20 pc. Assuming a Salpeter slope we estimate for the same region 8000 stars with $3M_\odot < M < 120M_\odot$. In this mass range the average stellar mass is 8.44M$_\odot$, resulting in a total of mass of 68000M$_\odot$ for the cluster. Changing M_L from 3M$_\odot$ to 0.1M$_\odot$ increases the total number of stars by a factor of 100, and the total mass by a factor of 4.

Several studies of the radial density profile of the inner regions of NGC2070 have been published in the past. Campbell et al. (1992) using aberrated WFPC HST observations give a power-law fit to the F336W surface brightness profile generated by integrating the stellar photometry in concentric annuli. Their data is well modeled by a single power-law between $0.4'' < R < 4''$, with an exponent of 1.72 ± 0.06. They detect no core, and set an upper-limit of $R_c < 0.25''$. De Marchi et al. (1993) also measure the surface brightness distribution with the aberrated HST but integrating directly from the frame to avoid completeness limit issues. For $R > 1.7''$ their data are well represented by a power-law with index -1.9 while for $r < 1.7''$ their data shows an abrupt change of slope to a value

of -0.8. However, this flatter slope is probably due to a few off-center, very bright, W-R and O stars. Malumuth & Heap (1994) assign masses to the stars with a photometric method and fit a King model to the surface mass density profile. Ignoring their highly uncertain point at $0.1''$, their data is well represented by a power-law of slope -1.7. The WFPC2 HST work of Hunter et al. (1995) also shows a surface brightness profile which is well fitted by a power law of index -2, but they report an upper limit for the core radius of $R_c < 0.25''$. Brandl et al. (1996) present a profile based on adaptive optics near IR observations; From their Fig. 15 we determine a slope of -1.9 for the surface mass density profile for $R > 0.6''$. These authors find a core radius which increases with decreasing mass, but unfortunately this is the same effect one would expect by a failure to apply the magnitude limit correction, which they do not appropriately consider.

The mass density profile therefore, appears to be well determined and to be much steeper than an isothermal R^{-1} profile (projected). This is probably the result of the young age of a cluster which is not totally relaxed. This would explain the 6 pc shell of stars described above where an excess of high mass stars was detected since the bump in the density profile would have been erased had relaxation been completed. The offset between the center of the 6 pc shell and the center of the cluster, $\approx 1\,\mathrm{pc}$, provides further evidence that this stellar system is not yet relaxed. Restricting an isothermal or a King distribution function to contain only radial orbits (extreme case of anisotropy) leads to density profiles that have asymptotic slopes between -2 and -3 (see e.g. Lynden-Bell 1973). This happens because the de-population of the small eccentricity orbits has a larger effect in decreasing the density at larger radii. Because NGC2070 is such a young cluster its steep density profile could be evidence that it still remembers initial conditions of collapse.

4. Conclusions

1. A new photometric method was designed that allows the determination of masses for even the most massive stars from UBV photometry alone without introducing biases towards smaller masses. As a check of the method we obtained a distance modulus of (m-M)$_0 = 18.45 \pm 0.15$ for 30 Doradus in excellent agreement with the best estimate for distance to the LMC, (m-M)$_0 = 18.50$.
2. For $M > 20M_\odot$ we find the reddening distribution to be independent of stellar mass. The data are not complete to allow an accurate determination of this distribution below $20M_\odot$. We find a different reddening distribution for the stars near the center of the cluster (larger reddening close to the center) confirming the conclusions from Paper I. If not considered, this differential reddening distribution could introduce serious systematic effects in the IMF.
3. We have uncovered a systematic effect due to variable reddening which is responsible for the flattening of the IMF close to the limit of the photometry and we have designed and applied a method to correct for this effect which we call *the magnitude-limit correction*.
4. We use our data to constrain the ages of stars with $M > 20M_\odot$, and find that the star-formation history is dominated by three bursts of increasing strength occurring 5My, 2.5My, and $\lesssim$1.5My ago. The number of high mass stars produced in each burst are approximately in proportion to the intensity of the burst, supporting Elmegreen's (1997) *stochastic sampling* interpretation of the IMF (with the exception of the somewhat flatter core and the 6 pc shell discussed below). The three bursts appear to be spatially disjoint with the youngest stars concentrated towards the center while the 2.5My stars appear to delineate a spherically symmetric structure of 6 pc radius slightly off-center. The observations are consistent with a picture where star formation propagated inwards in the cluster. The shell at 6 pc indicates a very complex structure for the ISM before the starburst.
5. For $r > 15''$ we find the IMF to be well represented by a power law with $\Gamma = -1.37 \pm 0.08$ for $3M_\odot < M < 120M_\odot$ consistent with the Salpeter slope. For $4.6'' < r < 19''$ and $10M_\odot < M < 120M_\odot$ we find $\Gamma = -1.37 \pm 0.10$. Combining our data with published HST observations we find $\Gamma = -1.25 \pm 0.05$ and $\Gamma = -1.17 \pm 0.05$ in this region, somewhat flatter than Salpeter. We reanalyze the Massey & Hunter (1998a) data and conclude, at variance with those authors, that the large number of O3 stars they observed in the core is not consistent with a Salpeter slope, and it is most likely due to a flattening of the IMF. The concentration of the most massive stars towards the center, irrespective of their ages, indicates that dynamical effects probably play an important role in shaping the spatial variations of the IMF.
6. The spatial density profile between 0.4 pc and 6 pc is well represented by a single power law with slope -2.85, steeper than isothermal. The density profile also shows an excess of stars within the 6 pc shell. Moreover, this shell appears to have a larger than normal proportion of high mass stars, providing evidence that Elmegreen's (1997) simple stochastic picture of star-formation is not the only mode at work in this complex region. The steeper overall profile of the cluster, together with the features in the density profile in the outer radial bins, indicates that the cluster is not relaxed, and that it might still have memory of its collapse.
7. We find that, if current evolutionary models are correct, there is evidence that the upper mass cut-off of the IMF is larger than 120M$_\odot$. It appear that the most massive stars in 30 Doradus have $M \approx 130M_\odot$, or that we are seeing the effects of rotation which for a given mass makes stars evolve at higher luminosities. Alternatively, the most massive stars in the cluster may all be binaries.

Acknowledgements. The authors would like to thank Dr. Peter Stetson for making his programs *Daophot II*, and `daomaster` available for this research. Special appreciation to the referee, Dr Bernhard Brandl, for a very careful reading and constructive criticism of the paper, thanks to which we hope it improved greatly.

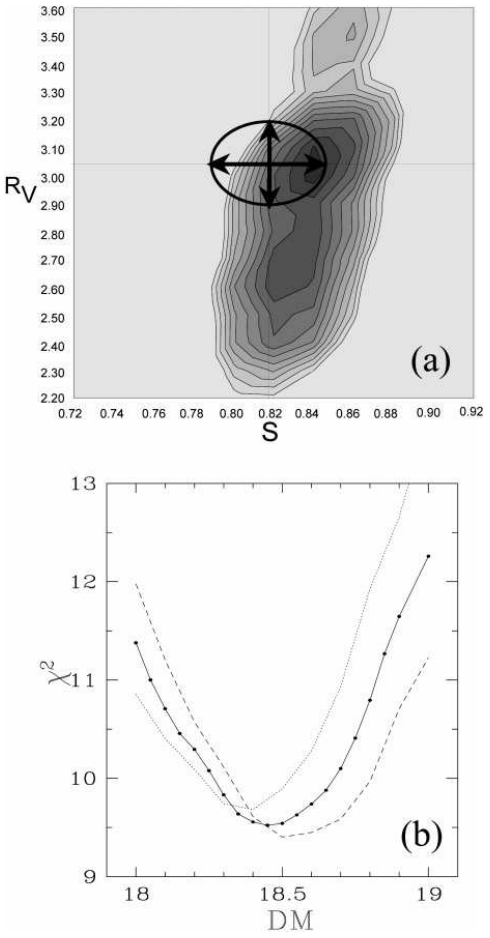

Fig. A1. a Photometric χ^2 map as a function of S and R_V. The ellipse marks the 1σ region around the best solution found in Paper I. **b** χ^2_{spec} as a function of the assumed $(m-M)_0$ to 30 Doradus. The curve for the best R_V value has a minimum at 18.45 magnitudes, in excellent agreement with previous determinations.

Appendix A: the distance to 30 Doradus

The performance of our Bayesian analysis of the CMS can be assessed by using it to determine the most likely values for $(m-M)_0$, S, and R_V. As explained in Paper I UBV data alone does not constrain R_V strongly. Nevertheless, it can be seen in Fig. A1a that both S and R_V determined photometrically agree with the values from Paper I. The best photometric values are thus S=0.84, $R_V = 3.05$.

Using $R_V = 3.05 \pm 0.15$ we find a true distance modulus of $(m-M)_0 = 18.45 \pm 0.15$ to 30 Doradus in excellent agreement with the best determined distance of $(m-M)_0 = 18.46 \pm 0.06$ to the LMC (Gieren et al. 1998).

References

Abraham R.G., 1999, In: Branes J.E., Sanders D.B. (eds.) Galaxy Interactions at Low and High Redshift. Kluwer, Dordrecht, p. 11

Abraham R.G., Tanvir N.R., Santiago B.X., et al., 1996, MNRAS 279, L47

Barnes J., 1998, astro-ph9811242

Barnes J., Hut P., 1986, Nat 324, 446

Bosch G., Terlevich R., Melnick J., Selman F.J., 1999, A&AS 137, in press (Paper II)

Brandl B., Sams B.J., Bertoldi F., et al., 1996, ApJ 466, 254

Brandt S., 1970, Statistical and Computational Methods in Data Analysis. North-Holland, Amsterdam

Campbell B., Hunter D.A., Holtzmann J.A., et al., 1992, AJ 104, 1721

Carpenter J.M., Meyer M.R., Dougados C., Strom S.E., Hillenbrand L.A., 1997, AJ 114, 198

Chlebowski T., Garmany C.D., 1991, ApJ 368, 241 (ChG)

Davis L.E., 1994, A reference Guide to the IRAF/DAOPHOT Package, NOAO

de Koter A., Heap S.R., Hubeny I., 1997, ApJ 477, 792

De Marchi G., Nota A., Leitherer C., Ragazzoni R., Barbieri C., 1993, ApJ 419, 658

Elmegreen B.G., 1997, ApJ 486, 944

Gieren W.P., Fouqué P., Gómez M., 1998, ApJ 496, 17

Glazebrook K., Ellis R.S., Colless M., et al., 1995, MNRAS 273, 157

Herbig G., 1962, ApJ 135, 736

Hunter D.A., Shaya E.J., Holtzman J.A., et al., 1995, ApJ 448, 179

Hunter D.A., O'Neil E.J., Lynds R., et al., 1996, ApJ 459, L27

Hunter D.A., Vacca W.D., Massey P., Lynds R., O'Neil E.J., 1997, AJ 113, 1691

Kendall M.G., Stuart A., 1977, The Advanced Theory of Statistics. Vol. 1, 4th edition, Charles Griffin, p. 212

Kurucz R.L., 1993, from ATLAS9 Stellar Atmospheres Programs and 2km s^{-1} Grid, CDROM13.COLORS, August 22, 1993, SAO

Langer N., 1992, A&A 265, L17

Lynden-Bell D., 1973, In: Contopoulos G., Henon M., Lynden-Bell D. (eds.) Dynamical Structure and Evolution of Stellar Systems. Saas-Fee 1973, p. 91

Malagnini M.L., Morossi C., Rossi L., Kurucz R.L., 1986, A&A 162, 140

Malumuth E., Heap S., 1994, AJ 107, 1054

Massey Ph., 1998, In: Gilmore G., Howell D. (eds.) The Stellar Initial Mass Function. Proceedings of the 38th Herstmonceux Conference, A.S.P. Conf. Ser. Vol. 142, p. 17

Massey Ph., Hunter D., 1998a, ApJ 493, 180

Massey Ph., Hunter D., 1998b, In: Howarth I. (ed.) Properties of Hot Luminous Stars. ASP Conf. Ser. 131, p. 355

Melnick J., 1985, A&A 153, 235

Melnick J., 1992, In: Tenorio-Tagle G. Prieto M., Sánchez F. (eds.) Star Formation in Stellar Systems. CUP, Campridge, p. 253

Meynet G., Maeder A., Schaller G., Schaerer D., Charbonnel C., 1994, A&AS 103, 97

Meyer M.R., 1996, Ph.D. Thesis, University of Massachusetts, Amherst

Mihos J.C., Hernquist L., 1994, ApJ 431, L9

Nota A., 1998, STScI Newsletter 15(4), 1

Parker J.Wm., Garmany C.D., 1993, AJ 106, 1471

Parker J.Wm., Garmany C.D., Massey P., Walborn N.R., 1992, AJ 103, 1205

Pettini M., Kellog M., Steidel C.C., et al., 1998, astro-ph/9806219

Press W.H., Teukolsky S.A., Vetterling W.T., Flannery B.P., 1994, Numerical Recipes in C: the art of scientific computing. Cambridge University Press

Salpeter E., 1955, ApJ 121, 161
Schaerer D., Meynet G., Maeder A., Schaller G., 1993, A&AS 98, 523
Schmidt-Kaler Th., 1982, In: Schaifers K., Voigt H.H. (eds.) Stars and Star Clusters. Volume 2b, part of the Landolt-Börstein series on Numerical Data & Functional Relationships in Science and Technology, chief ed. K.-H. Hellwege, Springer-Verlag, Berlin-Heidelberg, p. 1 (SchK)
Selman F.J., Melnick J., Bosch G., Terlevich R., 1999, A&A 341, 98 (Paper I)
Siriani M., Nota A., Leitherer C., Clampin M., De Marchi G., 1998, In: Howarth I. (ed.) Properties of Hot Luminous Stars. ASP Conf. Ser. 131, p. 363
Stahler S., 1985, ApJ 293, 207
Stetson P.B., 1997, The *Daophot II* User's Manual
Stothers R., 1974, ApJ 192, 145
Stothers R., 1992, ApJ 392, 706
Tolstoy E., Saha A., 1996, ApJ 462, 672
Vacca W.D., Garmany C.D., Shull J.M., 1996, ApJ 460, 914 (VGS)
Walborn N.R., Blades J.Ch., 1997, ApJS 112, 457
Walborn N.R., Parker J.Wm., 1992, ApJ 399, L87

Paper IV

The ionizing cluster of 30 Doradus IV. Stellar kinematics

A&A 380, 137 (2001)

G. Bosch, F. Selman, J. Melnick, and R. Terlevich

.

A&A 380, 137–141 (2001)
DOI: 10.1051/0004-6361:20011427

Astronomy & Astrophysics

The ionising cluster of 30 Doradus⋆

IV. Stellar kinematics

G. Bosch[1,2], F. Selman[3], J. Melnick[3], and R. Terlevich[1,⋆⋆]

[1] Institute of Astronomy, Madingley Road, Cambridge CB3 0HA, UK
[2] Facultad de Ciencias Astronómicas y Geofísica, La Plata, Argentina
[3] European Southern Observatory, Alonso de Córdova 3107, Santiago, Chile

Received 6 June 2001 / Accepted 4 October 2001

Abstract. On the basis of multislit spectroscopy of 180 stars in the ionising cluster of 30 Doradus we present reliable radial velocities for 55 stars. We calculate a radial velocity dispersion of ∼35 km s^{-1} for the cluster and we analyse the possible influence of spectroscopic binaries in this rather large velocity dispersion. We use numerical simulations to show that the observations are consistent with the hypothesis that all the stars in the cluster are binaries, and the total mass of the cluster is $\sim 5 \times 10^5$ $M_\odot$. A simple test shows only marginal evidence for dynamical mass segregation which if present is most likely not due to dynamical relaxation.

Key words. stars: early-type – stars: kinematics – binaries: spectroscopic – galaxies: clusters: general – galaxies: Magellanic Clouds

1. Introduction

A significant fraction of the old stars we now observe in galaxies appear to have formed in Starbursts. Therefore, understanding violent star formation becomes crucial if we want to understand the star formation history of the Universe. 30 Doradus in the LMC is the nearest and best studied example of a massive starburst cluster and thus it has become a sort of "Rosetta Stone" for deciphering the physics of violent star formation processes (Walborn 1991; Selman et al. 1999b (Paper III) and references therein).

Although 30 Dor has been the subject of intensive observational effort from the ground and space there are still a number of critical problems that remain unsolved. Perhaps the most burning open problem is the issue of mass segregation first raised by Malumuth & Heap (1995) that has important implications for our understanding of the process of cluster formation in general (Clarke 2001).

This Paper is the fourth of a series devoted to a comprehensive study of the 30 Doradus starburst cluster (NGC 2070). We can summarize the central results of the previous papers of this series as follows:

- The Initial Mass Function (IMF) of NGC 2070 between 3 and 120 $M_\odot$ is very well represented by a Salpeter power-law. The total "photometric" mass of the cluster – inside 20 pc – from 0.1 $M_\odot$ to 120 $M_\odot$ is $M_{\rm phot} \sim 3 \times 10^5$ $M_\odot$;
- The star-formation history of the cluster shows three distinct peaks centered 5 Myrs, 2.5 Myrs, and <1.5 Myrs ago with no evidence for a spatial segregation of ages;
- The density distribution of stars between 20 and 60 $M_\odot$ is a power-law of slope of −2.85. This means that the total mass increases very slowly with radius ($r^{0.15}$ or even logarithmically);
- There is some evidence for mass segregation revealed by the fact that the most massive stars appear to be more concentrated toward the center. However, there is a distinct "ring" of massive stars located at about 6 pc from the center of the cluster (R136). This ring contains stars of the three age groups described above.

The purpose of the present Paper is to study the stellar kinematics of the brightest stars in the cluster using the NTT observations described in Paper II of this series (Bosch et al. 1999). We use the data to investigate the presence of dynamical mass segregation in the cluster, and to attempt to constrain the lower end of the IMF from the comparison between the photometric and the dynamical masses.

2. Observations and data reduction

The observations – already described in Paper II – were obtained with the La Silla NTT telescope using

Send offprint requests to: G. Bosch,
e-mail: guille@fcaglp.unlp.edu.ar

⋆ Based on observations collected at the European Southern Observatory.

⋆⋆ Visiting Professor, INAOE, México.

the Multislit option of EMMI's RILD mode. In this mode, grism # 5 was used, which in combination with a 0.8 arcsec wide slit yields a resolution of 1.3 Å/pixel. The wavelength range is 3600 to 6000 Å in most cases, although the limits vary slightly between individual spectra, as they depend on the position of each slitlet within the mask. A total of 7 masks were produced each including an average of 35 slitlets. The basic reduction steps were described in Paper II including bias correction, flat fielding, wavelength calibration, and aperture extraction. Here we need to discuss some aspects of the wavelength calibration not included in Paper II that are particularly relevant for the determination of radial velocities.

During the observations a technical problem made the Argon lamp too weak to produce reliable identification lines for 2 masks while the strong He I 5875 Å arc line is saturated for several spectra. The problem is worst when both effects appear at the same time as there are no reliable comparison lines redwards He I 5015 Å. For example, this makes useless the He II 5411 Å absorption line for radial velocity measurements in the affected spectra.

The problems with the calibration lamps also altered the normal sequence in which the lamps were taken; the calibration exposures for the last three masks had to be taken at the end of the night. Although there were no telescope presets, the telescope was still tracking so the position angle of the instrument rotator slowly changed and this may introduce systematic errors. We address this issue in the following section.

3. Radial velocities

3.1. Zero-point errors

The problems with the calibration lamps may introduce systematic differences between the zero points of each mask. We have used the radial velocity of the [O I] 5577 Å Auroral line, whenever possible, to test for this effect.

The straightforward approach would be to add algebraically the radial velocity of the sky line to the velocity of each star. Unfortunately, however, the problems with the calibration lamps described above imply that several spectra have unreliable wavelength calibration in the region of [O I].

For most spectra the formal (measurement) error in the position of the sky line is ∼6.6 km s^{-1}. The mean radial velocity of the [O I] lines with reliable calibrations is −6.5 km s^{-1} with a dispersion of 12.9 km s^{-1}. Thus, while we cannot correct the individual velocities for systematic zero point errors, the radial velocity dispersion must be corrected by this effect by subtracting quadratically the [O I] dispersion $\sigma_{[\mathrm{O\,I}]} = \sqrt{12.9^2 - 6.6^2} = 10.9$ km s^{-1}.

3.2. Velocity determination

As mentioned above, the resolution of our combination of dispersion grating and camera yields 1.3 Å per pixel. For 2-pixel sampling this corresponds to a spectral resolution of about 165 km s^{-1} at 4750 Å. The ultimate limit attainable in the precision of Doppler shifts is dominated by the photon noise in the spectrum (Brown 1990). The uncertainty in the measured radial velocity for the case of a single line of width w and depth d, measured in units of the continuum intensity I_c, is given by

$$\delta v_\mathrm{rms} = \frac{c\,w}{\lambda\,d\,(N_w\,I_\mathrm{c})^{1/2}} \quad (1)$$

where N_w is the number of samples across the width of the line, c is the speed of light, and λ is the central wavelength of the line. For typical lines measured in our stars (λ = 4500 Å, $w = 7$ Å, $N_w = 6$, $d = 0.2$, and $I_\mathrm{c} = 2 \times 10^4$), we obtain $\delta v_\mathrm{rms} = 15$ km s^{-1}. This is smaller than the velocity dispersion expected if the cluster is virialised and the total mass is close to our photometric estimate. However, the signatures of expanding stellar atmospheres and binaries may be much stronger than the virial motions. Thus, it is very important to constrain these effects with the data at hand before embarking in a high spectral resolution survey of the kinematics of the cluster.

At our resolution the Balmer lines cannot be used to measure radial velocities because they are severely contaminated by nebular emission. Therefore, we have restricted our analysis to stars with well exposed HeI and HeII absorption lines. In order to have an indication of the presence of atmospheric motions we have only considered stars with at least three He lines detected. This further restricts our sample to 97 spectra, several of which correspond to the same star.

The centroids of the lines were determined from Gaussian fits using the package `ngauss` within IRAF. The fitting errors were used as weights to calculate the (weighted) mean velocity of each star. A conservative $\kappa-\sigma$ filter was used to reject stars with suspected internal (atmospheric) motions. Thus, all stars with a dispersion of more than 25 km s^{-1} between the measured lines were rejected. The final list is presented in Table 1 that gives, for each star, the Parker number, the spectral type from Paper II, position in arcsec from the cluster center, assumed to be R136 (Selman et al. 1999a), the weighted average radial velocity, and the weighted error. A number of stars appear to be binaries on the basis of showing double peaked lines (stars # 1024, 1369 and 1938), asymmetric line profiles (# 222, 613, and 1191), or different radial velocities for the He I and He II lines (# 1998). These stars tend to have larger internal errors as can be seen in the second part of Table 1.

4. Results

4.1. The distribution of radial velocities

In Fig. 1 we plot the spatial distribution of the measured stars in three different velocity bins in order to check for the presence large scale motions, such as rotation, or clustering of stars in large substructures of different kinematics. Unfortunately, the distribution of the points, dictated

Table 1. Stellar radial velocities.

Star id.	Sp.Type	$\Delta\alpha('')$	$\Delta\delta('')$	$\langle V_r \rangle$	$\sigma_{\rm int}$
15	O8.5 V	−107	107	234.9	14.0
32	O9 IV	−102	72	272.1	09.5
124	O8.5 V	−76	25	287.5	06.9
316	O6.5 V	−50	−164	265.9	09.5
541	O7.5 V	−29	−65	252.6	07.1
649	O8-9 V	−20	−106	323.7	09.4
713	O5 V	−15	−53	308.7	11.8
747	O6-8 V	−13	−142	364.3	22.8
791	O5 V	−09	141	310.7	08.8
805	O5-6 V	−08	−38	292.1	09.4
863	O6.5 V	−04	−03	308.0	06.5
871	O4 V((f*))	−04	−44	290.3	06.5
901	O3 V((f*))	−02	26	276.2	08.7
905	O9-B0 V	−02	61	198.2	16.3
975	O6-7 V((f))	02	−27	325.5	05.9
1022	O5: V	04	−139	320.6	07.2
1063	O6-7 V	06	108	267.0	16.5
1109	O9 V	09	−167	229.7	05.9
1139	B0 V	11	36	225.5	09.5
1163	O4 If:	12	−72	274.1	11.3
1247	B0.5 IV	17	91	333.0	11.6
1283	O6 V:((f*))	19	−09	352.2	06.7
1339	B0-0.2 IV	23	−60	265.5	12.0
1389	B1: V::	27	70	292.6	06.1
1419	B0-0.2 III-I	31	98	259.0	10.0
1459	O9.5 II	34	145	272.7	14.3
1460	B0-2 V	34	172	282.7	21.0
1468	O9.5 V	36	16	321.0	13.3
1500	B0.2 III	39	40	275.2	09.0
1531	O6 V((f))	43	−25	308.0	09.0
1553	O7 V	47	−09	321.5	07.3
1563	O7.5 II-III(f)	47	−04	271.6	06.9
1584	B0-1 V	50	−02	320.8	23.1
1604	B1 V	55	85	360.2	17.6
1614	O5-6 V((f))	56	09	291.2	06.6
1618	B0-0.2 III	56	128	270.1	07.6
1619	O8 III(f)	56	102	357.8	20.0
1643	O5 V	60	128	279.0	06.6
1661	B1 III	62	124	322.7	07.5
1685	B0.5-0.7 III-I	66	161	291.8	11.6
1729	B1 II-III	71	80	283.2	17.3
1737	B1.5 III	71	139	339.1	05.7
1969	B0.7 IV	113	74	329.6	12.7
1987	B2 I	120	−113	294.8	05.0
10001	O4 V			246.1	14.7
10003	B1-1.5 V			279.9	06.9
Suspected Binaries					
222	O9.5-B0 V	−62	143	198.9	26.4
613	O8.5 V	−23	−154	203.2	13.7
1024	O9-B0 V	05	−110	510.7	27.9
1191	B0.2-1 III-V	13	−30	345.7	28.8
1369	O8.5 V	26	−09	318.1	78.5
1938	O7.5 V	107	134	350.0	18.0
1988	B0.5 V	121	−22	300.0	18.0

by the geometry of the spectral masks, precludes a finer analysis, but a visual inspection of the graph reveals no evidence of clumping of stars with similar velocities, nor of rotation along the axis defined by the observational technique.

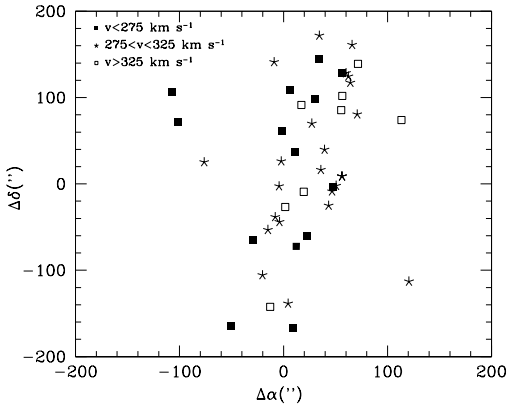

Fig. 1. Spatial distribution of stellar radial velocities. Two stars are missing, as they fall out of the photometry area.

We can safely proceed, therefore, to draw histograms and estimate velocity dispersions. Figure 2 presents velocity histograms of the single stars in Table 1 with two different bin sizes, and two different origins to check for sampling effect. The top two panels are for a binning of 11 km s^{-1} (corresponding to our estimate for the mean random error in the velocities) and the lower two for a binning of twice this error. The multiple peaks of the first plot disappear when the bins are shifted by 5 km s^{-1} (half a step), indicating that they are artifacts of the small number statistics. This is confirmed in the lower panel where shifting the sampling by half a step (11 km s^{-1}) does not change the distribution in any significant way. The hypothesis of a Gaussian distribution is valid, based on χ^2 tests performed to the distribution.

We conclude that there is no evidence for statistically significant peaks in the radial velocity distribution of the cluster. Thus, we can use all the data to estimate the velocity dispersion of the cluster. After correction for measurement (internal) errors and zero point errors (from the [O I] Auroral line), the radial velocity dispersion of 48 single stars in the cluster is 32 km s^{-1}. This is much larger that the value expected if the cluster is virialised with a total mass equal to the photometric mass and also much larger than our combined errors ($\sigma_{\rm tot} \sim 15$ km s^{-1}).

4.2. Binaries

Spectroscopic binaries are very difficult to detect in a single observation, specially single-lined ones. Clearly, therefore, the number of binary candidates listed in Table 1 is only a *lower limit*. This is consistent with the fact that studies of young open clusters indicate 30% to be a typical percentage of binaries detected in these systems (Garmany et al. 1980; Levato et al. 1991) to be compared to 13% in our sample.

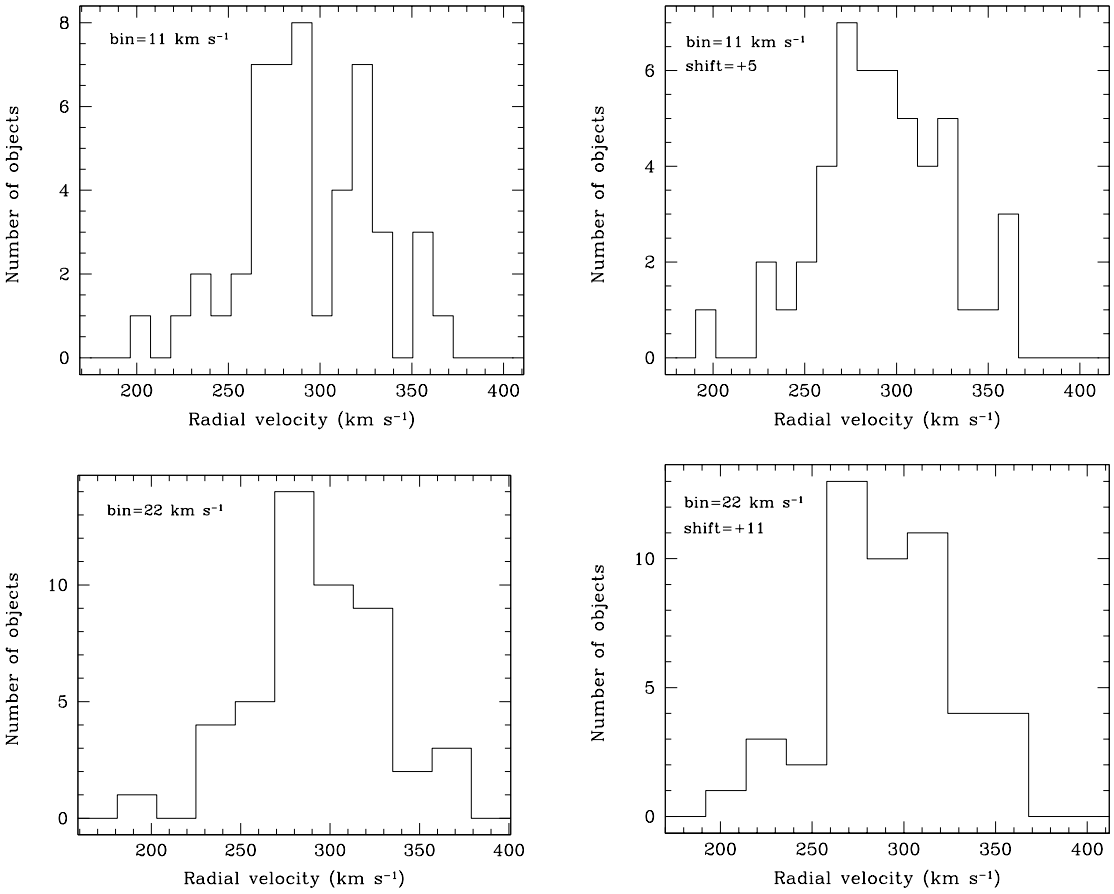

Fig. 2. Distribution of radial velocities for two bin sizes of corresponding to the typical measurement error (11 km s^{-1}, top panels) and twice that error (bottom panels). The histograms are shifted by half a bin between the left and the right panels to illustrate features due to sampling statistics.

Our data alone, therefore, can only be used to determine a lower-limit to the effect of binaries in the observed velocity dispersion of NGC 2070. An upper limit can be obtained using the Montecarlo simulations of Bosch & Meza (1998). Assuming that all the stars in the cluster are binaries with their center of mass at rest within the cluster the models predict a velocity dispersion of $\sigma_{\rm bin} \sim 35$ km s^{-1}. This must be compared with our observed dispersion of 46.5 km s^{-1} including the 55 stars of Table 1 (corrected for observational errors). If we exclude star #1024 with a radial velocity of 510 km s^{-1} which may not be a member of the cluster, the dispersion is reduced to 36.5 km s^{-1}. This result is consistent, within the uncertainties, with the hypothesis that most of our observed velocity dispersion for the cluster is due to binary motions. A (very uncertain) lower limit for the virial motions of the stars in the cluster potential is thus, $\sigma_{\rm vir} = \sqrt{36.5^2 - 35^2} \sim 10$ km s^{-1}.

For comparison purposes we can estimate the expected velocity dispersion assuming the cluster is virialised and the total mass is equal to the upper photometric mass limit from Paper III. From the density distribution derived in the same paper, we estimate a core radius of 0.5 pc which yields $\sigma_{\rm phot} = 18$ km s^{-1}.

4.3. Mass segregation

In Paper II, using only the stars with spectroscopy, we found that the most massive stars in NGC 2070 were preferentially found closer to the center of the cluster. This was interpreted as tentative evidence in favor of the existence of mass segregation, as was originally advocated by Malumuth & Heap (1995). This conclusion was somewhat weakened in Paper III which presented a detailed analysis of the IMF in several rings around the cluster center.

Table 2. Mass segregation.

Mass range	Mean mass	Velocity dispersion
>23.5 $M_\odot$	49.6 $M_\odot$	27.8 km s^{-1}
<23.5 $M_\odot$	19.4 $M_\odot$	36.7 km s^{-1}

The IMF was found to have the Salpeter slope almost everywhere with the exception of the very core where, combining intermediate mass HST data from Hunter et al. (1995) with our high mass end data, we found marginal evidence for flattening. The most important "mass segregation" was found in a "ring" 6 pc away from the cluster center, again weakening the idea that closer to the center we would find the major relative concentration of massive stars. We should point out in the context that, because of the strong density gradient, the half-mass ratio of the cluster is very small. This explains the large concentration of high mass stars in the central parsec of the cluster found by Massey & Hunter (1998).

The two-body relaxation time for NGC 2070[1] is about two orders of magnitude larger than the age of the stars. Therefore, if mass segregation is indeed present it must be primordial (Bonnel & Davies 1998; Elmegreen 2000). In either case, dynamical or primordial, we expect to see a difference in the velocity dispersion of the stars as a function of mass in the sense of it being lower for more massive stars. Moreover, if mass segregation has a dynamical origin, we expect to see energy equipartition between stars of different masses (Spitzer 1969).

We can test these hypotheses by splitting the observed non-binary stars into two equal groups of 24 objects according to their masses as indicated by their spectral types (Table 1). The result is presented in Table 2.

The Fischer F-test on both distributions gives a value of $F = 1.6$ corresponding to a probability of 27% that both samples are drawn from the same parent distribution. Thus, there is tentative, but not conclusive, evidence that the massive stars have a lower dispersion. The ratio of mean energy (M^2) between the two mass bins is $\sim$1.5$\pm$0.1, significantly different from the equipartition ratio, $r = 1$. So if the mass segregation is indeed present, it is most likely not due to two-body relaxation. We remark, however, that our radial velocity data samples very sparsely the inner 10 pc of the cluster, where we concentrated our photometric study, and which contains most of the cluster mass.

5. Conclusions

In spite of the relative low spectral resolution, our data already provide important new results about the dynamical state of the 30 Dor cluster. First, the velocity dispersion is much too large to be due random motions of the stars in the gravitational potential of the cluster. Instead, the observed dispersion seems to be entirely dominated by binary orbital motions. Thus, the first important results is that higher spectral resolution alone is not sufficient to probe the dynamics of the cluster; it is also crucial to have observations with good time resolution in order to find (and exclude) binaries. Second, there is no strong evidence for dynamical mass segregation in the sense of massive stars moving with lower random velocities. If present, the effect is masked by binaries, so again, it is crucial to obtain data for several epochs. Finally, the virial dynamical mass of the cluster is comparable within factors of a few with the photometric mass. Therefore, using a reasonable number of non-binary stars it should be possible to place useful constrains on the IMF slope below 1 $M_\odot$.

The strong conclusion of this investigation, therefore, is that it would be very worthwhile to obtain time resolved spectroscopy of a sample of 100–200 stars in the cluster. The FLAMES integral field spectrograph on the VLT appears ideally suited for such study.

[1] Although for systems with a wide spectrum of masses the relaxation times are much shorter (Inagaky & Saslaw 1985).

References

Aller, L. H., Appenzeller, I., Baschek, B., et al. 1982, in Landolt-Bornstein: Numerical Data and Functional Relationships in Science and Technology

Bonnell, I. A., & Davies, M. B. 1998, MNRAS, 295, 691

Bosch, G., & Meza, A. 1998, IX Latin American Regional Meeting, Rev. Mex. Astron. Astrofis. Conf. Ser., 11, 29

Bosch, G., Terlevich, R., Melnick, J., & Selman, F. 1999, A&AS, 137, 21 (Paper II)

Brown, T. M. 1990, ASP Conf. Ser., 8, 335

Clarke, C. J. 2001, IAU Symp., 207, in press

Elmegreen, B. G. 2000, ApJ, 539, 342

Garmany, C. D., Conti, P. S., & Massey, P. 1980, ApJ, 242, 1063

Hunter, D. A., Shaya, E. J., Hoiltzmann, J. A., et al. 1995, ApJ, 459, L27

Inagaki, S., & Saslaw, W. C. 1985, ApJ, 292, 339

Levato, H., Malaroda, S., Garcia, B., et al. 1991, Ap&SS, 183, 147

Massey, P., & Hunter, D. A. 1998, ApJ, 493

Malumuth, E. M., & Heap, S. R. 1995, AJ, 107, 1054

Selman, F., Melnick, J., Bosch, G., & Terlevich, R. 1999a, A&A, 341, 98

Selman, F., Melnick, J., Bosch, G., & Terlevich, R. 1999b, A&A, 347, 532 (Paper III)

Spitzer, L. 1969, ApJ, 158, L139

Walborn, N. R. 1991, The Magellanic Clouds, IAU Symp., 148, 145

.

Index